Evolution of the Martian Atmosphere and Hydrosphere based on Microprobe Studies of Martian Meteorites

A thesis submitted to the University of Manchester for the degree of Doctor of Philosophy in the Faculty of Science and Engineering

2002

Greg Holland

Department of Earth Sciences

Contents

List of Tables

List of Figures

Abstract

This thesis is a study of the isotopic and chemical characteristics of pre-terrestrial secondary minerals in Martian meteorites, with a view to constraining the environmental conditions on early Mars and its subsequent evolution. The majority of this work is concerned with the Martian meteorite Allan Hills 84001 (ALH84001) – the only known sample of ancient Martian crust.

High spatial resolution (as small as 10μm diameter) hydrogen and oxygen isotope measurements were obtained for ALH84001 carbonate using the Manchester and UCLA ion microprobes. Initial carbon isotope measurements were also conducted at Manchester. Textural and chemical studies of these secondary minerals by SEM and EPMA show commonly observed carbonate rosettes surrounded by previously unobserved Ca-rich carbonate (up to 80% Ca). Chemical and isotopic heterogeneity and encapsulation of carbonates rosette fragments by unfractured Ca-rich carbonate suggests the Ca-rich carbonate generation was deposited by low temperature hydrothermal fluids after the metasomatic episode that formed carbonate rosettes. Oxygen isotope data reflects the unique nature of the carbonates presented here ($\delta^{18}O_{SMOW}$ −10±2‰ compared to previous lowest values of 5±2‰ for carbonate rosettes). δD_{SMOW} ~+500‰ from the $\delta^{18}O$ carbonate proves the Martian origin.

These low $\delta^{18}O_{SMOW}$ values preclude the possibility of high temperature origin for ALH84001 carbonate. Kinetic isotopic fractionation during remobilisation and decarbonation of previously deposited carbonate followed by closed system Rayleigh fractionation can theoretical explain these low values but is not observed in terrestrial impact derived carbonate. Low temperature source fluids would be in the region of $\delta^{18}O_{SMOW}$ −40‰, similar to present day Antarctica due to rain-out of $\delta^{18}O$ enriched water during transport from equator to pole. Thus it is tentatively suggested that an analagous process operated at some time in Martian history, implying a substantially more massive (and Earth-like) atmosphere than is currently observed on Mars.

TOF-SIMS halogen studies have tentatively identified chromite associated with carbonate rosettes as the primary iodine carrier in ALH84001 (iodine may be useful as a biosignature). TOF-SIMS analyses of ALH84001 carbonate rosettes also suggests chlorine zoning from core to rim which is consistent with an evaporative origin for the carbonate rosettes.

Declaration

No portion of the work referred to in the thesis has been submitted in support of an application for another degree or qualification of this or any other university or institute of learning.

Notes on Copyright

Acknowledgements

I would like to thank my supervisors Prof. Grenville Turner, Dr. Ian Lyon, and Dr. Jamie Gilmour for their input into my understanding of all things Martian, and Dr. Ray Burgess for his supportive role as my advisor. I would also like to thank Dr. Ian Lyon and Dr John Saxton for patiently teaching me the mystical ways of the ion probe and Bev Clementson and Dave Blagburn for keeping it running.

A thankyou is also due to Dave Plant for help with the electron probe work and to collaborators Ben Cliff and Dr. Nick Lockyer at UMIST, and Prof. Kevin McKeegan and Dr. Chris Coath at UCLA. Dr. Ian Franchi is thanked for swift analyses of carbonate standards.

Most importantly, a heartfelt thankyou goes to all my family and friends who have supported me in the trials and tribulations of the last three (and a three quarters) years: I will not name names for fear of leaving people out. I imagine it to be a similar (but not as fortuitous) problem to that facing lottery winners who are suddenly left with the thorny problem of who deserves a windfall and who doesn't.

A final thankyou goes to PPARC for funding this studentship as well as paying for both a summer school in Austria and lab work at UCLA.

Chapter 1

Introduction

There is much evidence that the surfaces of Mars and Earth may have harboured similar environments during the early stages of planetary evolution. Images of the ancient cratered terrain on Mars, acquired by the Viking and Mars Global Surveyor spacecraft show compelling evidence of ancient water-cut valley networks, the possibility of an ancient ocean covering most of the northern hemisphere, evidence for sub-surface volatile reservoirs from impact crater ejecta and reduced erosion rates in more recent times. What appears to have been an environment carved by liquid water and a substantial atmosphere approximately 4Ga ago has evolved into a 6mbar present day Martian atmosphere containing only 300 p.p.m. of water (Owen, 1992). Clearly the Martian climate has evolved greatly over the past 4.5Ga in a markedly different way to both Earth and Venus.

Fundamental to understanding the timing and extent of processes involved in the evolution of the Martian hydrosphere and atmosphere are the twenty-six Martian meteorites. At present, these serve as our only samples of Mars. Fortunately they sample several periods of Martian history, spanning the majority of geological time from 4.5Ga ago to 180Ma ago. Within these meteorites are secondary mineral assemblages containing information on the nature of the volatile reservoirs from which they formed.

Isotopes are useful tools for tracing the history of Martian volatiles because they are fractionated by a variety of chemical and physical processes. Furthermore, these secondary mineral assemblages can also provide information on the depositional environment in which they were formed. To this end, a study of new textures in

ALH84001 has been performed to help better constrain the early Martian climate and provide information on the deposition environment of ALH84001 carbonates, which is still an unresolved question.

1.1 Aims and objectives

The principle aims of this research are:

- To perform petrographic, mineralogic and geochemical study of ALH84001 with the aim of understanding the carbonate textures and geological history of this meteorite.
- To use high spatial resolution ion microprobe in dynamic secondary ionization mass spectrometry mode to obtain oxygen and hydrogen and carbon isotopic compositions of ALH84001 carbonate.
- To use time-of-flight secondary ionization mass spectrometry to measure halogen concentrations in a search for clues to the regime of ALH84001 carbonate formation.
- To test the feasibility of performing carbon isotope analyses by ion microprobe.
- To place new ALH84001 carbonate oxygen isotope data in the context of previous work on ALH84001 and other martian meteorites, developing a coherent framework for the evolution of the martian climate by suggesting answers to the questions:
- *What were the conditions under which ALH84001 carbonate formation took place and what has been the geological history of ALH84001 since then?*
- *What were the environmental conditions approximately 4Ga ago on Mars? Although it seems clear that a more substantial martian atmosphere existed in the past, was it warm and dense, possibly comparable with Earth?*

- *If a warm, dense atmosphere once existed, what were the sources of the volatiles: solar wind? Outgassing? Comets?*
- *If a warm, dense atmosphere once existed, what was the fate of these volatiles: were they lost to space or fixed in surface minerals such as carbonates or a subsurface reservoir?*
- *How much exchange occurred between the different volatile reservoirs?*

1.2 Outline of thesis

The initial chapter of this thesis is a review of what is known about the evolution of volatiles on Mars using spacecraft and ground based observations. This is followed by a discussion of models invoked to explain these observations and the effects these models impart to martian isotopic ratios.

Chapter 3 is a discussion of the evidence for the conclusion that ALH84001 and the other SNC's are martian in origin.

Chapter 4 introduces the petrography, mineralogy and geological history of the martian meteorites, placing them in the context of a global perspective of Mars.

Chapter 5 is a detailed description of ALH84001 to establish both the geological context of the chemical and isotopic data to be presented in later chapters and to summarise the present state of knowledge regarding the origin of ALH84001 carbonates.

Chapter 6 is a review of the stable isotope studies of martian meteorites and the conclusions drawn from this about martian volatile evolution. Constraints from meteorite studies are then compared to theoretical global models.

Chapter 7 describes the procedures involved in sample preparation and characterization. It includes descriptions of the Scanning Electron Microscope (SEM)

and Electron Microprobe Analyser (EPMA) and also deals with analytical procedure and standardization of the Manchester and UCLA ion microprobes and the UMIST TOF-SIMS instrument (hereafter called Bio-TOF).

Chapter 8 presents the petrographic and mineralogic and chemical data of the SEM and EMPA. The implications of this data for ALH84001 carbonate formation and for martian volatile evolution in general are discussed.

Chapter 9 presents the oxygen, hydrogen and carbon isotopic

Chapter 10 describes a variety of models to account for oxygen and hydrogen isotopic data and attempts to place these data in a global context.

Chapter 11 is a brief discussion of inferences that may be made from initial isotopic carbon measurements obtained in this study.

Chapter 12 describes halogen analyses using Bio-TOF mass spectrometer. The implications of this data for the process of ALH84001 carbonate formation and for martian volatile evolution in general are discussed.

Chapter 13 presents the main findings of this research by attempting to answer the initial questions posed in the introduction.

Chapter 2

The Geological history of Mars

2.1 The stratigraphic record

Mariner 5 revealed the first evidence of major geological events on Mars and was used to the basis of Martian chronostratigraphy. These three major chronostratigraphic divisions are the Noachian, the Hesperian and the Amazonian Epochs. All epochs are dated from to crater impacting rates. As higher resolution global coverage maps were acquired by Mariner 9 and Viking 1 & 2 orbiters, an effort was made to further divide these broad time periods using Tanaka (1986) classification schemes and an impact crater flux model by Neukum *et al.* (1976).

Table 2.1: Martian epochs from crater densities. Data from Tanaka (1986) based on Neukum-Wise model.

Epoch	**Crater Density** N(D) = no. >(D) per 10^6km^2 N(2km)	N(5km)	N(16km)	**Absolute Ages** (Ga)
Late Amazonian	<40			0.70-0.00
Middle Amazonian	40-150	<25		2.50-0.70
Early Amazonian	8150-400	25-67		3.55-2.50
Late Hesperian	400-750	67-125		3.70-3.55
Early Hesperian	750-1200	125-400	<25	3.80-3.70
Late Noachian		200-400	25-100	4.30-3.80
Middle Noachian		>400	100-200	4.50-4.30
Early Noachian			>200	4.60-4.50

The Martian surface is broadly classified into two very different regions: the Southern Highland and the Northern Lowlands. From similar size frequency distributions of craters on the Moon and Mars (Neukum *et al.*, 2001), it is inferred that

the Southern Highlands date from the earliest epoch of Mars, and are therefore Noachian and Hesperian in age. This region contains evidence of major multi-ringed impacts with discrete lobes of ejecta implying subsurface fluids, extensive erosion features, large scale outwash channels (>50km across) apparently draining into the northern lowlands, and small scale valley networks (<5km across) that are probably the result of flowing water. They are mostly at elevation between 1-4km above Martian datum. The global dichotomy between northern and southern hemispheres can clearly be seen in figure 2.1

In contrast, the Northern Lowlands are almost all below Martian datum. The crater distribution is highly varied implying that the age of the northern lowland varies substantially and the plains have continually resurfaced throughout much of Martian geological history. These plains are Hesperian to Amazonian in age and are of volcanic or sedimentary origin. The plains of volcanic origin are clearly visible with superimposed flows of lava outpouring from the Tharsis and Elysium volcanic centres. The majority of the northern plains are fractured and textured, probably due to ground ice and flood sedimentation.

Highly chaotic highland material is found at the boundary between the two regions where, in the late Hesperian and into the Amazonian, domes and shields developed in the high standing Tharsis and Elysium regions. The massive tectonic canyon system of Valles Marineris formed and outflows poured from the canyons in the chaotic highland terrain to the lowland plains. Clearly, a major dichotomy exists between northern and southern hemispheres that has been shaped by a variety of processes. Table 2.2 below shows the areal extent of these different geological environments on Mars.

Table 2.2: areal extent of surface morphologies adapted from 'Mars' Kieffer *et al.* (1992)

Geologic Unit	Area ($10^3 km^2$)
Surficial material e.g. sands, slides, polar deposits	5,993
Channel-system material e.g. valleys, floodplains	4,326
Lowland terrain material i.e. northern plains	30,912
Highland terrain material i.e. plateau high-plains	81,570
Ubiquitous material e.g. impact craters, ridged plains	21,197

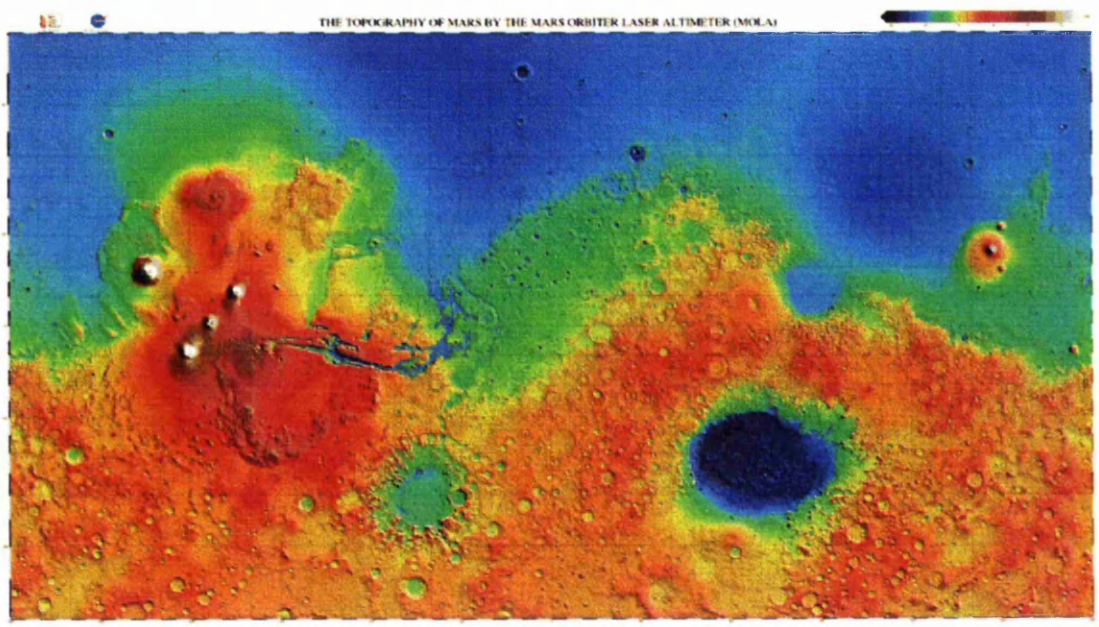

Figure 2.1: topography map from Mars Orbiter Laser Altimeter on Mars Global Surveyor. Note the high Tharsis region, the regional low of the Hellas impact basin and the global dichotomy in elevation and cratering between northern and southern hemispheres. (Image credit: MOLA science team)

2.2 Evidence for volatiles

Evidence for evolution of the hydrosphere and atmosphere of Mars is primarily from images acquired by orbiting spacecraft, principally Mariner 9, Viking 1& 2 orbiters and Mars Global Surveyor. These spacecraft have revealed many types of geological structure formed by surface and sub-surface volatiles from which a qualitative geological history of volatiles can be surmised. Therefore evidence for volatiles shall be dealt with in chronological order from the Noachian to the present day.

2.2.1 Valley networks

Owing to the scarcity of Martian plate tectonic activity and therefore of global volcanic resurfacing, almost all the martian surface is older than 3Ga and >50% of the surface (the southern highlands) is older than 4Ga (Tanaka *et al.*, 1986). Therefore, the most convincing evidence of ancient global climatic change on Mars may be evidence of a marked and ubiquitous change in the erosion rates of craters. Wind erosion and fluvial erosion / deposition (i.e. surface runoff) both play significant roles in crater degradation. The contrast between the extent of erosion of Noachian age craters and those of early Hesperian age is clear in many Viking images. Ejecta debris is still visible surrounding Hesperian age craters although it is universally absent on the surface surrounding Noachian age craters. The implication is that a substantially more dense atmosphere e.g. (2-10bars of CO_2 from Krasnopolsky *et al.* (1996)) existed in Martian geological history but was lost at around 3.8Ga. Analysis of craters at $^{+}$/- 30° latitude suggests that degradation ceased earlier at higher elevations (3-4km, Late Noachian) than lower elevations (1-2km, Early Hesperian) (Craddock *et al.*, 1998). This is consistent with desiccation and reduced precipitation at higher latitudes in an

environment that is rapidly losing its volatile reservoir. Numerous Viking images show obvious erosion of valley networks dated at 4.0Ga, but those formed at 3.5Ga show almost no erosion from that time until present (Golombek and Bridges, 2000).

In addition to the general trend of decreasing erosion with time during early Mars, there is evidence of early climate fluctuations: the morphology of some equatorial highland craters appears to record precipitation with no fluvial erosion. This has been interpreted as a drier period of early Mars when the local regolith was no longer saturated, hence the lack of water runoff (Craddock *et al.*, 1999).

Valley networks of late Noachian age are widely distributed across the Martian surface. Of the 827 valley networks presently mapped, 763 incise into solely Noachian age rocks, 34 cut Hesperian age or older units and a further 34 erode only Amazonian age surfaces (Carr, 1997). These Amazonian age networks are almost all in close proximity to Amazonian volcanoes and are presumably caused by localised volcanically associated hydrothermal streams or melted ground ice due to volcanic activity and are not necessarily climate dependent.

Although valley networks have similar morphologies to terrestrial river channels, it is not clear that the dominant formation process is erosion by flowing streams at the surface. Costard and Gaultier, (1998) shows morphological similarities between terrestrial and martian channels but other contributing factors to valley network erosion may include groundwater fed streams, hydrothermal systems, episodic small scale floods and ice/water mass wasting. All these processes, to varying degrees, may be invoked without requiring a substantial atmosphere. However. these processes do require the presence of water at the high elevations (4km) of many water network source regions, implying an active, global hydrologic cycle that appears to require a substantially different climate to that at the present Martian surface.

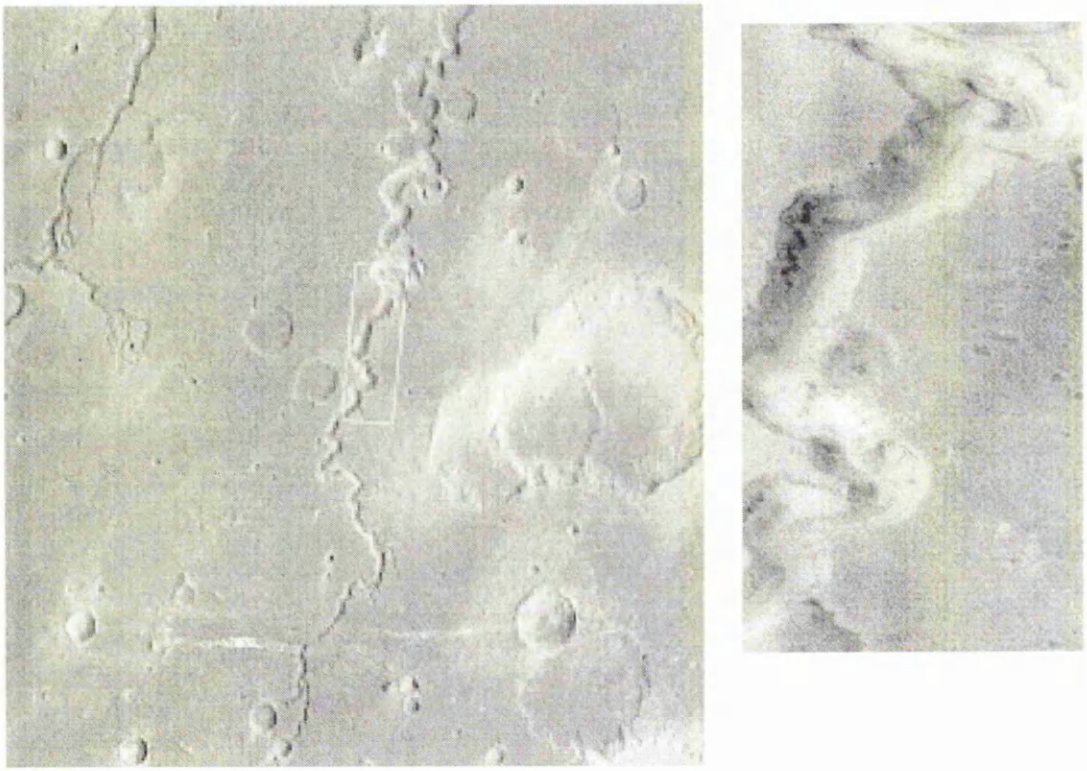

Figure 2.2: A small scale drainage channel which may be carved by flowing water at the surface. The valley shown on the right is 2.5km wide. (NASA/JPL/Malin Space Science Systems).

In contrast to large scale valley networks, figure 2.2 is an example of a much smaller scale fluvial channel. The greatly reduced volumes of water involved make this fluid channel far more susceptible to global climate. Thus it appears, temporarily at least, that the Hesperian period had a substantial atmosphere.

Figure 2.3: Mars Orbiter Camera image of an anastomosing fluvial channel south of Cerberus Rupes containing streamlined islands indicative of erosion by high volumes of water. Image is 4km across. Note also the ripples normal to the flow direction indicating high energy water flow (NASA/JPL/Malin Space Science Systems).

2.2.2 Outflow channels

The development of large outflow channels is predominantly a phenomenon of the Hesperian epoch. Outflow channels do not require an appreciably different atmosphere from the current Martian atmosphere because the large volumes of water (10^7–10^9 m^3 sec^{-1}) would render sublimation unimportant (Carr, 1996). Therefore, their Hesperian age does not require a continued presence of the substantial atmosphere inferred for fluvial channels. Impact craters superimposed on the flood channels suggest a wide variety of ages, implying minimal climate dependence of such a large body of water.

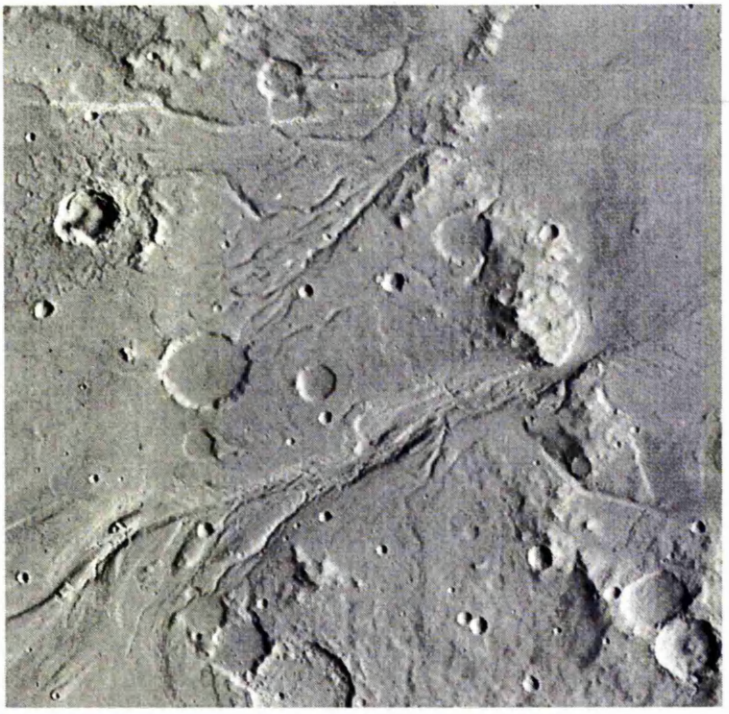

Figure 2.4: Outflow channels that start in the old cratered surface of Lunae Planum and discharge into the younger plains of Chryse Planitia, shown on the right side of the image. The area shown is 225 kilometers across. (courtesy JPL/NASA/Caltech)

Many of the outflow channels are sourced in regions of chaotic terrain where the regolith appears to have been deformed and disrupted beneath the surface. The implication is that massive groundwater bodies acted as flood sources. Groundwater flow into the equatorial canyons from plateaus that surround them may also have led to damming and catastrophic release of flood water. Indeed the presence of ice may have been required to allow the build up of pressure.

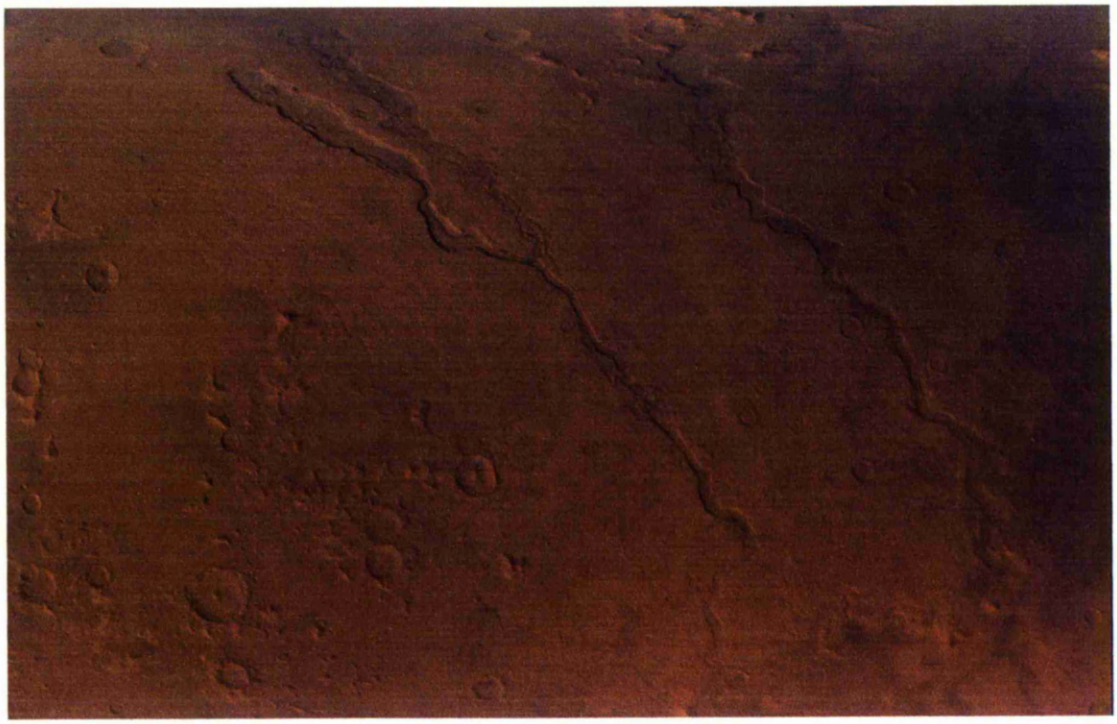

Figure 2.5: Three major valley systems east of the Hellas plains. From left to right, the first major valley, Dao Vallis. Niger Vallis joins Dao Vallis just above the center of the frame. Harmakhis Vallis is to the right. These valleys are believed to have been formed by large outbursts of liquid. The valleys are 1 km deep and a maximum of 40 km wide. Located around 40°S, 270°W, the picture covers an area approximately 800 km across and is illuminated by sunlight from the lower left. North is toward the left. (NASA/JPL/Malin Space Science Systems).

2.2.3 Lakes and oceans

Large bodies of water must have formed at the end of the large outflow channels. It is not known whether these bodies of water froze as lakes or flowed together to form oceans. A candidate basin is the Utopia Basin, which would serve as the catchment area for outflow channels emptying into the northern lowlands. Mars Orbiter Laser Altimeter (MOLA) data has recorded regular topographic terraces in this basin at an elevation of 4350m (Head *et al.*, 1999) (figure 2.6). This is also the height at which additional inflow of water would spill over into the North Polar Basin, hence this inferred shoreline should remain relatively constant. Owing to this coincidence, this basin is inferred to be a large standing body of water in a previously formed impact basin (figure 2.7). These volumes of water are no longer present near the surface and it is difficult to envisage such a large volume of water near the surface forming an ocean under present climatic conditions. Recently, this interpretation has been challenged by Withers and Neumann (2001), who claim that the postulated shorelines are tectonically induced wrinkle ridges. Thus the extent to which the martian surface was covered with liquid water is still unclear.

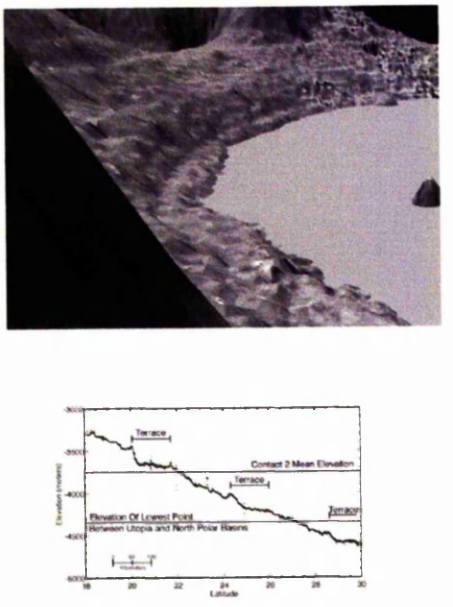

Figure 2.6: terracing of postulated shorelines in Utopia Basin on the margins of a possible north polar ocean from (Head *et al.*, 1999)

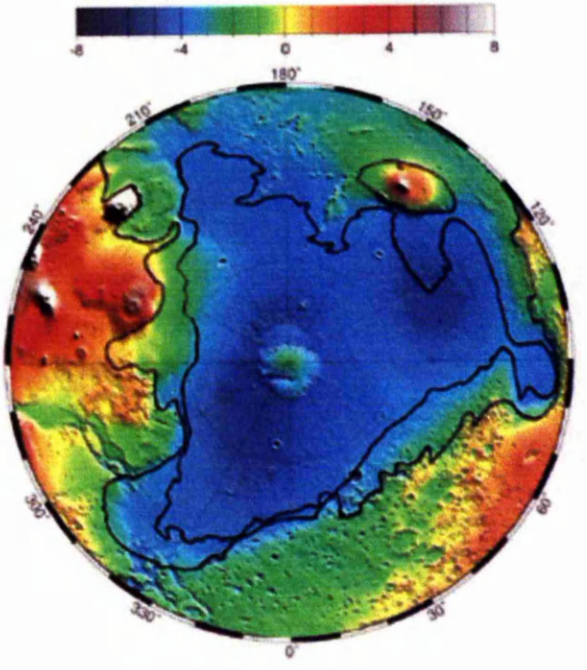

Figure 2.7: Hypothesised Mars northern ocean, the largest of the possible global drainage basins (Head *et al.*, 1999). The Utopia Basin is center-right edge.

2.2.4 Duricrust

The 'duricrust' present at both Viking Lander 1 (VL-1) and Viking Lander 2 (VL-2) sites appears to consist of a layer of indurated salts, implying movement of salts and fluids through the Martian regolith. It is unclear whether this process still operates at the Martian surface because the regolith is expected to be lacking in volatiles to a depth of 10's of metres, at least in the equatorial regions where the temperature is always greater than the CO_2 frost point. At the VL-1site, the duricrust is inferred to be deposited after the Hesperian bedrock, implying climate change possibly substantially later than the end of the Noachian period.

2.2.5 Regolith volatiles

Although much evidence suggests extensive loss of Martian volatiles, there is evidence of volatiles still present on Mars. The polar caps extend to ~10° from both poles and are several kilometres thick, hence they are a massive reservoir for CO_2 and H_2O. There is also a general softening of terrain morphology at high latitudes. This is attributed to creep of near surface ground ice which is present at high latitudes. The almost universal presence of multiple lobate flows (figure 2.8) surrounding craters >5km in diameter suggests ground ice or water almost everywhere at a depths of a few hundred meters. The abundance of these multiple lobe craters in the region 0° to 25°N and 315°W to 10°W (Barlow *et al.*, 1999) coincide with the proposed hematite deposit from MGS Thermal Emission Spectrometer (TES) data (Christensen, 1998), which may have formed due to hydrothermal activity. This would be consistent with the hypothesis that liquid water reservoirs cause multiple lobe ejecta blankets. Thus, water may exist as ice in the shallow impact-brecciated regolith or a groundwater in the deeper, porous megaregolith beneath the permafrost layer.

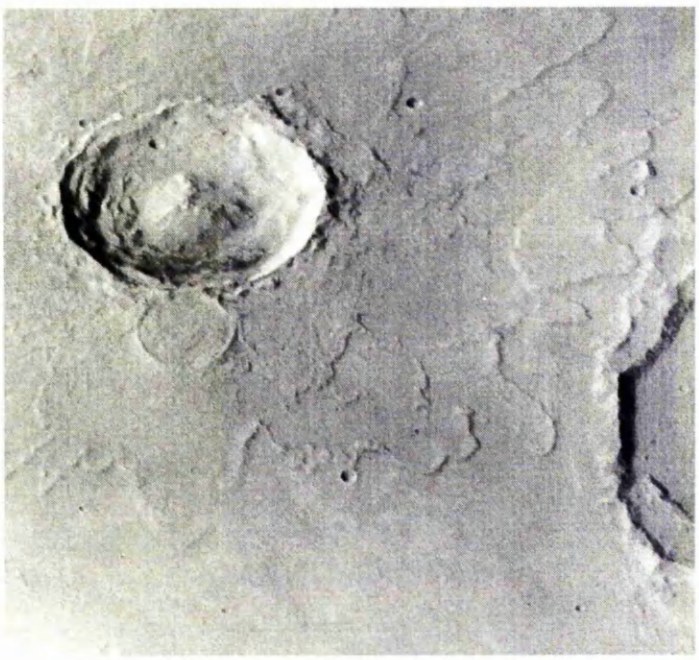

Figure 2.8: Impact crater Yuty (18 kilometers in diameter) This style of ejecta deposit is believed to form when an impacting object rapidly melts ice in the subsurface (courtesy JPL/NASA/Caltech)

The possibility of present day volatile reservoirs in the Martian crust has been supported by recent images from MGS showing apparent recent fluvial activity on the surface of Mars (figure 2.9) and from the Mars Odyssey high energy neutron detector (figure 2.10)

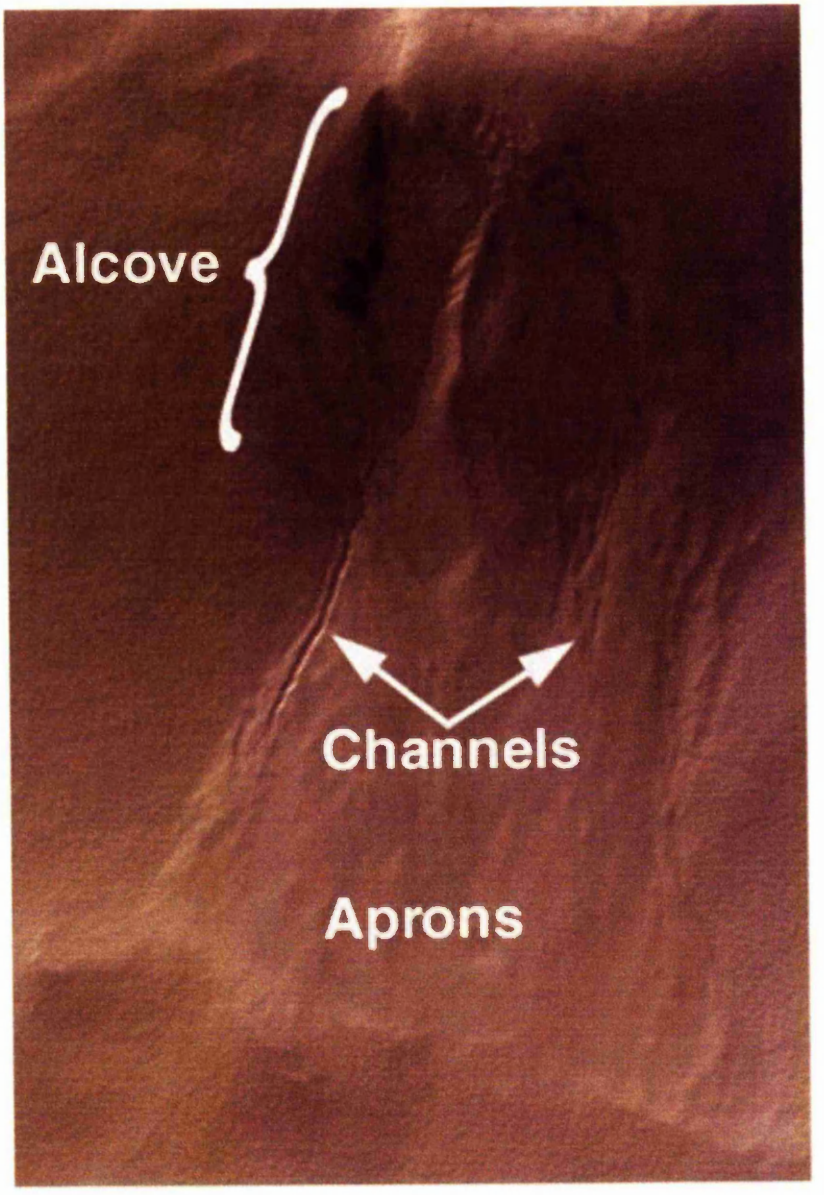

Figure 2.9: MOC image of evidence for very recent fluid flow on the surface of Mars. (NASA/JPL/Malin Space Science Systems) (Image is approxmately 10km across).

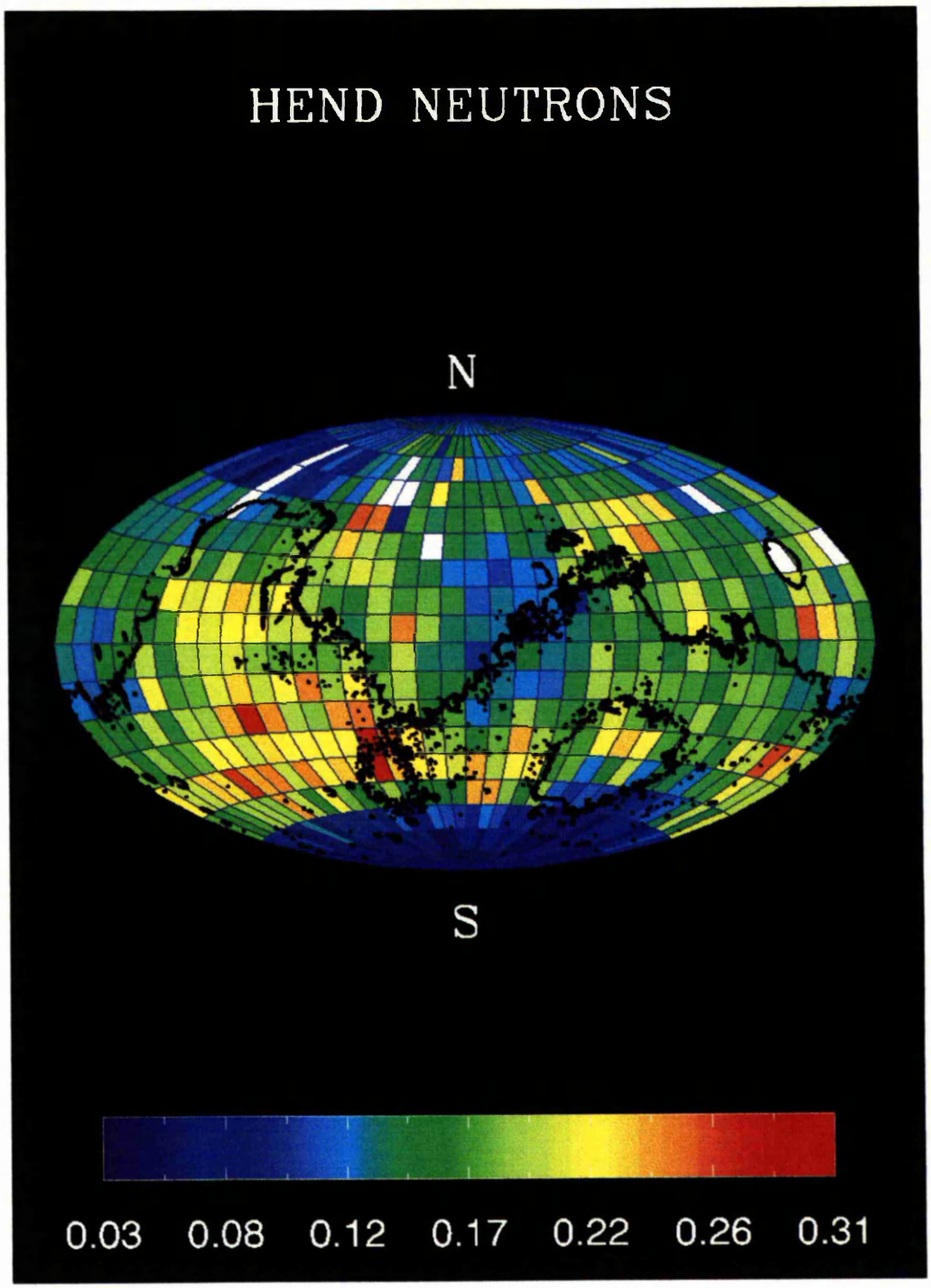

Figure 2.10: Hydrogen distribution in the near surface martian regolith. Blue is high hydrogen content in the upper 3m of regolith. The hydrogen is inferred to be water (courtesy NASA/JPL/University of Arizona)

2.3 Early Mars climate models

Early 1D (Pollack *et al*, 1979) and 2D (Hoffert *et al.*, 1981) models for Mars climate evolution were calculated using present day solar luminosities. With a refined model incorporating solar flux of 0.7 times present solar luminosity, Pollack *et al.* (1987) calculated an atmosphere composing 5bars of CO_2. With the addition of small quantities of active greenhouse gases such as NH_3 and CH_4 these CO_2 concentrations may be reduced by an order of magnitude. Although this may be useful way of producing temperatures >0°C required for the presence of liquid water, the high photolysis rates NH_3 and CH_4 make significant amounts of these reduced gases unlikely. A more feasible means of increasing the greenhouse effect is infrared scattering of CO_2 ice clouds, which can be reduce the amount of CO_2 required to 0.5 – 2bars, depending on water vapour concentrations (Forget and Pierrehumbert, 1997), although recent work (Haberle, 1998) suggests that CO_2 ice cloud scattering is not sufficient to produce an appreciable greenhouse effect.

2.4 Mechanisms of climate evolution and their isotopic effects

A number of competing processes are responsible for the Martian atmospheric evolution, the magnitude of which change with time (fig. 2.11).

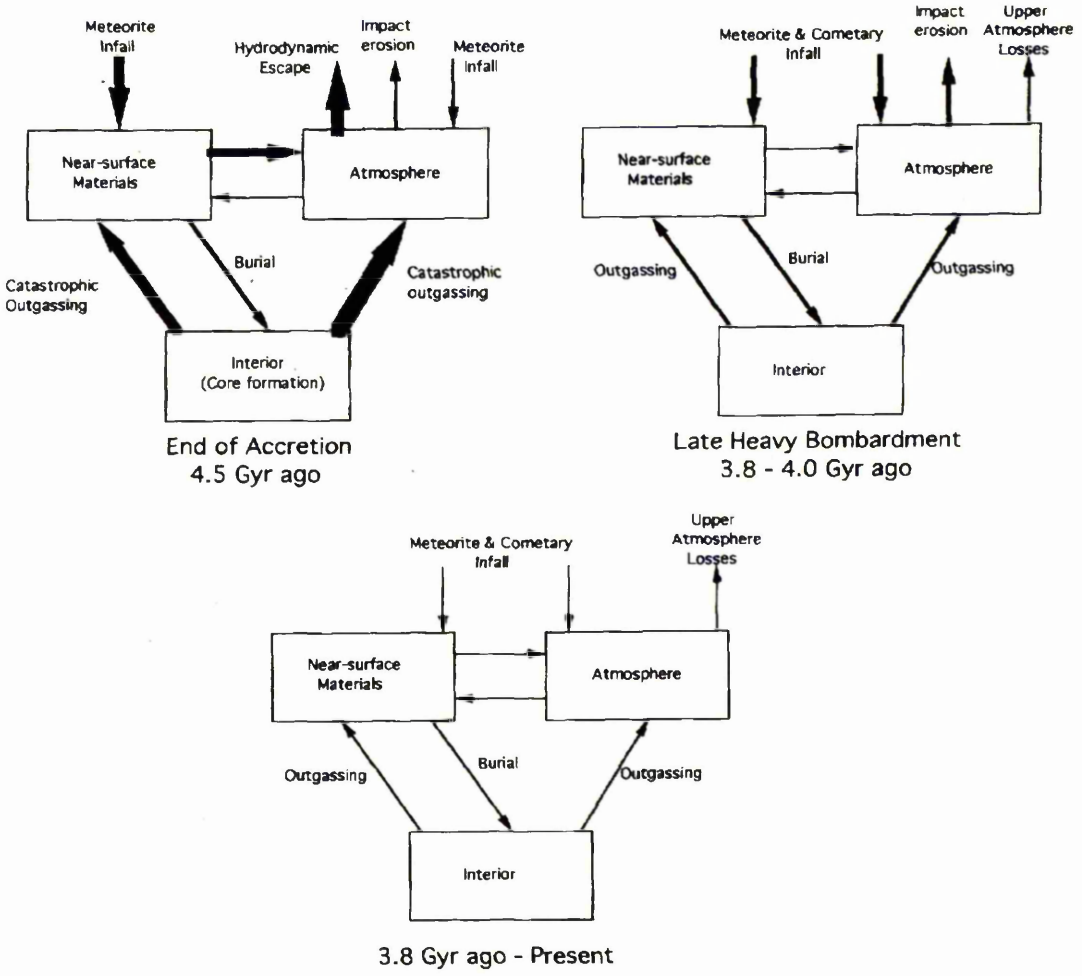

Figure 2.11: Loss / gain processes in the Martian atmosphere (from Carr, 1996)

These processes have produced the present day isotopic differences between Earth and Mars shown in table 2.3.

Table 2.3: Isotopic measurements of martian volatiles reproduced from Bogard *et al.*, (2001 and references therein)

Isotopic Ratio	**Comparison Standard**	**Atmosphere Viking**	**SNC-Glass**	**ALH84001**	**Interior SNCs**
$^{36}Ar/^{132}Xe$	ratio	350	900±100	50	≤5
$^{84}Kr/^{132}Xe$	ratio	11	20.5 ±1.5	6	<1.1
$^{2}H/^{1}H$	‰-terrestrial	~450*	~440	78	~50
$^{15}N/^{14}N$	‰-terrestrial	62	<50	0.7	-30
$^{36}Ar/^{38}Ar$	ratio	5.5±1.5	≤3.9	≥5	≥5.26
$^{40}Ar/^{36}Ar$	ratio	3000±500	~1800	≤128	≤212
$^{86}Kr/^{84}Kr$	‰-solar	n.r.	~0	~0	~0
$^{129}Xe/^{132}Xe$	ratio	~2.5	~2.6	2.16	<1.07
$^{136}Xe/^{130}Xe$	‰-solar	n.r.	~27	~0	~0
$^{13}C/^{12}C$	‰-terrestrial	0 ±50	?	~41	-30+40**
$^{18}O/^{16}O$	‰-terrestrial	0 ±50	F	F	F

F represents wide variation due to fractionation during chemical interactions

*Ground-based spectra measurement

**$^{13}C/^{12}C$ range measured in SNCs

2.4.1 Gain processes

Outgassing

Outgassing of the planetary interior is undoubtedly a major source of volatiles. Clayton and Mayeda (1988) assume high temperature (1000°C) outgassing of a CO_2-H_2O mixture by the interior. High temperatures allow equilibrium of the volatiles with each other and martian crust. On cooling the volatiles are inferred to maintain equilibrium with each other but not crustal silicate. With the appropriate fractionation factors, these values are then used to identify plausible temperatures and ratios of H_2O-CO_2 (hereafter called X= (H_2O/H_2O+CO_2) for producing secondary mineral assemblages in SNC's, as will be discussed later.

Cometary / meteoritic veneer

The importance of a late veneer of cometary and meteoritic material is not well constrained. Clearly, heavy bombardment occurred in the inner solar system for several hundred million years and brought material to the terrestrial planets. However, from an isotopic perspective, the effects of this are not clear. Solar nebula δD is approximately – 800‰$_{SMOW}$ of the present day terrestrial value (e.g. Mahaffy *et al.*, 1998; Geiss and Gloeker, 1998) whilst cometary H_2O has δD of approximately +1000‰$_{SMOW}$ (BockeLee-Morvan *et al*, 1998; Meier *et al*, 1998). Given that the initial martian D/H is unknown, any mixture of solar nebula and cometary material may have resided in early Mars and subsequently evolved to make a martian atmosphere of 4000‰ (Krasnopolsky *et al.*, 1998). The importance of cometary material in forming the Earth's hydrosphere is also unknown due to the uncertainties in the initial terrestrial D/H value. However, given that the similarities in relative xenon isotope abundances (excluding radiogenic ^{129}Xe) between Earth and Mars are completely outside the limits set by xenon in chondrites, a significant volatile contribution from cometary material seems likely (Owen, 2001). In addition, isotopically light nitrogen suggests a significant contribution from icy planetesimals (Owen and Bar-Nun, 2000).

2.4.2 Loss processes

Hydrodynamic escape

One of the principal loss processes in the early Martian atmosphere is loss to space by hydrodynamic escape. To account for mass fractionation of Xe isotopes it is postulated that this occurred when high hydrogen fluxes from the top of the atmosphere cause a hydrogen 'wind' which drags heavier atmospheric constituents out of the atmosphere (Pepin, 1994). This can have occurred only in the first few hundred million years after planetary accretion when the primitive hydrogen atmosphere is thought to

have been bombarded by extreme ultra-violet (EUV) radiation from the young sun. Hydrodynamic escape is the process invoked to explain the fractionation of noble gases, particularly enrichment of ^{134}Xe and ^{136}Xe, in the Martian atmosphere.

Impact erosion

Another important loss process for the Martian atmosphere is impact erosion. Mars has a smaller mass and therefore a smaller escape velocity than Earth, hence it is more susceptible to loss of atmosphere by large impacts. Melosh and Vickery (1989) calculate that, due to the lower escape velocity of Mars, an impacting silicate body 3km in diameter is sufficient to remove the entire atmosphere above the plane tangent to the point of impact. Assuming typical solar system bombardment rates, they calculated an atmosphere 100 times denser (~1bar) than at present although they argue that atmospheric erosion did not occur during accretion of Mars. This process is inferred to have removed 99% of the atmosphere in the first 0.8Ga of Martian geological history. Using crater density to integrate atmospheric loss after accretion, Brain and Jakosky (1998) revised this loss to a substantially lower value of only 60mbars. Clearly there is no conformity on the importance of impact erosion. It is important to note that although this process removes the atmosphere without mass fractionation. It may indirectly lead to depletion of ^{18}O (in water) in the Martian atmosphere and surface because it causes preferential removal of CO_2 which may have been previously enriched in heavy oxygen.

Burial

If liquid was present on the Martian surface in the Noachian, CO_2 would have reacted with crustal minerals producing carbonates. Extensive impacting from the heavy bombardment during this period (Turner *et* al., 1997) would then have buried these carbonates within the crust. Potentially the majority of a CO_2 atmosphere could be sequestered into the martian regolith early in martian history (Fanale *et al.*, 1992).

Griffith and Shock (1995, 1997) calculate that up to 1bar of CO_2 may be present in subsurface carbonates due to past hydrothermal activity whilst Pollack *et al.* (1987) infer from carbonate abundances in dust that 5bars of CO_2 exists in the upper 10km of regolith. However, as Saxton *et al.* (2000) demonstrated, this makes a difference of only a few permil to the isotopic composition of oxygen in the remaining hydrosphere.

Thermal escape

Loss by thermal escape occurs if Maxwellian distribution of energy permits the escape of the most energetic molecules or atoms to space. When this occurs diffusive height separation by mass above the homopause leads to isotopic fractionation. This can produce not only isotopic fractionation of $^{18}O/^{16}O$ but also permits non-mass dependent fractionation when accompanied by photochemical fractionation (Jakosky, 1993; Saxton *et al.*, 2000) producing enhanced $\Delta^{17}O$ as observed in secondary minerals of SNC's. The enrichment of ^{15}N in the Martian atmosphere can also be explained by this loss process (Zahnle *et al.*, 1990).

Non-thermal escape

Non-thermal escape occurs when solar wind impinges on the upper martian atmosphere and sputters ions into the magnetotail which then impacts the ions into atmospheric molecules at the exobase, causing loss to space. Since gravitational separation enriches lighter isotopes at the exobase, this process also leads to isotopic fractionation. For more abundant ions, loss due to sputtering by O^+ pickup ions has been estimated at up to 3×10^6 cm^{-2} s^{-1} by Kass and Yung (1995), leading to a total oxygen loss over the last 3.8Ga of 164 mbars (Haberle *et al.*, 1994).

Photochemical effects

Photochemical fractionation occurs in Earth's atmosphere via gas phase chemical reactions of atmospheric species formed from interaction with solar radiation. In the Earth's atmosphere, O_3 (Thiemens, 1999), H_2O_2 (Savarino and Thiemens, 1999), CO (Huff and Thiemens, 1998), O_2 (Luz *et al.*, 1999) and NO_2 (Cliff and Thiemens, 1997) also undergo mass dependent chemical fractionation, generating no zero $\Delta^{17}O$ values in the stratosphere. In addition, experimental studies show that UV radiation dissociates CO_2, generating $\delta^{17}O$ enrichments of up to 100‰ in CO (Huff and Thiemens, 1998). This may be relevant to a CO_2 dominated but UV transparent martian atmosphere. Although not a loss process in itself, the net downward flux of these $\delta^{17}O$ enriched species to the surface fractionates atmospheric oxygen isotopes over time.

2.5 Summary of atmospheric evolution

The general consensus from modelling is that atmospheric loss processes alone (hydrodynamic escape, impact erosion and solar wind sputtering) do not account entirely for the loss of an early CO_2 atmosphere that permitted liquid water at the surface. Sequestration of CO_2 and H_2O into the regolith and polar caps is inferred as an additional process responsible for removal of volatiles from the atmosphere. The lack of substantial fractionation of oxygen and carbon isotopes in the present Martian atmosphere also imply an exchangeable reservoir substantially larger than the amount stored in the atmosphere. Polar water ice deposits and CO_2 rich subsurface regolith have been suggested as possible reservoirs. The lack of evidence for carbonates on the present surface of Mars (Christensen *et al.*, 2001) imply that if sequestration of carbon and oxygen into the regolith did occur, it removed volatiles from the atmosphere early in Martian geological history, producing deposits which have been subsequently

covered by fine material or buried by impact. In addition to the uncertainties in the atmosphere-space and atmosphere-regolith flux rates, the initial inventories of volatiles and their present reservoirs are also poorly known. Dreibus and Wanke (1987) used the SNC ratio of refractory La to volatile K to infer a Martian mantle more volatile rich than the terrestrial interior as would be expected in a planet further from the Sun than Earth. However, it is uncertain how much water was consumed in core formation: the process which is by far the most important 'loss' process for water in terms of its availability at the surface.

Calculations have also been performed to estimate the inventory of CO_2 in the atmosphere prior to sequestration into the regolith that would allow liquid water to exist at the Martian surface. These estimates vary due to uncertainties in:

i) solar luminosity at 4.5 Ga, which is estimated to have been only 70% of present luminosity.

ii) trace gases such as NH_3 and CH_4 (and H_2O if water vapour existed in the atmosphere due to a high surface heat flux)

iii) surface albedo

iv) scattering by CO_2 clouds

Recent greenhouse model calculations suggest that even with several bars of CO_2 (2-10 bars Krasnopolsky *et al.*, 1996; 2-5 bars Pollack *et al.*, 1987) mean surface temperatures 4Ga ago would not be significantly different to present day values (Haberle, 1998).

Chapter 3

Martian Meteorites - evidence for a Martian origin

3.1 Introduction

The Martian meteorites are basaltic and ultramafic rocks which, although they are shocked and often contain abundant shocked feldspathic glass, are essentially unbrecciated. Martian meteorites are classified by their petrology into three groups: shergottites, nakhlites and chassignites (SNC's), and the anomalous Martian meteorite Allan Hills 84001 (ALH84001). The shergottites consist of rapidly cooled basalts and slower cooled, cumulate bearing peridotites. The nakhlites are clinopyroxene rich basalts probably related to the olivine rich dunite, Chassigny, the only chassignite. ALH84001 consists almost entirely (approximately 95%) of orthopyroxene (Mittlefehldt, 1994). The nakhlites and ALH84001 are shallow level intrusives in contrast to the shergottites and Chassigny, which were emplaced at depth. The Martian meteorites sample every epoch of Martian history spanning from ALH84001 which crystallized 4.5Ga ago (Nyquist *et al.*, 1995) to the shergottites, which formed approximately 180Ma ago (Shih *et al.*, 1982; Chen and Wasserburg, 1986). Most Martian meteorites contain secondary mineral assemblages of clays, carbonates and salts, formed by low temperature alteration and / or precipitation which are preterrestrial (e.g. Gooding, 1986). Table 3.1 lists basic facts about the twenty-six known Martian meteorites.

Table 3.1: Basic facts of all known Martian meteorites

Meteorite name	Age (Ga)	Date fall / found	Mass (g)	Type
Chassigny	~1.35	3 Oct, 1815	~4000	Chassignite
Shergotty	~0.18	25 Aug, 1865	~5000	Shergottite
Nakhla	~1.3	28 June, 1911	~10000	Nakhlite
Lafayette	~1.3	1931	~800	Nakhlite
Governador Valadares	~1.3	1958	158	Nakhlite
Zagami	~0.18	3 Oct, 1962	~18000	Shergottite
ALHA 77005	~0.18	29 Dec, 1977	482	Shergottite
Yamato 793605	~0.21	1979	16	Shergottite
EETA 79001	~0.18	13 Jan, 1980	7900	Shergottite
ALH 84001	~4.5	27 Dec, 1984	1940	Orthopyroxenite
LEW 88516	~1.8	22 Dec, 1988	13	Shergottite
QUE 84201	~0.33	16 Dec, 1994	12	Shergottite
Dar Al Gani 476 Dar Al Gani 489 Dar Al Gani 735 Dar Al Gani 670 Dar Al Gani 876	~0.75	1 May, 1998 1997 1996-1997 1998-1999 7 May, 1998	2000	Shergottite
Los Angeles 001 Los Angeles 002	~0.17	30 Oct 1999 30 Oct 1999	452.6 245.4	Shergottite
Sayh al Uhaymir 005 Sayh al Uhaymir 008 Sayh al Uhaymir 051 Sayh al Uhaymir 094 Sayh al Uhaymir 060 Sayh al Uhaymir 090		26 Nov, 1999 26 Nov, 1999 01 Aug, 2000 08 Feb, 2001 27 June, 2001 ??	1344 8579 436 233.3 42 94	Shergottite
Dhofar 019	~0.57	24 Jan, 2000	1056	Shergottite
GRV 9927		08 Feb, 2000	9.9	Shergottite
Dhofar 378		17 June, 2000	15	Shergottite
Northwest Africa 480		Nov 2000	28	Shergottite
Y000593 Y000749		29 Nov, 2000 3 Dec, 2000	13700 1300	Nakhlite
Northwest Africa 817		Dec 2000	104	Nakhlite
Northwest Africa 856		March 2001	320	Shergottite
Northwest Africa 1068 Northwest Africa 1110		April 2001 Sept 2001	654 118	Shergottite
Northwest Africa 998		Sept 2001	456	Nakhlite
Northwest Africa 1195		March 2002	315	Shergottite
YA1075		??	55	Shergottite

3.2 Evidence for a Martian origin

3.2.1 Trapped Martian atmosphere

Several lines of evidence point to a Martian origin for the SNC meteorites and ALH84001. The present Martian atmosphere has been analysed elementally and isotopically by Viking landers and Earth based spectroscopy (Owen *et al.*, 1977). This composition is not observed in volatile reservoirs elsewhere in the solar system, being strongly enriched in heavy isotopes of H, N and Ar relative to both solar and terrestrial compositions (table 3.2) (Pepin, 1991).

Table 3.2: summary of elemental and isotopic data (from Treiman *et al.*, 2000 and references therein)

	SNC	Mars	Earth	Solar
δD (‰)	4400	4500	0	–
$\delta^{15}N$ (‰)	450	620±160	0	–
$^{40}Ar/^{36}Ar$	1800	3000±500	296	–
$^{129}Xe/^{132}Xe$	2.6	2.5±1	0.98	1.04
CO_2 %	95	95.32	0.035	–
N_2 %	2.5	2.7	78.05	–
Ar %	1.5	1.6	0.93	4.4 p.p.m.
Ne p.p.m	3	2.5	18	0.013
Kr p.p.m.	0.3	0.3	1.1	–
Xe p.p.m.	0.08	0.08	0.087	–

The Antarctic Martian meteorite EETA79001 was found to contain shock glasses possessing noble gases that correlate isotopically and elementally with the present Martian atmosphere (Bogard and Johnson, 1983; Becker and Pepin, 1984). Gas studies of EETA79001 were also extended to N_2 and CO_2 (Becker and Pepin, 1984; Carr *et al*, 1985) to produce elemental and isotopic correlations presented in figure 3.1.

The process of shock induced implantation of atmospheric gas into a meteorite is not susceptible to chemical or isotopic fractionation (Wiens and Pepin, 1988) and is highly efficient, thus relative and absolute abundances of Martian atmosphere and EETA79001 are also similar.

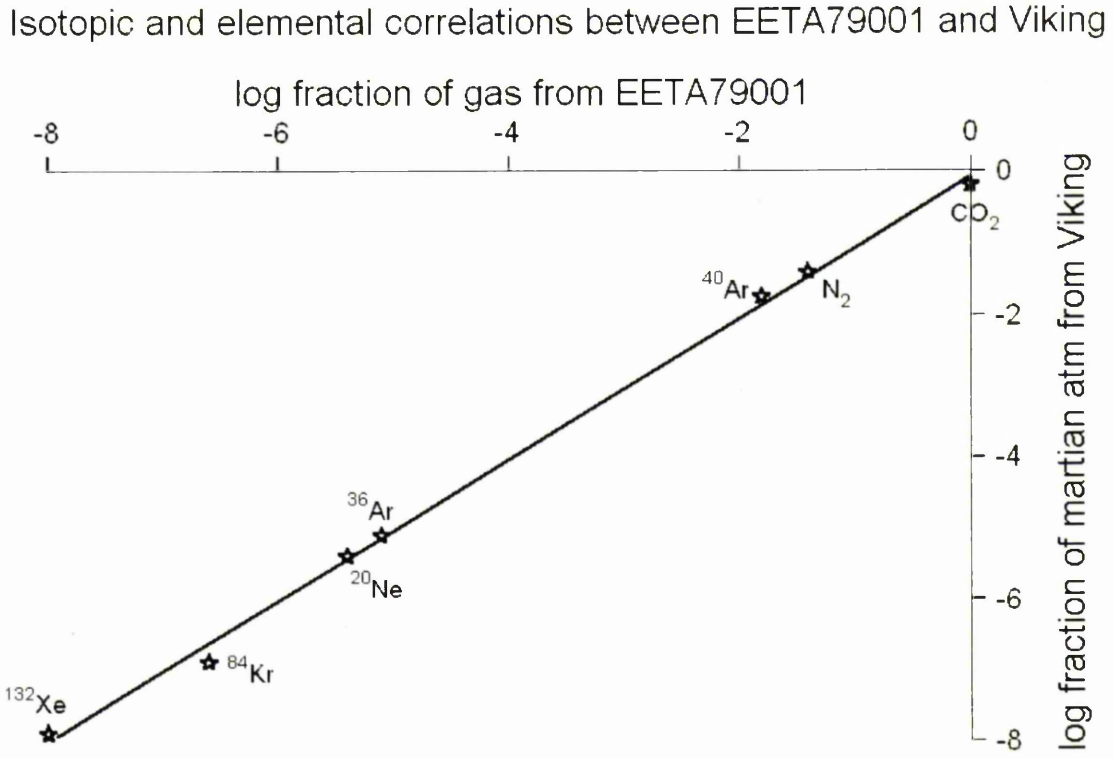

Figure 3.1: Elemental and isotopic abundances of gas species in the present Martian atmosphere and trapped gasses in EETA79001.

3.2.2 Oxygen isotopes

Oxygen isotopes link all SNC meteorites to the same parent body.. Oxygen isotope analysis is a powerful tool for determining the origins of meteorites due to solar nebula heterogeneity with respect to oxygen isotopes. These initial differences can be observed in all major meteorite groups (Clayton and Mayeda, 1996). Simple mass dependent fractionation gives the relationship:

$$\delta^{17}\mathbf{O} = \mathbf{0.515}\delta^{18}\mathbf{O}$$

where $$\delta^{17}O = 1000\left(\frac{\left(\frac{^{17}O}{^{16}O}\right)_{sample}}{\left(\frac{^{17}O}{^{16}O}\right)_{std}} - 1\right)$$

and $$\delta^{18}O = 1000\left(\frac{\left(\frac{^{18}O}{^{16}O}\right)_{sample}}{\left(\frac{^{18}O}{^{16}O}\right)_{std}} - 1\right)$$

and referenced to a terrestrial standard, SMOW (**S**tandard **M**ean **O**cean **W**ater).

Thus an initial complement of oxygen isotopes will fractionate along a line of slope 0.515 when plotted on $\delta^{17}O$ v $\delta^{18}O$ graph and meteorite groups occupy a different region in 3 isotope space.

It has been noted (Karlsson *et al.*, 1992; Franchi *et al.*, 1999) that whole rock samples of all Martian meteorites, including EETA 79001 containing the trapped Martian atmosphere, lie on a fractionation line of slope 0.515 but are offset from terrestrial rocks by approximately 0.3‰ indicating a separate parent body common to all SNC's which is distinct from all other meteorite reservoirs (figure 3.2).

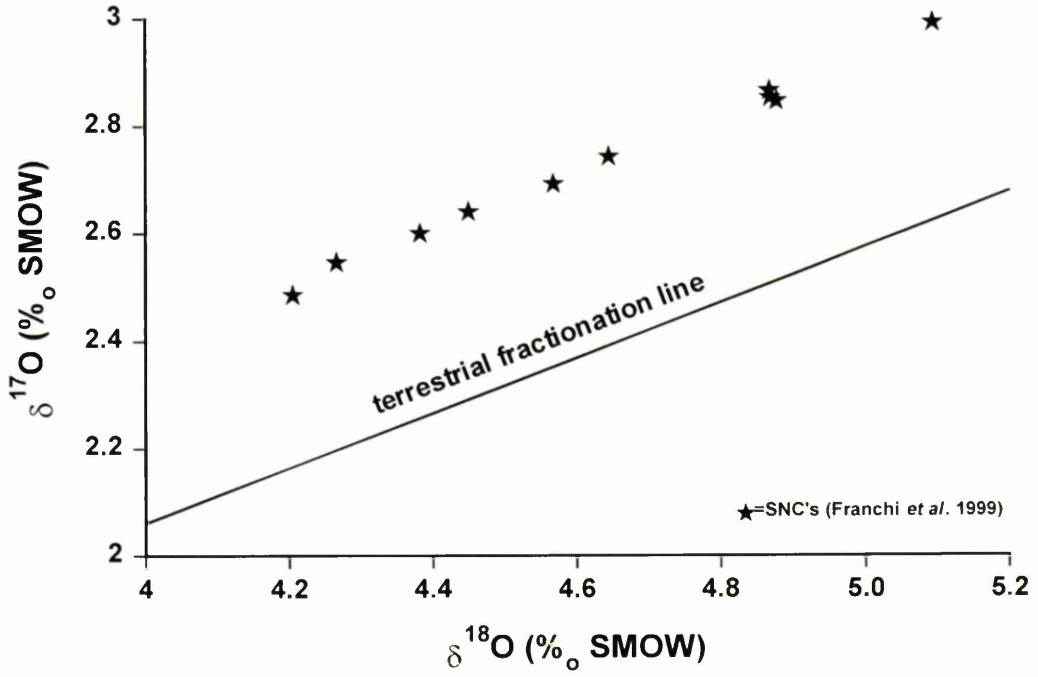

Figure 3.2: $\delta^{17}O$ v $\delta^{18}O$ plot for SNC's, indicating differences in Martian and terrestrial $\Delta^{17}O$. Note also the fractionation of SNC's parallel to the terrestrial fractionation line indicating extensive differentiation and fractionating processes on the parent body (from Franchi *et al.*, 1999).

The offset between the terrestrial and the Martian meteorite line is given the notation $\Delta^{17}O$ so for parent body X, $\Delta^{17}\mathbf{O}_x = \delta^{17}\mathbf{O}_x - \mathbf{0.515}\ \delta^{18}\mathbf{O}_x$. The small range in the value of $\Delta^{17}O$ offsets of bulk samples (Table 3.3) implies that the parent body was thoroughly mixed initially.

Table 3.3: $\Delta^{17}O$ of Martian meteorites (Franchi *et al.*, 1999)

Meteorite	$\Delta^{17}O$ (‰)
ALHA77005	0.326 ± 0.034
Dar al Gani 476	0.317 ± 0.024
EETA79001	0.321 ± 0.020
QUE 94201	0.327 ± 0.010
Shergotty	0.335 ± 0.034
Zagami	0.343 ± 0.028
Lafayette	0.310 ± 0.023
Nakhla	0.305 ± 0.016
Governador Valadares	0.321 ± 0.010
Chassigny	0.300 ± 0.029
ALH 84001	0.327 ± 0.031
Dhofar 019	0.357
YA1075	0.196
Dhofar 378	0.223
Mean	0.321 ± 0.013

3.2.3 SNC meteorite ages

Once it is established that all the SNC meteorites have a common origin and that the origin of one of these meteorites (EETA 79001) must be Mars, it is clear that the young age of twenty-five of the twenty-six Martian meteorites is not surprising. All other achondrites have crystallisation ages of >4.5Ga ago because they originate from asteroids that crystallised very early in the history of the solar system. No known asteroid is large enough to have retained sufficient internal heat to allow crystallisation of any of the SNC meteorites at such a late stage as <200Ma ago. Mercury and the Moon have been geologically inactive for several billion years whilst Venus, although possessing a young surface, has a massive 90bar atmosphere making ejection of surface rocks during impact unlikely. Among all the sizeable bodies in the solar system (including outer planet moons) only Mars has a surface that spans the entire geological timescale required to produce meteorites from 4.5Ga to 0.18Ga in age.

3.2.4 Chemical evidence

Chemical similarities between *insitu* Viking / Mars Pathfinder data and SNC's are also suggestive of a Martian origin (fig 3.3). FeO / MnO ratios reflect oxidation states of during planetary core formation and Na/Al reflect temperature histories during accretion due to the volatility of alkali metals. These combinations of elements and the information they provide about the environment in which the parent body accreted are sufficient to separate lunar meteorites, angrites, eucrites and terrestrial rocks whilst placing SNC's in a field that overlaps with the composition of Martian surface rocks (Treiman *et al.*, 2000).

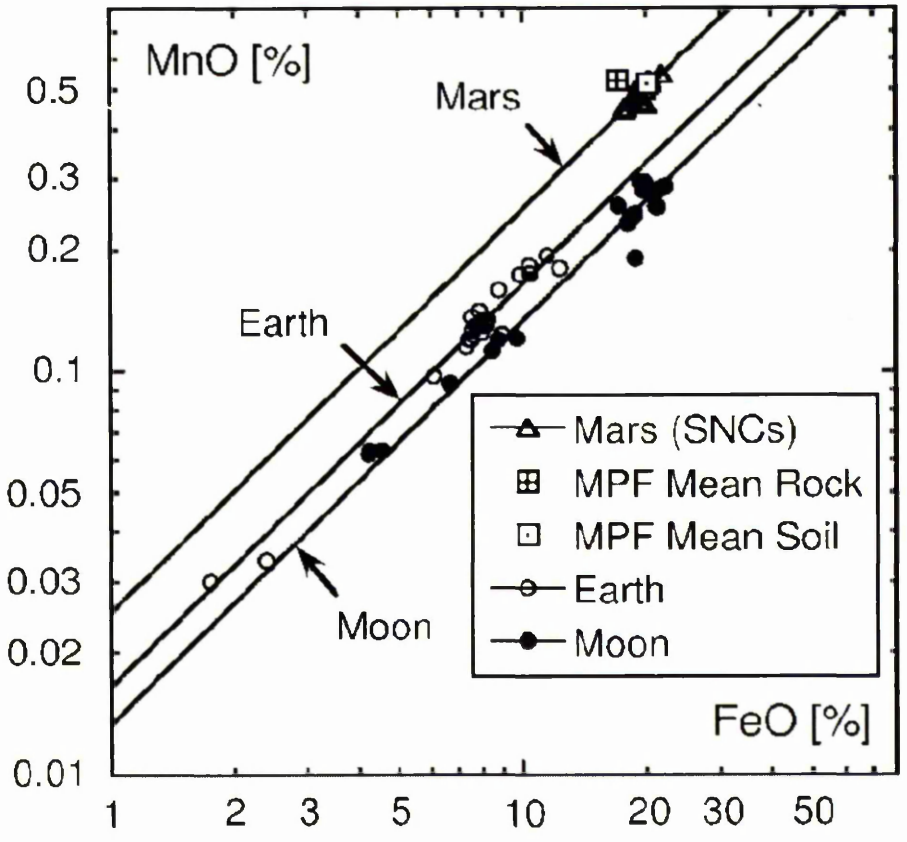

Figure 3.3: MnO v FeO showing similarity of Mars Pathfinder (MPF) soil and rock with SNC's, compared to Earth and Moon values (reproduced from Wanke *et al.* 2001 (using references therein)).

In addition, the oxidized nature of the Martian surface can be used as another indicator of Martian origin for SNC's. Hematite is thought to be the cause of the red surface of Mars. This is consistent with the abundance of oxidized FeS_2 (pyrite) and $Fe_{1-x}S$ (pyrrhotite) in SNC's compared to FeS (troilite) in other basaltic meteorites.

3.3 Summary

At present, there are no data returned from Mars which conflicts with data from SNC's. There are small discrepancies, often due to lack of precision of *in-situ* and many things that are not known about Mars. However, if the SNC's were not Martian in origin, a different parent body that had a sizeable atmosphere and was recently geologically active both volcanically and hydrologically is required. This is a far more unlikely prospect than Mars as the SNC parent body.

Chapter 4

An SNC overview

4.1 Introduction

As a study of secondary minerals in Martian meteorites forms the bulk of this study, description will be restricted to those meteorites containing secondary mineral assemblages and / or information regarding the volatile history of Mars. Of the twenty-six recognised Martian meteorites, 7 contain secondary minerals. These are three nakhlites Nakhla, Lafayette and Governador Valadares, shergottites, Shergotty and EETA79001, and the unique meteorites ALH84001 and Chassigny. In addition QUE94201, LEW88516 and Zagami contain hydrous minerals. The study of secondary minerals in ALH84001 forms all the work presented in this thesis and shall be discussed in greater detail separately.

4.2 Nakhlites

4.2.1 Nakhla

Petrography and geological history

Nakhla is a cumulate pyroxenite, predominantly consisting of subhedral to euhedral magnesian augite ($Wo_{40}En_{40}Fs_{20}$). with lesser amounts of Fe-rich olivine (Fa_{65-75}), plagioclase ($Or_4Ab_{62}An_{34}$), and K-feldspar ($Or_{74}Ab_{24}An_{2.4}$) in the mesostasis (McSween, 1994). Grain size varies from sub-millimetre to ~3mm diameters (Wadhwa and Crozaz, 1995). Nakhla crystallised 1.31-1.37Ga ago as inferred from Rb-Sr dating (Gale, 1975), 1.26 ± 0.07Ga ago from Sm-Nd dating and 1.28 ± 0.03Ga ago from U-Pb dating (Nakamura *et al.*, 1982).

Secondary mineralisation

Nakhla has relatively abundant secondary minerals (1-2%) which are truncated by fusion crust, indicating a pre-terrestrial origin (Gooding *et al.*, 1991). These are dominated by clays rich in sulphur, phosphorus and chlorine. Small grains of ferrihydrite, hematite, halite, anhydrite and Ca carbonates are also present (Gooding *et al.*, 1991). Fe-Mn carbonates (siderite) have also been identified in Nakhla (Chatzitheodoridis and Turner, 1990). A wide range of carbonate compositions are present in Nakhla: $Ca_{0.00-0.06}Mg_{0.02-0.41}Fe_{0.23-0.87}Mn_{0.01-0.40}$ with a compositional gap where carbonates have Mn concentrations ≥mol30% or ≤20mol% (Bridges and Grady, 1999b). In addition to the low temperature alteration implied by the presence of clays, Bridges and Grady (2000) argue that the halite-siderite-anhydrite-chlorapatite mineral assemblages are indicative of a evaporitic origin.

4.2.2 Lafayette

Petrography and geological history

Like Nakhla, Lafayette principally contains subhedral magnesian augite $Wo_{39}En_{39}Fs_{22}$ with lesser Fe-rich olivine Fa_{65} in a microcrystalline mesostasis (Harvey and McSween, 1992). It is also enriched in volatiles and LREE, suggesting it may have been co-magmatic with Nakhla (Wadhwa and Crozaz, 1995). The mesostasis consists of plagioclase, orthopyroxene, pigeonite, alkali feldspar, Ti-magnetite, ilmenite, pyrite and silica-glass. Olivine and pyroxene are relatively homogeneous indicating re-equilibration during cooling (Harvey and McSween, 1992. Lafayette is inferred to have crystallised 1.27 ± 0.07Ga ago from Rb-Sr data and 1.32 ± 0.05Ga ago from Sm-Nd data (Stoffler, unpublished data). This is supported by $^{40}Ar/^{39}Ar$ dates of 1.33Ga ± 0.03Ga for all nakhlites (Podosek, 1973; Bogard and Husain, 1977).

Alteration / secondary mineralisation

Lafayette has the most abundant secondary minerals of all Martian meteorites and also contains the most Martian water (0.387 wt. %) (Karlsson *et al.*, 1992). The meteorite contains secondary mineral deposits smectite, ferrihydrite and magnetite on the walls of veinlets in olivine and patches that replace olivine, pyroxenes and high-Si glass (Treiman *et al.*, 1993). The presence of ferrihydrite suggests that the upper temperature limit for alteration is <100°C because ferrihydrite decomposes to hematite below 100°C. The presence of cross-cutting relationships of the pre-terrestrial veins of hydrous alteration minerals implies an episodic alteration fluid infiltrating the rock rather one pulse of trapped fluid (Treiman *et al.*, 1993). Some veinlet deposits are carbonates, ~25μm wide with major element composition of $Fe_{0.65}Ca_{0.27}Mg_{0.0}Mn_{0.08}$ that vary little within the veinlet although some fine scale banding in K and Na is visible (Vicenzi and Eiler, 1998). The carbonates are spatially correlated with regions of iddingsite (Vicenzi and Eiler, 1998) and illite/smectite (Bridges and Grady, 1998) suggesting that low temperature hydrous fluids were involved in the carbonate formation. The Na content may reflect nano-metre salt inclusions as noted in other nakhlite studies (Gooding *et al.*, 1991), implying further evidence for saline hydrothermal alteration fluids. Swindle et al. (2000) have attempted to date the iddingsite and reported K-Ar ages of a few hundred million years, suggesting relatively recent liquid water activity in the Martian regolith.

4.2.3 Governador Valadares

Petrography and geological history

Governador Valadares also has the same composition as Nakhla and Lafayette and is inferred to be the same age, hence all three nakhlites are considered comagmatic. Mesostasis made up of glass, skeletal Fe-rich pigeonite, plagioclase, K-feldspar, silica, apatite, magnetite and sulfides. The 1.3Ga age is supported by 1.33 ± 0.01Ga age from Rb-Sr data (Wooden *et al.*, 1979), 1.32 ± 0.04 Ga from $^{40}Ar/^{39}Ar$ (Shih *et al.*, 1996).

Alteration / secondary mineralisation

Petrographic studies reveal the presence of siderite of composition $Ca_{0.04-0.11}Mn_{0.01-0.02}Mg_{0.09-0.29}Fe_{0.64-0.72}$ up to 30μm in length which is often in association with gypsum and minor chlorapatite. Veins of gypsum 450μm by 5μm also exist within the augite and olivine (Bridges and Grady, 1999a). The siderite-gypsum assemblage is similar to that of siderite-anhydrite in Nakhla, although no halite is present in Governador Valadares. This veining may also be associated with smectite and illite. Bridges and Grady (1999a) consider the secondary mineral assemblages to have formed by either:

i) precipitation from percolating fluid as implied by illite and smectite.

ii) crystallisation from a late-magmatic hydrous fluid >700°C as implied by the textural relationship of siderite, augite and plagioclase.

4.3 Shergottites

4.3.1 EETA 79001

Petrography and geological history

EETA 79001 (together with Shergotty and Zagami) is a shergottite basalt consisting of three lithologies: A, B & C. A geological contact exists between lithology A & B: lithology A is a basaltic melt containing numerous inclusions of mafic minerals as xenocrysts whereas lithology B is a basalt. Lithologies A and B consist of the clinopyroxenes pigeonite and augite with minor amounts of titanomagnetite, ilmenite, pyrrhotite, fayalite, quartz and apatite. In addition, lithology A contains xenocrysts of olivine, orthopyroxene and chromite (McSween, 1994). Lithology A is also finer grained. The composition of the pyroxenes varies from zoned pigeonite to sub-calcic augite which varies from Mg-rich to Fe-rich. Lithology C is a microcrystalline 'glass' containing trapped gases resembling the Martian atmosphere, which is now used to define the composition of the Martian atmosphere, and white 'drusy' calcite. All basaltic shergottites are relatively rich in volatile elements but lacking in water. The origin of the two lithologies A & B is controversial. There are two hypotheses which suggest either a magmatic origin for both lithologies (Wadhwa *et al*, 1994) or that Lithology A is an impact melt which has incorporated Lithology B as a clast. (Mittlefehldt *et al*, 1997).

The timing of formation of the basaltic shergottites is also controversial. They appear to have a Sm-Nd whole rock age of ~1.3Ga, interpreted as the crystalllisation age. However, Rb-Sr data and U-Th-Pb data on mineral separates give ages of 180 ± 20Ma (Shih *et al.*, 1982) and 190 ± 30Ma (Chen and Wasserburg, 1986) respectively, which are interpreted as a shock age. However, shock experiments fail to reset the Rb-Sr system (Nyquist *et al.*, 1987), hence the shock age may be the crystallisation age and

the 1.3Ga value may merely be mixing between crustal and mantle reservoirs and therefore EETA79001 may have crystallised ~0.185 Ga ago. Recent work by Nyquist *et al.* (2001) gives ages of 173 ± 10Ma for Lithology A and 185 ± 25Ma for Lithology B suggesting this younger age is correct.

Alteration / secondary mineralisation

Secondary minerals in EETA 79001 are restricted to Ca-carbonate and Ca-sulphate in lithology C. They are often spatially related (Gooding *et al.*, 1988). The sulphate occurs as laths and needles which, based on crystal structure, are probably gypsum. These are associated with pure, anhedral calcite crystals up to 20μm across (Gooding *et al.*, 1988). Calcium carbonate not associated with the sulphate has significant magnesium content in the form of either Mg-calcite with dissolved phosphorus or Mg-sulphate. The presence of these secondary carbonates together with gypsum / anhydrite suggests that the minerals precipitated from a hydrous fluid, possibly as part of an evaporite sequence.

4.3.2 Shergotty

Petrography and geological history

Shergotty (and Zagami) are petrologically and chemically distinct from the rest of the shergottites. Shergotty is fine grained and dominated by pigeonite and calcic augite with Fe-rich rims. There are two trends: Ca-rich from $En_{48}Fs_{19}Wo_{33}$ to $En_{25}Fs_{47}Wo_{28}$, and Ca-poor from $En_{61}Fs_{26}Wo_{13}$ to $En_{21}Fs_{61}Wo_{18}$. Maskelynite grains are zoned with average composition $An_{51.2}Ab_{46.5}Or_{2.3}$. The coexistence of fayalite, Ti-magnetite and a silica glass indicates late-stage crystallization under relatively high oxygen fugacity (Smith and Hervig, 1979). Jagoutz and Wänke (1986) reported a Rb/Sr

age of 167 Ma using maskelynite and mesostasis which is consistent with a recently recalculated Ar age of 165 Ma (Bogard and Garrison, 1999).

Alteration / secondary mineralisation

Shergotty contains the secondary mineral assemblage of gypsum, halite, sulphate and minor phyllosilicates (Wentworth and Gooding, 2000) within fractures. It also contains amphibole with Martian D/H signatures within melt inclusions (Watson *et al.*, 1994)

4.3.3 Zagami

Petrography and geological history

Zagami is another basaltic shergottite and therefore possesses the same ambiguity regarding its crystallisation age as Shergotty and EETA 79001. The mineralogy is also similar for the normal NZ lithology, except that Zagami possesses amphibole melt inclusions within pigeonite. A second, dark-mottled-lithology, extends the range of composition of phases found in NZ to higher Fe and higher Na and is inferred to be a residual melt. These lithologies are separated by veins of shocked glass containing Martian atmosphere. Rb-Sr crystallisation ages vary from 180Ma to 186Ma (Nyquist *et al.*, 1995) for both lithologies

Alteration / secondary mineralisation

Stepped combustion analyses of Zagami implies that it possesses one carbon bearing component inferred to be carbonate (Grady *et al.*, 1997).

4.3.4 QUE94201

QUE94201 is a coarse grained basalt containing Fe-rich pigeonite (44%) and maskelynite (46%) with minor opaques, whitlockite and mesostasis. Extreme zoning of pyroxene (Mg-rich pigeonite cores mantled by Mg-rich augite and rimmed by Fe-rich pigeonite) in QUE94201 indicates that it cooled quickly from magmatic temperatures (e.g. McSween *et al.*, 1996). These pyroxenes do not appear to be cumulate phases, as is the case for Shergotty, Zagami and EETA79001B. Fe-Ti oxide compositions indicate a formation environment more reducing than the other shergottites (McSween *et al.*, 1996).

Mesostasis pockets similar to Zagami contain silica and fayalite, as well as, maskelynite, whitlockite, Fe-Ti oxides, sulfides, minor augite, chlorapatite and a Zr-rich phase, probably baddelyite. Shock melted glass contains remelted phosphate (Mikouchi *et a*l. 1998). Borg *et al.* (1997) reported a Rb-Sr age of 327 ± 12 Ma whilst Dreibus *et al.* (1996) reported a K/Ar age of 1.33 Ga. Jull *et al.* (1997) found that ^{14}C activity was nil, consistent with an old terrestrial age.

4.4 Chassigny

Petrography and geological history

Chassigny is a dunite consisting of Fe-rich olivine, with minor pigeonite, augite, alkali feldspar, chromite, troilite, marcasite (FeS_2), pentlandite ($FeNi_9S_8$), chlorapatite, ilmenite, rutile and baddeleyite (McSween, 1994). Igneous chromite contains substantial Fe^{3+} proving crystallization under oxidizing conditions.

Chassigny has a crystallisation age of 1.32 ± 0.07Ga by $^{40}Ar/^{39}Ar$ dating (Bogard and Garrison, 1999).

Alteration / secondary mineralisation

The Chassigny secondary minerals occur as veins along fractures in olivine, pyroxene and Cr-spinel. Rhombohedral morphology suggests that the some carbonate is calcite and some is Mg-carbonate. Gypsum and/or bassanite ($CaSO_4.½H_2O$) are also present (Wentworth and Gooding, 1994). Occasionally the carbonates and sulphates are intermixed in a similar fashion to many other SNC's. Unlike the nakhlites however, there are no clays or oxides present, therefore the alteration fluid is inferred to have been cold, short-lived and incapable of oxidising Chassigny (Wentworth and Gooding, 1994).

Chapter 5

ALH84001 carbonate origins

5.1 Introduction

ALH 84001 was recovered from the Antarctic ice sheet Allan Hills and was originally classified as a diogenite but was noted to contain unusual Mn/Fe ratio, abundant Fe^{3+} in chromite (Mittlefehldt, 1994) and Martian oxygen isotope composition (Clayton, 1993). Therefore it was later reclassified as a Martian meteorite (Score and Mittlefehldt, 1993). ALH 84001 is unique among the Martian meteorites because it has a crystallisation age of ~4.5Ga, much older than the other twenty-five, and contains a relatively high proportion (1%) of carbonates.

5.2 Petrography

Petrographically ALH84001 is a cumulate coarse grained orthopyroxenite impact breccia, comprising 95% orthopyroxene of mean composition ($Wo_{3.3}En_{69.4}Fs_{27.3}$) (Mittlefehldt, 1994). It also contains minor phases of euhedral to subhedral chromite (~2%), interstitial maskelynite (~1%) of mean composition ($An_{32.6}Ab_{60.1}Or_{7.3}$) (Turner *et al.*, 1997), ($An_{31.1}Ab_{63.2}Or_{5.7}$) (Mittlefehldt, 1994), and carbonate (~1%) of mean composition ($Cc_{11.5}Mg_{58.0}Sd_{29.4}Rd_{1.1}$) (Mittlefehldt, 1994) with small amounts of pyrite, augite, apatite and olivine (Mittlefehldt, 1994; Dreibus *et al.*, 1994).

5.3 Geological history

Initial study of the geological history of ALH84001 led Mittlefehldt (1994) to postulate slow cooling to produce an homogeneous cumulate dated at 4.5Ga (Nyquist *et*

al., 1995) followed by deposition of chemically zoned carbonate. A shock event then formed fine grained crush zones traversing ALH84001 and mobilized the zoned carbonate into these crush zones. A narrower range of carbonate in the crush zones compared to the zoned clasts was attributed to this partial remobilization event (Mittlefehldt, 1994). This is consistent with the age of a shock event in ALH 84001 using ^{40}Ar-^{39}Ar stepped heating and laser probe methods which yield an age of ~3.9Ga for the maskelynite associated with the carbonate (Turner *et al.*, 1997).

Treiman (1995) found no evidence of this differing carbonate chemistry, claiming that deposition of zoned carbonate in the crush zones occurred after crush zone formation in an earlier shock event. A solitary carbonate deposition event was then followed by a second shock that fractured the carbonates. The common association of maskelynite and carbonate and textural relationship between the two was interpreted as replacement of maskelynite (formed in the initial shock event) by carbonate (Gleason *et al.*, 1997; Kring *et al.*, 1998). The 3.92 ± 0.04 age for maskelynite (Turner *et al.*, 1997) and 3.90 ± 0.04 age for carbonate (Borg *et al.*, 1999) are consistent with this interpretation.

In contrast, Treiman (1998) presents evidence for five impact events, two of these after a carbonate deposition event. Treiman (1998) envisages a complex geological history beginning with deformation that produces crystalline granular bands (crush zones of Mittlefehldt, 1994). These were thermally metamorphosed to cause homogenisation of the minerals. Feldspathic glass was formed in a second deformation event, which produces a second set of granular bands that offset the first granular bands. Deposition of carbonate 'pancakes' occurs in fractures and carbonate globules form as clasts in association with maskelynite in the granular bands. Later deformation events fracture the carbonate globules and pancakes bending old fractures and forming new

ones, before a final deformation rotates rock fragments and their palaeosignatures prior to ejection from the Martian surface. Recent work on the composition and textural relationships of feldspathic and silica glasses (Greenwood and McSween, 2001) argues for mixed composition of stoichiometric feldspars from a single, pre-carbonate, shock event followed by one, less severe, post-carbonate shock event, describing a geological history more akin to Treiman (1995).

The one impact model of Scott *et al.* (1997; 1998a) proposes from petrological studies that a single impact melted and partly redistributed carbonate, plagioclase and silica whilst causing crushing of pyroxene into the 'granular bands' of Treiman (1995; 1998). Scott *et al.* (1998b) cite evidence of multiple brecciation and crosscutting melt veins in single terrestrial impacts as an explanation of granular band cross-cutting relationships. However, pyroxene diffusion rates several orders of magnitude slower than those of carbonates do not appear to agree with observational data of micron scale strongly chemically zoned carbonates globules (Mittlefehldt, 1994; Treiman, 1995; Harvey and McSween, 1996) and homogeneous pyroxenes (Treiman, 1998). Feldspathic material also appear much less brecciated than the associated carbonates, implying remobilisation and healing of feldspar fractures after carbonate deposition (Warren, 1998), hence multiple periods of shock deformation.

5.4 Petrography of carbonates

ALH 84001 contains fracture zones of impact origin which contain secondary carbonate minerals. These carbonates have varying textures with associated nomenclature. The fine grained, crystalline, partially aligned carbonates will be described as 'granular bands', a term used by Treiman (1998). These are the same 'crush zone' carbonates of Mittlefehldt (1994). The elliptical clasts of carbonate are

described as 'pancakes' and the strongly chemically zoned globules are referred to as carbonate 'rosettes'.

All carbonate clasts appear to have the same structure, internal stratigraphy and composition, hence Treiman (1995, 1998) and Harvey and McSween (1996) assumed that ALH 84001 had undergone a single period of metasomatic alteration, albeit by different processes. Scott *et al.* (1997) with their one impact hypothesis require a single phase of carbonate deposition by definition. The general zoning pattern from core to rim is:

i) a relatively Ca / Fe rich core (~30% Ca, ~35% Fe, ~35% Mg)

ii) gradual trending to more Mg rich mantle (~10% Ca, ~35% Fe, ~55%Mg)

iii) sometimes a sharp gradation to a Ca and Fe rich band occurs within the mantle

iv) a sharp, narrow Fe rich band surrounds the increasingly Mg rich mantle

v) an Mg rich rim (~95% Mg, ~5% Ca) surrounds the sharp Fe rich band

vi) sometimes a second sharp Fe rich rim surrounds the broader Mg rich rim.

vii) Mn concentrations correlate with Ca

The rosettes are also zoned isotopically, with core to rim isotopic evolution in all carbonate rosettes: e.g.$\delta^{18}O_{SMOW}$+9.5‰ ±1.1‰ to $\delta^{18}O_{SMOW}$+20.6‰ ±1.3‰ (Valley *et al.*, 1997), ~+8‰ to $\delta^{18}O_{SMOW}$+22‰ (Saxton *et al.*, 1998) and $\delta^{18}O_{SMOW}$+5.4‰ ±0.8‰ to $\delta^{18}O_{SMOW}$+25.3‰ ±0.8‰ (Leshin *et al.*, 1998).

5.5 Possible processes for carbonate formation in ALH 84001

The complex geological history of ALH 84001 and the extensive amount of work on the varied textures have led to an array of very different models for ALH 84001 carbonate deposition. This section aims to evaluate current hypotheses for carbonate formation.

5.5.1 Hydrothermal formation

A favoured hypothesis for the formation of ALH84001 carbonates is hydrothermal alteration by percolating fluids. Evidence concerning hydrothermal processes in ALH84001 is of additional interest because of the possibility that evidence of ancient primitive Martian life is present in the carbonates (McKay *et al.*, 1996): a low temperature hydrothermal system seeming to be the environment most likely to harbour primitive life. The compositional zoning, particularly the oscillating chemical compositions observed in the rosette mantles, implies a change in the fluid temperature or multiple fluid influxes with distinct compositions (Romanek *et al.*, 1994; Treiman, 1995). The persistence of the fine (micron) scale chemical zoning seems to require low temperature fluids, as sub-micron Fe-Mg carbonate grains homogenise in days at 500°C and a month at 350°C (Treiman, 1995). With the exception of very low (~0°C) temperatures, the major problem with all hydrothermal metasomatism models, be they high or low temperature closed or open systems, is the rarity of hydrated silicates in ALH 84001: only Brearley (1998; 2000) appears to have found conclusive evidence of mica (phlogopite), which is interpreted as a shock heating induced breakdown product of clay. The degree of hydrothermal alteration is dependent on temperature (hence rate of alteration) and duration of alteration period. A hydrothermal period, which requires elevated temperatures to instigate the cycling of fluid, will therefore have elevated temperatures (>300°C) for at least 1000 years (Gulick, 1991) over a period of up to 500,000 years if Martian hydrothermal systems are similar to terrestrial cycles. Add to this, a rock with internal fluid pathways and a greatly increased surface area due to brecciation prior to carbonate deposition (e.g. Treiman, 1998) and the possibility of no silicate alteration seems highly unlikely.

Many of the carbonate textures in ALH 84001 consist of intimately related maskelynite and carbonate. Treiman (1995) suggests replacement of plagioclase by carbonate, the remaining plagioclase altering to maskelynite during a later shock episode. Gleason *et al.* (1997) suggest replacement of feldspathic glass and Treiman (1998) observes partial replacement of glass along relict crystalline cleavage planes, implying that a certain degree of crystalline and glassy feldspar was present when carbonate replacement occurred. The absence of Si, Al and Na rich regions that should exist as a consequence of plagioclase replacement is also difficult to explain unless significant chemical transport occurred to remove these cations. This is exacerbated by the lack of evidence for orthopyroxene alteration.

One possibility is that the fluid was extremely CO_2 rich, but this would tend to imply remobilisation of CO_2 which is not compatible with a hydrothermal system and is more relevant to shock hypotheses (Harvey and McSween, 1996; Scott *et al.* 1997, 1998a). A lack of alteration minerals may be explained by the sequential reactions.

$$MgSiO_3 \text{ enstatite} + CO_2 \rightarrow MgCO_3 \text{ magnesite} + SiO_2$$

$$3MgSiO_3 + SiO_2 + H_2O \rightarrow Mg_3Si_4O_{10}(OH)_2 \text{ talc}$$

$$Mg_3Si_4O_{10}(OH)_2 + 3CO_2 \rightarrow 3MgCO_3 + 4SiO_2 + H_2O$$

However, these reactions are heavily dependent on xCO_2, which would require fortuitous changes of environment that are highly unlikely. The lack of silica present in ALH 84001 in comparison to the abundance of carbonate strongly suggests that this sequence of reactions did not occur.

Several other lines of evidence also seem to conflict with a low temperature aqueous fluid. PIXE analysis of trace elements chromium and potassium in ALH 84001 carbonates gives approximate concentrations of both as 500 p.p.m. This is much greater than expected in a carbonate which, if it formed from an aqueous fluid at low

temperature, should have concentrations of <110p.p.m and <40p.p.m. respectively (Gilmour *et al.*, 1997b). An aqueous fluid is also unlikely from $Cl/^{36}Ar$ ratios. A $Cl/^{36}Ar$ value of $>10^6$ has been determined in ALH 84001 which would equate, with corrections for the difference in atmospheric partial pressure, to a terrestrial value of 2×10^3. This is much lower than the terrestrial value of 10^7-10^8, hence Gilmour *et al.* (1997a) suggest it is unlikely the carbonates were generated from a hydrothermal fluid.

5.5.2 Hot CO_2 fluid metasomatism

Impact metasomatism has been suggested (Harvey and McSween, 1996) as a mechanism for carbonate formation. This hypothesis considers the possibility of brecciation of the orthopyroxenite primary igneous rock, followed by injection of a hot anhydrous CO_2 fluid (>650°C). This fluid arises from surface carbonates or surficial CO_2 ice deposits vapourised during the impact. Therefore the fluid is inferred to be nearly pure CO_2 (xCO_2>0.85). Harvey and McSween (1996) and Harvey (1998) suggest that only one type of carbonate exists: a circular or semi-circular, radially zoned, space-filling carbonate. This has led them to suggest that one event, an impact, was responsible. Injection of hot fluid into relatively cold orthopyroxene results in rapid cooling of the CO_2 fluid which can be invoked to explain that micron scale concentric zoning of the carbonates nucleating from point sources and growing from core to rim.

Harvey and McSween (1996) state that the major element compositions of the ALH 84001 carbonates can help constrain the fluid composition and temperature and therefore invoke geothermometry of the complex intermixing of carbonates within the zoned carbonate rosettes. For the purposes of geothermometry, the complex carbonate assemblage was treated as a calcite-ankerite and an ankerite-siderite system which yielded formation temperatures of 685°C and 660°C respectively. This is in accordance

with a 700°C estimate from the amount of Ca in the magnesite-siderite stability field (Mittlefehldt, 1994). In addition, the absence of solid solutions between dolomite-magnesite and calcite-siderite imply temperatures >500°C. The high CO_2 content (xCO_2>0.85) is required to allow the carbonate formation reactions between ultramafic minerals and fluids (equation below) and also explains the rarity of hydrous minerals from fluid metasomatism.

$$(Mg,Fe,Ca,Mn)SiO_3 + CO_2 \rightarrow (Mg,Fe,Ca,Mn)CO_3 + SiO_2$$

The presence of magnetite grains associated with the carbonates may indicate vapour deposition and therefore a high fluid temperature (Bradley *et al.*, 1996). Also, fluid inclusions several microns across have been identified in ALH 84001 orthopyroxene crystals (Bodnar, 1999). Motion of bubbles in the inclusions indicates a liquid phase and optical behaviour suggests the presence of liquid and vapour CO_2, implying that CO_2 rich fluid must have migrated through these rocks at some time in their history, supporting the CO_2 metasomatism hypothesis.

There are several problems with this hypothesis. The most intractable problem is the extreme rarity of silica in ALH 84001 given the reaction in equation above. Even assuming that some Ca^{2+} ions were provided from the vapourised surface carbonates, the 95% orthopyroxene host minerals are the only plausible source of Mg^{2+}, Fe^{2+}, Mn^{2+} ion required to form the zoned carbonates (Warren, 1998) therefore this reaction is required to be extensive. Depending on the silica phase, the ratio of silica / carbonate by volume is anticipated to be 0.7-0.84. An average carbonate abundance by volume is ~1% (e.g. Romanek *et al.*, 1994; Treiman, 1995) whereas silica is hard to find in ALH 84001. Therefore, mineralogical abundances do not support an impact metasomatism model.

There are also textural arguments against impact metasomatism formation. Although CO_2 vapour can react with silica to produce carbonate globules in terrestrial impacts, the carbonates are compositionally uniform with no evidence of the fine scale isotopic zoning of ALH 84001 carbonates (Martinez *et al.*, 1994). Terrestrial analogues are also pumice-like because the fluid forms vesicular cavities within the carbonate. This is not the case with ALH 84001 carbonates, although it may be possible that feldspathic glass, remobilised by later shock events may have filled the former void spaces.

Support for a high temperature formation from geothermometry requires evidence of complete chemical equilibration. Although equilibrium would be expected when cooling from a high temperature, there is no evidence of this (Treiman and Romanek, 1998). Indeed the micron scale chemical and isotopic zoning implies a lack of diffusion and hence no attainment of equilibrium. Harvey and McSween (1996) state that the presence of dolomite-magnesite *and* calcite-siderite assemblages without solid solution compositions proves a high formation temperature but this assumes chemical equilibrium and formation of a rosette during one metasomatic episode of which there is no evidence. This reliance on one metasomatic episode does not seem reconcilable with the oscillatory zoning observed in carbonate rosettes.

5.5.3 Rapidly cooled, shock-mobilised carbonate

Similarly. Scott *et al.*, (1998a) incorporate into their hypothesis shock melting of pre-existing carbonate which is then subsequently redeposited in cracks in the igneous groundmass caused by impact (e.g. Scott *et al.*, 1998a). Shock melted plagioclase and silica are assumed to be have been deposited simultaneously. Despite the different morphology of the carbonates, Scott *et al.* (1998a) claim that the textural and chemical similarity between the carbonate disks, veins and irregular nodules imply formation in

the same process (also Harvey and McSween, 1996). They suggest that carbonate fluid filled open fractures that closed as the carbonate cooled. They also cite evidence of broad Ca-rich cores and narrow Mg-rich tips as evidence of chemical fractionation and fracture closure during cooling. Magnesite microdisks in close proximity to the veins and globules are attributed to crystallisation of the residual trapped fluid by a similar chemical fractionation process. Also, the diverse shapes of ALH 84001 carbonates are similar to impact melted troilite in ordinary chondrites. Finally, Scott *et al.*, (1998a) observe that small carbonates form irregular boundaries with pyroxene while large carbonates form rounded or subhedral boundaries, which is consistent with a slower cooling CO_2 rich region.

The hypothesis of Scott *et al.* (1998a) is not convincing because it does not explain the chemical zoning of the lenticular carbonates. If a CO_2 rich fluid did produce the carbonates by infilling fractures, one would expect to see cooling from the edges inwards which would therefore exhibit chemical zoning exactly opposite to what is observed with 'rosettes', which most authors agree formed with a calcium rich core first. Neither can the oscillatory zoning observed in many carbonate rosette mantles be explained by a single cooling of CO_2 rich vapour. However, Scott *et al.* (1998b) claim that poor knowledge of high temperature and pressure kinetics cannot rule out the observed crystalllisation sequence.

5.5.4 Evaporitic origin

It has been suggested that the carbonates may have formed from evaporation of brines at low temperatures ($<<100°C$) in a restricted drainage basin such as an ancient crater floor (McSween and Harvey, 1998). The carbonates are inferred to have formed at the bottom of this saline lake. A common sequence of minerals precipitated from a terrestrial evaporating saline fluid are calcite > dolomite > magnesite, which is broadly

similar to the zoning found in ALH 84001 carbonates. The lack of sulphates in ALH 84001 appears inconsistent with evaporitic conditions but McSween and Harvey (1998) state that terrestrial alkaline lakes are concentrically zoned with an absence of sulphates at the edges of the evaporating lakes. Alkalinity may be a possible explanation although a high pCO_2 atmosphere would imply acidification of standing water.

Warren (1998) suggests that the ALH 84001 carbonates formed at low temperatures from saline lake waters that percolated into the Martian regolith beneath in a playa / sabhka analogue. The absence of sulphates is explained by Warren (1998) to be a consequence of early Ca-bearing carbonates causing Ca depletion to the point where Ca-sulphates (gypsum and anhydrite) cannot form. Alternatively, Warren suggests that crusts of carbonate and sulphate could have formed at the highly concentrated lake /atmosphere interface of a compositionally stratified lake. This may have prevented further evaporation that would have lead to sulphate formation towards the end of the evaporite sequence. Sulphate precipitation then fails to occur if the seepage rate of brine away from the regolith is greater than the reduced rate of evaporation.

Warren (1998) also considers a closely related model which employs a sudden influx of groundwater that flows downhill, evaporating upwards through the Martian regolith during fluid flow. With an absence of sulphates, ALH84001 would therefore be near the source region of this groundwater 'flood', in which carbonate precipitation dominates with sulphates precipitating out further downhill from the increasingly concentrated groundwater.

Both of these models (McSween and Harvey, 1998; Warren, 1998) are capable of explaining major problems that other models (except very low temperature hydrothermal systems) incur because evaporation models operate at low temperature.

The lack of abundant hydrated minerals and pyroxene alteration in ALH84001 is possible in this type of environment because the short duration, highly saline fluids and low temperature may sufficiently reduce the extent of alteration of orthopyroxene to clay (Barratt *et al.*, 1999). The fine scale chemical and isotopic zoning seen in the carbonate globules can also be retained at these reduced (<<100°C) temperatures. These models also explain the absence of sulphates in ALH 84001 and, as a consequence, suggest why carbonates have not yet been observed at the Martian surface and why Martian fines are highly concentrated in sulphate (Rieder *et al.*, 1997). Additionally, heavy isotope enrichment as observed in carbonate 'rosettes' can be produced qualitatively in an evaporating environment, assuming no isotopic buffering by the atmosphere.

However this model appears to require void filling by precipitation of carbonates. This is not consistent with the majority of the carbonate occurrences, which appear to replace feldspathic glass, which is highly unlikely at low temperatures. This process also fails to produce examples of terrestrial carbonate rosettes. Although calcite disks are known to have formed in Tatahouine meteorite (Barrat *et al.*, 1998), these formed at the surface and are therefore not a true Martian regolith analogue. The closest terrestrial analogues may be found in spinel lherzolite xenoliths (Mojzsis *et al.*, 1999; Blake *et al.*, 1999): a very different environmental setting. Finally, Mg-Fe carbonates are rare in terrestrial evaporitic sequences. Nakhla, containing salts, seems more likely to be part of an evaporite sequence than ALH 84001.

This evaporite hypothesis has been incorporated into an impact mobilisation hypothesis (Scott, 1999), which suggests that a surficial evaporite-carbonate deposit has been remobilised by an impact into the near crustal rocks, where it is redeposited as the carbonates found in ALH84001.

5.6 Inferences from oxygen isotopes

Three step acid dissolution experiments (Romanek *et al.*, 1994) reveal oxygen isotopic zoning from $\delta^{18}O_{SMOW}$ +13.3‰ in the Ca-rich core to $\delta^{18}O_{SMOW}$ +22.3‰ in the Mg-rich rim. Using a similar method, Jull *et al.* (1995) acquired a carbonate bulk average of $\delta^{18}O_{SMOW}$ +15‰ ±5‰. High spatial resolution ion microprobe analyses yield carbonate rosette core to rim isotopic zoning from $\delta^{18}O_{SMOW}$ +9.5‰ ±1.1‰ to $\delta^{18}O_{SMOW}$ +20.6‰ ±1.3‰ (Valley *et al.*, 1997), $\delta^{18}O_{SMOW}$ +8‰ to $\delta^{18}O_{SMOW}$ +22‰ (Saxton *et al.*, 1998) and $\delta^{18}O_{SMOW}$ +5.4‰±0.8‰ to $\delta^{18}O_{SMOW}$ +25.3‰ ±0.8‰ (Leshin *et al.*, 1998). The correlation of mineral chemistry with the isotopic zoning present in all chemically zoned carbonate rosettes (e.g. Leshin *et al.*, 1998 and Saxton *et al.*, 1998) indicates that the isotopic zonation is directly related to the progress of carbonate crystallisation and can therefore be used to derive quantitative constraints on formation conditions. The two broad scenarios that exist for carbonate formation from fluids are open and closed systems, in which the carbonates are either buffered or unbuffered (isotopic exchange with the surrounding silicates may or may not be a significant process).

A closed system model as suggested by Leshin *et al.* (1998) assumes a finite reservoir of fluid which undergoes isotopic fractionation as carbonate formation proceeds. Leshin *et al.* (1998) proposed a scenario where at a constant temperature of 0°C, the observed core to rim isotopic variation can be produced if CO_2 in the fluid decreases from $xH_2O=0$ to $xH_2O=0.8$ (where X is molar fraction of water in the mixed H_2O-CO_2 fluid). The observed variation can also be achieved at a constant 500°C if xCO_2 is reduced to 0.05, hence a large range of formation temperatures seem possible in a closed system with an initial CO_2 rich fluid. This would seem to agree with the CO_2 metasomatism model of Harvey and McSween (1996) and the shock melting and

subsequent CO_2 mobilisation and redeposition hypothesis suggested by Scott *et al.* (1997). Saxton *et al.* (1998) argue that the minor increase in $\delta^{18}O$ from the mantle of the carbonate globule to the rim is not in accordance with closed system Rayleigh isotopic fractionation, which should produce greatest $\delta^{18}O$ enrichment towards the end of the crystallisation sequence, hence the closed system scenario may be invalid.

Open system scenarios have also been considered by several authors (Romanek *et al.*,1994; Leshin *et al.*, 1997; Valley *et al.*, 1997; Saxton *et al.*, 1998). Romanek *et al.* (1994) used an earlier model proposed by Clayton and Mayeda (1988), which assumed a fluid $xH_2O=0.8$ that attained high temperature equilibrium with Martian basalt prior to cooling. Using their three step acid dissolution data, they derived carbonate formation temperature $0°C>T_{dep}>80°C$. This approach was also used by Leshin *et al.* (1998), inferring $0°C>T_{dep}>250°C$ from a wider range of $\delta^{18}O$, where the highest $\delta^{18}O$ is assumed to have formed at 0°C. Assuming a nearly pure aqueous fluid and isotopically heaviest (rim) carbonates to have formed at 0°C, rosette core deposition is inferred to begin at 125°C, cooling to 0°C for the rims. However, if the isotopically lightest carbonate is assumed to be in equilibrium with the orthopyroxene at >800°C, the isotopically heaviest carbonates are inferred to form at 100°C. However, $\Delta^{17}O$ values determined by Karlsson *et al.*, (1992) show enrichment of isotopically heavy oxygen in the carbonate compared to the host silicate, implying little or no isotopic exchange between the metasomatic fluids and the crustal orthopyroxenes. Saxton *et al.* (1998) assume no silicate buffering with initial conditions of the Clayton and Mayeda (1988) model of $xH_2O=0.8$. This gives an initial $\delta^{18}O_{SMOW}$ value of –2.6‰ for the source fluid and corresponding core and rim formation temperatures of 210°C and 80°C respectively.

Regions of ankerite are found outside the carbonate rosettes that have an unclear relationship to the rosettes. These ankerites have $\delta^{18}O$ 0±2‰ (Saxton *et al.*, 1998) requiring a temperature of 410°C to form from fluid of xH_2O=0.8. However invoking such high formation temperatures may be problematic. It is unclear if some carbonate-silicate equilibration occurs at 400°C. If this is the case, the observed $\Delta^{17}O$ excesses in the carbonate would be erased and the $\delta^{18}O$ of the carbonate would be limited to ~+8‰ at 500°C or ~+6.5‰ at 700°C. These low $\delta^{18}O$ values preclude heavy enrichment of early fluids due to atmospheric loss as envisaged by Jakosky (1993) and Hutchins and Jakosky (1997).

5.7 Outstanding questions from ALH84001 work

Biogenic presence in ALH84001?

McKay *et al.* (1996) proposed that the magnetite rich regions in ALH84001 carbonates were kinetically controlled by biological organisms indigenous to Mars. Chemical evidence suggests a high abundance (~1p.p.m) of polycyclic aromatic hydrocarbons (PAH's) on interior fracture surfaces containing regions rich in carbonate. In ancient terrestrial sedimentary rocks, PAH's are fossil molecules of biological precursors that have undergone chemical aromatization, hence the proximity of elevated levels of PAH's to carbonate globules suggests a biological origin. Concentrations from Antarctic weathering are in the region of 10p.p.t. to 1p.p.b. therefore terrestrial contamination of 1p.p.m. is unlikely (McKay *et al.*, 1996). The increase in PAH concentration with depth in ALH84001 also implies terrestrial contamination is not responsible; more likely the sparsity of PAH's near the surface of the sample is due to pyrolysis during atmospheric entry. Stephan *et al.* (2001) suggest that there is no spatial

correlation between PAH concentrations and carbonate regions implying universal terrestrial contamination and casting doubt on the relevance of PAH's.

The presence of magnetite is critical to the argument for the presence of fossilized biological organisms (McKay *et al.*, 1996), who claim that magnetite grains are the product of microbial metabolism. In terrestrial bacteria these magnetites occur as 'single magnetic domains' due to their size and are therefore strongly magnetic. This is useful for terrestrial bacteria that need to sense magnetic field orientation. McKay *et al.* (1996) and others Thomas-Keprta et al. (1998, 1999) claim that many of the ALH84001 magnetites have this same size and shape, and therefore may have served the same purpose. Contrary to this, Thomas-Keprta *et al.* (1999) state that many of the ALH84001 magnetites are too small to be stably magnetized and are therefore unlikely to be biogenic in origin. Also it is unclear why magnetotactic bacteria would choose to live in an igneous rock containing other magnetic minerals: these types of bacteria are absent from terrestrial igneous rocks.

The morphological evidence cited by McKay *et al.* (1996) hinges on the interpretation of carbonate surface features. McKay *et al.* (1996) argue that ovoid and elongate 'worm' shapes up to 100nm long may be the fossilised remains of bacteria, stating the similarities between their bacteria and nanofossils found in terrestrial travertine. As the carbonates are inferred to be indigenous to Mars, the possible nanofossils are also likely to be Martian in origin.

McKay *et al.* (1996) state that these features are not artifacts of the Au-Pd covering applied to the samples because they are not present in a control lunar sample, although this has been disputed (Sears and Kral, 1998). McKay *et al.* (1996) also state that terrestrial contamination is not responsible because other heavily weathered ordinary chondrites from the same icefield show none of these surface features.

One of the crucial problems with this hypothesis is the size of the supposed Martian bacteria: they are often only 20nm across. When the several nanometre thick Au/Pd coating is taken into consideration, the internal metabolism of the bacteria has <10nm in which to function, which seems unlikely. Clearly this hypothesis is heavily dependent on the formation temperature and deposition mechanism for the carbonates which host the possible fossilised nanobacteria.

Mechanism of formation of carbonate?

Although the postulated deposition mechanisms all have some evidence to support them, there appear to be significant problems with most hypotheses. Evidence suggesting high temperature deposition based on chemical equilibria is highly questionable because the carbonates appear to have formed from multiple influxes of fluid that never attained equilibrium. Similarly, low temperature hydrous fluid precipitation seems to be incompatible with the lack of hydrous alteration. The increasing Mg content of the carbonates towards the rims is the opposite of increasing ferroan compositions that occur from carbonate liquid evolution (Treiman, 1998). The secondary minerals are not typical of a sabhka assemblage. No one hypothesis seems free of problems when the many lines of available evidence are taken into account.

Temperature of carbonate formation?

Clearly the mechanism of formation to some extent governs the temperature of formation. However, if the most widely accepted model of a percolating fluid is accepted, isotopic modeling permits a wide range of temperature from 0°C up to 500°C.

Composition of fluid that deposited the carbonates?

This is also closely linked to the mechanisms of carbonate formation and the assumptions about temperature of deposition. Owing to the lack of temperature constraints, CO_2-H_2O fluids of any composition could generate ALH84001 carbonate.

Origin of fluid that deposited the carbonates?

Perhaps the key question in attempting to explain ALH84001 carbonate formation is the origin of the source fluid itself. Again, because formation temperatures range from 0°C to 700°C, the chemical and isotopic composition of the source fluid itself is unclear. However, some recent isotopic data from carbonates of $\delta^{18}O$ ~0‰ (Saxton *et al.*, 1998; Eiler *et al.*, 2002) challenges the validity of common models: a greater range in isotopic composition causes difficulty for a simple hydrothermal system model with a source fluid of one isotopic composition. Equally the lightest carbonates challenge the view that high temperature exchange may have occurred. An even greater range of carbonate composition would be able to lend more weight to these arguments, possibly allowing some models to be ruled out entirely which, in turn, would limit the range of source fluid composition and temperature, constraining the source fluid environment.

Chapter 6

Stable isotopes

6.1 Hydrogen

The present day Martian atmosphere contains water enriched in deuterium by a factor of ~5 over terrestrial values (terrestrial D/H ratio is $\sim 1.5 \times 10^{-4}$). Expressed as δD, the deviation in parts per thousand of D/H ratio from terrestrial SMOW, this equates to δD 4200 ± 200‰ (Bjoraker *et al.*, 1989). Terrestrial δD varies from – 300‰ to +100‰ (Hoefs, 1997). It is generally assumed that Earth and Mars formed with similar initial D/H ratios and that subsequent loss of hydrogen from the Martian atmosphere has led to deuterium enrichment over time (Owen *et al.*, 1988).

Initial stepped heating studies of D/H ratios in Martian meteorites (Fallick, 1983; Yang and Epstein, 1985) yielded terrestrial values. Discarding the low temperature step, Fallick (1983) reported δD of –37‰ for H_2O evolved from Nakhla in a 350°C-1000°C step, δD –32‰ for water from Chassigny during the same temperature release and –47‰ for Shergotty water released between 440°C and 1000°C. Similarly, Yang and Epstein (1985) reported δD for Shergotty water as –80‰ to +52‰ in three temperature steps from 350°C-1100°C. Later work (Kerridge, 1988) with significantly more material (2g of Lafayette and 2.8g of Shergotty) yielded δD +878 and +456 respectively for a single 450°C-1050°C step: the first indication of a heavy Martian atmosphere signature in Martian meteorites. More recent stepped heating work (Leshin *et al.*, 1996) reveals elevated δD values in Nakhla, Lafayette, Governador Valadares, Shergotty, Zagami, EETA 79001 and ALH 84001 with only Chassigny lacking a significantly positive δD.

Table 6.1: Summary of δD analyses by stepped heating of Martian meteorite ([a]Leshin *et al.*, 1996; [b]Kerridge, 1988)

Sample	Temperature (°C)	H_2 (μmole/g)	δD (‰)
Nakhla[a]	>200	28.4	+291
Nakhla[a]	>300	14.0	+491
Lafayette[a]	>200	110	+493
Lafayette[a]	>300	72.5	+689
Governador Valadares[a]	>200	41.7	+141
Governador Valadares[a]	>300	18.4	+126
Shergotty[a]	>150	16.9	+602
Shergotty[a]	>350	8.9	+1171
Zagami[a]	>150	21	+557
Zagami[a]	>350	10.6	+1102
EETA79001 lithology A[a]	>150	17.4	+95
EETA79001 lithology A[a]	>350	6	+1472
ALH84001[a]	>150	30.4	+284
ALH84001[a]	>350	14.1	+573
Chassigny[a]	>150	32.3	-41
Chassigny[a]	>300	19	-7
Lafayette[b]	>450	29.2	+456
Shergotty[b]	>450	6.6	+878

None of the step heating extractions yields δD 4200 ± 200 of the present Martian atmosphere. Leshin *et al.* (1996) measured terrestrial values at low temperature extractions, followed by decreasing yield but increasing δD with higher temperature. This is indicative of terrestrial contamination by H_2O released at low temperature with release of pre-terrestrial tightly bound H at higher temperatures. However, the possibility of a contribution from terrestrial contamination at high temperatures cannot be excluded and δD values are still increasing with temperature at the highest

temperature extraction, suggesting the true Martian signature is higher still and stepped heating values represent lower limits.

Shergottites have the highest δD values, nakhlites have intermediate δD values with variable water content followed by ALH84001 and finally Chassigny, which has D/H indistinguishable from terrestrial water. Higher yields in Lafayette relative to Nakhla but similar release patterns are indicative of similar alteration products in both meteorites but a higher abundance in Lafayette. Shergottite stepped heating extractions are less easy to interpret: a decreasing yield with increasing temperature suggests siting of Martian H in low temperature alteration products. However these alteration products are rare in shergottites. Amphiboles and apatites have elevated δD values (Table 6.2) but are not abundant enough to account for the whole rock value. Siting of shergottite preterrestrial hydrogen in pyroxene and feldspar is also unlikely as higher yield at higher temperature extractions would be expected. ALH84001 release patterns are also indicative of low temperature alteration products although clays and micas have been observed only in minute quantities (Brearley, 1998; 2000). Table 6.2 shows that ALH84001 maskelynite and carbonate, may be the carriers for hydrogen in ALH84001, despite the lack of crystallographic site for hydrogen in carbonate. Chassigny, despite yielding elevated δD values in amphibole and biotite does not yield a Martian D/H ratio on heating. This is puzzling since elevated but heterogeneous biotite and amphibole δD values (Watson *et al.*, 1994) imply infiltration of fluids and subsequent mixing between an enriched atmospheric source and a terrestrial like magmatic source. This infiltration would be expected to increase the whole rock value of Chassigny. Analysis of primary water-rich apatites in QUE94201 suggests mixing between an elevated atmospheric ratio and an elevated mantle component of approximately +1000‰ (Leshin, 2000).

Table 6.2: Summary of δD analyses by ion microprobe ([a]Leshin-Watson *et al.*, 1994; [b]Boctor *et al.*, 1999a; [c]Boctor *et al.*, 1999b; [d]Boctor *et al.*, 1998; [e]Suguira and Hoshino, 2000; [f]Leshin, 2000).

Sample	mineral	δD variation (‰)
Chassigny[a]	Kaersutite (amphibole)	+897±81>δ**D**>+1879±48
Chassigny[a]	Biotite	+987±40
Shergotty[a]	Kaersutite	+512±89
Zagami[a]	Kaersutite	+1498±62>δ**D**>+1672±57
Zagami[a]	Apatite	+2963±141>δ**D**>+4358±185
ALH84001[b]	Feldspathic glass	+969±13>δ**D**>+1755±36
EETA79001[b]	Feldspathic glass	+1727±59>δ**D**>+2757±38
EETA79001[b]	Mafic glass	+2023±34>δ**D**>+2901±23
ALH84001[c]	Carbonate globules	+791±12>δ**D**>+1156±33
ALH84001[c]	Irregular carbonate	+336±4>δ**D**>+491±4
ALH84001[c]	Feldspathic glass	+1197±15>δ**D**>+1596±19
EETA79001[c]	Feldspathic glass	+1612±91>δ**D**>+1779±58
EETA79001[c]	Mafic glass	+2662±36>δ**D**>+2852±40
ALH84001[d]	Whitlockite (phosphate)	+201±14>δ**D**>+287±12
ALH84001[d]	Carbonate globules	+165±11>δ**D**>+313±5
ALH84001[e]	Carbonate globules	+293>δ**D**>+1344
QUE94201[f]	Apatite	+1683±134>δ**D**>+3565±228

6.2 Oxygen

ALH84001

Three step acid dissolution experiments (Romanek *et al.*, 1994) have yielded oxygen isotopic data of $\delta^{18}O_{SMOW}$+13.3‰ in the Ca-rich core to $\delta^{18}O_{SMOW}$+22.3‰ in the Mg-rich rim. Using a similar method, Jull *et al.* (1995) acquired a carbonate bulk average of $\delta^{18}O_{SMOW}$+15‰ ±5‰. Ion microprobe analyses have yielded carbonate globule core to rim isotopic zoning from $\delta^{18}O_{SMOW}$+9.5‰ ±1.1‰ to $\delta^{18}O_{SMOW}$+20.6‰

±1.3‰ (Valley *et al.*, 1997), $\delta^{18}O_{SMOW}$ +8‰ to $\delta^{18}O_{SMOW}$+22‰ (Saxton *et al.*, 1998) and $\delta^{18}O_{SMOW}$+5.4‰±0.8‰ to $\delta^{18}O_{SMOW}$+25.3‰ ±0.8‰ (Leshin *et al.*, 1997).

Nakhla

The siderite in Nakhla has an isotopic composition of $\delta^{18}O_{SMOW}$ +34 ± 1‰ (Saxton *et al.*, 2000) which is sufficiently different from the silicate ratios $\delta^{18}O_{SMOW}$ +4.1‰ (Clayton and Mayeda, 1996) to rule out a primary igneous origin for the siderite.

Lafayette

The $\delta^{18}O_{SMOW}$ values of carbonate are +30.7‰ ± 1.1‰ to +36.2‰ ± 0.8‰ (Vicenzi and Eiler, 1998). Fluorination techniques by Farquhar *et al.* (1999) indicate lower $\delta^{18}O_{SMOW}$ values of +27.6‰. Acid dissolution experiments on aliquots of whole rock powder (Wright *et al.*, 1992) yield $\delta^{18}O_{SMOW}$ values of carbonate +26‰ and $\delta^{13}C_{PDB}$ values of +1‰.

Governador Valadares

Acid dissolution experiments on aliquots of whole rock powder (Wright *et al.*, 1992) give $\delta^{18}O_{SMOW}$ values of carbonate +24‰ and $\delta^{13}C_{PDB}$ values of +11‰.

EETA79001

The calcite present in EETA79001 has a $\delta^{18}O_{SMOW}$ of +21.0‰ and a $\delta^{13}C_{PDB}$ of +9.7‰ (Clayton and Mayeda, 1988). This is comparable to the calcite values of +21.1‰ for oxygen and +6.8‰ for carbon obtained by Wright *et al.* (1988). The silicate has a $\delta^{18}O_{SMOW}$ of +4.2‰ therefore the carbonate is not of igneous origin.

Zagami

Jull *et al.* (1997) suggests one heavy end member for Zagami carbonates with a near-terrestrial composition and a lighter carbonate with $\delta^{13}C_{PDB}$ of -17‰ to -20‰ and $\delta^{18}O_{SMOW}$ of +16‰ to +3.2‰. These reservoirs do not appear to have the same isotopic

composition as the reservoirs suggested for ALH84001 and the nakhlites (Jull *et al.*, 1997).

Chassigny

Acid dissolution experiments on aliquots of whole rock powder (Wright *et al.*, 1992) give carbonate $\delta^{18}O_{SMOW}$ values of +29‰ and $\delta^{13}C_{PDB}$ values of -5‰.

Table 6.3: Summary of $\delta^{18}O$ analyses. [a]Saxton *et al.*, 1998; [b]Leshin *et al.*, 1998; [c]Valley *et al.*, 1997; [d]Romanek *et al.*, 1994; [e]Jull *et al.*, 1995; [f]Jull *et al.*, 1997; [g]Eiler *et* al., 1998; [h]Wright *et al.*, 1992; [i]Saxton *et al.*, 2000; [j]Vicenzi and Eiler, 1998; [k]Farquhar *et al.*, 1999; [l]Clayton and Mayeda, 1988; [m]Wright *et al.*, 1988

Sample	**mineral**	**$\delta^{18}O$ (‰)**
ALH84001[a]	Carbonate rosettes core → rim	+8 → +22
ALH84001[b]	Carbonate rosettes core → rim	+5 → +25
ALH84001[c]	Carbonate rosettes core → rim	+9 → +21
ALH84001[d]	Carbonate rosettes core → rim	+13 → +22
ALH84001[e]	Bulk carbonate	+15
ALH84001[f]	Bulk carbonate	+10 → +17
ALH84001[a]	ankerite	0
ALH84001[g]	carbonate	0
Nakhla[h]	carbonate	+23 to +26
Nakhla[i]	siderite	+34
Lafayette[j]	carbonate	+31 to +36
Lafayette[k]	carbonate	+28
Lafayette[d]	carbonate	+26
Governador Valadares[d]	carbonate	+24
EETA79001[l]	carbonate	+21
EETA79001[m]	carbonate	+21
Chassigny[d]	carbonate	+29
Zagami[f]	carbonate	+3 to +16

In addition to specific information regarding the ALH84001 carbonate formation temperature (see chapter 5), oxygen isotopes in secondary minerals of all Martian meteorites can also be used to constrain a global Martian hydrosphere. The range of oxygen isotope values in table 6.3 can be produced by a single H_2O source of $\delta^{18}O$ –2‰ (figure 6.1), in which the case the isotopically lightest carbonate (+5‰ ALH84001 ankerite) is formed at ~350°C while the heaviest carbonate (+34‰ Nakhla siderite), formed at ~10°C. If the 0‰ ankerite is included, a single H_2O-rich source with a $\delta^{18}O$ of –5‰ is just capable of generating all carbonates.

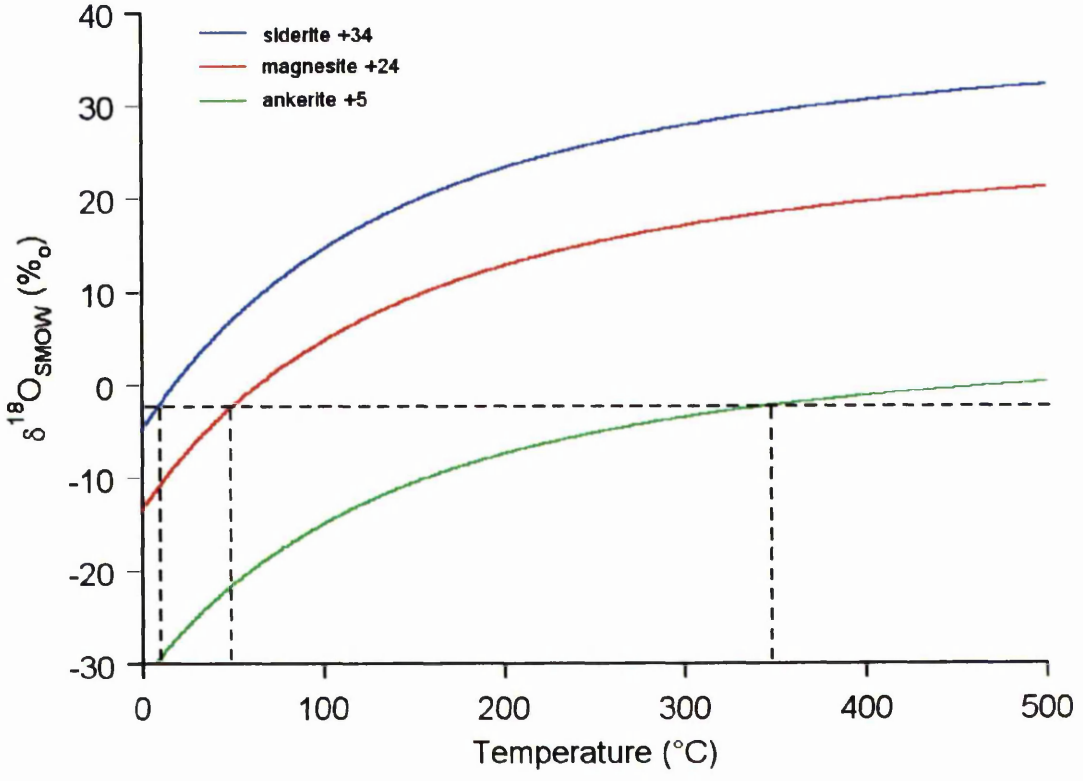

Figure 6.1: $\delta^{18}O$ of water capable of precipitating ALH84001 ankerite and magnesite (Leshin *et al.*, 1998; Saxton *et al,* 1998), and Nakhla siderite (Saxton *et al.*, 2000).

Extraction of water from the Martian meteorites with $\Delta^{17}O$ in excess of 0.4‰ relative to Martian silicate (Karlsson *et al.*, 1992) implies a subsequent oxygen isotope reservoir that is not in equilibrium with the crustal rocks. Karlsson *et* al. (1992) inferred late accretion of a hydrosphere with a different oxygen isotopic complement to that of bulk Mars. Nakhla and Lafayette carbonates and sulphates have yielded $\Delta^{17}O$ as high as 1.3‰ (Farquhar and Thiemens, 2000) relative to the silicate, further demonstrating the degree of disequilibrium.

The preservation of different $\Delta^{17}O$ between the secondary and primary minerals is inferred to be the result of the lack of crustal recycling on Mars and therefore a lack of exchange between surface and magmatic oxygen reservoirs. It also implies low temperature deposition of the secondary minerals because very high temperature fluids would have isotopically equilibrated with the host rock and any $\Delta^{17}O$ anomalies in the fluid (assuming fluid/rock ratio is almost zero) would have been lost.

6.3 Carbon

Carbon isotope measurements in Martian meteorites can be split into two categories: $\delta^{13}C$ enriched carbon in carbonate and $\delta^{13}C$ depleted carbon within the whole rock. Of all carbonate-bearing Martian meteorites, only ALH84001 and Nakhla contain significant $\delta^{13}C$ enrichment. The $\delta^{13}C$ depleted carbon is inferred to be magmatic in origin, implying a mantle value of approximately –25‰ on Mars (Wright *et al.*, 1992). This is substantially lighter than the –5‰ of terrestrial mantle, although buffering from carbonate ions in Earth's oceans may affect this value, causing $\delta^{13}C$ heterogeneity in the upper mantle. In contrast, the heavier carbonates are thought to have formed from a surficial carbon reservoir which had isotopically exchanged with an atmosphere that, previously, had undergone non thermal loss of CO_2 to space.

Table 6.4: $\delta^{13}C$ of Martian carbonate and reduced carbon by H_3PO_4 dissolution ([a]Jull *et al.*, 1997; [b]Romanek *et al.*, 1994; [c]Jull *et al.*, 1995; [d]Wright *et al.*, 1992; [e]Clayton and Mayeda, 1988; [f]Wright *et al.*, 1988)

Sample	Phase	$\delta^{13}C$ (‰$_{PDB}$)
ALH84001[a]	Carbonate	~+40-45
ALH84001[b]	Carbonate	$+39.5<\delta^{13}C<+41.8$
Nakhla[c]	Carbonate	$+15<\delta^{13}C<+55$
Nakhla[d]	Carbonate	+9
Lafayette[d]	Carbonate	+1
Governador Valadares[d]	Carbonate	+11
Chassigny[d]	Carbonate	–5
EETA79001[e]	Carbonate	+9.7
EETA79001[f]	Carbonate	+6.8
ALH84001[a]	Reduced C	–15
Nakhla[d]	Reduced C	–31
Lafayette[d]	Reduced C	–29
Governador Valadares[d]	Reduced C	–26
Chassigny[d]	Reduced C	–32
EETA79001[d]	Reduced C	–33
Zagami[d]	Reduced C	–34

Carbon isotopic values for Martian carbonates vary from –20‰ to +50‰ with no relation to crystallisation age. Thus the isotopically heavy carbonates may be formed from ^{13}C enriched fluids from the hydrosphere and atmosphere while the isotopically light carbonates reflect a primary bulk Mars value. However, this implies that the bulk value for carbon in Mars is substantially lighter than the bulk value for the Earth (–5‰ to –8‰) which is difficult to explain unless significant fractionation occurs between the Martian crust and mantle. The heavy enrichment in ^{13}C (up to +50‰) cannot be

explained by equilibrium isotopic fractionation therefore substantial kinetic fractionation by loss processes in the atmosphere is required.

6.4 Summary

There appears to be negative correlation between $\delta^{13}C_{PDB}$ and $\delta^{18}O_{SMOW}$ within the nakhlites, Chassigny and EETA79001. This is in contrast to Zagami, which appears to have positive $\delta^{13}C_{PDB}$ and $\delta^{18}O_{SMOW}$ correlation (Jull *et al.*, 1997) and lower $\delta^{13}C_{PDB}$ values, probably reflecting a isotopically lighter, magmatic source. ALH84001 appears to show no correlation between oxygen and carbon isotopic ratios (Jull *et al.*, 1995; 1997). The isotopic data from nakhlites (Wright *et al.*, 1992) places limits on the endmember isotopic composition of the reservoirs. The postulated reservoirs have a composition of isotopically light $\delta^{13}C_{PDB}$ –5‰ with isotopically heavy $\delta^{18}O_{SMOW}$ of +29‰ and a composition of relatively heavy carbon $\delta^{13}C$ >+11‰ and relatively light oxygen $\delta^{18}O_{SMOW}$ <+23‰, although due to the lack of knowledge of temperature and H_2O-CO_2 ratios of fluids, these values require several assumptions. Saxton *et al.* (2000) calculate a surficial oxygen reservoir with $\delta^{18}O_{SMOW}$ –6 to +22‰ from ALH 84001 magnesite and Nakhla siderite constraints, the variation reflecting the lack of knowledge of formation temperature. This is not in conflict with Jull *et al.* (1997), who estimate, from ALH84001 and Nakhla, a heavy carbon reservoir (40-45‰) to have a $\delta^{18}O_{SMOW}$ between –12‰ and +28‰.

Isotopic ratios of volatiles in Martian meteorites suggest that at least two distinct volatile reservoirs are present on Mars. One is presumably the interior with a volatile inventory unchanged from that present during Mars accretion. The remaining reservoirs are likely to be surface and atmospheric, with the variation due to late stage heterogeneous accretion (e.g. comets) and / or mass fractionation as the hydrosphere /

atmosphere evolved. The lack of equilibrium between these components may be a result of the lack of subduction tectonics and therefore a lack of interior-surface volatile exchange.

Chapter 7

Methodology

7.1 Sample preparation

Samples for oxygen and carbon analyses were prepared differently. For oxygen analysis, grains of ALH84001 were mounted in Lakeside™ epoxy and polished to present a flat surface for chemical and isotopic analysis. The epoxy impregnates the mounted sample, particularly the more friable components (i.e. carbonate) to give a mineral surface suitable for polishing and subsequent electron and ion beam analyses. Epoxy is suitable as a mounting medium for samples that require oxygen isotope analyses because the O^- signal from epoxy is an order of magnitude less than that of a mineral. Any contamination of the O^- signal by a contribution from the epoxy is also easily recognised by the presence of a large $^{16}OH^-$ signal.

Carbon measurements require a different mounting medium because C^- counts from epoxy are approximately two orders of magnitude greater than C^- counts from carbonate. Given the likelihood of carbonate impregnation by epoxy, it is clear that contamination of the carbonate C^- signal by C^- from epoxy would be unavoidable. Therefore samples for carbon isotopic analysis were set in high mercury dental amalgam within copper blocks and polished on a tin polishing lap using aluminium oxide powder and water to keep carbon contamination to a minimum. These 'carbon-free' samples were originally coated in a thin (approx 10nm) conductive layer of aluminium to prevent charging during EDS analyses and allow charge compensation during ion probe analyses. However, it appeared that due to its reactive nature, aluminium acted as a hydrocarbon getter which trapped organic material beneath the coat leading to unacceptably high levels of contamination. This source of

contamination could be removed effectively by rastering the primary beam over the analysis areas to clean the surface. It was found that thin gold coat did not cause a contamination problem.

7.2 Optical microscopy

Reflected light optical microscopy was used to identify carbonates that were present at the surface, or those that may be brought to the surface after further polishing. Carbonate rosettes observed in partially polarised reflected light are characteristically orange and are apparent in reflected light due to the greater surface roughness after polishing when compared to silicate.

7.3 Mineralogical / chemical analyses

7.3.1 JEOL JSM 6400 Analytical Scanning Electron Microscope

Preliminary scanning electron microscopy studies of selected grain mounts were conducted using the JEOL JSM 6400 Analytical SEM at Manchester. This instrument was used in both imaging (BSE emission) and quantitative analysis (secondary electron emission) modes. Back scattered images were obtained to locate rosettes, employing the high contrast between the dark grey of lower average atomic mass magnesium rich rims and the light grey of the higher average atomic mass calcium / iron rich cores. Accompanying quantitative data was collected to map the extent of the carbonate rosettes, particularly those rosettes which are found interspersed with maskelynite over a relatively large area. An accelerating voltage of 15kV and a working distance of 39mm were used when obtaining images and a spot size of ~5 μm^3 was employed for quantitative analysis.

7.3.2 Cameca SX100 Electron Microprobe

Higher precision quantitative chemical analyses of carbonate rich areas determined by SEM analysis were undertaken using the Cameca SX100 electron microprobe at Manchester. The electron microprobe utilises a finely focused beam of electrons (~0.1 μm diameter) to produce a characteristic X-ray spectrum from the sample surface. Five wavelength dispersive spectrometers and an energy dispersive spectrometer measure these X-rays to give chemical analyses with a spatial resolution of a ~5 μm^3 and a detection limit of 0.01wt% and 0.1wt% respectively. Cameca element maps are 512*512 pixels or 256*256 pixels with an approximate resolution of 1 pixel per micron. Chemical analyses using the electron microprobe consist of individual spots and line scans consisting of equally spaced spot measurements with ZAF correction procedure. Oxygen and carbon were not measured therefore C and O were used to normalise the totals to 100% using the C:O ratio as a free parameter. Multiple element maps were also produced to find candidate areas for ion probe analysis.

7.4 Isotope analyses

7.4.1 VG Isolab 54 ion microprobe

The VG Isolab 54 ion microprobe in Manchester has been designed, built and modified to measure isotopic abundances of elements with high spatial (~10μm) resolution by secondary ionisation mass spectrometry (SIMS), resonance ionisation mass spectrometry (RIMS) and thermal ionisation mass spectrometry (TIMS). The ion microprobe also has the capability to measure elemental abundances, but for this study, only SIMS measurements of isotopic abundances have been conducted.

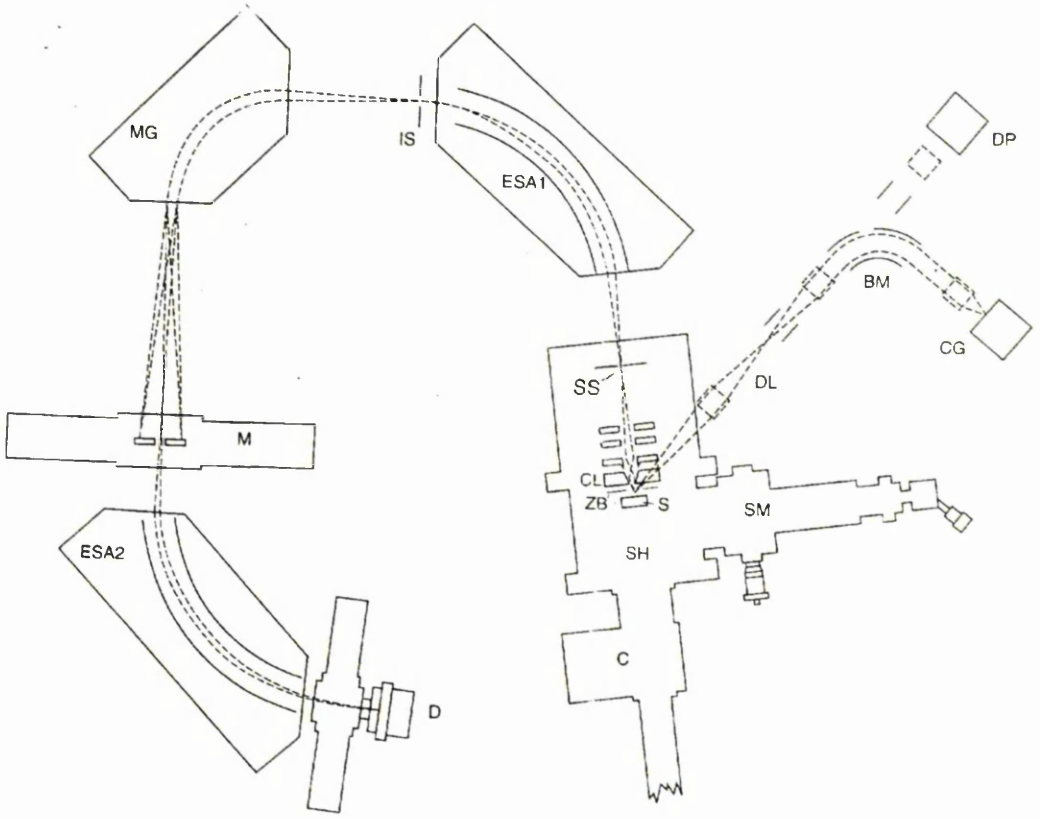

Figure 7.1: Manchester Isolab VG 54 ion microprobe (from Saxton *et al.*, 1996)

Primary ions are produced by the caesium gun (CG) or duoplasmatron (DP). Caesium passes through the beam combiner (BM) and dog-leg (DL) to remove energetic neutrals before focusing onto the sample (S). Samples are inserted from the carousel (C) and presented to the extraction optics using the sample manipulator (SM). The z-bias (ZB) and condenser lens (CL) focus the secondary ions on the source slit (SS). Ions are then dispersed in energy in ESA 1 and in mass by the magnet (MG) to achieve mass resolution before reaching the multi-collectors (M). If high abundance sensitivity is required a second ESA and a Daly collector (D) is available.

Primary ions

For analysis of electronegative secondary ions H^-, C^- and O^-, a focused beam of Cs^+ ions are used as the primary ion beam. These ions are produced by evaporation of caesium metal onto a tungsten frit and accelerated to 10kV, focused and steered through

90° by a beam combiner. Further deflection removes neutral atoms before the Cs^+ ion beam passes through an aperture of 50μm or 100μm to give a spot size on the sample of approximately 10μm or 20μm respectively.

Secondary ions

The sample was biased at –8kV when the ion probe is detecting negatively charged secondary ions sputtered from the sample surface. Approximately 1% ionization yield is achieved using the SIMS method. The important negative ions when measuring oxygen isotopic are $^{16}O^-$, $^{17}O^-$, $^{18}O^-$ and similar molecular mass $^{16}OH^-$. Similarly, carbon isotopic measurements require sputtered $^{12}C^-$, $^{12}C^1H^-$, $^{13}C^-$ ions.

Analysers

The analyser consists of a 350mm radius 81.5° electrostatic analyser and a 270mm radius which, because of a 26.56° exit pole angle, has an actual dispersion length of 54cm (double the radius). This is the basis of the instrument name 'VG Isolab 54 ion microprobe'. The ions produced by secondary ionization have a range of energies from a few electronvolts (eV) to several hundred eV with a peak in the 10eV-20eV range. These secondary ions of differing initial energies are admitted to the 1st ESA where they are passed through a fixed electric field for a given extraction potential and hence sorted by kinetic energy to negate the initial energy dispersion, increasing mass resolution for the mass spectrometer. The intermediate slit between the first ESA and the magnet has a 22eV window, allowing 30-50% transmission depending on the ionic species (Saxton *et al.*, 1996). The dispersion of the magnet by mass and energy is equal and opposite to the ESA such that all ions are focused to a point at the detector slit on exiting the magnet, regardless of their initial energy and hence their vector within the magnet.

This double focusing by both mass and energy allows high mass resolution, which is essential when attempting to resolve the overlapping tail of the usually much more abundant ^{16}OH ions from the ^{17}O ions. Owing to a mass difference of only 0.0036 mass units between these two ions, the mass resolving power (M / ΔM) is required to be in excess of 6000. This mass resolving power (MRP) is dependent on the source and detector slit sizes, hence the ^{16}O detector slit is 1mm (MR=540), the ^{18}O slit is 250μm (MR=2000) and the ^{17}O slit is 70μm (MR=6000).

Detectors

The ion microprobe detectors are usually set up to measure the isotopic ratios of oxygen with all three isotopes measured simultaneously. The detector array for this type of analysis consists of a Faraday cup collector for ^{16}O (high count rate $>10^6$ s^{-1}), where the secondary ion intensity is sufficient to measure the current directly, and two electron multipliers with conversion dynode systems (CDS) detectors for ^{17}O and ^{18}O (low count rate $<10^6$ s^{-1}). The electron conversion dynode is required to produce a uniform yield of electrons for amplification in the channeltron, independent of where the ions enter the detector, giving a very stable detector gain. The conversion dynode uniformity is increased by operating the front of the multiplier at ground potential and the back at 2.3kV, as is required when measuring negative oxygen ions.

Modes of operation

The standard method of ion probe operation is spot analyses, which measures individual circular regions of the sample to a spatial resolution of approximately 10μm. For several months, attempts were made to develop 'trench mode'. This required software controlled stepping of the secondary deflector plate voltages so that the primary beam was sequentially stepped along the sample with the intention of improving internal precision and therefore obtaining useful $\Delta^{17}O$ measurements. A

typical trench involved 16 steps over a 90μm length. However, reproducibly of $^{18}O/^{16}O$ ratios was poor and this method was abandoned as a means of acquiring data for a series of spots simultaneously.

Ion imaging was employed to digitally raster the beam over the sample in a well defined grid. The secondary ion beam signal from each grid location was then processed to give images of ion intensities across the area of interest. This method was used to precisely locate the primary beam on the sample by utilizing the enhanced $^{16}OH^-$ signal off regions lacking a carbon coat due to previous ion probe analyses or deliberate 'location' spots.

Fractionation effects

Two major sources of error are inherent in the acquisition of isotope ratios by ion probe. These are isotopic fractionation when passing ions through the secondary column optics and fundamental fractionation that occurs when ions are sputtered from the sample by the primary beam.

Instrument effects

Instrumental isotopic fractionation occurs because there is a wide range of energies and angular distributions imparted to the secondary ions. This is inherent in the SIMS sputtering process and geometry of the primary beam and sample, Therefore, unless 100% transmission of ions through the secondary optics occurs, isotopic fraction is inevitable. With the introduction of narrow slits to afford high mass resolution required for oxygen isotopic analyses, 100% transmission is not feasible and isotopic fractionation is a possibility.

The first source of instrumental isotopic fractionation is the energy spread of secondary ions leaving the sample. Different ions have different energy spectra, although there is a plateau region at ~20eV where very little fractionation occurs with a

change in the energy spectra peak. Methods used to acquire this plateau are described in Lyon *et al.* (1994).

A second, more problematic source of instrumental fractionation is the 'chromatic aberration' also described in detail by Lyon *et al.* (1994). This fractionation is introduced because the spatial distribution of different isotopes is not uniform as they pass through the pre-spectrometer slit. Thus, the 5-10% transmission through a 20-30μm slit required for a MRP of 6000 induces fractionation. This source of fractionation is removed by rapidly (12kHz) sweeping the whole beam across the source slit and therefore integrating the three isotopes (Lyon *et al.*, 1994).

When attempting to reliably record ^{17}O, high MRP requires that the ion beam remains centred on the narrow source slit during data collection otherwise fractionation may occur. Mass stability as controlled by the magnet has been seen to drift by 10's of p.p.m. per hour, which is not sufficiently stable for ^{17}O measurements (Saxton *et al.*, 1996). Therefore an electrostatic centring unit (ECU) was built to scan the difference between the half intensities of the $^{16}OH^-$ peak (voltage differences are approximately proportional to the mass drift) then 'hop' back a known offset to the ^{17}O peak. This reduces the mass drift to an acceptable 1‰ hr^{-1} (Saxton *et al.*, 1996).

Matrix effects

A second major source of isotopic fractionation arises from variability in ionization probability with chemical composition of the sample (known as the 'matrix effect'). This can lead to measured differences in $^{18}O/^{16}O$ ratio of up to 20‰ between minerals of very different chemical composition but the same isotopic composition. This is unacceptable when accuracies of 1-2‰ are required. Variation in surface chemical composition, impurities and oxidation state compound this problem.

In an attempt to eliminate these effects when analyzing for oxygen, calcite, magnesite, siderite, ankerite and dolomite standards of known chemical and isotopic composition are analysed. It had previously been determined that the matrix effect depends on calcium content (Saxton *et al.*, 1998). The matrix effects of Martian carbonate of intermediate compositions are then inferred from the end member effects.

In previous work using the Manchester Isolab ion microprobe (Saxton *et al.*, 1998), the effect of different matrix cations on secondary ion yields appeared to be dependent on Ca content. Analyses of additional standards with compositions similar to those of Ca-rich ALH84001 carbonate ($Ca_{50}Mg_{39}Fe_{10}Mn_{00}$, $Ca_{51}Mg_{22}Fe_{25}Mn_{02}$) suggest that there is also a minor 'matrix effect' dependant on Fe and Mg content in the ankerite-dolomite region of the ternary diagram (table 7.1). Ankerite of composition $Ca_{51}Mg_{16}Fe_{31}Mn_{02}$ was used as the day to day standard over the period December 1999-April 2000 during which isotopic analyses of ALH84001 were performed. I assume the 1σ uncertainty of each ALH84001 carbonate measurement to be equal to the scatter in this ankerite standard over this four month observing period. The 1σ scatter of 50 day-to-day ankerite and calcite standards was 2.4‰. This includes error induced by varying detector sensitivities, any variation in instrumental fractionation due to retuning and variation due to change in external (lab) temperature. Errors associated with counting statistics are typically <1‰ therefore uncertainty for all ALH84001 measurements is taken to be the same as the uncertainty for the standard measurements: 2.4‰.

Analyses of ALH84001 at UCLA were conducted together with a dolomite $Ca_{50}Mg_{39}$ $Fe_{10}Mn_{00}$ standard and an ankerite $Ca_{51}Mg_{22}Fe_{25}Mn_{02}$ standard. Previously determined matrix effects (Leshin *et al.*, 1998) were used for more magnesian carbonate and the above standards were used for Ca-rich (>50%Ca) carbonate (Table 7.1).

Table 7.1: SIMS carbonate matrix effects relative to magnesite.

Mineral	**Manchester (this work and Saxton *et al.*, 1998) (‰)**	**UCLA (this work and Leshin *et al.*, 1998) (‰)**
Magnesite	0	0
Siderite	0.6	6
Ankerite	17.7	9.2
Dolomite	19.6	10.4
Calcite	20	13.6

Although the approximate trend of increasing matrix effect correction with Ca content is observed in both the Manchester and UCLA ion microprobes, some differences are apparent in the region of the siderite standard. This difference might be due to differences in charge neutralization: Manchester uses a 10 keV electron beam focused on the sample whilst UCLA uses a low energy electron 'flood gun'. Despite the differences in matrix corrections, the analyses of standards on both machines are reproducible. Proximity of the terrestrial standards to ALH84001 compositions are shown in the figure 7.2.

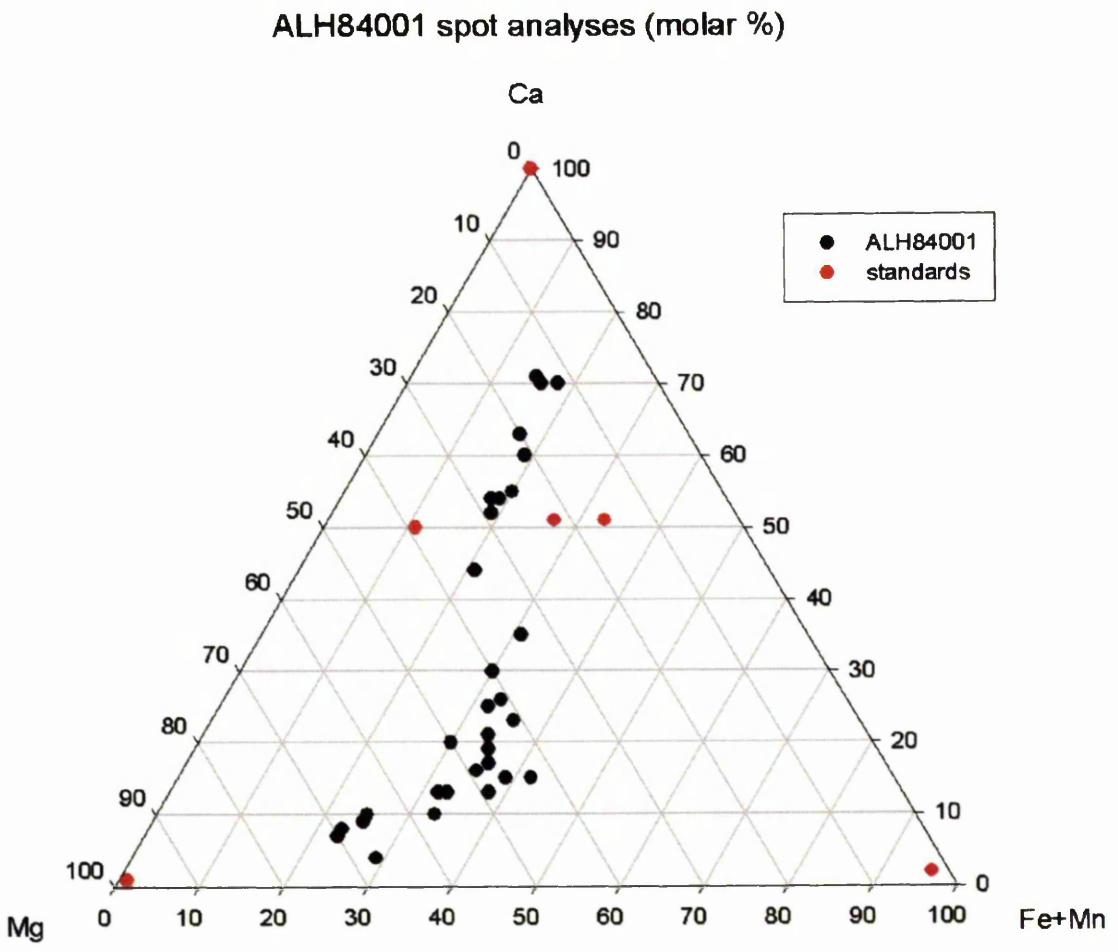

Figure 7.2: average chemical composition of ion probe spot analyses (Manchester and UCLA) errors in chemical composition are expected to be <5%. Red spots are terrestrial standards.

A similar process was undertaken for D/H measurements, using a dolomite, ankerite and siderite terrestrial standard (figure 7.3). The precise D/H ratio of these standards is not known, but is assumed to be within a few permil of SMOW. This is acceptable given that hydrogen matrix corrections are less crucial than oxygen corrections because the Martian D/H values can be several orders of magnitude greater than terrestrial values.

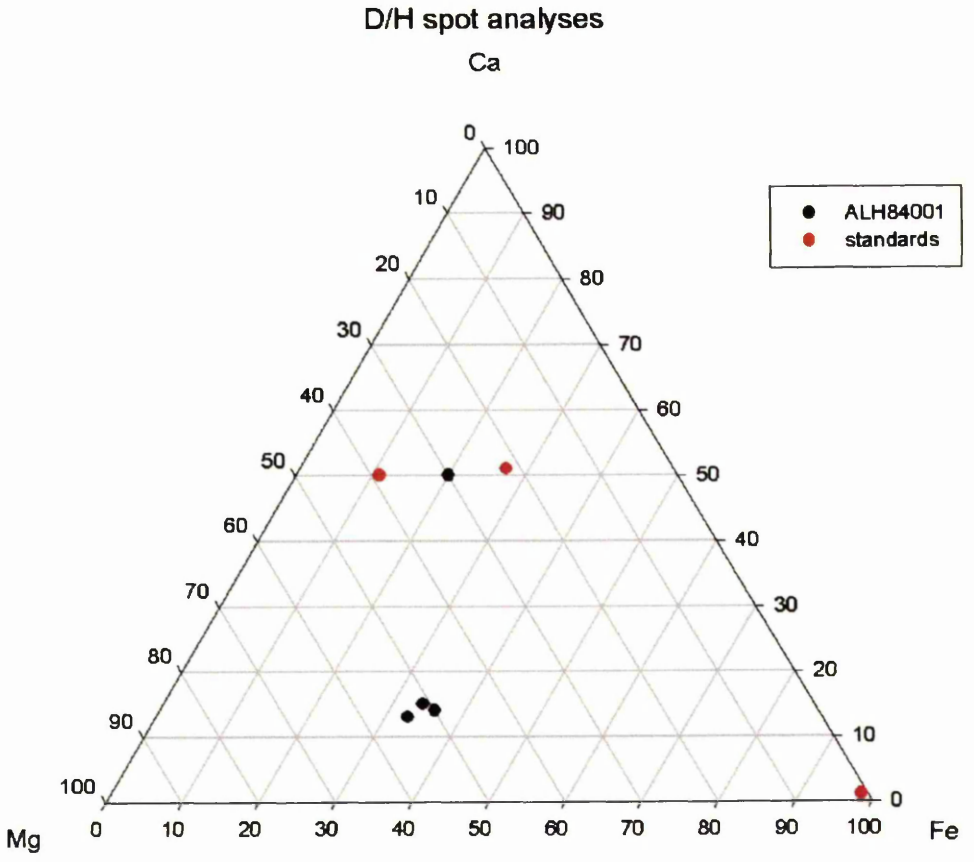

Figure 7.3: chemical composition of hydrogen spot analyses and accompanying standards

Procedure for taking measurements

Oxygen and carbon

Initially the primary beam was tuned to give maximum Cs current on the sample (usually approximately 0.07nA for 10μm spot size). Once the carbon coat (gold or aluminium when measuring carbon) over the analysed spot had been removed (100-200 secs), the electron beam was overlapped with the Cs beam to prevent charging of the spot. When the secondary ion signal was stable, the secondary ion optics were manually

tuned to give maximum signal into the detectors and the secondary beam was centred in the detectors using the ECU (^{16}OH peak when measuring oxygen and ^{12}CH peak when measuring carbon). First, a profile across the source slit was obtained to correct for deadtime on the detectors (deadtime corrections were <5‰ with errors due to uncertainty in the deadtime correction <<1‰) which was factored in during data reduction. Standards are run at the beginning and the end of the day, bracketing sample analyses, to correct for any changes in instrumental fractionation due to external conditions (e.g. lab temperature change).

Hydrogen

Tuning up for hydrogen analyses is identical to that for oxygen analyses except the ECU peak jumps between ^{16}OD and ^{17}OH in a process analagous to ECU centering on ^{16}OH. Despite the low count rate, these species were used in preference to ^{16}OH and ^{16}OD because a relatively large mass jump of 1 mass unit was not required at the high mass resolution used to resolve ^{16}OD and ^{17}OH. This method of analysis assumes $^{17}O/^{16}O$ is a constant, which is acceptable because any uncertainty is significantly less than the huge variation in δD exhibited by Martian samples. Inherent in any D/H measurement is a contribution of OH^- which is deposited from the vacuum onto the charged spot produced by the Cs^+ ions. Thus the ^{16}OD / ^{17}OH signal is a mixture of OH inherently associated with the mineral and terrestrial contamination OH from the vacuum. Clearly this would reduce any value from a deuterium enriched Martian carbonate. Deconvolution of the two sources of OH, vacuum OH and OH from carbonate, is not a simple process. If varying primary beam duty cycles are initiated on the same spot and $^{16}OH/^{16}O$ is plotted against $1/^{16}O$ (figure 7.4), the very low duty cycle data points (least kcps ^{16}O therefore largest $1/^{16}O$) have the highest $^{16}OH/^{16}O$ ratio. The high $^{16}OH/^{16}O$ are inferred to be dominated by surface H_2O that diffuses onto

the clean spot whilst the primary beam is off. The $^{16}OH/^{16}O$ ratio decreases with increasing duty cycle to the point where $1/^{16}O = \infty$ at the y intercept. This intercept is inferred to be the $^{16}OH/^{16}O$ ratio for the carbonate endmember.

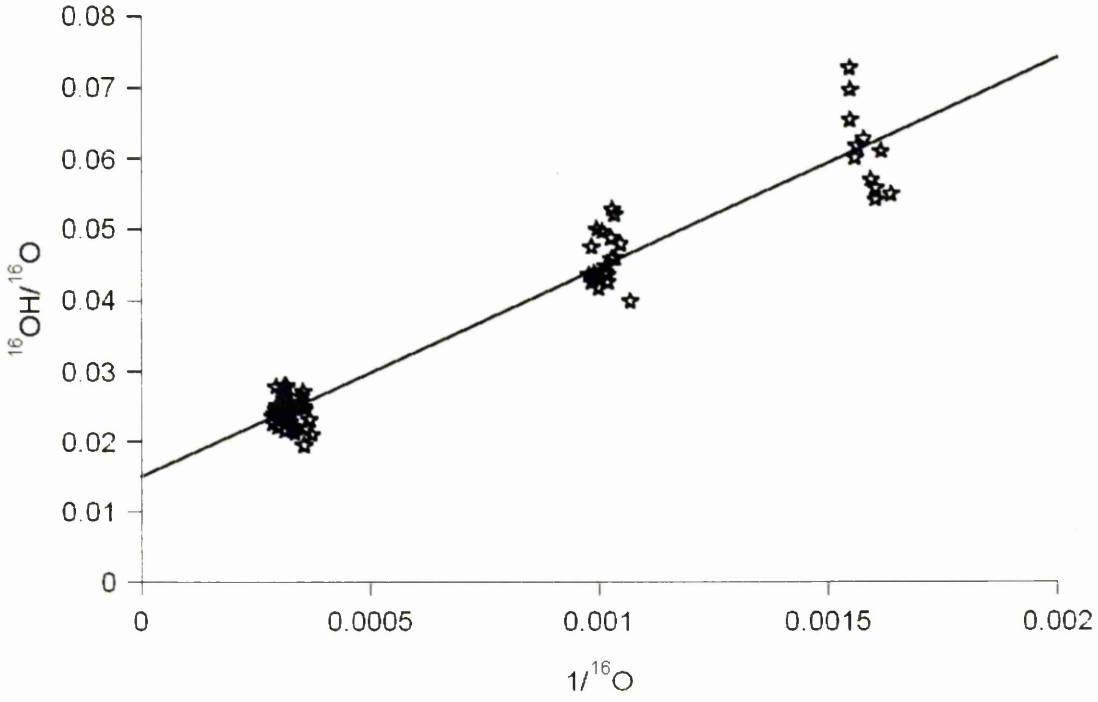

Figure 7.4: OH contamination from H_2O in vacuum system with low duty cycle.

If, when analysing a Martian sample, we then plot $^{16}OD/^{17}OH$ vs.$^{16}OH/^{16}O$ for pulsed and non-pulsed beams, we see an increased $^{16}OD/^{17}OH$ ratio with increased duty cycle due to the dilution of Martian D/H by terrestrial D/H. The 'true' $^{16}OD/^{17}OH$ signature of the carbonate is the $^{16}OD/^{17}OH$ ratio at the $^{16}OH/^{16}O$ value determined from figure 7.4 (in that case 0.0015). For this spot (Figure 7.5) the 'end member' $^{16}OD/^{17}OH$ is 0.625.

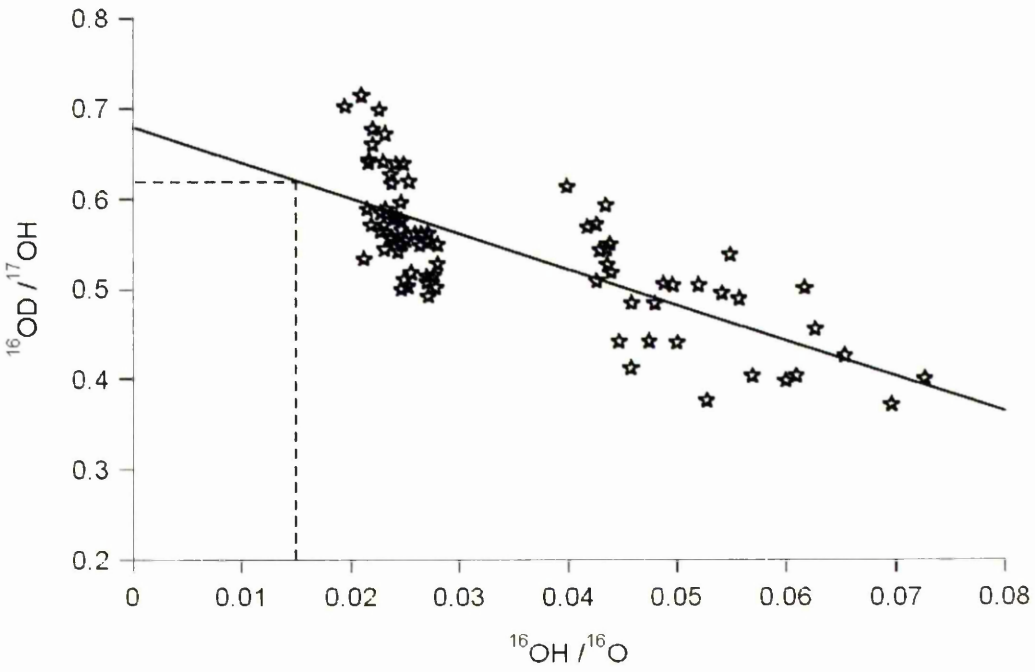

Figure 7.5: extrapolation of the measured Martian carbonate to the true δD of the mineral.

Using the same pulsed beam technique dolomite, ankerite and siderite terrestrial standards show no increased $^{16}OD/^{17}OH$ ratio with increased duty cycle (figure 7.6).

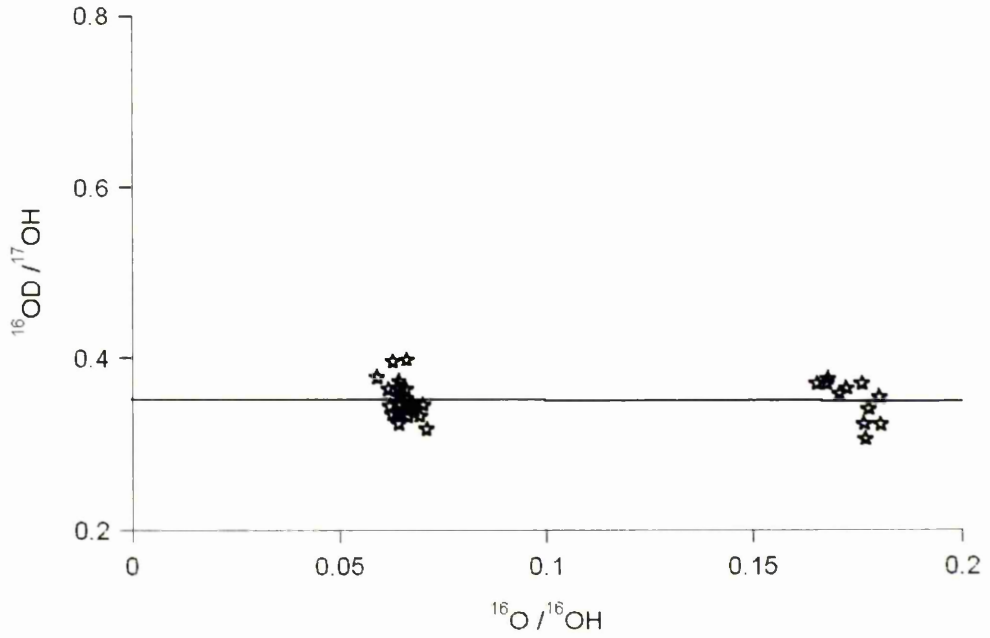

Figure 7.6: Pulsed and non-pulsed terrestrial siderite standard showing no significant instrumental fractionation

The $^{16}OD/^{17}OH$ ratio is 0.35±0.02 for the siderite standard to 0.38±0.04 for ankerite and dolomite standards: identical within error. Unfortunately the δD of the terrestrial standards in not known. However, all carbonate standards are hydrothermal in origin, which limits δD of the source fluid to between –20‰ and –60‰ (Taylor, 1994). If we include mineral OH – H_2O fractionation at hydrothermal temperatures (400°C) (Xu and Zheng, 1999), the hydrothermal carbonate typically possesses δD of between –50‰ and –90‰.

If there were no instrumental fractionation and the δD of the terrestrial standards was 0‰ relative to SMOW, the measured ^{16}OD / ^{17}OH ratio would be:

$$\frac{^{16}O\times^{2}H}{^{17}O\times^{1}H}=\frac{99.762\times0.015}{0.038\times99.985}=0.394$$

The measured ^{16}OD / ^{17}OH of the three standards has an average of 0.365±0.03. This equates to δD –75‰±75‰ in carbonate which is in the expected range of –50‰ to –90‰ in terrestrial hydrothermal carbonates. Thus it appears that there is no major instrumental fractionation effects. I assume a carbonate of δD 0‰ would yield ^{16}OD / ^{17}OH of 0.394. The ^{16}OD / ^{17}OH measurements of the Martian carbonate are then converted into δD with values from 100% duty cycle spots.

7.4.2 Cameca IMS 1270 ion microprobe

Oxygen isotope data collected in Manchester were supplemented by data using the Cameca IMS 1270 ion microprobe at University of California, Los Angeles (UCLA). Negative secondary ions were sputtered from polished grain surfaces by a ~2nA Cs^+ primary beam focused to a ~25 micron diameter spot. A normal incidence electron flood gun provided charge neutralisation. High primary beam currents provided typical count rates of $\sim2.5\times10^7$ counts per second of ^{16}O allowing

simultaneous measurement of $^{16}O^-$ and $^{18}O^-$ ions in Faraday cups to give precision of approximately 0.1‰. Each measurement comprised a 120s sputter time prior to analysis followed by a 120s spot measurement time. Background counts were measured after every 3 or 4 analyses and typical background counts were <1000 counts per second of ^{16}O. A Si^- ion image was taken prior to analysis to minimise contamination of carbonate areas with pyroxene or maskelynite. In this way it is estimated that at worst there is <5% contamination by silicon.

7.5 Chemical analyses: BioToF SIMS

The BioTofSIMS instrument is a chemical imaging time-of-flight mass spectrometer. The primary ion source is a Ionoptika liquid metal Gallium gun which emits Ga^+ ions with an energy of 25keV at the source. These ions are focused to a minimum spot size of ~50nm. The primary beam has a variable pulse width, typically 100ns for analyses carried out in this research. The mass analyser is a two-stage reflectron mounted vertically in a 3metre flight tube. Charge compensation is provided by a 10-1000eV electron flood gun which is pulsed between ion gun pulses. Time of flight analyses were obtained using the BioTofSIMS instrument at UMIST (figure 7.7) (Braun *et al.*, 1998) Negative secondary ion data were acquired using a digitally rastered 13 keV Ga^+ primary beam. The Ga^+ gun was operated in high-current (50nA) mode to obtain high count rates whilst still providing sufficient spatial resolution (~2μm) to investigate possible relationships between halogen concentration and mineral phase. In addition, a submicron (4nA) Ga^+ beam was used for analyses of a single carbonate rosette fragment with higher spatial resolution.

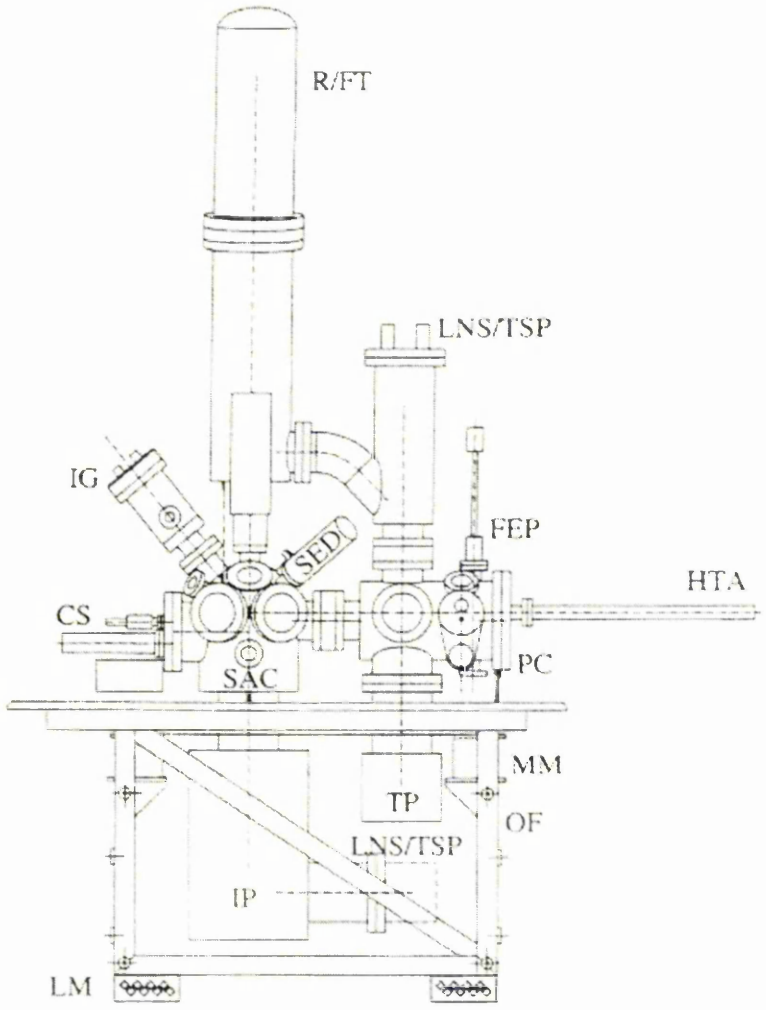

Figure 7.7: Schematic of BioTofSIMS instrument (from Braun *et al.*, 1998)

The outer frame (OF) is isolated from the floor on lattice mounts (LM). The inner frame is further isolated on motor mounts (MM). Ultrahigh vacuum is established using an ion pump (IP), liquid nitrogen shroud, titanium sublimator pump (LNS/TS) and turbo-molecular pump (TP). The preparation chamber (PC) supports the horizontal transfer arm (HTA) which delivers the sample into the surface analysis chamber (SAC) that supports the ion gun (IG), cold stage (CS) and secondary electron detector (SED). Secondary ions are extracted vertically into the reflectron / flight tube (R/FT).

Chapter 8

Results: Petrography of ALH84001

8.1 Introduction

Previous petrographic work has concentrated on the relationship between feldspars and carbonate (Kring *et al,* 1997; Gleason *et al.*, 1997; Treiman, 1998; Greenwood *et al.*, 2001), and the timing of deformations relative to carbonate deposition. This chapter focuses on carbonate-maskelynite textural and chemical relationships by use of high resolution SEM imaging in back scattered electron (BSE) mode, quantitative SEM chemical analyses, semi-quantitative EPMA element mapping and quantitative spot analyses. The chemical and textural information can then be compared to other recent studies, highlighting the similarities and differences as well as aiding interpretation of oxygen isotopic data. SEM and EPMA data tables of carbonate and maskelynite are presented in the appendix.

8.2 Petrography, mineralogy and chemistry

Four carbonate regions were observed, each in a separate grain of ALH84001 subsample 287. Grains 2 3 and 4 contain feldspathic glass (maskelynite) intimately associated with carbonate over the majority of the 200μm^2 carbonate region. Grain 1 contains very minor feldspar.

8.2.1 Grain 1

Grain 1- SEM BSE

The black region to the left of Figure 8.1 is epoxy and the light grey region down the right third of the image is pyroxene. The center region (with some marking due to ion probe analyses) is carbonate. The large fracture through the carbonate down

the centre of the image was incurred during sample preparation and although there is minor faulting within the carbonate, the carbonate-pyroxene boundary, particularly in the center right of the image, is not microfaulted hence the original relationship between carbonate and pyroxene is preserved here. Minor anhedral olivine of composition Fa_{34}, approximately 10μm across, is completely enclosed in pyroxene as observed by Shearer *et al.* (1999). Three white spots on the pyroxene are surface contaminants, whilst the <5μm grain in the center of the carbonate is a sulphide. The most noteworthy feature of this sample is the presence of 20μm by 30μm carbonate fragments within the main 100μm by 200μm body of carbonate. The BSE image shows these fragments to be darker (more Mg-rich) than the surrounding carbonate and heterogeneous with an Mg-rich rim similar to that of carbonate rosettes. The interface of these carbonate fragments and the carbonate 'matrix' within which they are found is indistinct. This texture of zoned Mg-rich carbonate encapsulated by light grey (Ca-rich) carbonate has not been observed before. Henceforth the carbonate encapsulating possible rosette fragments and terminating at a pyroxene boundary with Ca-rich cores and a lack of Mg-rich rims shall be referred to as 'Ca-rich carbonate' Minor feldspathic material is spatially associated with fragments of Mg-rich (dark) carbonate in the center of figure 8.1.

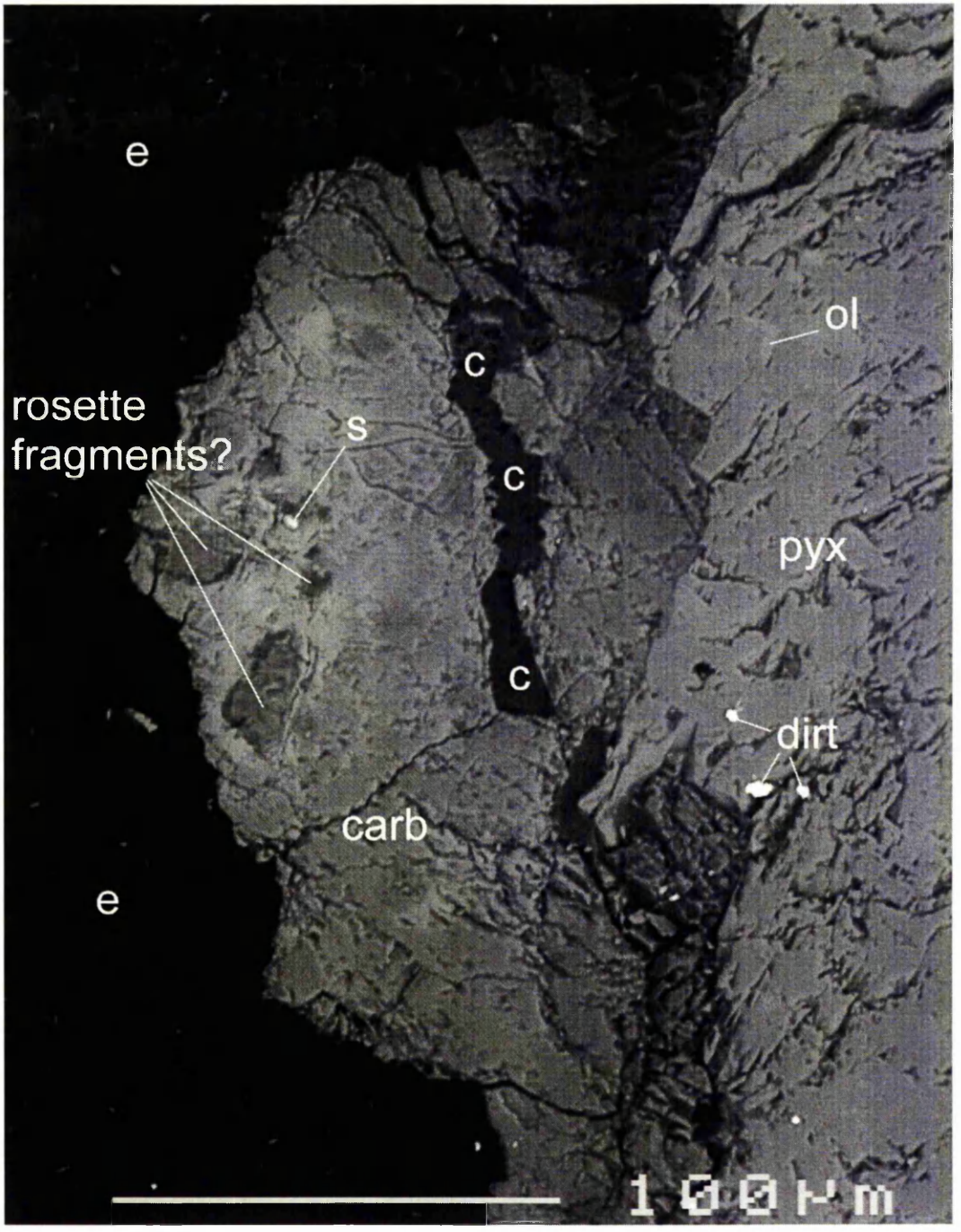

Figure 8.1: Back scattered SEM image of grain 1 showing texture of Mg-rich carbonate fragments within Mg-poor carbonate matrix. (e) epoxy; (c) crack formed during sample preparation; (ol) olivine; (s) sulphide; (pyx) pyroxene; (carb) carbonate.

Grain 1 EPMA element maps (figures 8.2a – 8.2d)

EPMA element maps were acquired using five wavelength dispersive spectrometers. Elemental analysis of the major cations in ALH84001 carbonate (Ca, Mg, Fe, Mn) and Si were performed by detection of cation Kα lines. Element maps are 256×256 pixels with an approximate spatial resolution of 1μm per pixel.

The Ca element map shown in figure 8.2a clearly shows the Mg-rich fragments encapsulated in Ca-rich carbonate. In contrast to the complicated chemical zoning observed in carbonate rosettes (e.g. Harvey and McSween, 1996), this Ca-rich carbonate ($Ca_{74}Mg_{14}Fe_{12}Mn_{08}$) zones to less Ca-rich compositions ($Ca_{15}Mg_{51}Fe_{32}Mn_{02}$) at the boundary with pyroxene without the presence of an Mg-rich rim containing the characteristic Fe-rich magnetite bands. Zoning to Ca-poorer compositions towards the pyroxene is interrupted by a ~10μm wide Ca-rich carbonate band ($Ca_{25}Mg_{41}Fe_{28}Mn_{04}$) accompanied by a thinner Mn band (figure 8.2d and figures 8.4a-c). The continuity of Ca/Mn-rich banding clearly shows that the carbonate matrix has not been fractured. If precipitation proceeds from Ca-rich to Ca-poor carbonate, it would appear that this Ca-rich carbonate has nucleated on the Mg-rich 'rosette fragments'. A second nucleation centre appears to have formed below and right of the main Ca-rich region, although it has not been sectioned through the Ca-rich core. The heterogeneity of the Mg-rich fragments within the Ca-rich carbonate is seen in the Mg element map (Figure 8.2b) with the bright Mg-rich rims ($Ca_{0.09}Mg_{0.78}Fe_{0.12}Mn_{0.01}$) clearly discernible from the rest of the Mg-rich fragment ($Ca_{0.05}Mg_{0.69}Fe_{0.24}Mn_{0.01}$). In Figure 8.2c, the Si map shows rare feldspar associated with carbonate and the Mn map (figure 8.2d) the narrower (<5μm) Mn-rich band.

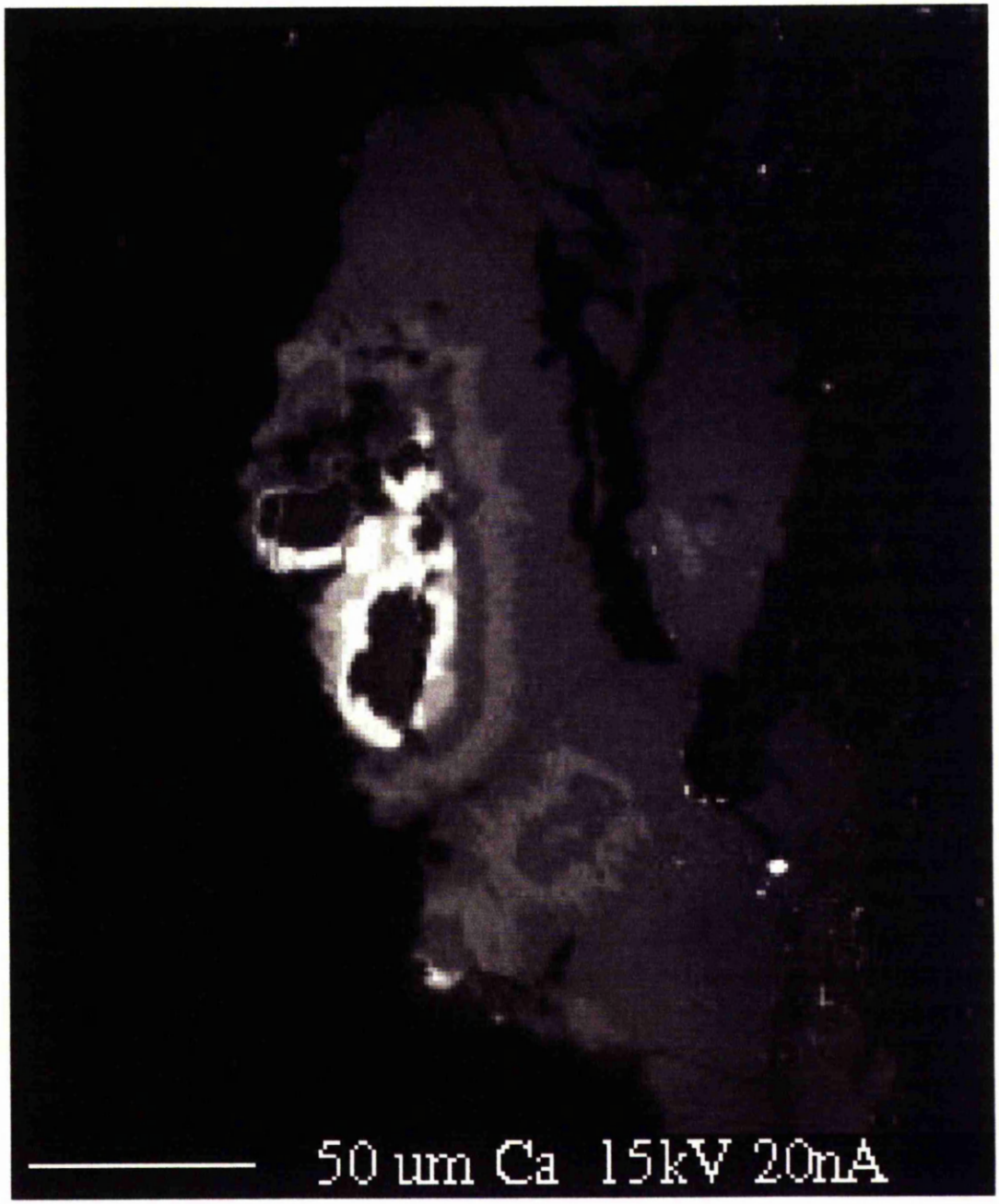

Figure 8.2a: Ca element map of grain 1

Note the white Ca-rich (70-75 molar % Ca) carbonate encapsulating Mg-rich fragment (probable rosette fragment). Note the homogeneous Ca-Mn band that occurs as precipitation continues outwards from Ca-rich cores. It is ~10μm across and has significantly less Ca than the Ca-rich material surrounding the rosette fragments (30 molar%Ca and ~70molar %Ca respectively)

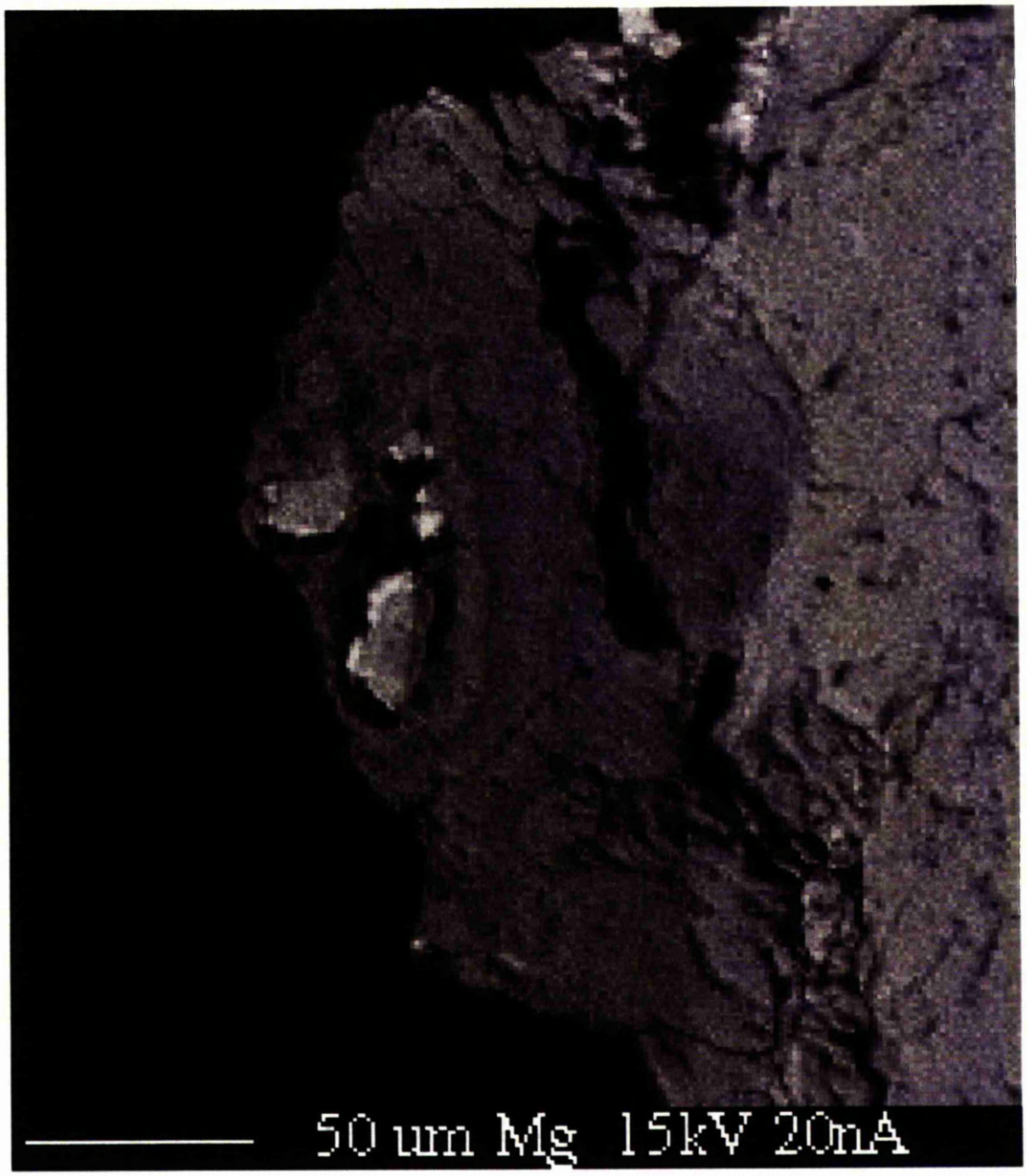

Figure 8.2b: Mg element map of grain 1

Note the probable rosette fragments centre left of figure (light grey) surrounded by dark grey Ca-rich (Mg poor) carbonate. White edges to the probable rosette fragments hint at rosette rim type zoning.

Figure 8.2c: Si element map of grain 1

Note that only minor amounts of feldspathic glass associated with the Ca-rich carbonate.

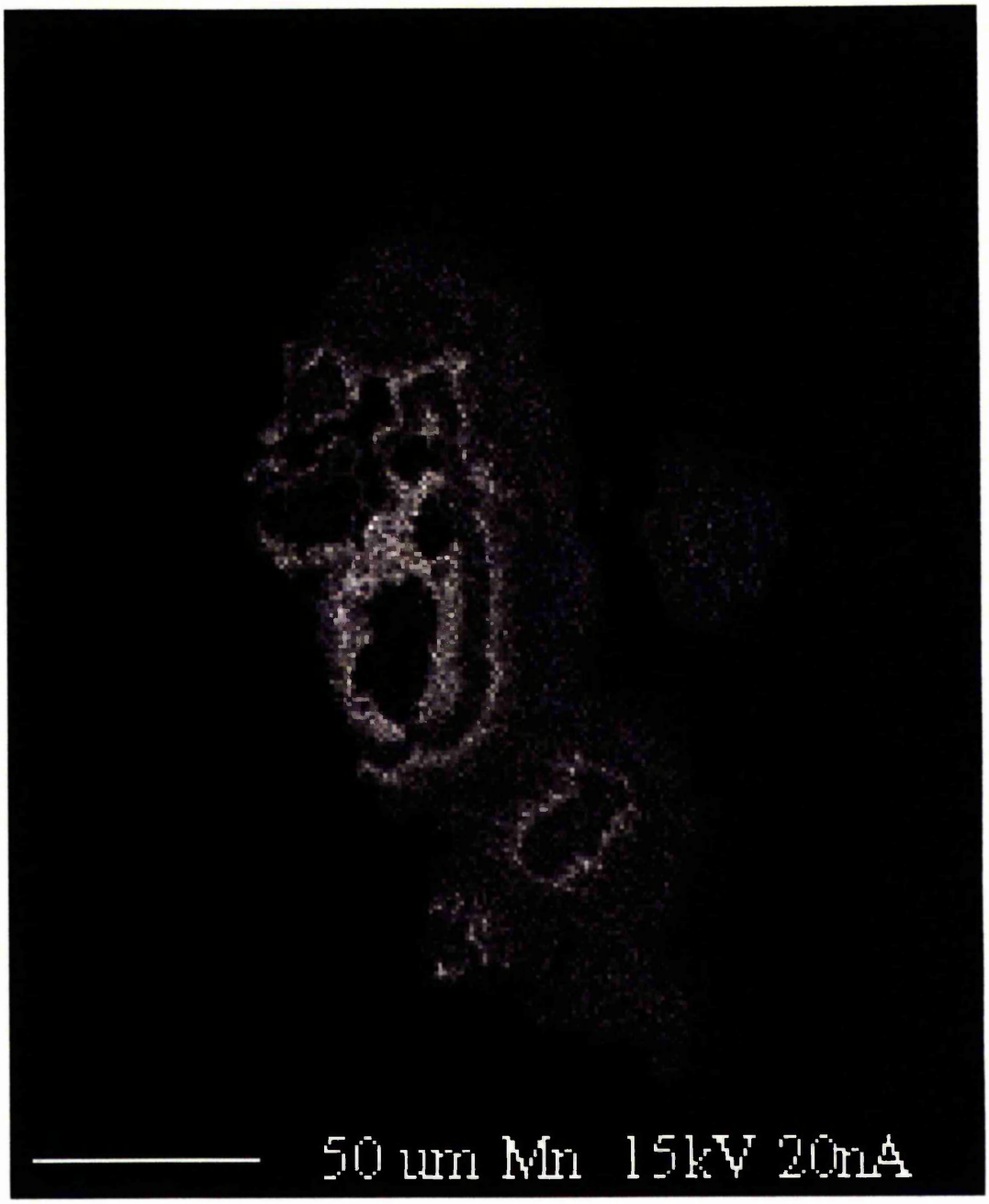

Figure 8.2d: Mn element map of grain 1.

Note the general agreement between Ca content and Mn content. However, there are two important differences:

i) The Ca-Mn band is narrower (<5μm) when observed in Mn than in Ca (~10μm)

ii) The Mn content in the Ca-Mn band is approximately the same as Mn content of the carbonate encapsulating the rosette fragments (~7%Mn) but Ca content in the Ca-Mn band is much less (~30% Ca) than in the carbonate surrounding the rosette fragments (~70%).

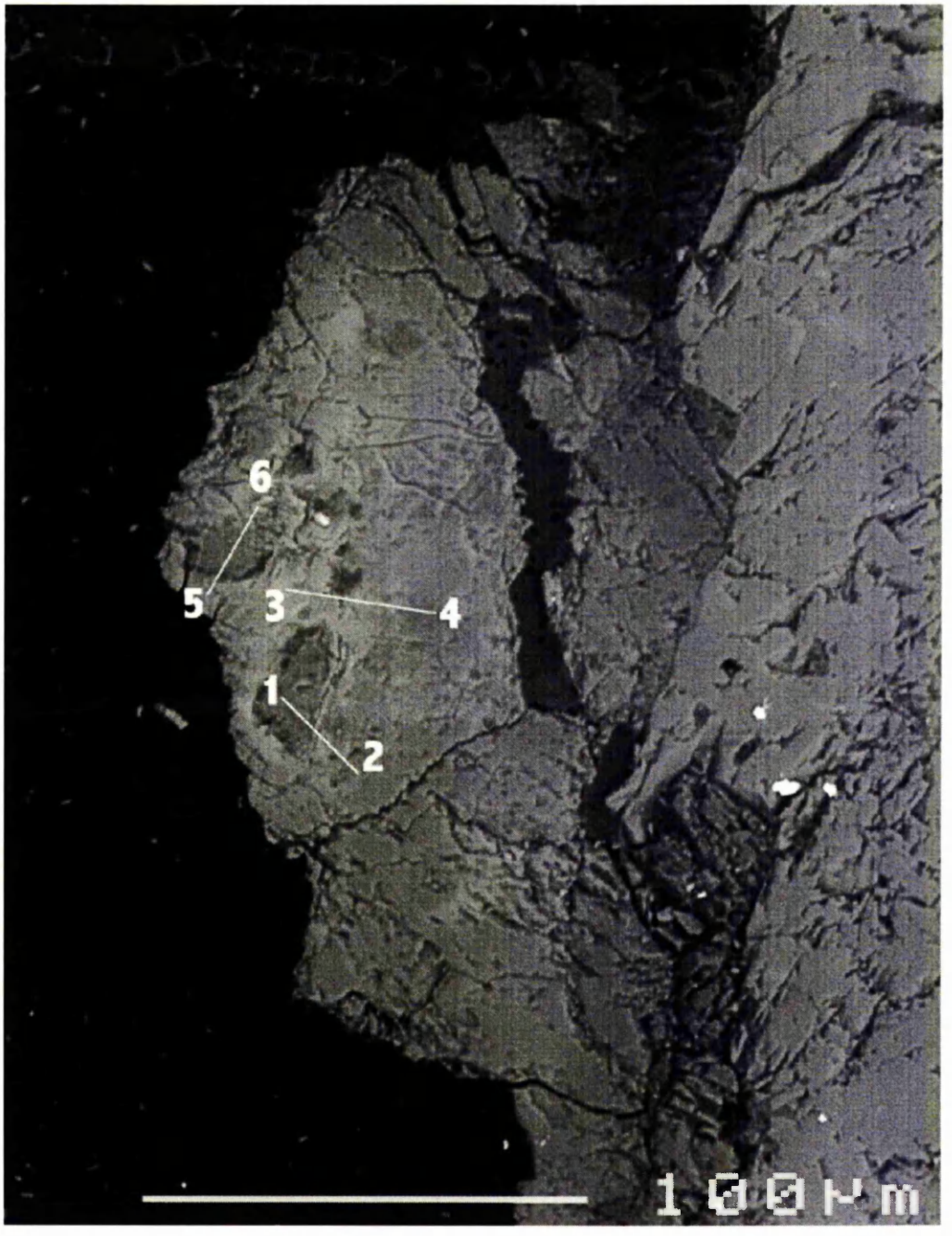

Figure 8.3: location of EPMA linescans for quantitative chemical analyses of carbonate in grain 1

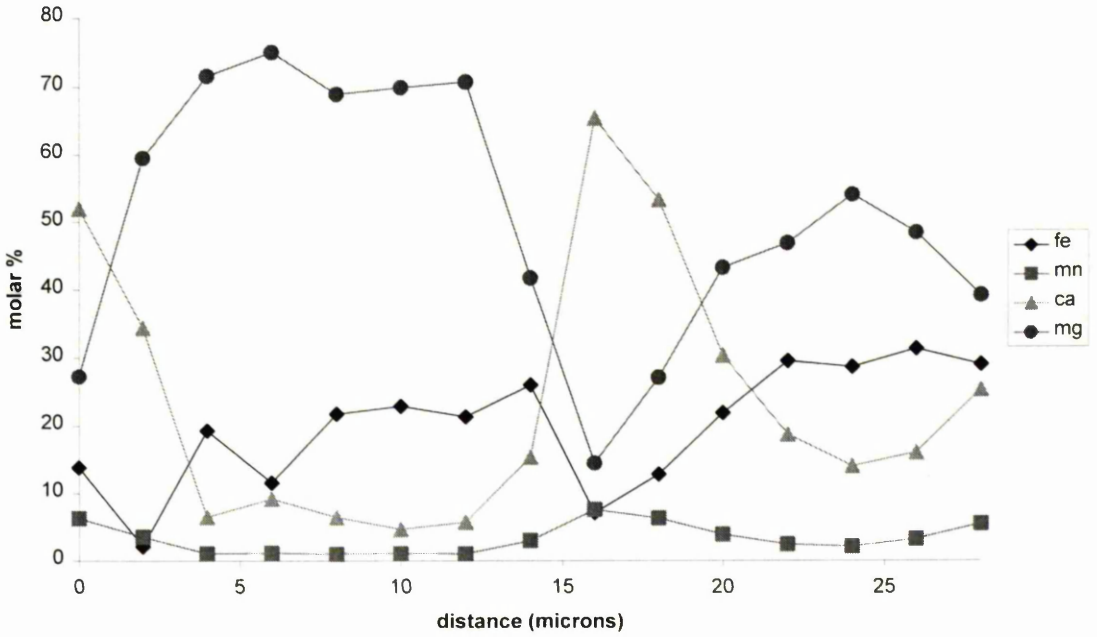

Figure 8.4a: EPMA linescan 1-2 showing quantitative analyses chemical zoning of carbonate in grain 1. In all EPMA carbonate composition diagrams, errors are smaller than data point symbols.

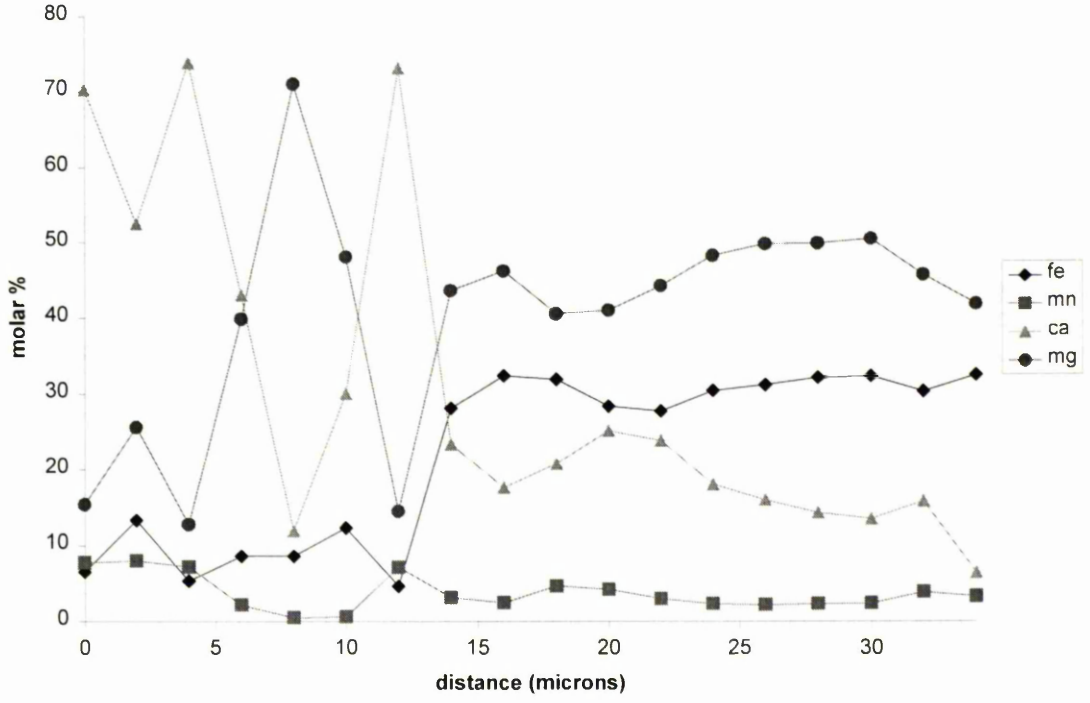

Figure 8.4b: EPMA linescan 3-4 showing quantitative analyses chemical zoning of carbonate in grain 1

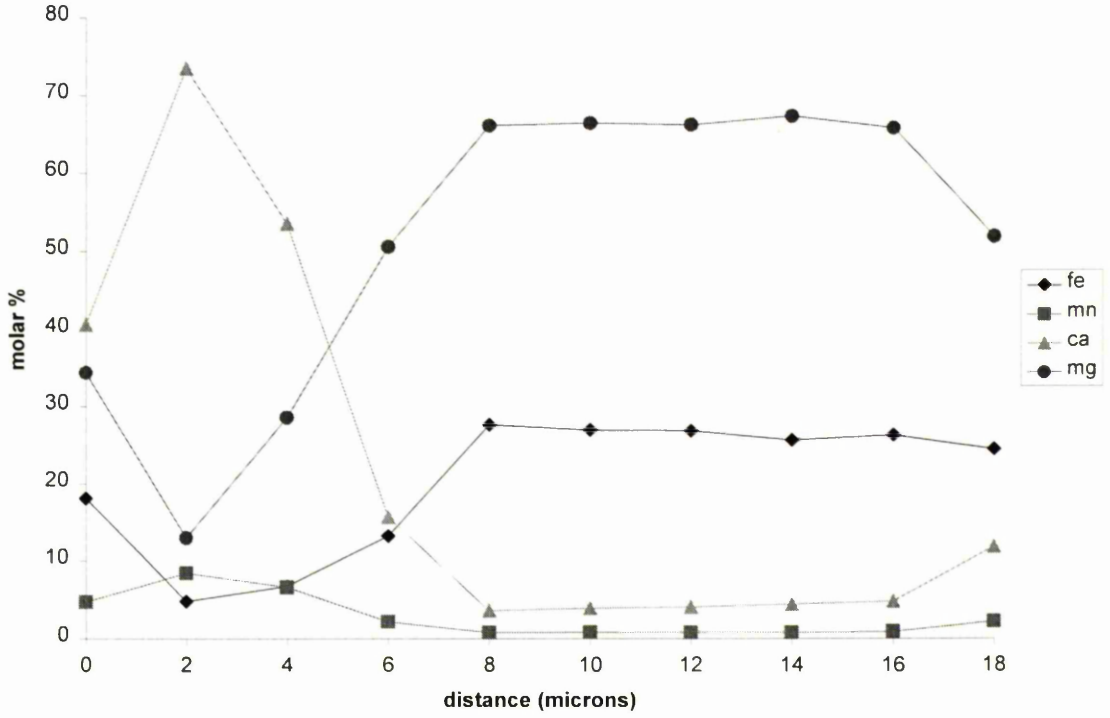

Figure 8.4c: EPMA linescan 5-6 showing quantitative analyses chemical zoning of carbonate in grain 1

8.2.2 Grain 2

Grain 2 SEM BSE

The black region to the left and bottom of Figure 8.5 is epoxy and the light grey region is pyroxene. The centre-left region has a mottled appearance due to intimately associated carbonate and maskelynite. At its rightmost edge, this carbonate-maskelynite region is bounded by fragmented carbonate rosette rims. Several rosette fragments to the right of this region are associated with fragmented chromite (white in BSE), and medium grey feldspathic glass enclosing pyroxene. Again minor anhedral olivine is present. The black grain above the fragmented rosettes is a grain of salt (NaCl), presumably introduced to the grain during preparation. Two fractures are present in this section: one of which cuts both the interspersed maskelynite-carbonate region and the pyroxene (f1) and one across the top of figure 8.5 which contains deposits of mixed-

feldspathic glass and chromite along its length (f2). It is unclear whether f1 is a genuine fracture or an artefact of sample preparation but f2 as it is associated, at least in part, with mineralisation is likely to be genuine. Minor fracturing occurs within the carbonate-maskelynite region but the carbonate-pyroxene boundary is not microfaulted with carbonate embaying into pyroxene. Clearly, the magnesite rosette rims and rosette fragments are heavily fractured and interspersed with small fragments of chromite. This is in stark contrast to the relatively unfractured maskelynite-carbonate region. Other surface features on the pyroxene are the result of uneven polishing. Carbonate-maskelynite relationships are best observed in the element maps of Figures 8.7a - 8.7d. Maskelynite compositions will be dealt with in a later section.

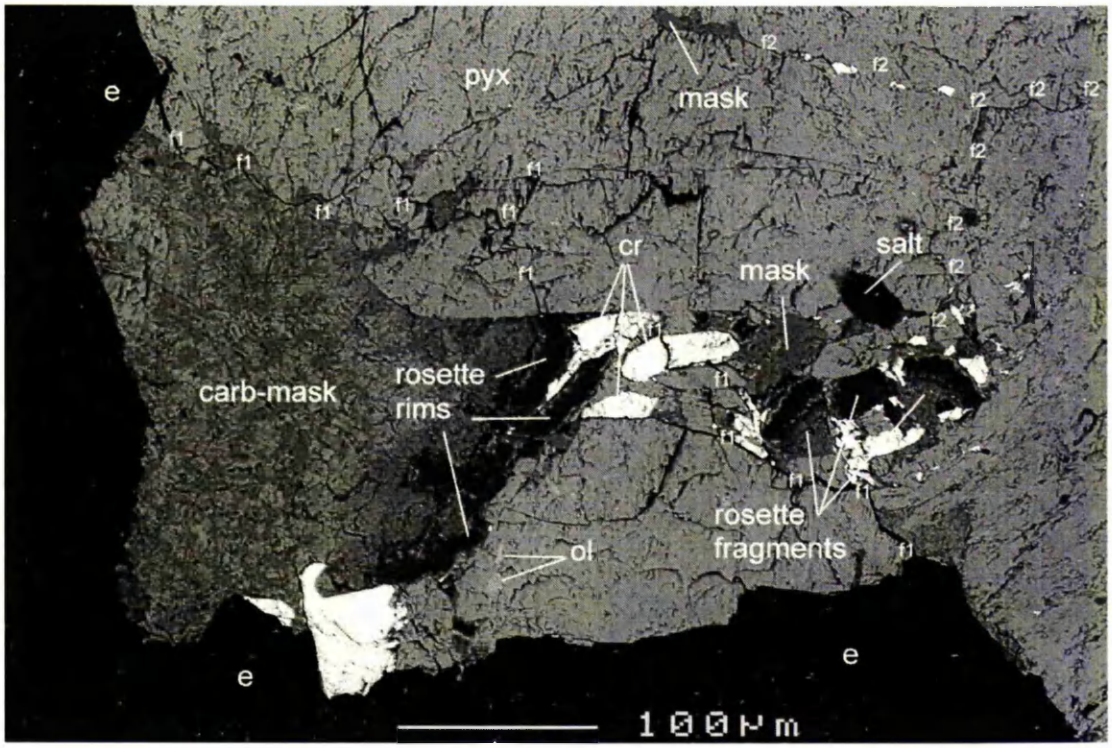

Figure 8.5: Back scattered SEM image of grain 2. (ol) olivine; (e) epoxy; (f1) fracture 1; (f2) fracture 2; (cr) chromite

Grain 2 EPMA element maps (figures 8.6a – 8.6d)

EPMA element maps were acquired using five wavelength dispersive spectrometers. Elemental analysis of the major cations in ALH84001 carbonate (Ca, Mg, Fe, Mn) and Si were performed by detection of cation Kα lines. Element maps are 512×512 pixels with an approximate spatial resolution of 1μm per pixel.

The Ca element map (figure 8.6a) clearly shows many Ca-rich cores of similar composition ($Ca_{76}Mg_{12}Fe_{05}Mn_{06}$) to the Ca-rich region in grain 1. Again the Ca/Mn-rich band (Figures 8.6a & 8.6d) is present during zoning to more magnesian compositions as observed previously (figure 8.8). However, in contrast to grain 1, there are multiple Ca-rich regions which imply multiple nucleation cores for precipitating carbonate. In the extreme bottom left and above centre left of the Mg element map (figure 8.7b) Mg-rich carbonate is again surrounded by Ca-rich carbonate. Thus, in grain 2, Ca-rich carbonate appears to nucleate on:

i) host orthopyroxene at the edge of the carbonate region

ii) magnesium rich carbonates

The Mg element map reveals the distribution of maskelynite within the carbonate containing the multiple Ca-rich cores.

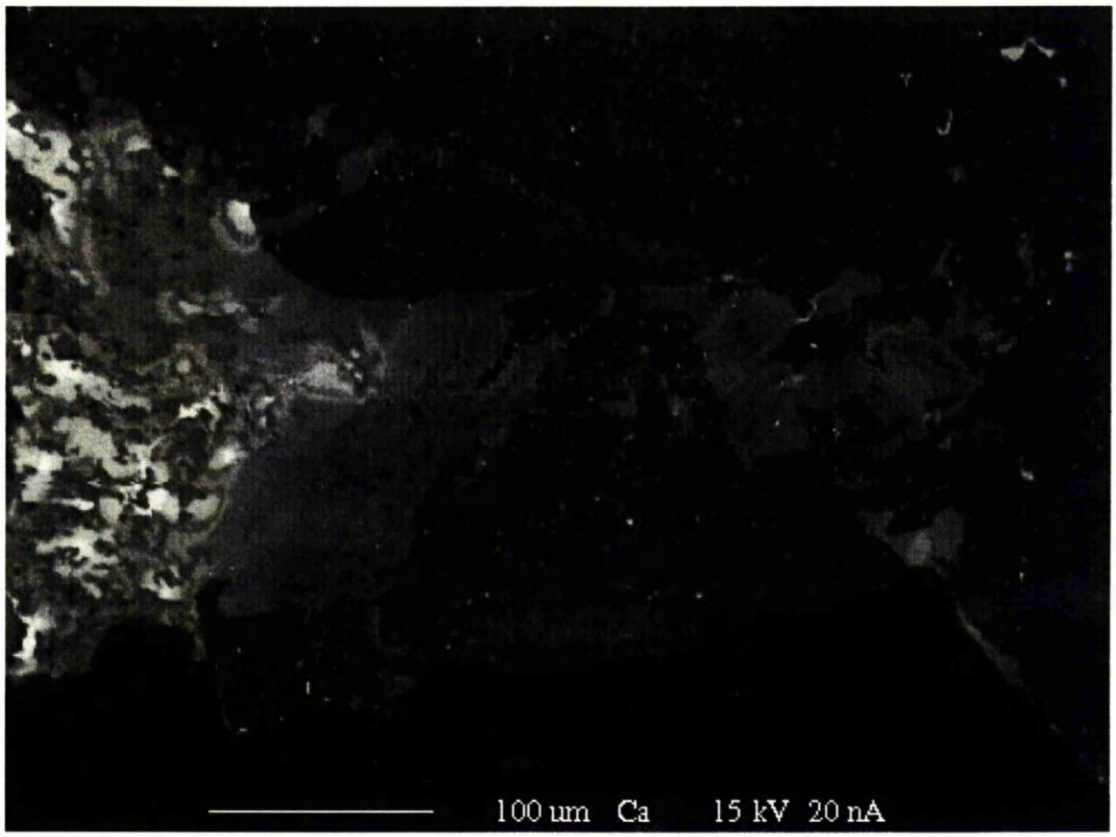

Figure 8.6a: Ca element map of grain 2

Note evidence of multiple nucleation cores (white areas) of the carbonate-feldspathic glass region in the left half of the figure. Chromite with no Ca content (black) is observed in the centre and lower left of the figure, associated with rosette rim carbonate (figure 8.6b). Rosette fragments and a feldspar grain are medium grey in the centre right of the figure. Note again that the Ca content of the first nucleating Ca-rich carbonate is greater than the Ca content in the Ca-Mn band.

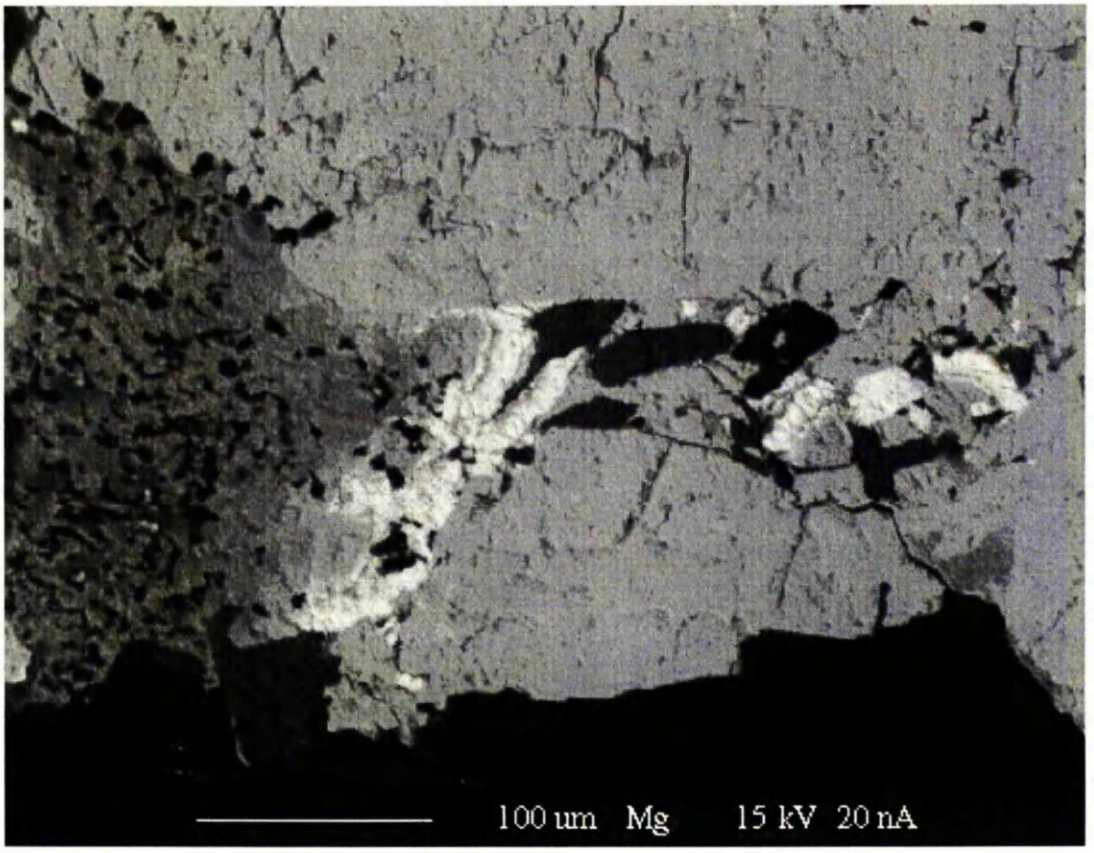

Figure 8.6b: Mg element map of grain 2.

Note the white, pure magnesite, rosette rims. The intimate association of feldspathic glass (black) and carbonate (medium grey) in the left half of the figure. Note also in the extreme left of the figure, several Mg rich carbonate regions acting as apparent nucleation sites of Ca-rich carbonate (figure 8.6a).

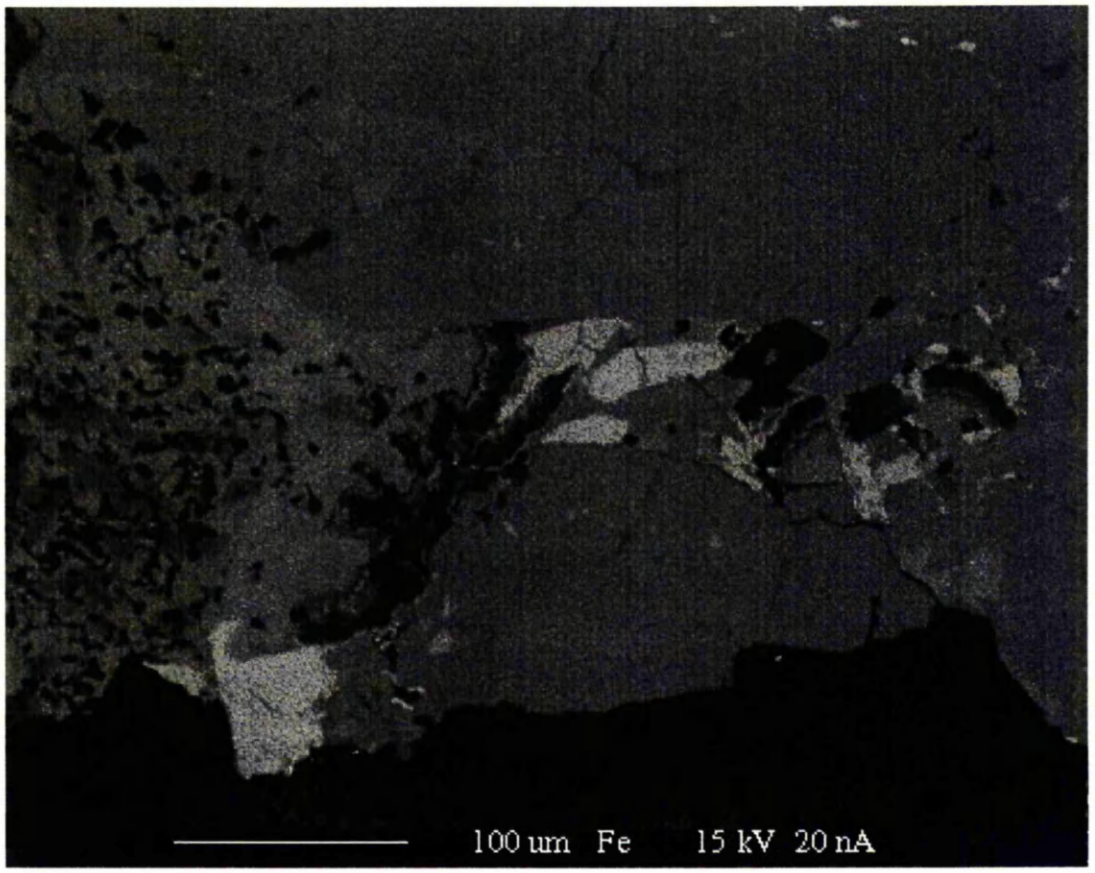

Figure 8.6c: Fe element map of grain 2

Note the high Fe content of the chromite (light grey) associated with Fe poor (black) the rosette rims and feldspathic glass.

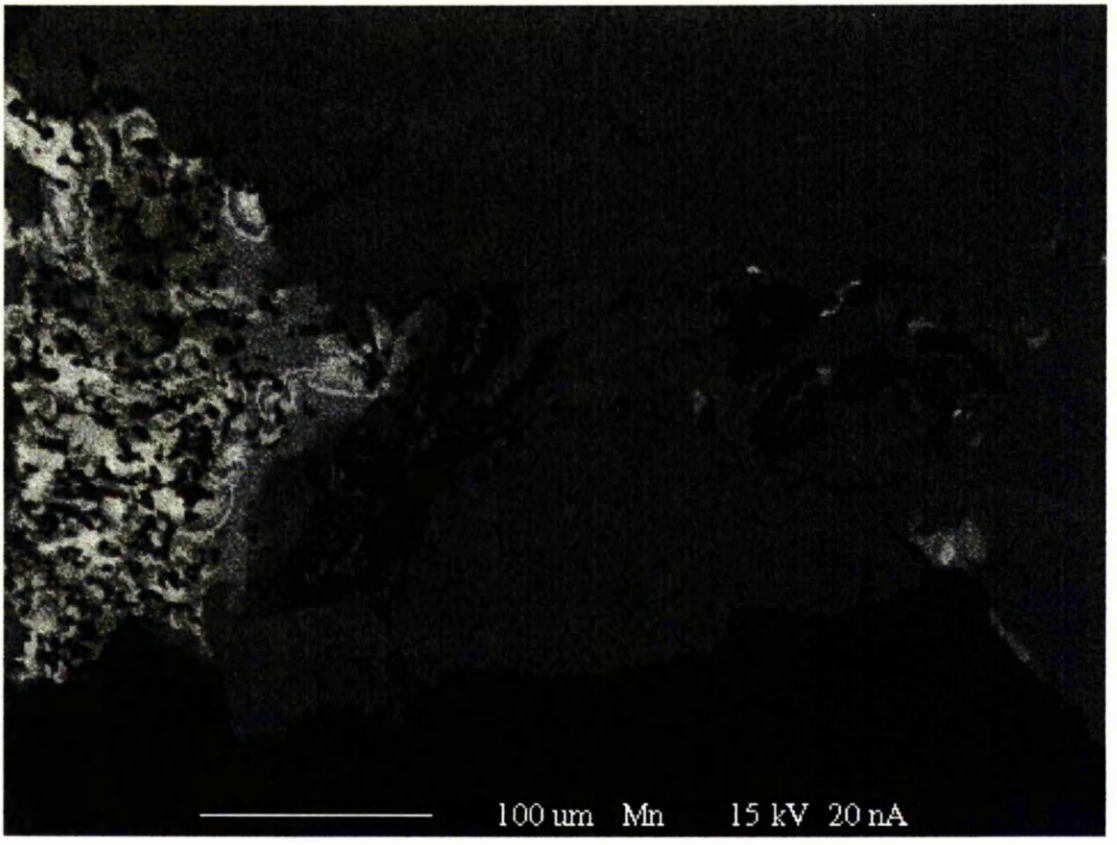

Figure 8.6d: Mn element map of grain 2

Note again the similarity in Mn content between the first nucleating carbonate and the Mn content in the Ca-Mn band

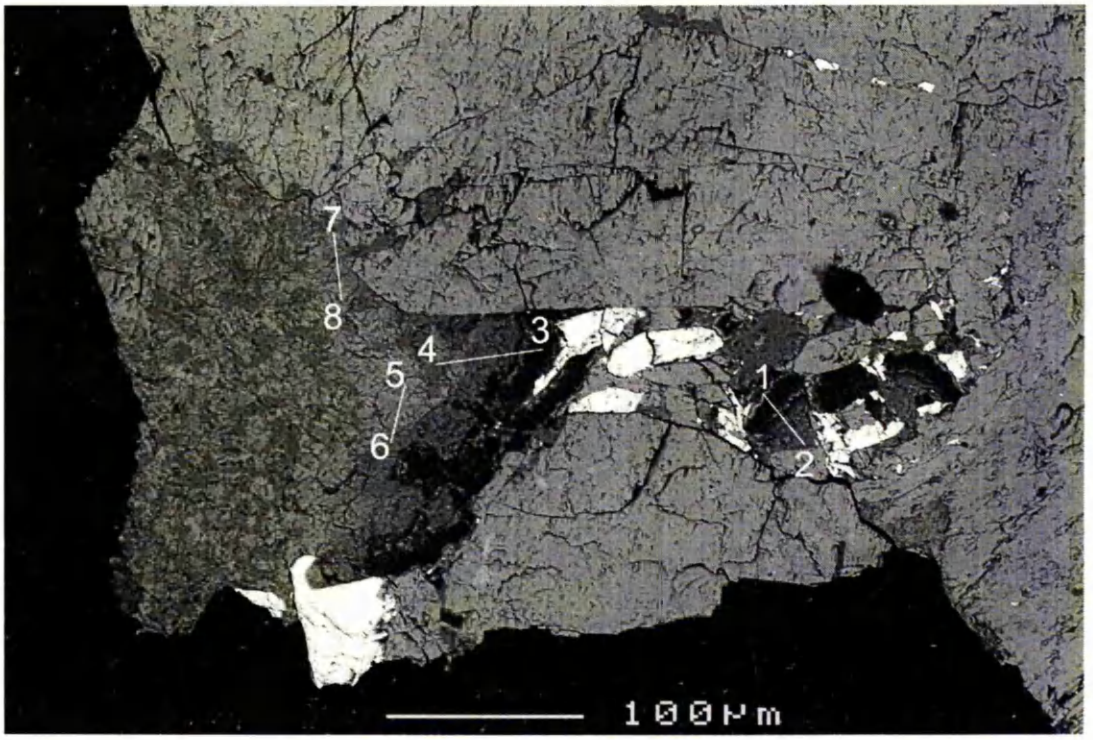

Figure 8.7: location of EPMA linescans for quantitative chemical analyses of carbonate in grain2

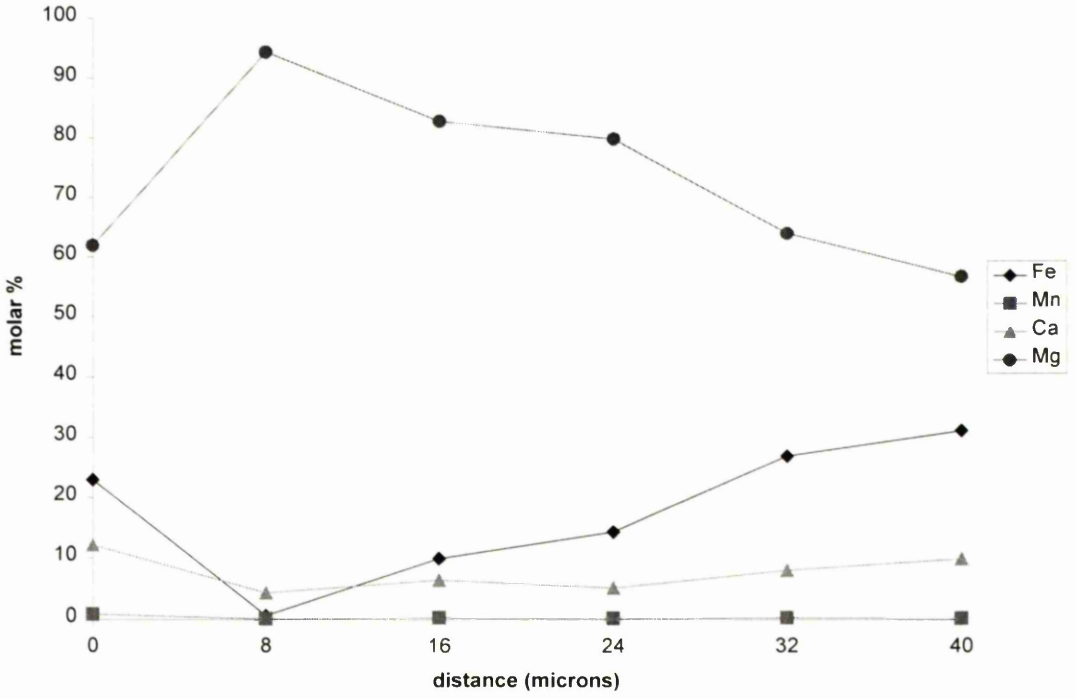

Figure 8.8a: EPMA linescan 1-2 showing quantitative analyses chemical zoning of carbonate in grain 2

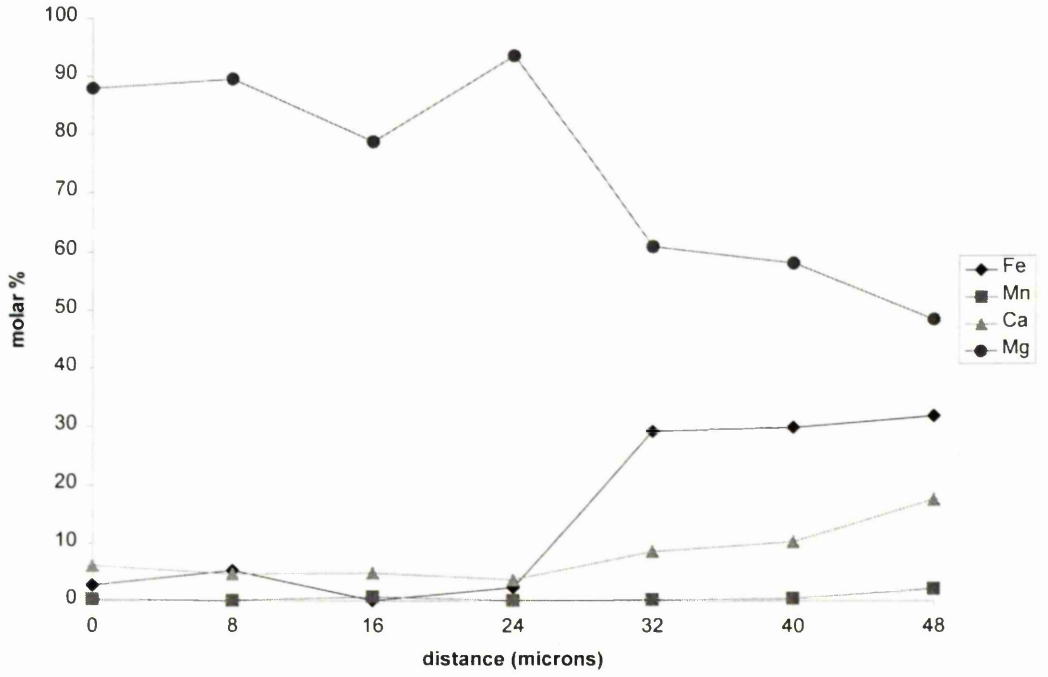

Figure 8.8b: EPMA linescan 3-4 showing quantitative analyses chemical zoning of carbonate in grain 2

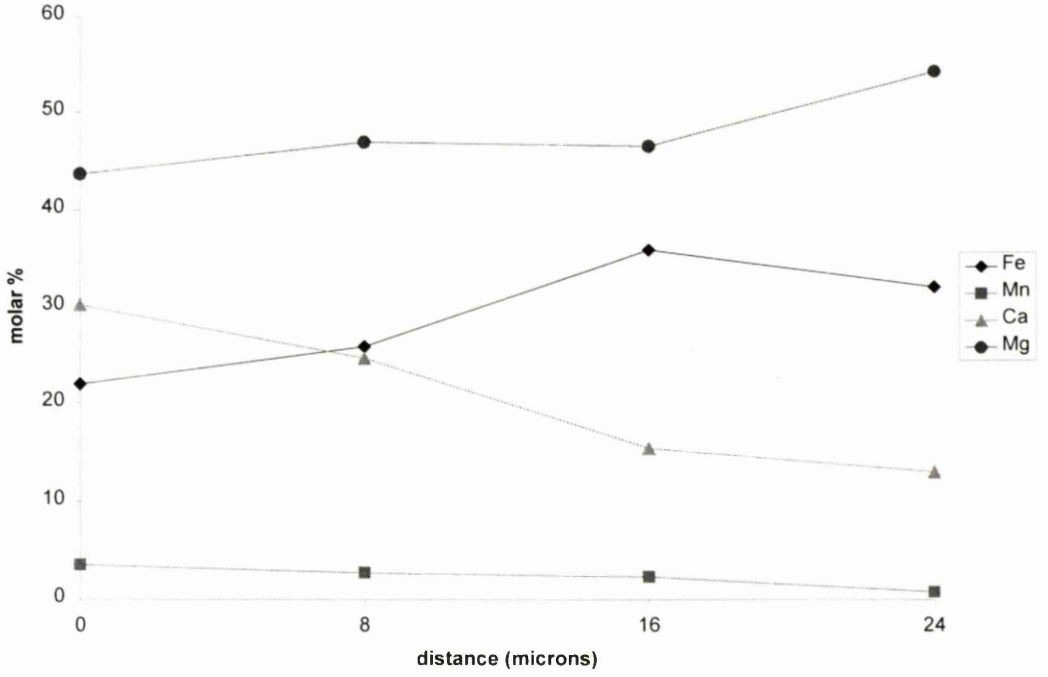

Figure 8.8c: EPMA linescan 5-6 showing quantitative analyses chemical zoning of carbonate in grain 2

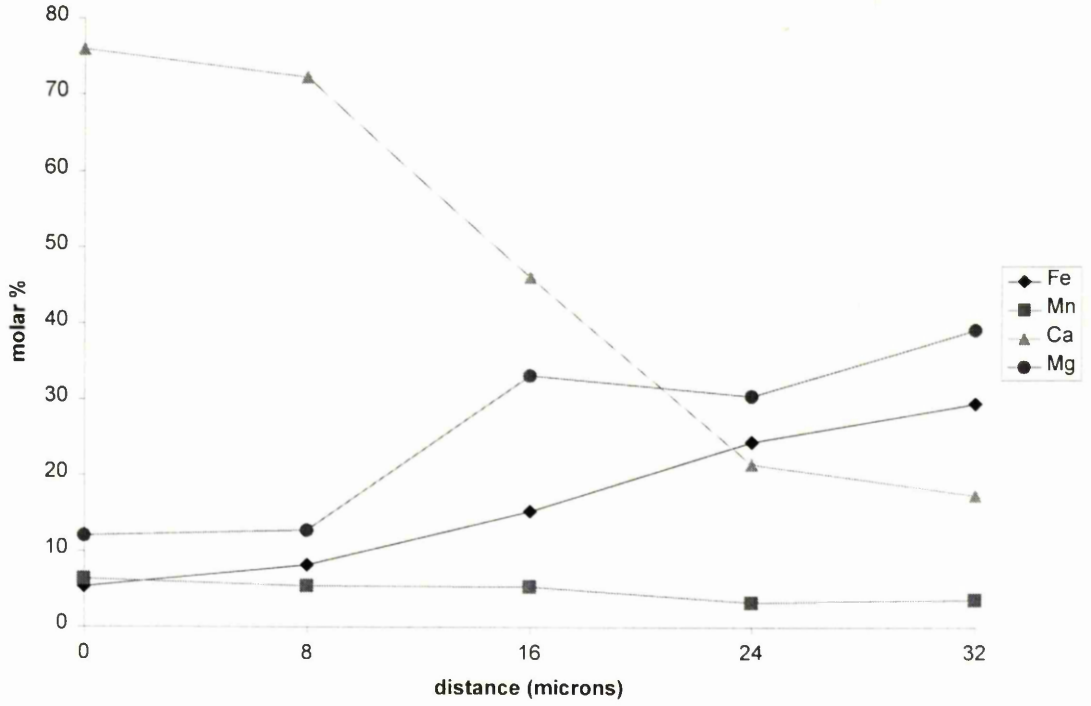

Figure 8.8d: EPMA linescan 7-8 showing quantitative analyses chemical zoning of carbonate in grain 2

If the thresholds are altered on the Ca element map of grain 2 to enhance the differences in Ca content of the Ca-poor pyroxene, Figure 8.9 is the result. The pyroxene has lost >50% of its Ca content along the f2 fracture and in the vicinity of the carbonate-maskelynite region. This shall be discussed in a later section.

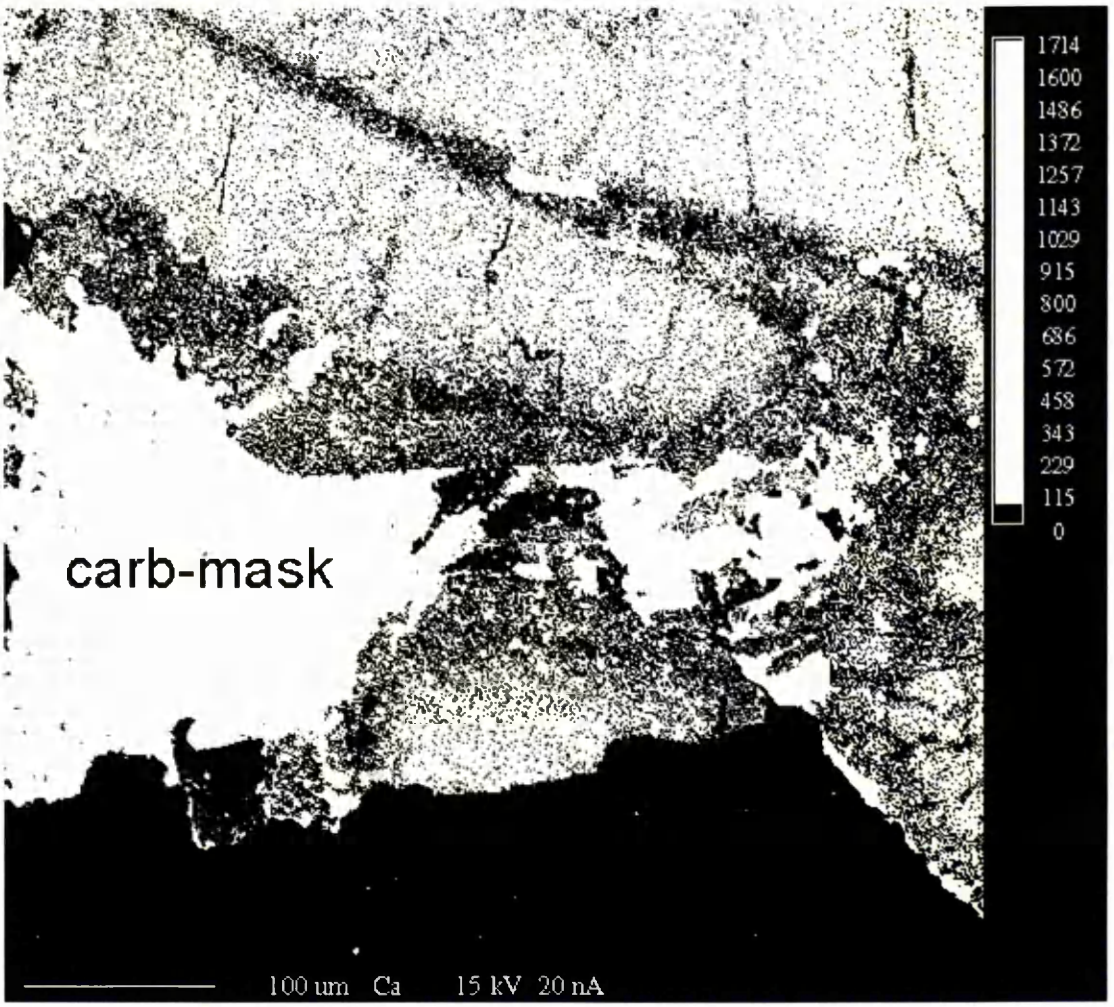

Figure 8.9: EPMA Ca element map rebinned to emphasise Ca depletion along crack on pyroxene and around carbonate-maskelynite region.

8.2.3 Grain 3

Grain SEM BSE

The black region to the top of Figure 8.10 is epoxy and the light grey region is pyroxene. The centre-left region has a mottled appearance similar to grain 2 which is due to a similar texture: interspersed carbonate and maskelynite. The maskelynite in grain 3 is a more continuous fabric than the small amorphous bleb of maskelynite in grain 2. Fragments of chromite (white) are again associated with rosette fragments are again observed in the most heavily fractured region of grain 3, where chromite is

observed infilling fractures in pyroxene. Again minor (<10μm) anhedral olivine is present enclosed in pyroxene. The carbonate-pyroxene boundary is faulted along some of its length and is deeply embayed in other regions. The carbonate-maskelynite region is noticeably more fractured than that of sample 2, although no fractures persist from carbonate into maskelynite. The carbonate fragment labelled 'rosette fragment?' has a rosette-like core composition but does not zone to the Mg-rich rim like a normal rosette: the Mg-rich band inward of the magnetite band is thickened by a factor of 2-3 and the magnesite outer rim is absent. A more convincing example of a rosette fragment engulfed in Ca-rich carbonate than sample 1, is present towards the bottom of figure 8.10. An enlargement of this region (Figure 8.11) shows chemical zoning identical to rosette zoning across the core-rim transition. Other surface features on the pyroxene are the result of uneven polishing. Carbonate-maskelynite relationships are best observed in the element maps of figures 8.12a – 8.12d. Maskelynite compositions will be dealt with in a later section.

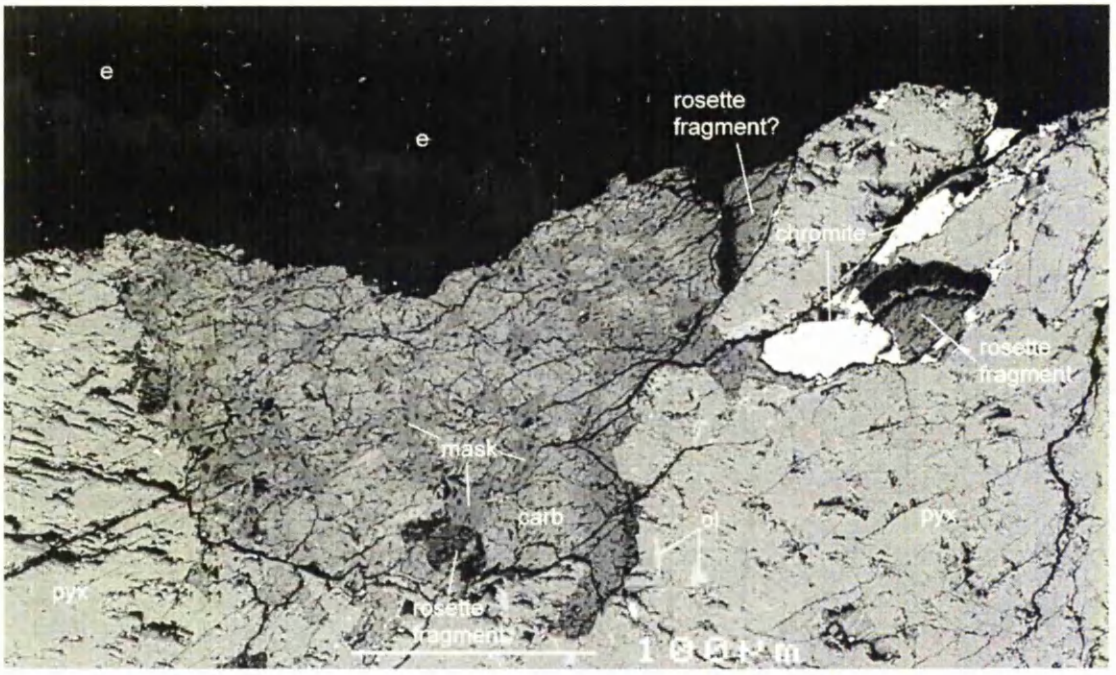

Figure 8.10: Backscattered SEM image of grain 3. (ol) olivine; (e) epoxy; (pyx) pyroxene; (mask) maskelynite

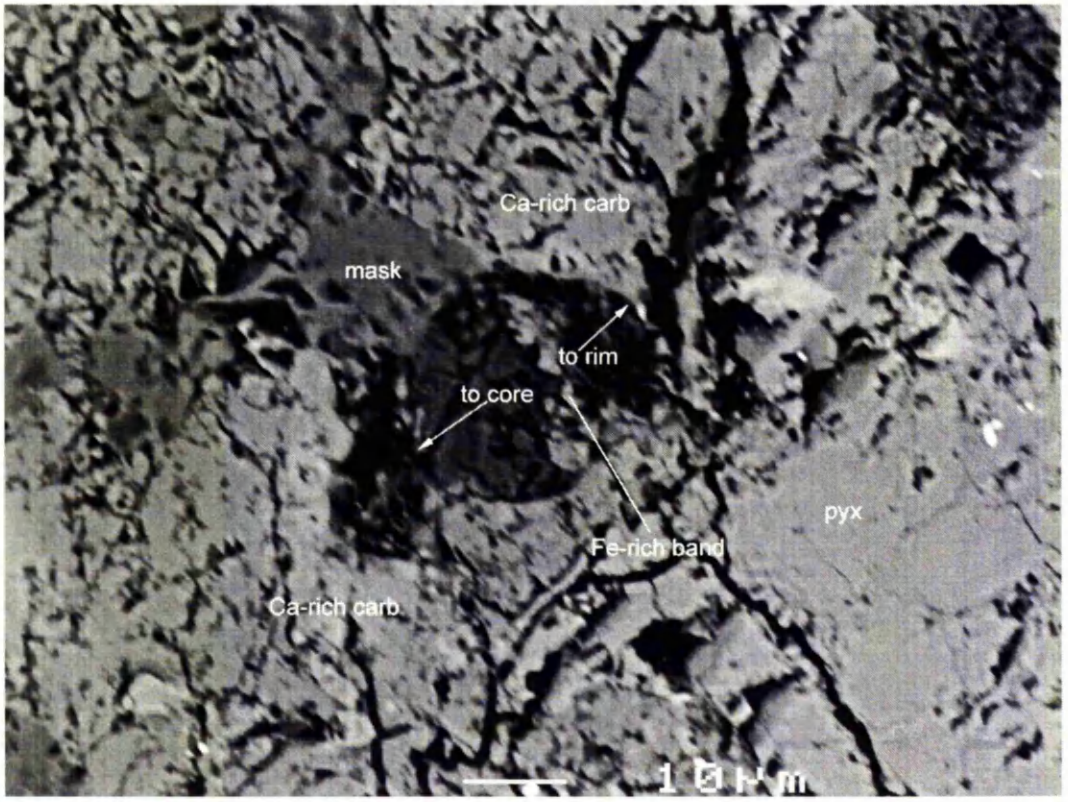

Figure 8.11: enlarged BSE image of rosette fragment surrounded by Ca-rich carbonate

Grain 3 EPMA element maps (Figures 8.13a – 8.13d)

EPMA element maps were acquired using five wavelength dispersive spectrometers. Elemental analysis of the major cations in ALH84001 carbonate (Ca, Mg, Fe, Mn) and Si were performed by detection of cation Kα lines. Element maps are 512×512 pixels with an approximate spatial resolution of 1μm per pixel.

The Ca element map reveals the major calcium rich region just below the centre of figure 8.12a. This Ca-rich carbonate ($Ca_{76}Mg_{12}Fe_{05}Mn_{06}$) encompasses both filaments of maskelynite (black strings in the Mg element map) and a rosette fragment (white region below center on Mg element map). Again the Ca-rich band (and the narrower Mn-rich band) is present during zoning to more magnesian compositions as observed previously (figure 8.14a) and can be traced across the Ca-rich generation carbonate from lower right towards the top left corner of the image, indicating no major post-deposition displacement of the Ca-rich carbonate. There are multiple Ca-rich regions which appear to nucleate on the rosette fragment and maskelynite. Embayment of the maskelynite by carbonate suggests replacement of maskelynite with carbonate. Fragmented carbonate rosettes with cores of composition $Ca_{0.09}Mg_{0.60}Fe_{0.28}Mn_{0.01}$ and rims of composition $Ca_{0.09}Mg_{0.72}Fe_{0.17}Mn_{0.01}$ are present near the top of the images (figure 8.14b).

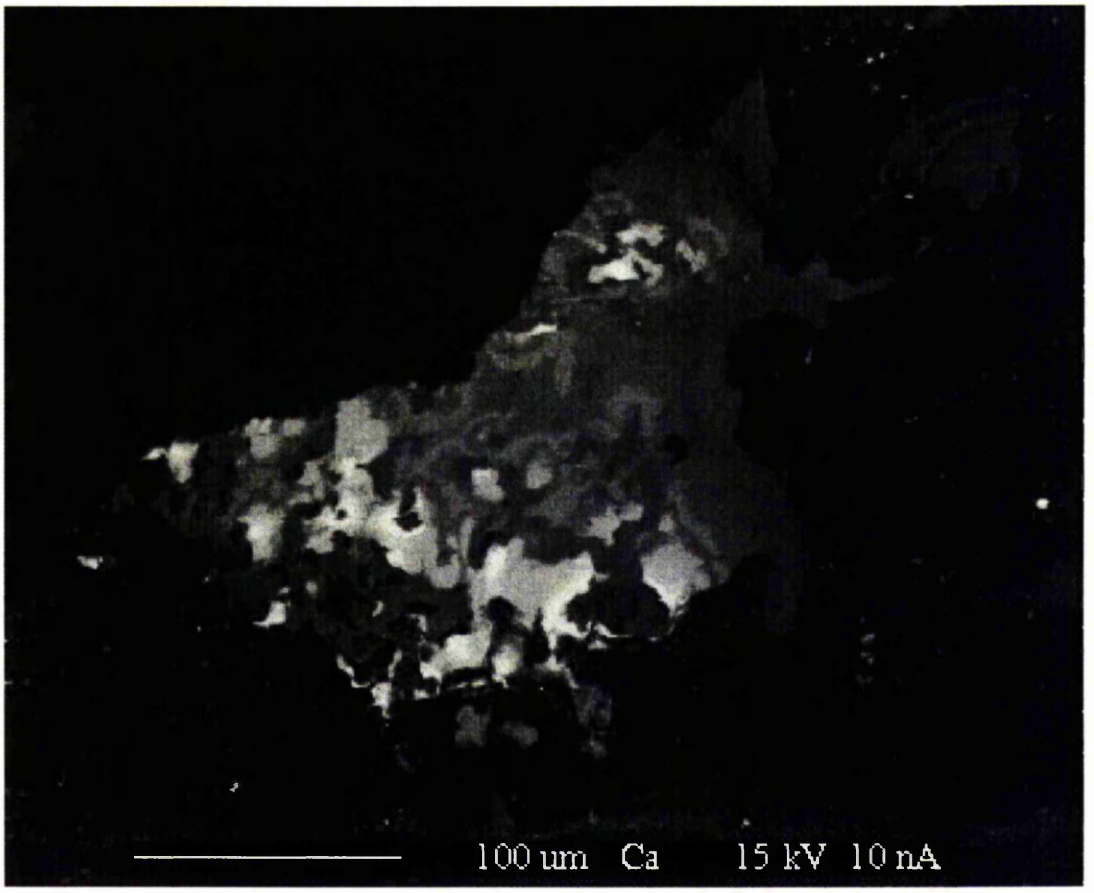

Figure 8.12a: Ca element map of grain 3

This grain shows larger regions (30-40μm) of >50% molar Ca carbonate, permitting ion microprobe analyses at UCLA (see chapter 7) in addition to those at Manchester. Mg-rich carbonate again provides a nucleation site for Ca-rich carbonate.

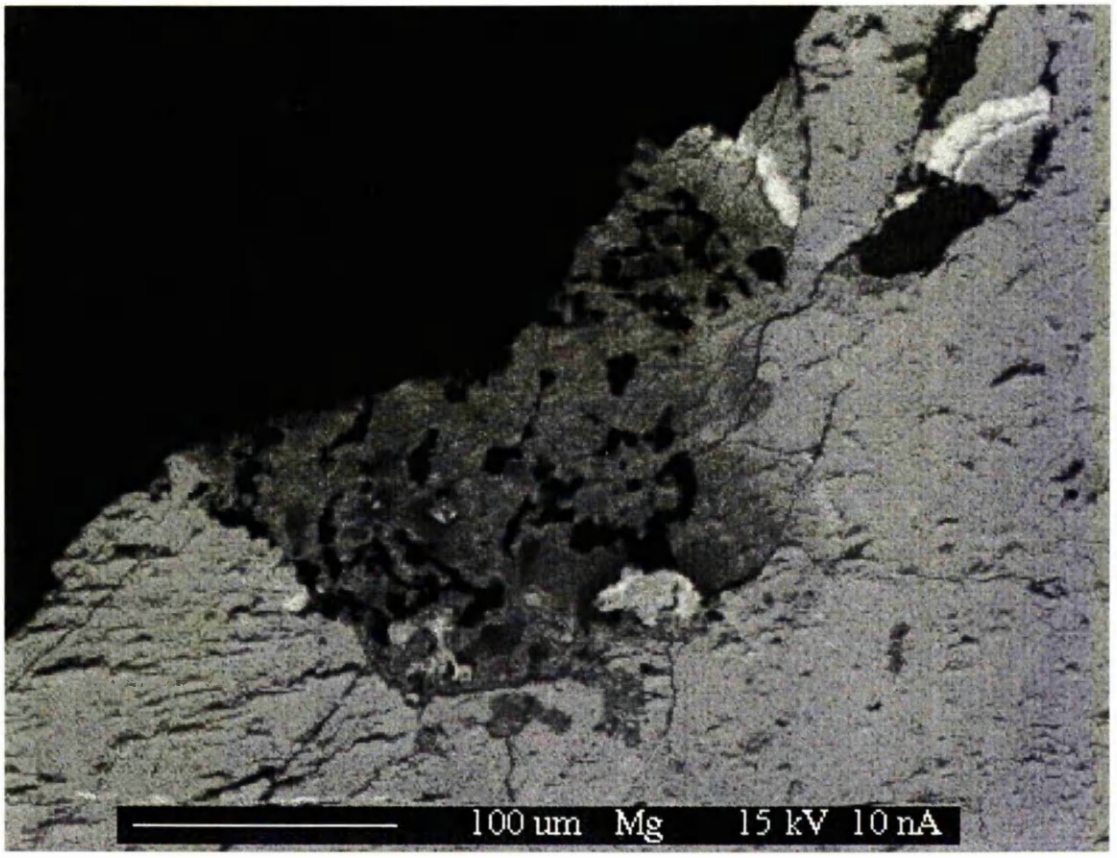

Figure 8.12b: Mg element map of grain 3

Note the typical rosette fragment with Mg-rich rims in the upper right of the figure. Black regions in the upper right are chromite. Black regions in the centre of the figure are feldspathic glass associated with the Ca-rich carbonate generation. The white region slightly below and right of centre is the best example of a rosette fragment within the Ca-rich carbonate (figure 8.11).

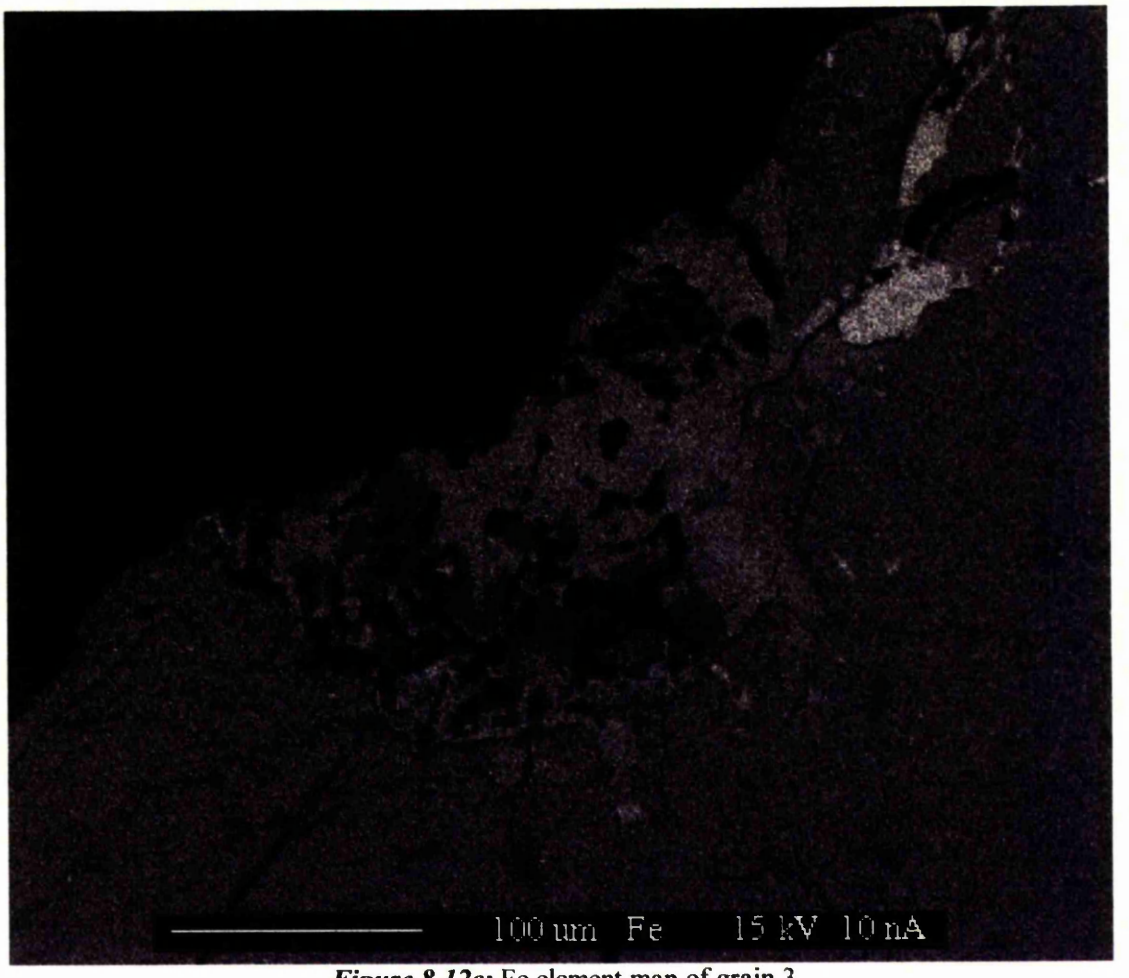

Figure 8.12c: Fe element map of grain 3

Note the high Fe content of the chromite (light grey) associated with rosette fragment and fractures within the pyroxene.

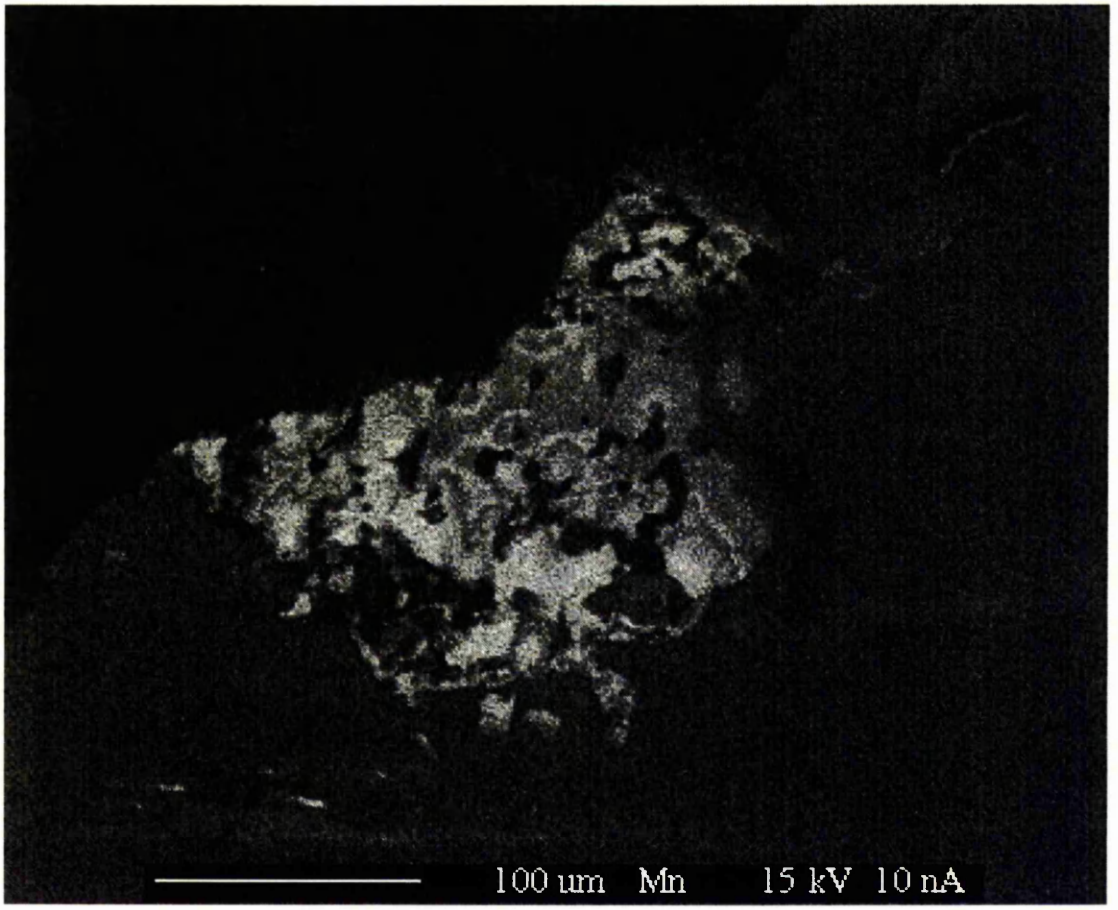

Figure 8.12d: Mn element map of grain 3

Note again the similarity in Mn content between the first nucleating carbonate and the Mn content in the Ca-Mn band. Also note the narrow nature of the Ca-Mn band in figure 8.12d (Mn map) compared to the broader Ca-Mn band in figure 8.12a (Ca map).

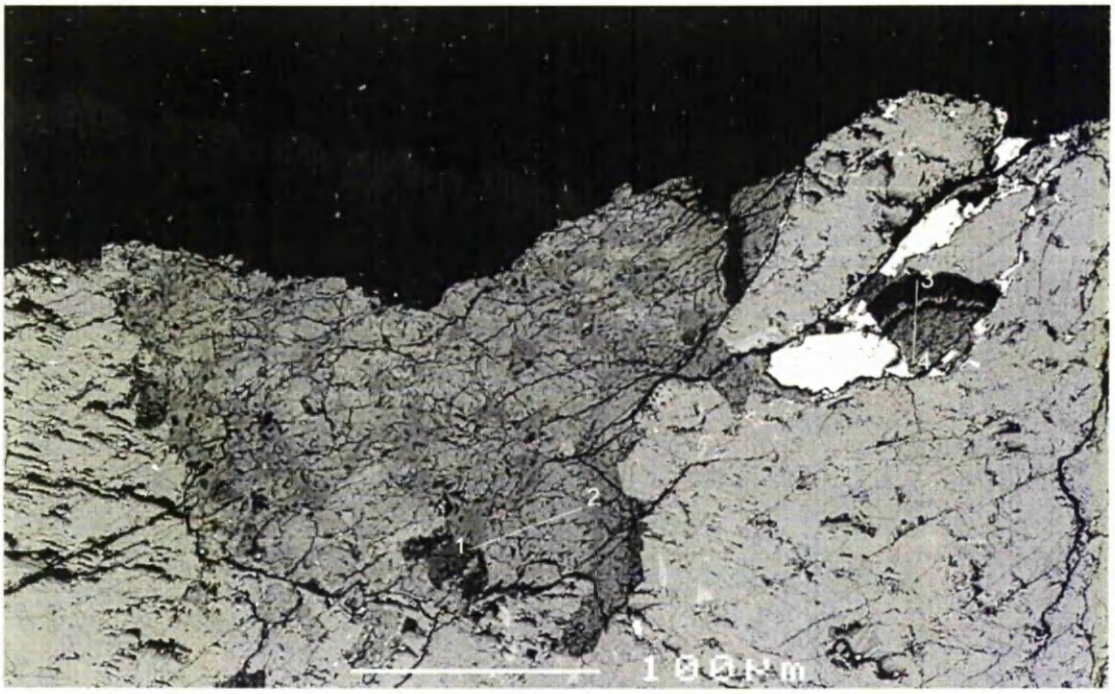

Figure 8.13: location of EPMA linescans for quantitative chemical analyses of carbonate in grain 3

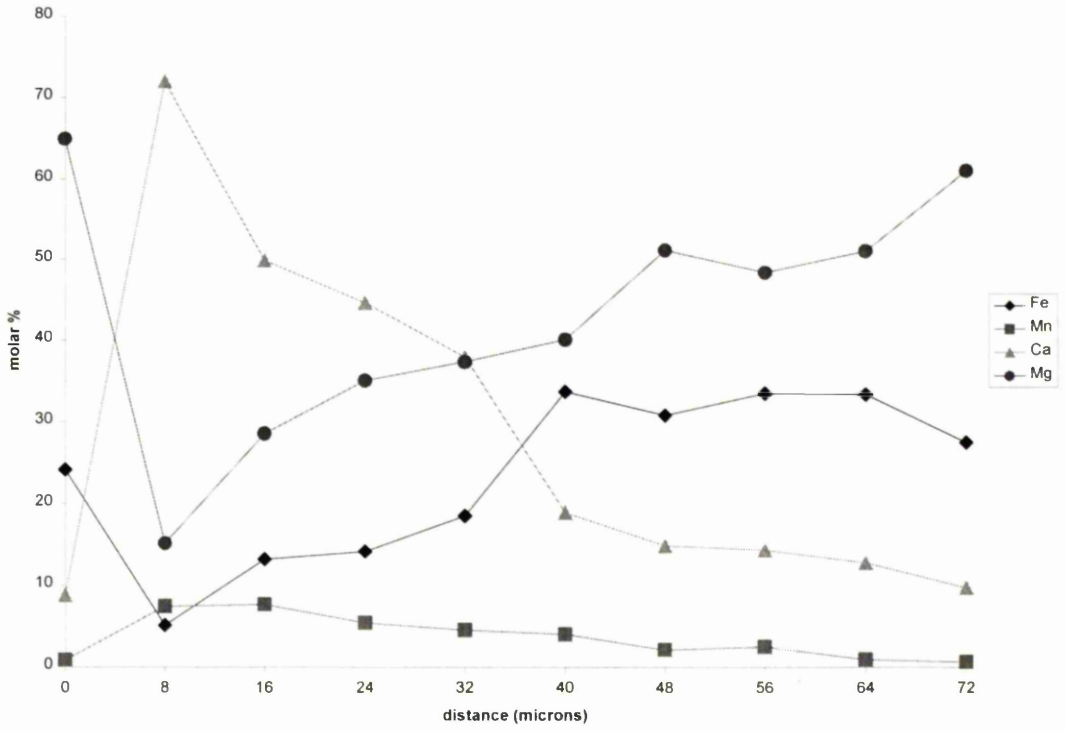

Figure 8.14a: EPMA linescan 1-2 showing quantitative analyses chemical zoning of carbonate in grain 3

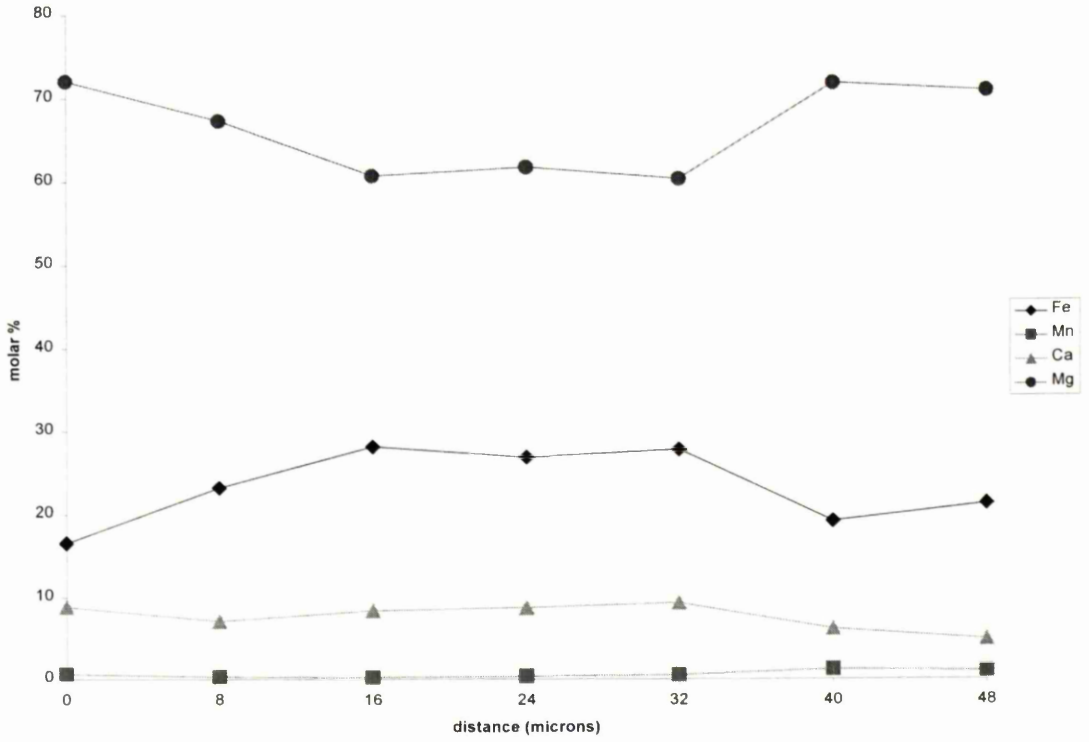

Figure 8.14b: EPMA linescan 3-4 showing quantitative analyses chemical zoning of carbonate in grain 3

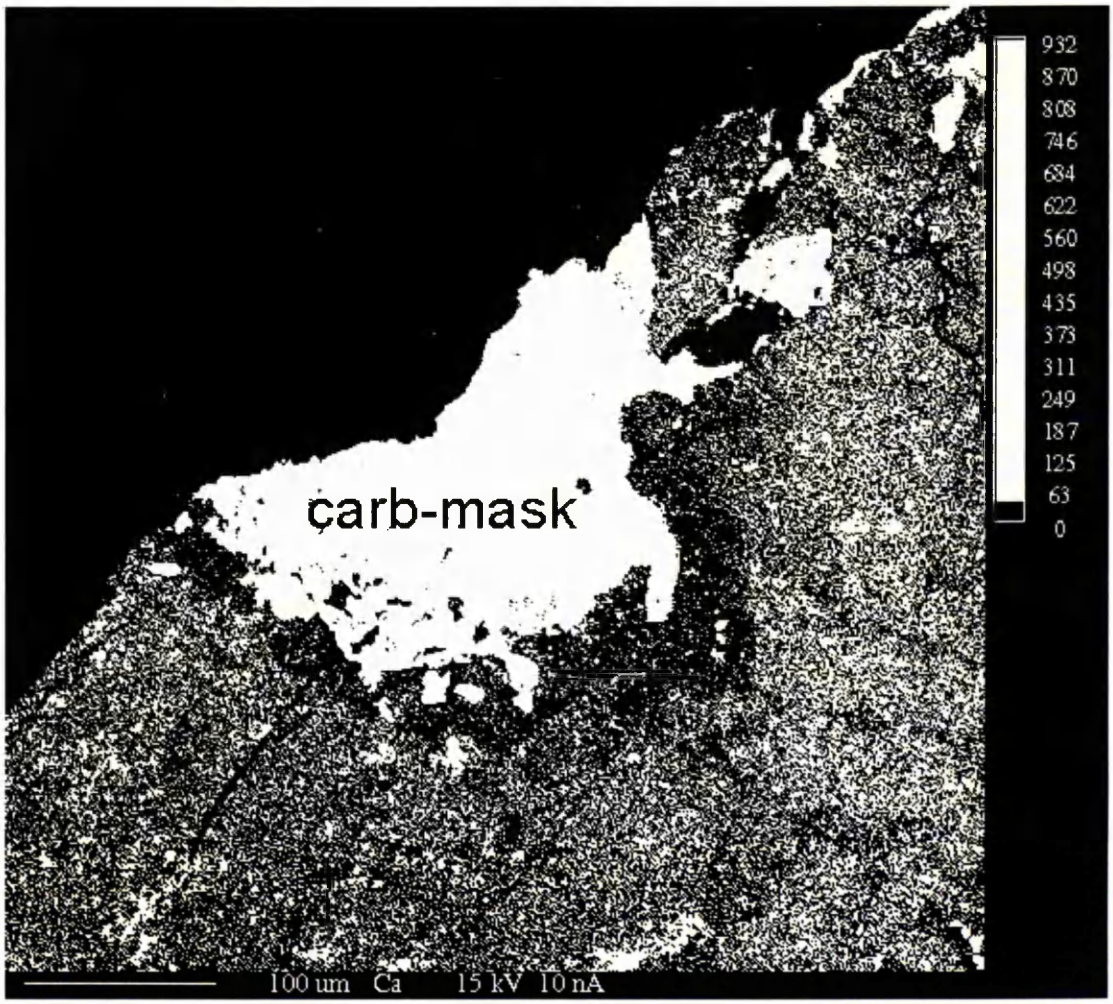

Figure 8.15: EPMA Ca element map rebinned to emphasise Ca depletion along crack on pyroxene and around carbonate-maskelynite region.

If the thresholds are altered on the Ca element map of grain 3 to enhance the differences in Ca content of the Ca-poor pyroxene, Figure 8.15 is the result. The pyroxene has lost >50% of its Ca content within 30 to 50μm of the Ca-rich carbonate-maskelynite region.

8.2.4 Grain 4

(2221) SEM BSE

The black region on the right of Figure 8.16 is epoxy. The light grey area is pyroxene. Medium and dark-grey heavily fractured regions are carbonate and medium grey unfractured phase associated with the carbonate is maskelynite. Small (<10μm) fragments of orthopyroxene are observed within feldspathic glass but not in Ca-rich carbonate. The small white region centre right is an iron sulphide. Zoning in the Ca-rich carbonate is less obvious than in the previous three grains: although there are three regions where Ca-rich carbonate appears to nucleate on Mg-rich carbonate, elsewhere Ca-rich regions (>50% Ca) occur with no obvious zoning. Again, embayment of pyroxene by carbonate and feldspathic glass is present. Other surface features on the pyroxene are the result of uneven polishing. Carbonate-maskelynite relationships are best observed in the element maps of Figures 8.6 and 8.7. Maskelynite compositions will be dealt with in a later section.

Grain 4 EPMA element maps (Figures 8.17a – 8.17d)

EPMA element maps were acquired using five wavelength dispersive spectrometers. Elemental analysis of the major cations in ALH84001 carbonate (Ca, Mg, Fe, Mn) and Si were performed by detection of cation Kα lines. Element maps are 512×512 pixels with an approximate spatial resolution of 1μm per pixel.

The Ca element map reveals the major Ca-rich region ($Ca_{78}Mg_{12}Fe_{05}Mn_{05}$) just above the centre of figure 8.17a. This Ca-rich carbonate appears to nucleate on sulphide. Again the Ca-rich band and the narrower Mn band present during zoning to more magnesian compositions as observed previously, can be traced across the Ca-rich generation carbonate in the centre left of figure 8.17a, indicating no major post-

deposition displacement of the Ca-rich carbonate. There are three Ca-rich regions ($Ca_{45}Mg_{33}Fe_{15}Mn_{07}$) which appear to nucleate on the Mg-rich carbonate (although in this case it is unclear whether these are rosette fragments) and then proceed to more magnesian and less calcic carbonate ($Ca_{13}Mg_{55}Fe_{33}Mn_{03}$). Embayment of the maskelynite by carbonate suggests replacement of maskelynite with carbonate.

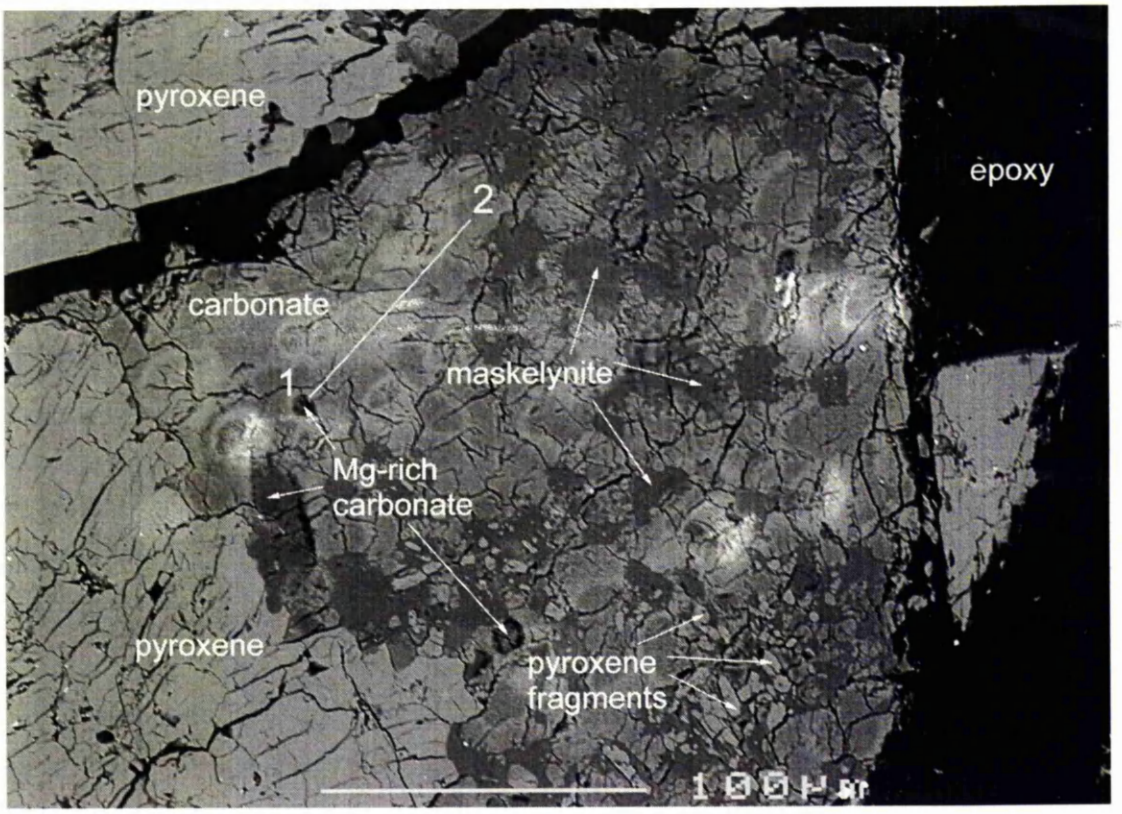

Figure 8.16: BSE image of grain 4.

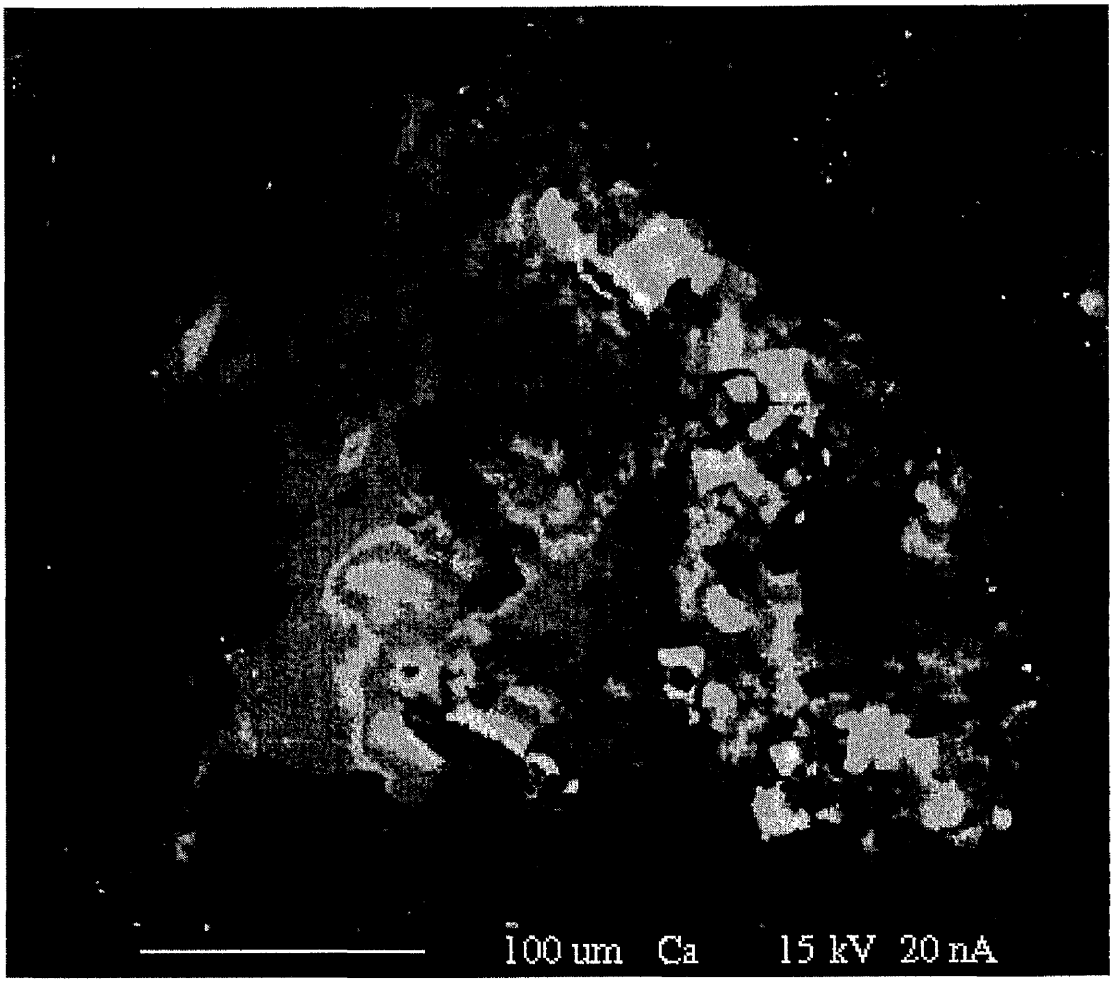

Figure 8.17a: Ca element map of grain 4

Note several regions of Ca-rich carbonate up to 80% molar Ca (white), nucleating on several regions of Mg-rich carbonate (lower centre of figure). The large ~50μm region of Ca-rich carbonate in the upper half of the figure appears to be nucleating on sulphide.

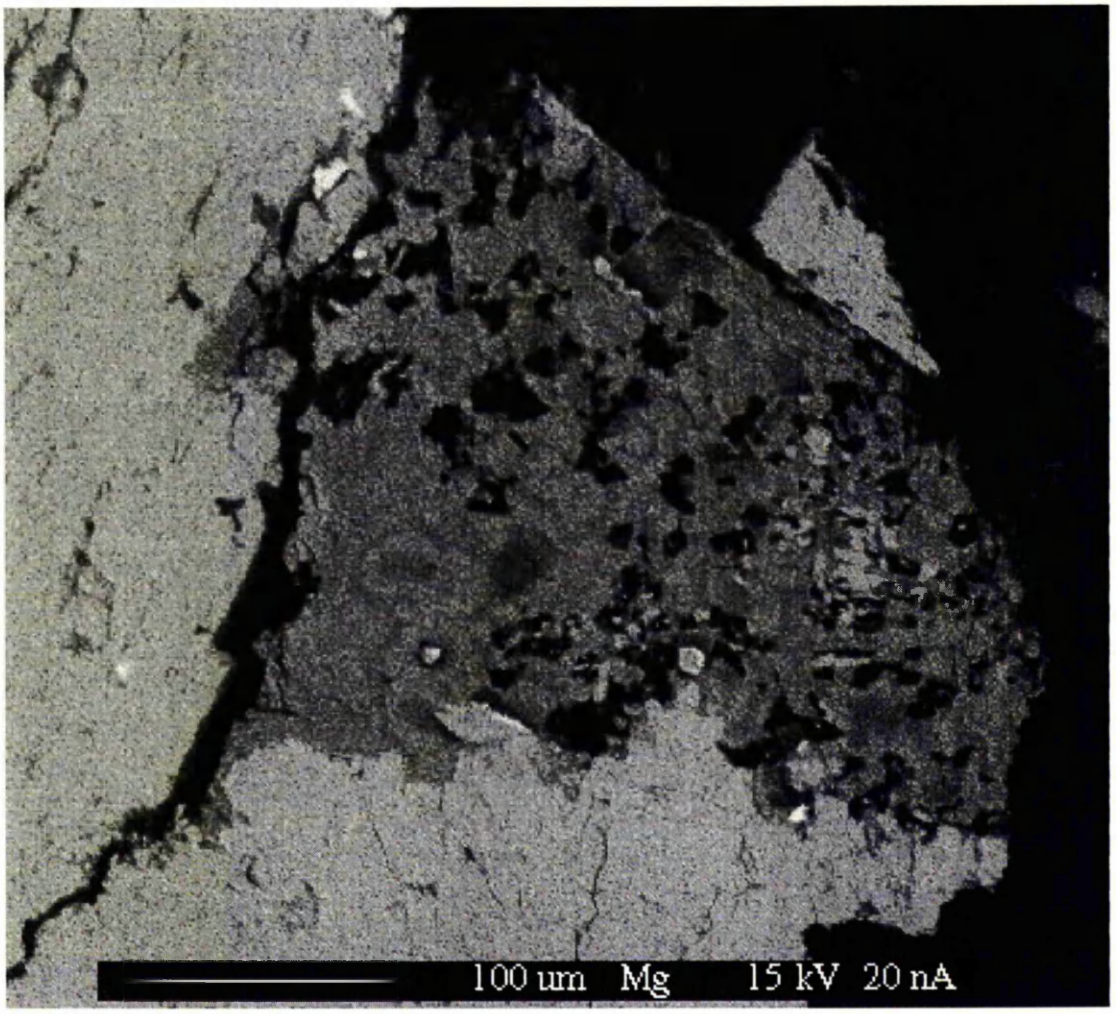

Figure 8.17b: Mg element map of grain 4

Figure 8.17b shows maskelynite fragments (black) interspersed throughout the medium-grey Ca-rich generation of carbonate. Light grey/white circular regions in the lower center of the figure are Mg-rich carbonate, again with magnesite (white) along one edge, typical of rosette mantle and rim compositions.

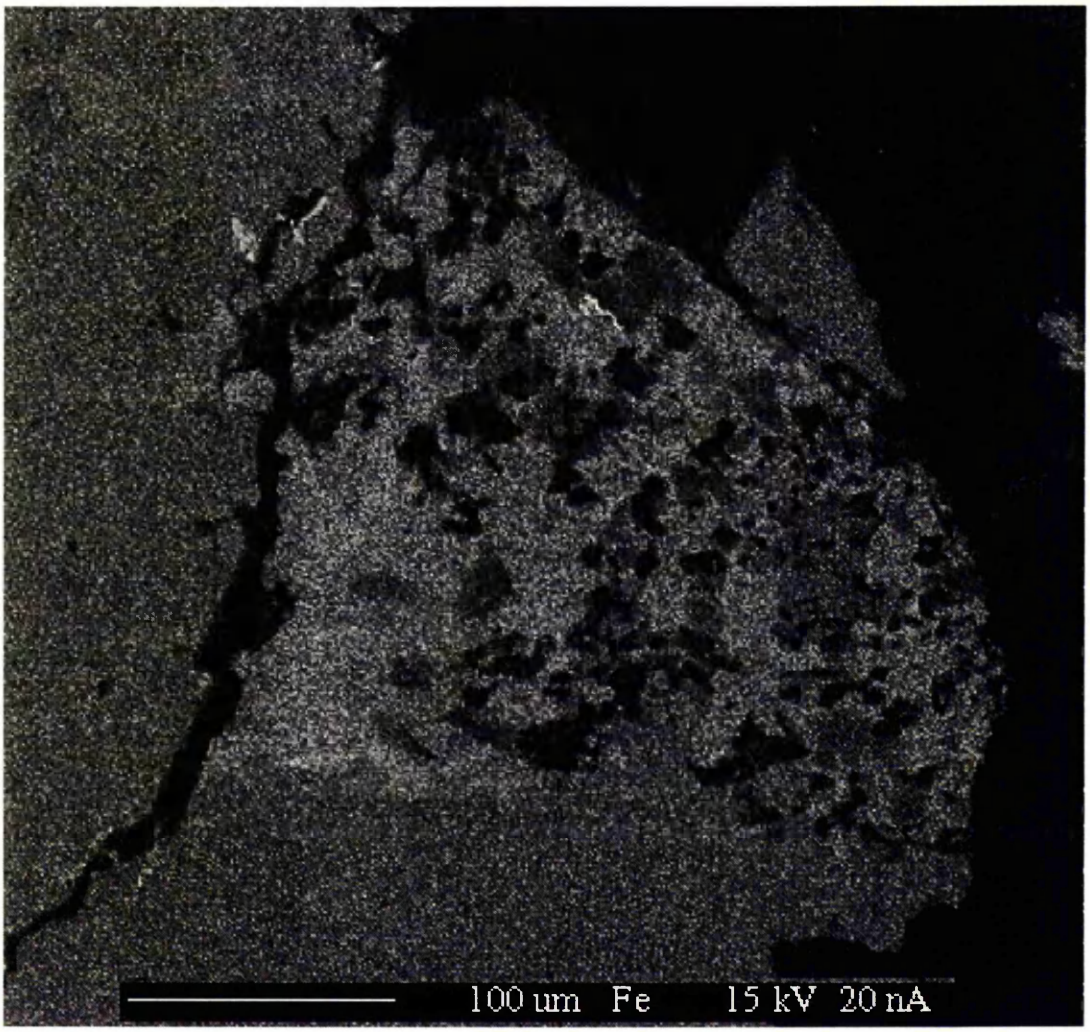

Figure 8.17c: Fe element map of grain 4

Figure 8.17c shows Fe sulphides (white regions). The sulphide above centre is an apparent nucleation site for the Ca-rich carbonate generation.

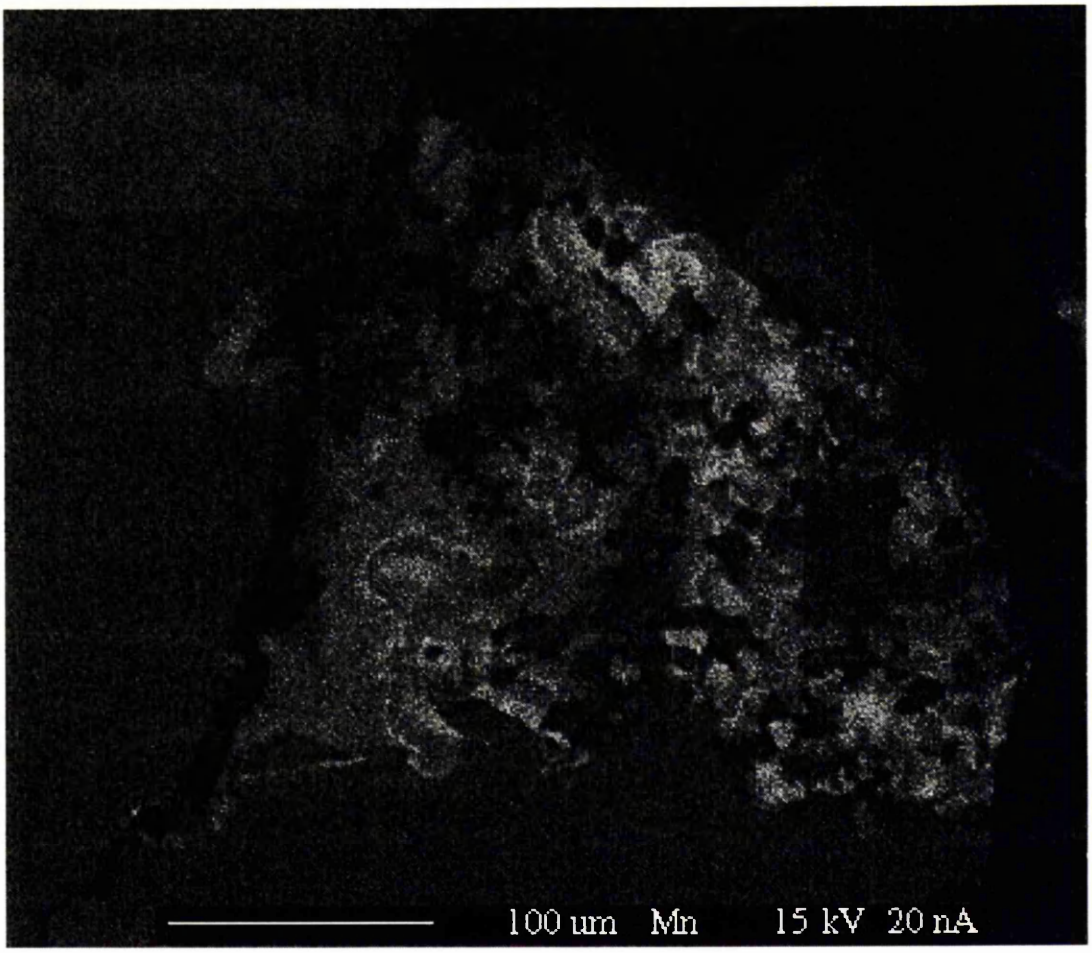

Figure 8.17d: Mn element map of grain 4

Note again the similarity in Mn content between the first nucleating carbonate and the Mn content in the Ca-Mn band. Also note the narrow nature of the Ca-Mn band in figure 8.12d (Mn map) compared to the broader Ca-Mn band in figure 8.12a (Ca map).

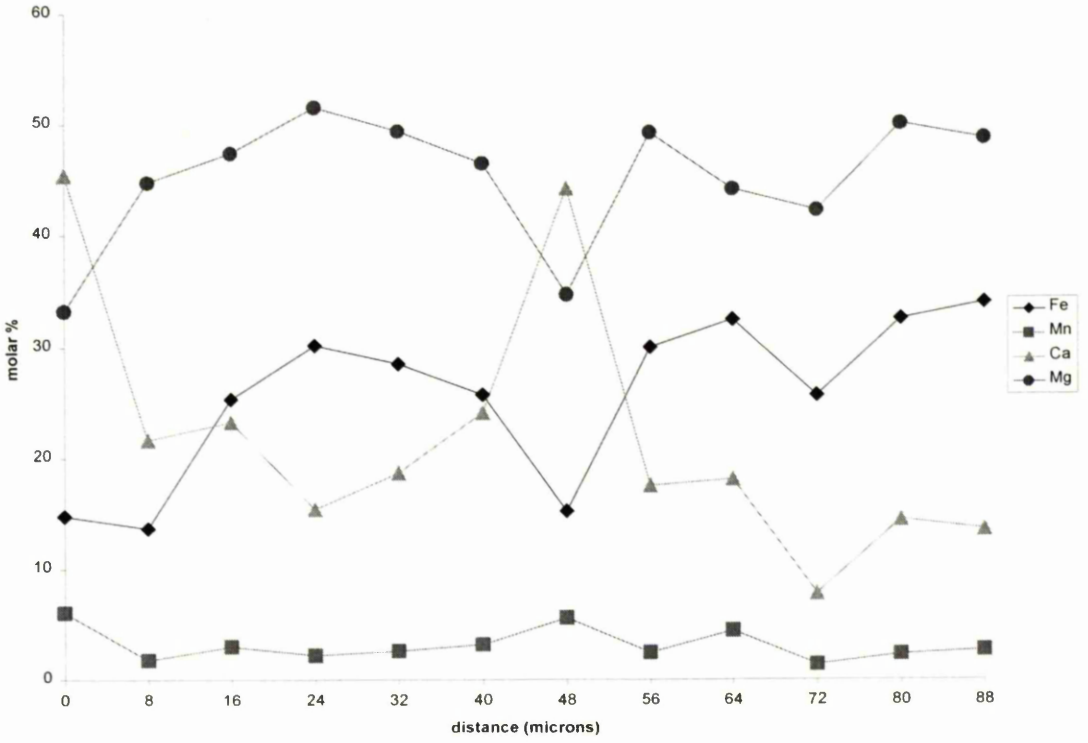

Figure 8.18: EPMA linescans showing quantitative analyses of carbonate in grain 4

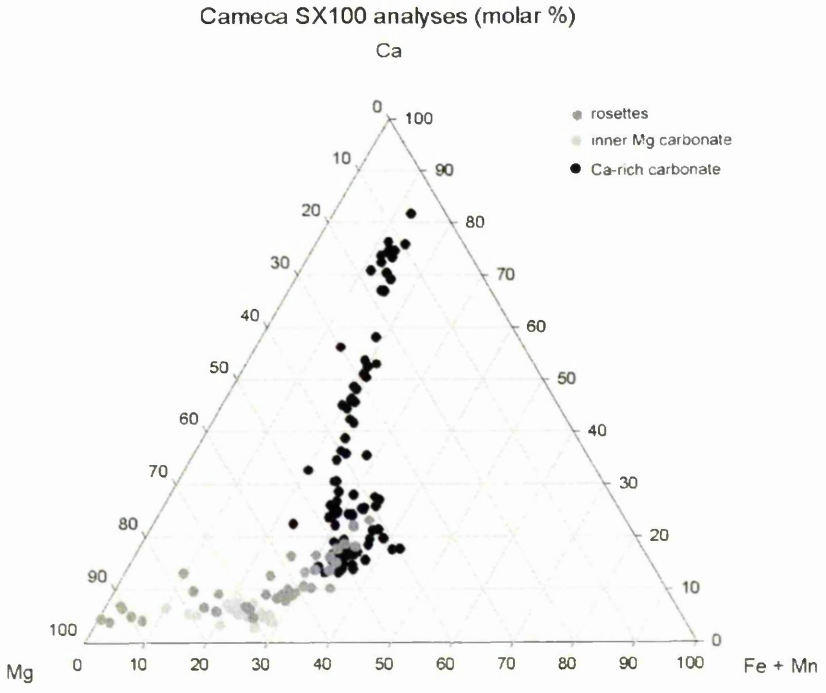

Figure 8.19: Cameca WDS spot analyses of four ALH84001 carbonate samples (errors smaller than data points)

All WDS analyses of probable rosette fragments encapsulated with Ca-rich carbonate, typical rosette fragments and Ca-rich carbonate are plotted in the ternary diagram (figure 8.19). Analyses with Si content >1molar% were excluded. There is a continuous compositional trend from Ca-rich carbonate to more magnesian compositions similar to typical rosettes. It is important to note the variation in composition of the inner Mg carbonate (probable rosette fragments) is entirely within the compositional field of typical rosettes.

8.2.5 Maskelynite chemistry

SEM EDS analysis of maskelynite associated with carbonates has been performed in samples 2, 3, and 4. Figures 8.20a-c show the chemical composition of maskelynite relative to 8 oxygens. For stoichiometric maskelynite, M(Ca+Na+K)=1 and T(Si+Al)=4. Clearly all three samples are not stoichiometric, showing a deficiency in metal cations relative to Si and Al. However, Si and Al are not present in excess (T is approximately 4) therefore the lack of stoichiometry present here is attributed to loss of metal cations. It is noted that relative to other studies of maskelynite (e.g. Greenwood and McSween, 2001) these samples have very low Na contents. Loss of Na under electron beams has been noted previously (Mittlefehldt, 1994) and is to be expected in these samples given the electron bombardment received during elemental mapping. Figures 8.20a-c show that the maskelynite analyses trend along a line given by sodium loss (theoretical stoichiometric and 50%Na loss are given for reference). The inference is that all deviation from stoichiometry is due to analytically induced Na loss not Si excess. As no silica was observed to be interstitial with maskelynite this is to be expected. Note there is no chemical zoning of the maskelynite in these samples despite the intimate association of maskelynite and strongly zoned carbonate.

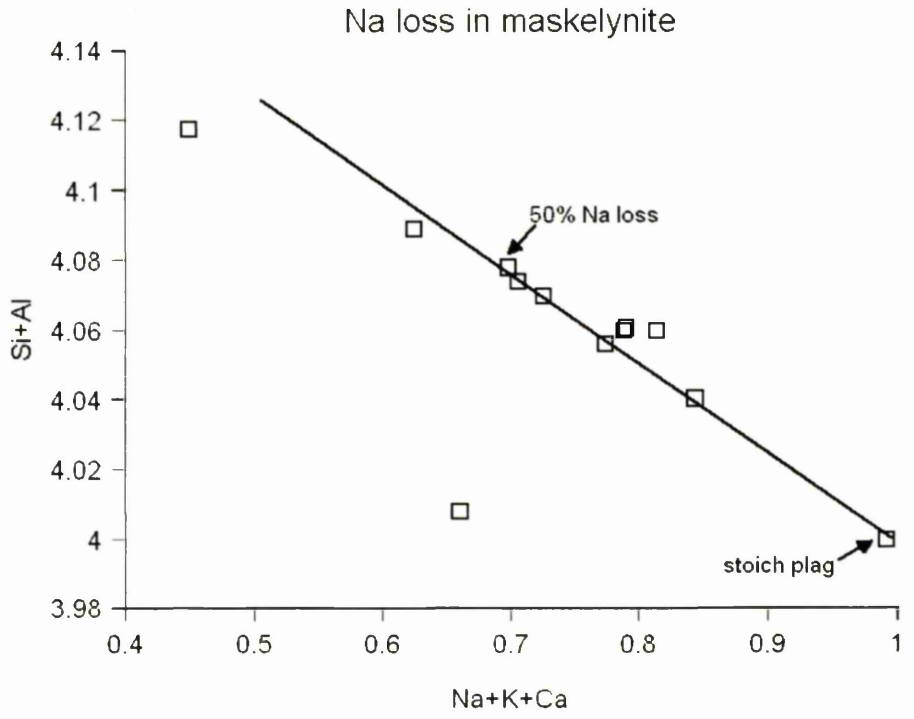

Figure 8.20a: deviation from stoichiometry and its relationship to Na loss in grain 2. Solid symbols are calculated end-members

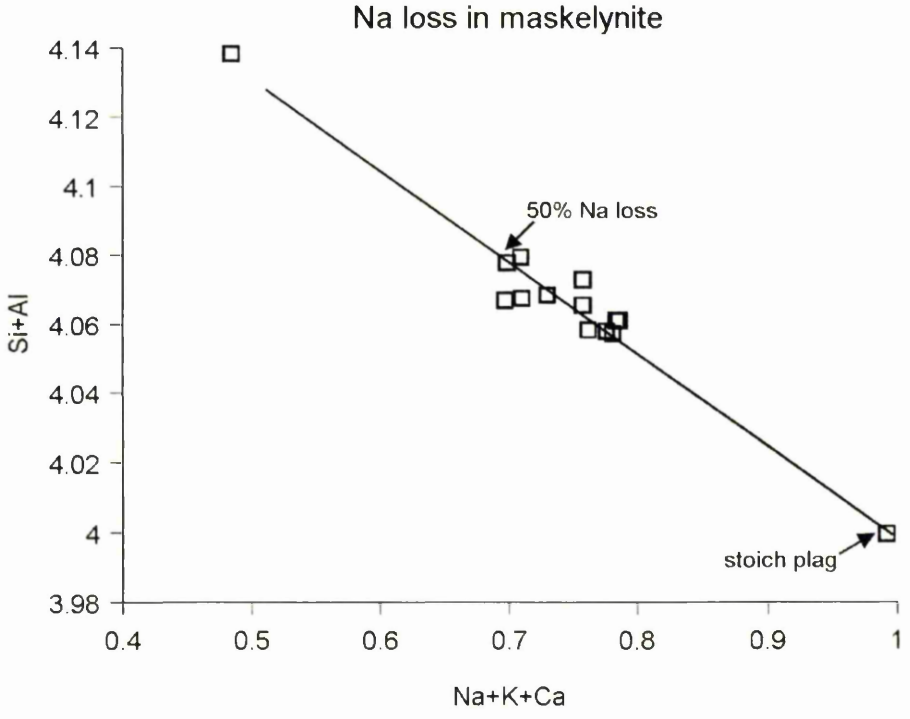

Figure 8.20b: deviation from stoichiometry and its relationship to Na loss in grain 3. Solid symbols are calculated end-members

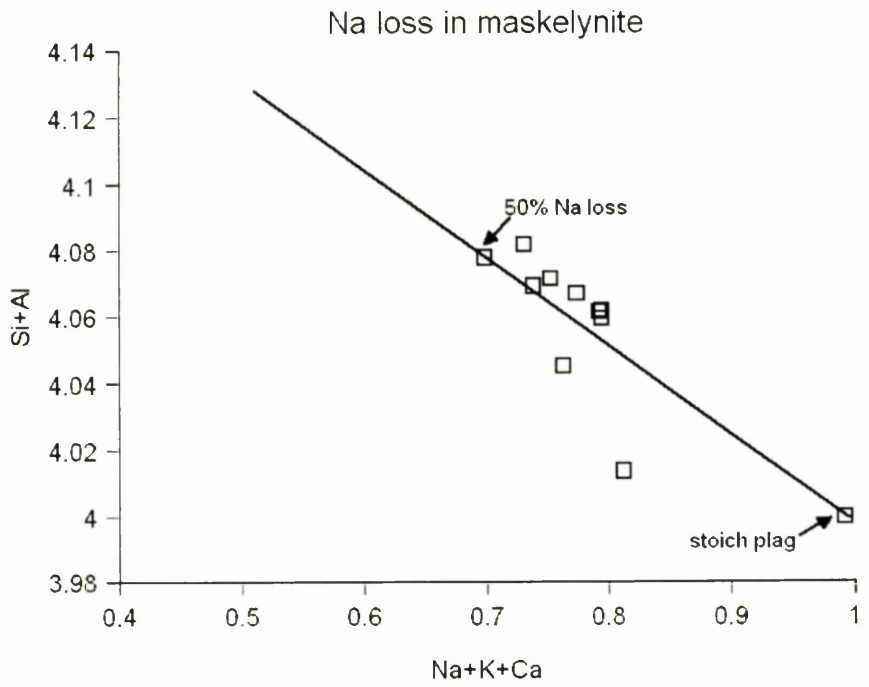

Figure 8.20c: deviation from stoichiometry and its relationship to Na loss in grain 4. Solid symbols are calculated end-members

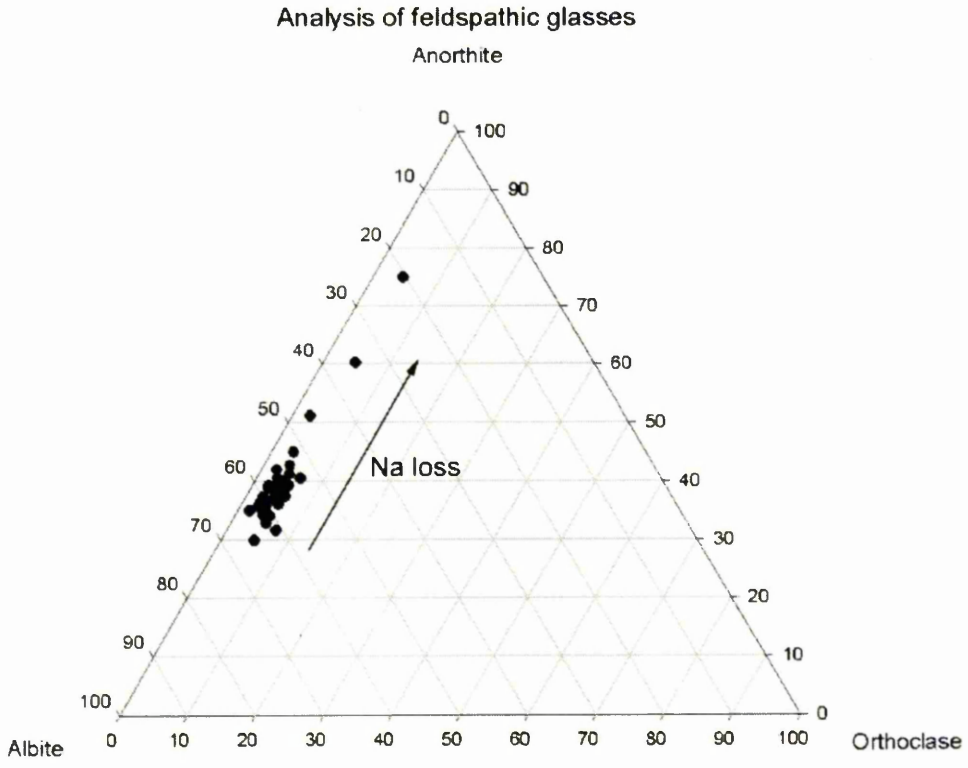

Figure 8.21: ternary plot showing maskelynite composition and Na loss. Errors are smaller than data point symbols.

Plotting the maskelynite analyses on a feldspar ternary diagram shows that all feldspar is plagioclase of average composition $An_{34}Al_{62}Or_{04}$, similar to initial measurement of maskelynite composition $An_{31.1}Al_{63.2}Or_{5.7}$. In contrast to Turner *et al.* (1997) and Greenwood and McSween (2001), no K-rich feldspar is observed. Thus this feldspar is not mixed feldspar from melting and remobilisation as described by Greenwood and McSween (2001).

8.3 Discussion

8.3.1 Depletion of calcium in pyroxene

Grains 2 and 3 (Figures 8.9 and 8.15) show approximately 50% depletion of calcium along cracks and adjacent to the regions of Ca-rich carbonate. Some of these fractures contain maskelynite and sulphide, implying that the cracks acted as conduits for Si-rich fluids which may also have leached Ca from pyroxene. It is likely that later carbonate and maskelynite would also enter the rock and precipitate along these cracks, giving rise to the proximity of the Ca-depleted pyroxene and the pyroxene-carbonate interface.

8.3.2 Ca-rich carbonate

All 3 grains show evidence of Mg-rich carbonate appearing to provide a nucleation site for subsequent Ca-rich carbonate. Grains 2 and 3 contain what appear to be partially replaced rosette fragments enclosed in Ca-rich carbonate. Indistinct boundaries between rosette fragments and Ca-rich carbonate suggest a gradual process of precipitation rather than instantaneous deposition, implying that the Ca-rich carbonates were deposited by a percolating fluid rather than forming from a rapid shock event. The oscillatory zoning of Ca and Mn also suggests a complex deposition history, thus Ca-rich carbonate has not been shock mobilized into its current siting. Also,

preservation of micron scale chemical zoning requires temperatures <400°C and probably <200°C in a prolonged hydrothermal system (Fisler and Cygan, 1998; Kent *et al.*, 2001) hence high temperature may be unrealistic. The textures presented here are in agreement more with Treiman (1995;1998), Kring *et al.* (1997) and Gleason *et al.* (1997) than the hypothesis of Scott *et al.* (1997; 1998) that carbonate was shock-melted and rapidly deposited. In addition, high spatial resolution field emission scanning electron microscope data clearly show that feldspathic fragments intruded and mobilised solid fragments of carbonate indicating that shock melting of ALH84001 carbonate by impact did not occur (Schwandt *et al.*, 1999). Although the carbonate textures presented here were not observed by Schwandt *et al.* (1999) it is inferred that if rosette carbonate was not shock-melted then neither were the (later) Ca-rich carbonates.

A second argument against a shock mobilised carbonate origin concerns the Ca-Mn ratios within the Ca-rich carbonates. Whilst the onset of the Ca-Mn band is sharply defined in Ca and Mn concentrations, it reduces rapidly after a few microns with respect to Mn. This is not true of Ca, which exhibits a constant concentration throughout the Ca-Mn band. Also the Mn concentration is approximately constant in the first formed ~70% Ca carbonate and within the Ca-Mn band (~7% Mn in both cases). Again this is not true for Ca, which has Ca content ~70% molar Ca where it nucleates on the probable rosette fragments but <30% molar Ca in the Ca-Mn band. This lack of consistency in Ca-Mn ratios (in contrast to Ca-Mn data from Eiler *et al.*, (2002)) is inconsistent with a rapidly cooling, shock mobilised fluid. Two of these grains show evidence of Ca-depletion in pyroxene along original fractures, possibly due to leaching of Ca by passage of a hydrothermal fluid. Thus if Ca can be leached from ALH84001 pyroxene, the Ca-band may represent a later phase of fluid initially enriched in Ca from pyroxene. Soon after, with much of the Ca source depleted, the Ca content of the

carbonate also falls. This is not true of the Mn content because there is no evidence of Mn loss from pyroxene along cracks, therefore an initial Mn-rich band may reflect the first pulse of fluid which contained Mn from elsewhere.

8.3.3 Ca-rich carbonate – pyroxene relationships

These grains show partially fractured boundaries between carbonate and pyroxene. However, grains 2 3 and 4 shows unfractured carbonate-pyroxene interfaces which are deeply embayed. This is suggestive of partial replacement of pyroxene during Ca-rich carbonate deposition by a percolating fluid rather than an instantaneous deposition event.

8.3.4 Feldspathic glass origins

Zoning within the Ca rich carbonate is observed to continue through the maskelynite framework without displacement and in contrast to Mg-rich fragments, Ca rich carbonate does not appear to nucleate on feldspar. This suggests the feldspathic glass was not emplaced prior to influx of Ca-rich carbonate although the extent to which carbonate preferentially nucleates on carbonate rather than feldspathic glass is unclear. The presence of angular pyroxene fragments exclusively in the feldspar indicates a shock episode which mobilised a siliceous fluid and fragmented pyroxene, which was then incorporated into the solidifying feldspathic glass. Therefore, at least, I can conclude that the Ca-rich carbonate was not co-genetic with the feldspathic glass: the opposite conclusion to that drawn by Eiler *et al.*, (2002) from similar textures. There is little rosette – maskelynite association because the majority of the carbonate is the Ca-rich carbonate. Given a 3.92Ga ± 0.04 annealing age for maskelynite (Turner *et al.*, 1997) and 3.90Ga ± 0.04 age for carbonate (Borg *et al.*, 1999) we assume that these feldspathic regions do not represent the maskelynite annealing age of Turner *et al.*, (1997). This is credible considering the apparent rarity of this Ca-rich carbonate and

associated bleb-like feldspathic textures observed here. As discussed above, all maskelynite intimately associated with carbonate appears to be stoichiometric plagioclase once Na loss has been taken into account. This is suggestive of feldspar precipitation because a shocked melted and flowed glass would likely mix with silica and K-feldspar to produce a non-stoichiometric feldspar of widely varying chemical composition (Greenwood and McSween, 2001). This argues against the model that the pyroxene fragments were injected into a shock mobilised siliceous fluid, unless the source of the feldspathic glass was homogeneous feldspar.

A plausible sequence of events to explain the textural relationships may be:

i) deposition of carbonate rosettes.

ii) fragmentation of carbonate rosettes.

iii) Precipitation of Ca rich carbonate from a later generation of fluid.

iv) Shock induced fragmentation of pyroxene and incorporation into feldspar shock mobilized feldspar.

8.36 Source of Ca-rich carbonate

What was the source of the Ca rich carbonate? The compositional range of carbonate rosettes is ~$Ca_{40}Mg_{36}Fe_{19}Mn_{05}$ to ~$Ca_{03}Mg_{97}Fe_{00}Mn_{00}$ with a mean composition of $Ca_{11.5}Mg_{58.0}Fe_{29.4}Mn_{1.1}$ (Mittlefehldt, 1994). This is significantly different from the compositional range of the carbonate surrounding the probable rosette fragments which zone from the calcic end member ~$Ca_{80}Mg_{07}Fe_{05}Mn_{08}$ to ~$Ca_{15}Mg_{50}Fe_{35}Mn_{00}$. There is some overlap in chemical composition between the two types of carbonate but volumetrically, relatively Ca-rich carbonate in rosette cores is insignificant, suggesting that remobilised rosette carbonate did not provide the cations for the later calcic carbonates. The reaction:

$$(Mg,Fe,Ca,Mn)SiO_3 + CO_2 \rightarrow (Mg,Fe,Ca,Mn)CO_3 + SiO_2$$

describing cation exchange between mobilised carbonate and host orthopyroxene could, in theory, supply the required Ca^{2+} ions. However, this is very unlikely given the absence of silica in these samples and the rarity of silica in ALH84001 in general. Depending on the silica phase, the ratio of silica / carbonate by volume is anticipated to be 0.7-0.84. An average carbonate abundance by volume is ~1% (e.g. Romanek *et al.*, 1994; Treiman, 1995) whereas silica is hard to find in ALH 84001. It is also noted that orthopyroxene, constituting 95% of the host rock, has a mean composition of $Wo_{3.3}En_{69.4}Fs_{27.3}$ (Mittlefehldt, 1994). Thus any cation exchange with carbonate would produce more Fe-Mg rich carbonates rather than the calcic carbonates observed here. Alternatively, the evaporite hypotheses of Warren (1998) and Harvey and McSween (1998) provide a later source of near surface volatiles. Using measurements of oxygen isotope ratios I shall explore the possibility that the Ca-rich carbonates in ALH84001 originated from a near surface source of volatiles different from and later than the source of rosette carbonates and present evidence against remobilisation of pre-existing 'rosette-type' carbonate.

Chapter 9

Results: stable isotopes

9.1 Introduction

Although small areas of Ca-rich carbonate (up to 80 molar % Ca) have been observed before (Harvey and McSween, 1996), their stable isotopes have not been measured previously and the relationship between Ca-rich carbonate and rosettes has remained unclear. The most Ca-rich carbonate measured by ion microprobe is <50 molar% Ca (Leshin *et al.*, 1998). The relatively large size (up to 30 μm across) of Ca-rich carbonate in my samples provided an opportunity to measure $\delta^{18}O$ of carbonate with Ca content >50 molar %Ca. Highest resolution ion microprobe analyses were performed on the smaller (10μm-20μm) Ca-rich regions at Manchester. The larger regions were analysed at using the UCLA ion microprobe for $\delta^{18}O$, where the higher beam currents produce an inherently larger spot size (approximately 25μm). ALH84001 carbonate of rosette composition was analysed for $\delta^{13}C$ at Manchester.

9.2 Oxygen isotopes

The following section presents ion microprobe spot analyses of three grains of ALH84001 carbonate, described as grain 1, 3 and 4 in chapter 8.

Table 9.1: measured $\delta^{18}O$ values and matrix correction relative to day-to-day ankerite standard. Grain 4 using the Manchester ion microprobe.

Sample and spot number	**Measured $\delta^{18}O$ ‰**	**Matrix correction ‰**	**$\delta^{18}O_{SMOW}$ ‰**	**Average chemical composition**
Grain 4 spot 1	-1.6	+13.4	11.8	$Ca_{13}Mg_{49}Fe_{37}Mn_{01}$
Grain 4 spot 2	-3.0	+11.9	8.9	$Ca_{17}Mg_{47}Fe_{34}Mn_{02}$
Grain 4 spot 3	-9.9	0.0	-9.9	$Ca_{71}Mg_{14}Fe_{07}Mn_{08}$
Grain 4 spot 4	-2.0	0.0	-2.0	$Ca_{60}Mg_{21}Fe_{12}Mn_{07}$
Grain 4 spot 5	-2.9	0.0	-2.9	$Ca_{55}Mg_{25}Fe_{14}Mn_{06}$
Grain 4 spot 6	-3.6	0.0	-3.6	$Ca_{54}Mg_{28}Fe_{13}Mn_{05}$
Grain 4 spot 7	-4.0	+8.7	4.7	$Ca_{26}Mg_{41}Fe_{30}Mn_{03}$
Grain 4 spot 8	-3.2	0.0	-3.2	$Ca_{54}Mg_{27}Fe_{13}Mn_{06}$
Grain 4 spot 9	-5.6	+10.5	4.9	$Ca_{21}Mg_{45}Fe_{32}Mn_{02}$
Grain 4 spot 10	-1.4	+2.2	0.8	$Ca_{44}Mg_{35}Fe_{16}Mn_{05}$
Grain 4 spot 11	-3.9	+ 12.6	8.7	$Ca_{15}Mg_{46}Fe_{38}Mn_{01}$
Grain 4 spot 12	-7.2	+7.2	0.0	$Ca_{30}Mg_{40}Fe_{26}Mn_{04}$
Grain 4 spot 13	-2.4	+9.8	7.4	$Ca_{23}Mg_{41}Fe_{33}Mn_{03}$
Grain 4 spot 14	-6.6	+11.2	4.6	$Ca_{19}Mg_{46}Fe_{33}Mn_{02}$
Grain 4 spot 15	-5.3	+ 8.4	3.7	$Ca_{25}Mg_{40}Fe_{30}Mn_{03}$

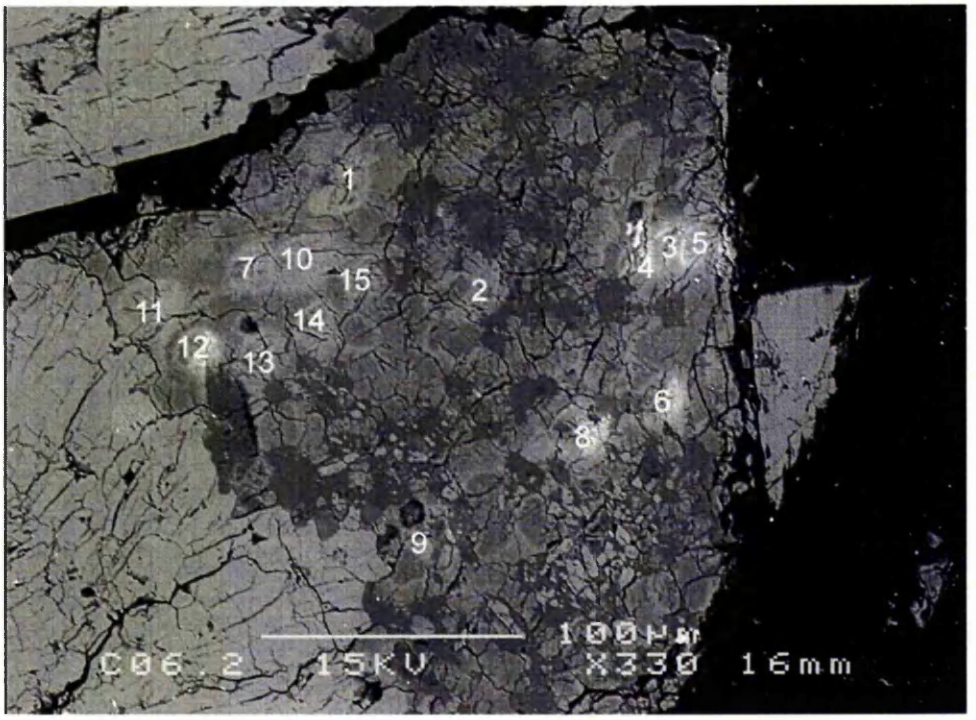

Figure 9.1a: Backscattered SEM image showing location of Manchester ion microprobe analyses in grain 4. Some craters are discernible

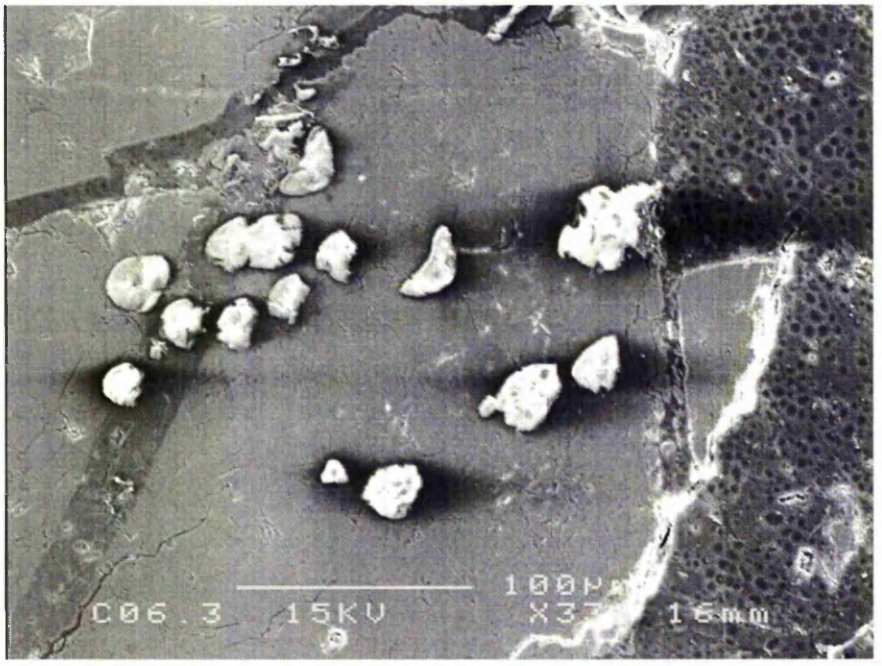

Figure 9.1b: SEM secondary electron image showing location of Manchester ion microprobe analyses in grain 4. White regions show where carbon coat has been removed during spot analyses.

Table 9.2: measured $\delta^{18}O$ values and matrix correction relative to day-to-day ankerite standard. Grain 1 (1888) using Manchester ion microprobe.

Sample and spot number	Measured $\delta^{18}O$ ‰	Matrix correction ‰	$\delta^{18}O_{SMOW}$ ‰	Average chemical composition
Grain 1 spot 1	-6.5	+10.8	4.3	$Ca_{21}Mg_{45}Fe_{32}Mn_{02}$
Grain 1 spot 2	8.7	+15.5	24.2	$Ca_{07}Mg_{70}Fe_{22}Mn_{01}$
Grain 1 spot 3	1.4	+12.6	14.0	$Ca_{15}Mg_{43}Fe_{40}Mn_{02}$
Grain 1 spot 4	0.1	0.0	0.1	$Ca_{70}Mg_{14}Fe_{09}Mn_{07}$
Grain 1 spot 5	-2.5	+14.3	11.8	$Ca_{10}Mg_{55}Fe_{30}Mn_{01}$
Grain 1 spot 6	-0.2	+10.8	10.6	$Ca_{20}Mg_{50}Fe_{28}Mn_{02}$
Grain 1 spot 7	4.4	+16.2	20.6	$Ca_{04}Mg_{67}Fe_{29}Mn_{00}$
Grain 1 spot 8	7.6	+15.2	22.8	$Ca_{08}Mg_{69}Fe_{22}Mn_{01}$

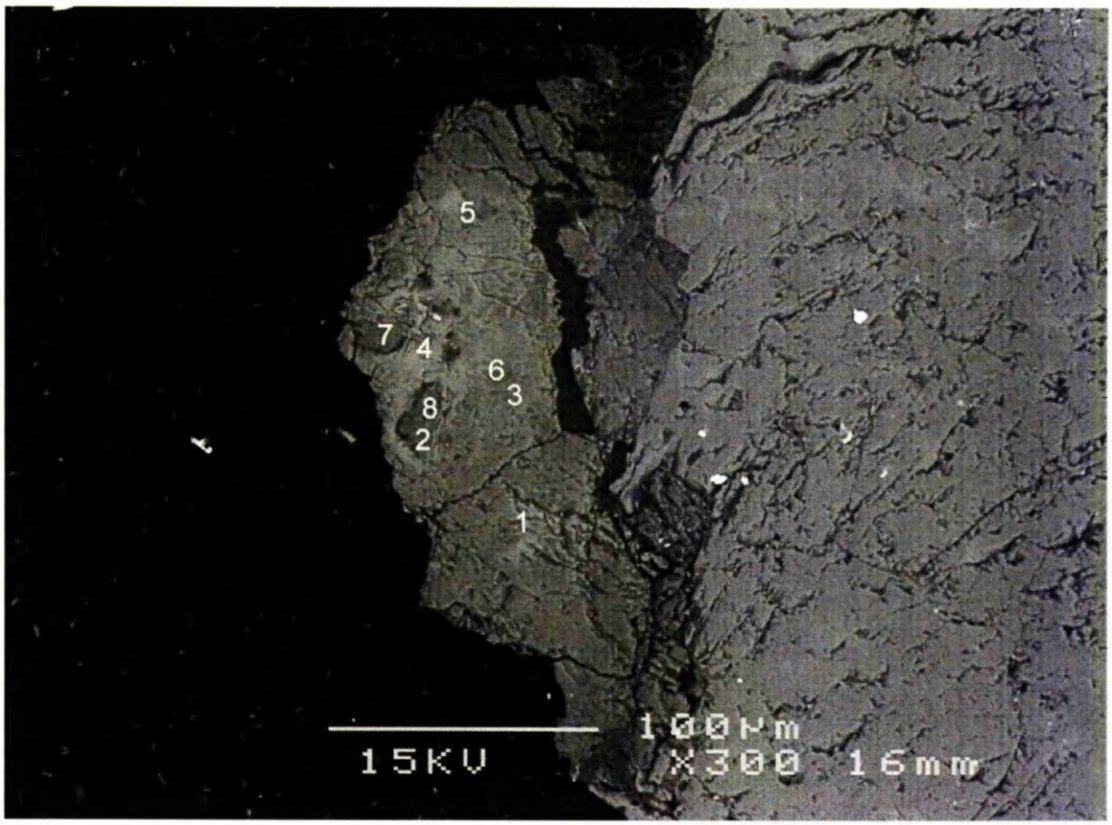

Figure 9.2: Backscattered SEM image showing location of Manchester ion probe analyses in grain 1.

Table 9.3: measured $\delta^{18}O$ values of Grain 3 and Grain 4 relative to ankerite using UCLA ion microprobe. Spots measured in grain 4 on the Manchester ion probe did not overlap areas of grain 4 measured at UCLA.

Sample and spot number	**Measured $\delta^{18}O$ ‰**	**Matrix correction ‰**	**$\delta^{18}O_{SMOW}$ ‰**	**Average chemical composition**
Grain 3 spot 1	-8.6	+7.0	-1.6	$Ca_{51}Mg_{29}Fe_{13}Mn_{06}$
Grain 3 spot 2	-1.6	+12.0	+10.4	$Ca_{13}Mg_{53}Fe_{31}Mn_{02}$
Grain 3 spot 3	3.5	+13.0	16.5	$Ca_{08}Mg_{65}Fe_{24}Mn_{01}$
Grain 3 spot 4	-8.6	+12.0	3.4	$Ca_{13}Mg_{53}Fe_{31}Mn_{02}$
Grain 3 spot 5	1.8	+8.0	14.8	$Ca_{08}Mg_{65}Fe_{24}Mn_{01}$
Grain 3 spot 6	-10.8	+5.0	-5.8	$Ca_{63}Mg_{20}Fe_{10}Mn_{07}$
Grain 3 spot 7	-3.5	-	-	-
Grain 3 spot 8	-0.8	-	-	-
Grain 4 spot 1	-4.6	+10.0	4.4	$Ca_{35}Mg_{33}Fe_{26}Mn_{05}$
Grain 4 spot 2	-0.2	+11.0	10.8	$Ca_{19}Mg_{46}Fe_{32}Mn_{03}$
Grain 4 spot 3	-3.2	+11.0	7.8	$Ca_{16}Mg_{49}Fe_{32}Mn_{03}$

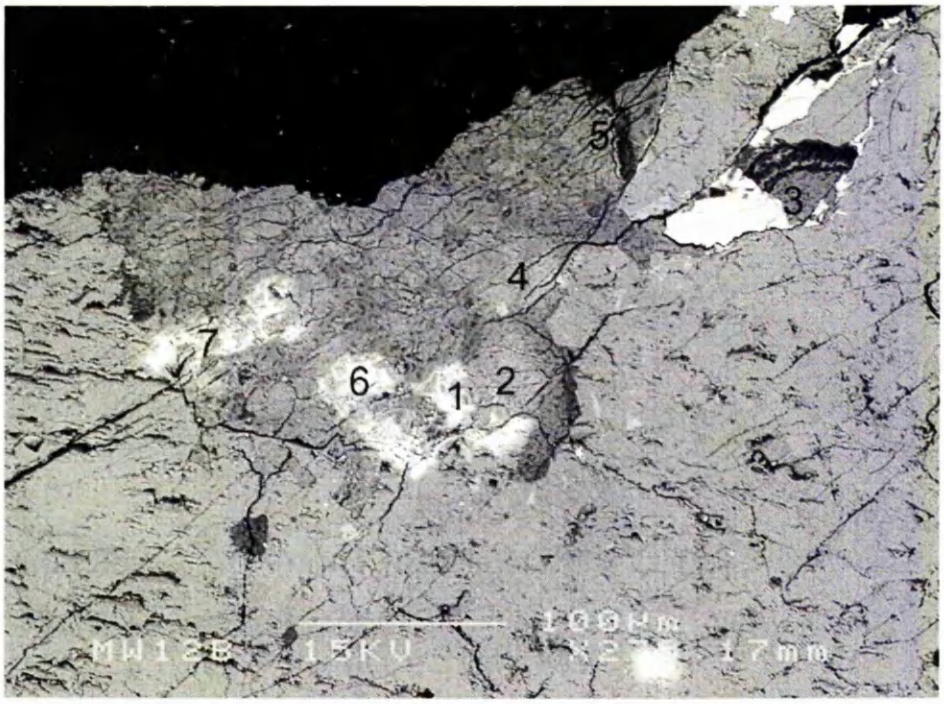

Figure 9.3a: Backscattered SEM image showing location of UCLA ion microprobe analyses in grain 3. Some craters are discernible

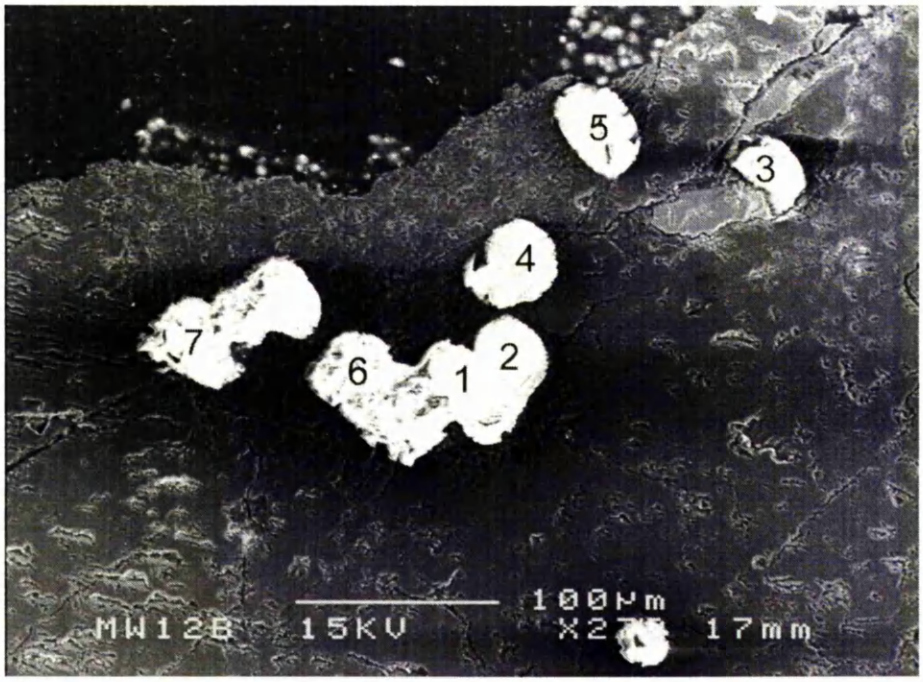

Figure 9.3b: SEM secondary electron image showing location of UCLA ion microprobe analyses in grain 3. White regions show where carbon coat has been removed during spot analyses.

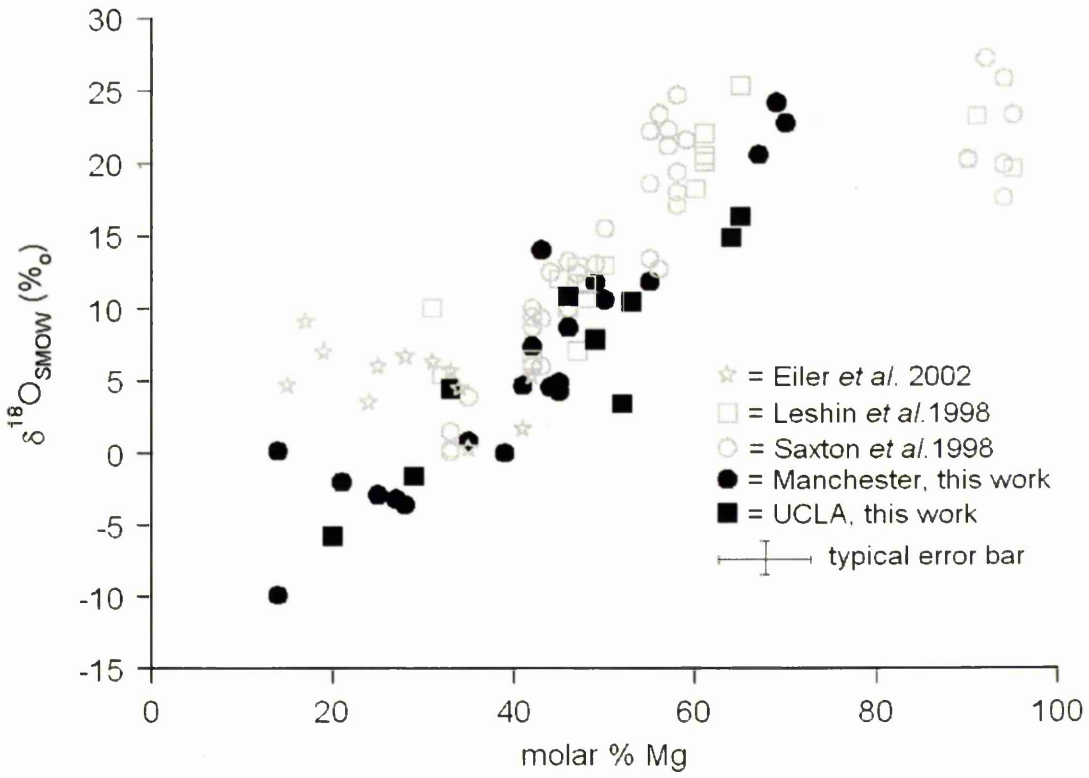

Figure 9.4: isotopic zoning of carbonate with Mg content. Comparison of isotopic data from Leshin *et al.* (1998) ankerite from Saxton *et al.* (1998), ankerite from Eiler *et al.* (2002), and data described in this thesis (including UCLA). Error bars (shown once for clarity) are <5% for chemical composition and 2.4‰ $\delta^{18}O$ values.

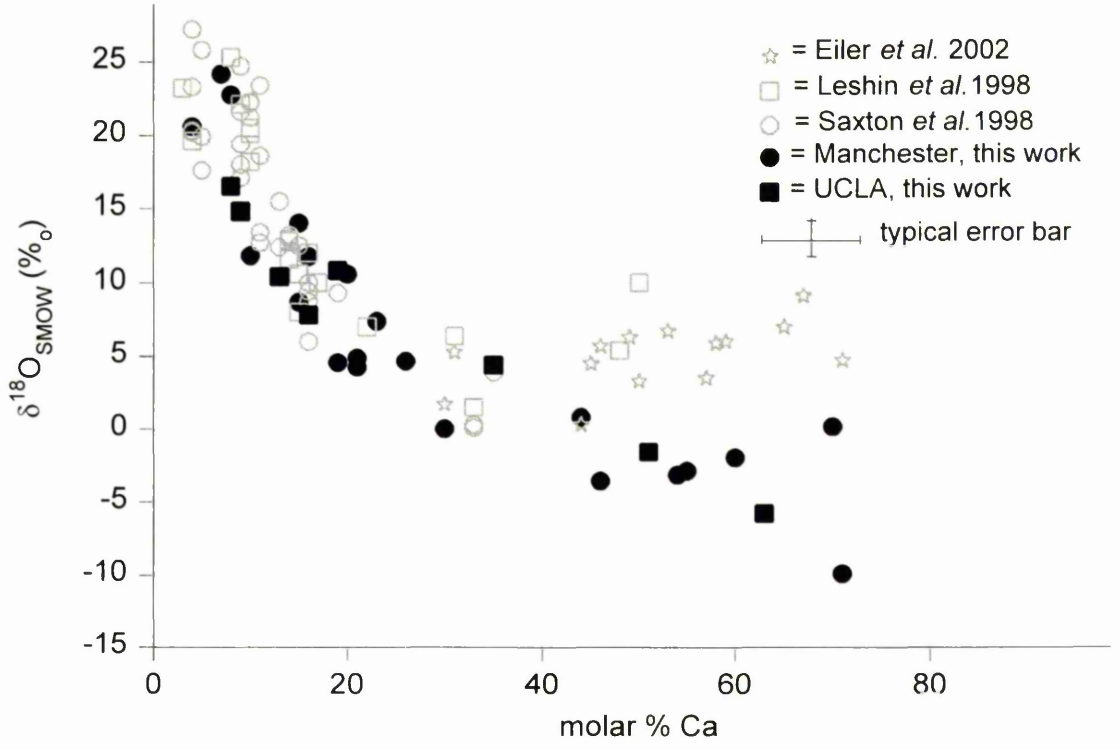

Figure 9.5: isotopic zoning of carbonate with Ca content. Comparison of isotopic data from Leshin *et al.* (1998) ankerite from Saxton *et al.* (1998), ankerite from Eiler *et al.* (2002) and data described in this thesis (including UCLA). Error bars (shown once for clarity) are <5% for chemical composition and 2.4‰ $\delta^{18}O$ values.

Clearly there is a correlation between cation chemistry and $\delta^{18}O$ values (figures 9.4 and 9.5). However, the chemical zoning of the carbonates is not a continuous trend because the rosette fragments are encapsulated by the most Ca-rich carbonates. This is depicted in figure 9.6, where the dramatic variation in cation chemistry is accompanied by the large variations in $\delta^{18}O$ values (+20‰ to +25‰ for the rosette fragments and -10‰ to 0‰ in the surrounding Ca-rich carbonate).

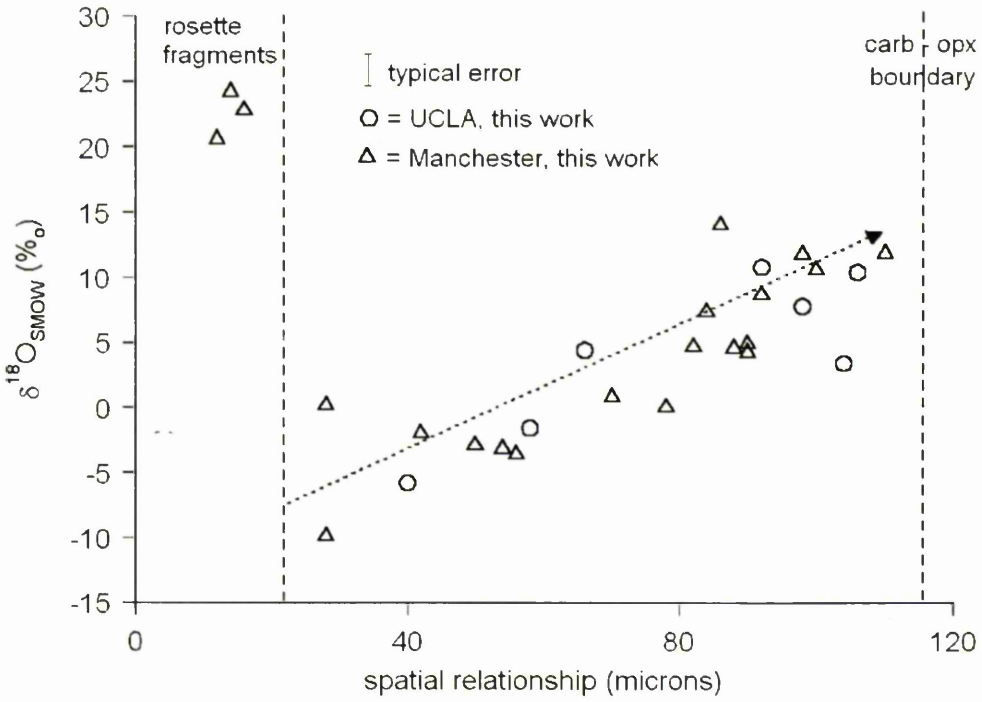

Figure 9.6: approximate spatial relationship of rosette fragments (inner Mg-rich carbonate) to Ca-rich carbonate. Carbonate with the highest Ca content is directly adjacent to the rosette fragments. $\delta^{18}O$ increases with decreasing Ca content and increasing distance from rosette fragments Data from all grains.

Key points of this dataset are:

i) The Ca-rich regions (up to 80% Ca) (figure 9.5-9.7) have very low $\delta^{18}O$ down to $-10‰ \pm 2‰$.

ii) Adjacent to the 80% Ca carbonate, the inner Mg-rich regions have $\delta^{18}O$ of ~+22‰±2‰ (figure 9.5-9.7), similar to that of rosette mantles and rims (Leshin *et al.* 1998; Saxton *et al.*, 1998).

iii) $\delta^{18}O$ of relatively Ca-rich regions (approximately 30% Mg) agree with Saxton *et al.* (1998) but are in disagreement with Leshin *et al.* (1998) and Eiler *et al.* (2002) (figure 9.5-9.7).

iv) Relatively Mg-rich (Ca-poor) carbonate terminating at the pyroxene boundary has $\delta^{18}O$ up to ~+14‰±2‰ (figure 9.5-9.7).

v) Large isotopic heterogeneity (~30‰) exists over a few microns between the inner Mg-rich regions and the surrounding Ca-rich carbonate.

9.3 Preliminary hydrogen and carbon isotope data

Accompanying hydrogen isotope data from four approximately 20μm diameter spots within the Ca-rich generation of carbonate are presented in table 9.4

Table 9.4: average of 100% pulsed spots and extrapolated endmember δD for ALH84001 carbonate.

Grain	Chemical composition	Measured δD (‰)	Extrapolated δD (‰)
3	$Ca_{13}Mg_{53}Fe_{13}Mn_{02}$	385±150	585±150
3	$Ca_{50}Mg_{30}Fe_{13}Mn_{07}$	340±125	420±125
4	$Ca_{14}Mg_{50}Fe_{33}Mn_{02}$	400±100	510±100
1	$Ca_{15}Mg_{51}Fe_{32}Mn_{02}$	430±125	495±125

This section includes the first attempt at measuring $\delta^{13}C$ of carbonates on the Manchester ion microprobe. As discussed in chapter 7, ion probe analyses of carbon are complicated by the inefficient generation of C^- secondary ions from carbonate. Owing

to these difficulties we have only measured one terrestrial siderite standard and consequently any matrix effects between carbonates of different chemical compositions are poorly defined. The 1σ scatter of the day-to-day siderite standard (Fe_{100}) was ~5‰ therefore uncertainty for all ALH84001 $\delta^{13}C_{PDB}$ measurements is taken to be the same as the uncertainty for the standard measurements: ~5‰. One ALH84001 carbonate spot of average chemical composition $Mg_{75}Fe_{18}Ca_{06}Mn_{01}$ (rosette mantle) yielded $\delta^{13}C_{PDB}$ ~+50‰. This is in agreement with recent work of Niles *et al.*, (2002) which suggests $\delta^{13}C_{PDB}$ zones from ~+30‰ in rosette cores to +50‰ in rosette outer mantles. ALH84001 pyroxene also yielded $\delta^{13}C_{PDB}$ ~+50‰ although the matrix effect of silicate is unknown.

Chapter 10

Interpretation of isotopic data

10.1 Introduction

The oxygen and hydrogen isotope data from secondary mineral assemblages are important: they can provide constraints on Martian volatile evolution. The processes of evaporation, atmospheric precipitation, atmospheric loss to space, water-rock interaction and fractionation during mineral deposition all alter the $\delta^{18}O$ values of Martian reservoirs. Thus, oxygen isotopic data are crucial to the understanding of evolving global Martian volatiles over time.

Despite the fractionation of hydrogen, carbon and nitrogen (Owen, 1992) and retention of heavy isotopes observed in noble gases (e.g. Pepin, 1994), it is unclear whether oxygen shows similar isotopic enrichment in ^{18}O due to the large errors on spectroscopic data (Krasnopolsky *et al.*, 1996). If there is no oxygen enrichment, buffering of the atmosphere by exchange with polar caps, subsurface regolith and silicate alteration are possible mechanisms by which oxygen enrichment may have been prevented. In the absence of direct oxygen isotopic measurements of near surface reservoirs, interpretation of the isotopic record preserved in SNC secondary minerals remains the best way of constraining the evolution of Martian volatiles. Therefore, this section will attempt to constrain the isotopic composition and size of the Martian volatile reservoirs and the near surface environmental conditions.

First I will discuss global isotopic models for Mars, making comparison between the data presented here and previous work on ALH84001 carbonate. Isotopic data from secondary minerals in younger Martian meteorites will also be used in an attempt to quantify isotopic evolution of near surface reservoirs. Different environmental

conditions and formation mechanisms will be studied to explore how simple isotopic models may define $\delta^{18}O$ values of Martian reservoirs.

10.2 Hydrogen

10.2.1 Martian origin for Ca-rich carbonate

Ion microprobe analysis of this carbonate gives δD values in the range ~+500<δD‰, which is significantly above –400‰ to +100‰ of the terrestrial δD values (Pillinger, 1984). Standard Light Antarctic Precipitation (SLAP) has a nominal δD of -428‰ and –400‰ is routinely found in Antarctic ice cores (e.g. Mazaud A. *et al.* 2000). In addition, mineral OH – H_2O fractionation generates even lighter mineral H (85‰ at 0°C for MgOH-H_2O) (Xu and Zheng, 1999). Although these measured Martian D/H ratios are up to 1000‰ above Antarctic terrestrial D/H ratios, they are still towards the less enriched range of ALH84001 carbonate (Boctor *et al.*, 1999a;1999b), who attributed the smaller enrichments to partial terrestrial contamination. The lack of a crystallographic site for hydrogen makes this plausible but replacement and recrystallisation is required to affect the oxygen isotopic ratios. Minor fractures are still present within the Ca-rich carbonate, demonstrating the lack of recrystallisation. Thus even if minor dilution of the Martian D/H signature has occurred, this has not effected the oxygen isotopic composition of the Ca-rich carbonates.

10.2.2 Modelling atmospheric loss using D/H ratios

First, I attempt to model hydrogen data, together with other recent work (Boctor *et al.*, 1999a,b; Suguira and Hoshino, 2000; this work) to constrain the size of near surface reservoirs. I have presented evidence for δD values in Ca-rich carbonate of δD ~+500‰. This is between +336‰±4>δD>+491‰±4 for irregular carbonate and

+791‰±12>δD>+1156‰±33 for carbonate rosettes of Boctor *et al.*, (1999a) and consistent with the broad range of carbonate rosette values +293‰>δD>+1344‰ obtained by Suguira and Hoshino (2000). If we assume that the dominant hydrogen loss process over time is Jeans escape from the top of the atmosphere, the fractional loss of hydrogen over time to give the present day δD value of +4200‰: (Donahue, 1995)

$$\frac{[H(t_1)]}{[H(t_2)]} = \left(\frac{R(t_2)}{R(t_1)}\right)^{\frac{1}{1-f}}$$

where f is 0.32, the fractionation factor for hydrogen loss by Jeans escape (Yung *et al.*, 1988) and R is the D/H ratio. Krasnopolsky, (1998) suggests f is only 0.02 thus I shall use both these values in the modelling.

The modelled fractional loss of hydrogen can also be used to estimate the size of the initial and present reservoirs. For a given escape rate and fractionation factor, the change in D/H ratio is related to the size of the reservoir e.g. a smaller change in R requires a larger reservoir. The size of the reservoir is 1/(R-1) (Donahue, 1995). Modelling this and varying the fractionation factor and loss rates gives the range of reservoir sizes presented in table 10.1. Scenario 1 is the simplest possible case for Mars, where the present day δD +4200‰ has been acquired continuously over the past 4.5Ga with an initial complement of δD 0‰. Scenario 2 has a constraint of an atmospheric δD value of +500‰ at 4.0Ga as inferred from ALH84001 carbonate data.

Table 10.1: modeled initial and current water reservoirs on Mars in terms of m of water equivalent over planet surface

Scenario	Loss rate ($cm^{-2} s^{-1}$)	F	Initial reservoir (m)	Current reservoir (m)
1	2.4×10^{8}	0.32	5.6 (4.5Ga)	0.5
2	2.4×10^{8}	0.32	9.8 (4.0Ga)	0.9
1	2.4×10^{8}	0.02	6.3 (4.5Ga)	1.2
2	2.4×10^{8}	0.02	20.0 (4.0Ga)	1.8
1	2.4×10^{10}	0.32	560 (4.5Ga)	50
2	2.4×10^{10}	0.32	980 (4.0Ga)	90
1	2.4×10^{10}	0.02	630 (4.5Ga)	120
2	2.4×10^{10}	0.02	2000 (4.0Ga)	180

Thus one can calculate that with δD +500‰ at 4Ga and a δD +4200‰ today, the initial volatile reservoir would be 1-3 times greater than if δD +4200‰ enrichment occurred steadily over time from a value of δD +0‰ at 4.5Ga, depending on f. Given the likelihood of a more massive atmosphere with a higher water content in the past, current loss rates can be assumed to provide a lower limit for volatile reservoirs of 5.6m initially and 0.5m now, which increases to 9.8m and 0.9m respectively if scenario 2 is realistic. The size of the reservoir will have importance for evolution of oxygen, as the initial size will, for a given loss rate, determine the percentage loss of oxygen and hence the extent of fractionation this loss will impose. This will be discussed in detail later, in the discussions on oxygen evolution.

If we take into account hydrogen exchange and fractionation with the surface, the time evolution of atmospheric hydrogen becomes:

$$\frac{[H(t_1)]}{[H(t_2)]} = \left(\frac{R(t_2)}{R(t_1)} \right)^{\frac{\phi_1+\phi_2}{(1-f_1)\phi_1+(1-f_2)\phi_2}}$$

(Ghosh and Mahajan, 1998)

where ϕ_1 is upward escape flux of H and ϕ_2 is downward flux of H (surface sink) and f_2 is the surface fractionating factor (0.79 for H_2O ice / vapour 0.93-0.98 for clay (Yung *et al.*, 1988). Combining the equation above with 1/(R-1) gives plausible initial and current reservoirs for volatiles on Mars (figure below). Important factors to note are that a surface flux term reduces the size of reservoirs because fractionation with the surface favours sequestration of the light isotope into the regolith (as with brucite) thus the atmosphere is enriched in D relative to a situation with no surface flux. Many of the parameters are unknown: the major conclusion from figure 10.1 is that Martian H_2O reservoirs could have initially been anything from <1m global coverage to several thousand m of global coverage.

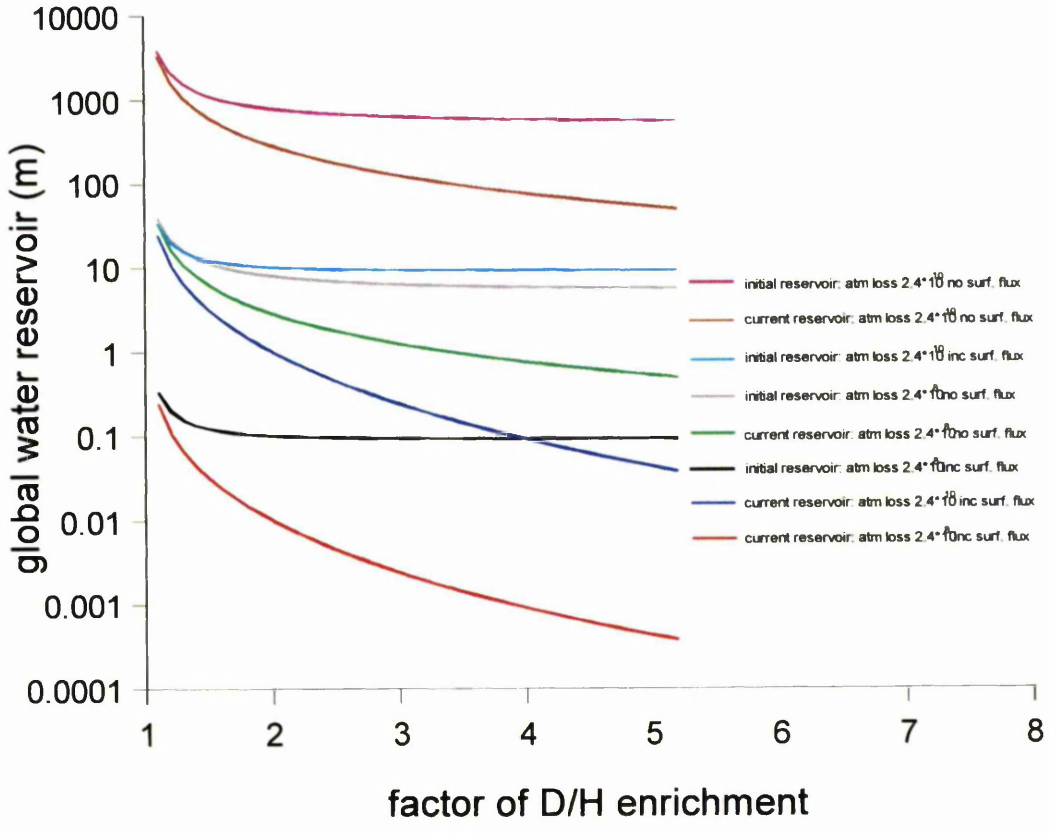

Figure 10.1: global reservoirs for water on Mars assuming fractionation during atmospheric escape f_1=0.32 and surface fractionation f_2=0.85. Surface flux is $1*10^9$ cm^{-2} s^{-1}, for a range of enrichments (5.2 if initial D/H is terrestrial D/H).

All the above calculations assume that the only loss process is thermal escape. Thermal escape may have been the most important loss process of the past 4Ga but with the enhanced UV from the early Sun and a more substantial atmosphere, hydrodynamic escape was likely to have been the principle means of atmospheric loss to space pre 4Ga.

In contrast to D/H fractionation during atmospheric (thermal) escape which has a value (f) between 0.02 and 0.32, hydrodynamic escape is estimated to have a fractionation factor of 0.8-0.9 (Zahnle *et al.*, 1990). Using a fractionation factor of 0.8 and the method employed by Donahue (1995), fractionation from 0‰ to 500‰ over the

first 5×10^8 yrs requires 99% loss of the initial hydrogen complement. Here we treat all hydrogen as one reservoir by assuming continuous degassing of water from the crust with no isotopic fractionation. This is different to the surface flux fractionation during mineral exchange which is invoked as an important process later in Martian history (figure 10.1).

Using current thermal loss rates and the constraint evolution from 0‰ at 4.5Ga to +500‰ at 4.0Ga, it has been calculated that hydrogen inventories at 4.0Ga were approximately 10m global water (table 10.1) Combining 99% hydrogen loss by hydrodynamic escape up to 4.0Ga with a reservoir at 4.0Ga of ~10m gives an initial value at 4.56Ga between 1000m and 10000m global depth of water. This is similar to the global loss of water inferred from geomorphology (e.g. Carr, 1996). Clearly few constraints can be placed on the size of the Martian reservoir from D/H analyses because the rate of loss processes greatly outweighs constraints from volatile evolution in Martian meteorites. Early thermal loss rates and the relative importance of surface interactions can vary absolute volumes of water by several orders of magnitude. In addition, the importance of hydrodynamic loss in the first few hundred million years is poorly constrained, and may increase the initial reservoir inferred from thermal loss by at least another order of magnitude.

Another problem arising from D/H modeling is that the initial complement of D/H on Mars is unknown. Analysis of primary water-rich apatites in QUE94201 (Leshin *et al.*, 2000) suggests mixing between the present day elevated atmospheric ratio of +4200‰ and an elevated mantle component of approximately +1000‰. This hypothesized mantle enrichment may have been generated by deuterium enriched cometary (Owen, 2000) material circulated deep into the crust by subduction or impact. If the initial complement of Martian D/H was found to be elevated initially, this would

reduce the amount of hydrogen loss required to produce present day D/H ratios by a factor of 2-3 (Leshin *et al.*, 2000) and would make water reservoir estimates based on D/H evolution from 4.5Ga to 4.0Ga (described here) incorrect. Indeed, if an initial magmatic value of δD +1000‰ did exist, generation of +500‰ in rosettes and Ca-rich carbonates with ages <4.0Ga from a global hydrogen reservoir is problematic.

10.3 Oxygen

The carbonates I shall first consider are rosettes of isotopic composition $\delta^{18}O$ +5‰ to +22‰ and Ca-rich carbonate of isotopic composition $\delta^{18}O$ -10‰ to +14‰.

10.3.1 Initial outgassing to produce global hydrosphere

A useful starting point in attempting to interpret information about the Martian hydrosphere and atmosphere and the formation conditions of ALH84001 carbonate is to calculate the range of $\delta^{18}O$ values of H_2O that may have existed on early Mars. A common model, devised by Clayton and Mayeda (1988) and used by many workers (Romanek et al., 1994; Wright et al., 1992; Leshin et al., 1998; Saxton et al., 1998) invokes planetary outgassing of a high temperature (1000°C) CO_2-H_2O fluid in which the CO_2-H_2O components are in equilibrium with each other and the Martian silicate crust. On cooling, the CO_2 and H_2O components are envisaged to remain well mixed and in isotopic equilibrium with each other but decoupled from the silicate. At 1000°C, $\delta^{18}O$ of H_2O is +6.4‰ and the corresponding CO_2 is +8.5‰ when in equilibrium with silicate of +4.6‰ (for ALH84001) (Shearer et al., 1999). An early estimate of X=0.8 (where X is the mole fraction H_2O in the fluid) was invoked by Clayton and Mayeda (1988) to account for low temperature 0°C deposition of $\delta^{18}O_{V\text{-}SMOW}$ +21‰ carbonate in EETA79001 (table 10.2).

Table 10.2: Range of $\delta^{18}O$ in CO_2 and H_2O using different outgassed amounts of CO_2 and H_2O

X	$\delta^{18}O_{V\text{-}SMOW}$ of H_2O at 0°C	$\delta^{18}O_{V\text{-}SMOW}$ of CO_2 at 0°C
0	–37.6	8.5
0.1	–33.2	12.9
0.2	–28.8	17.3
0.3	–24.4	21.7
0.4	–20	26.1
0.5	–15.6	30.5
0.6	–11.2	34.9
0.7	–6.8	39.3
0.8	–2.4	43.7
0.9	2	48.1
1	6.4	52.5

The $\delta^{18}O$ difference between CO_2 and H_2O reservoirs in equilibrium is temperature dependent and given by:

$$1000\ln\alpha_1 = \frac{-0.0206\times10^6}{T^2} + \frac{17.9942\times10^3}{T} - 19.97 \qquad (1)$$

where T is temperature in Kelvin (Friedman and O'Neil, 1977).

This relative difference can be used to produce an absolute $\delta^{18}O$ value for H_2O for a given temperature as a function of X (mole fraction of H_2O in the fluid), using:

$$\delta^{18}O_{water} = 6.4X - (6.4 - (\delta^{18}O_{CO_2} - \delta^{18}O_{H_2O}))(1-X) \qquad (2)$$

(Wright *et al.*, 1992), where $1000\ln\alpha_1$ from equation is $\delta^{18}O_{CO2} - \delta^{18}O_{H2O}$ in equation 2.

Once $\delta^{18}O$ of the source fluid has been derived, one can then calculate the equilibrium fractionation between the fluid and the carbonate precipitating out of that fluid. This is also dependent on temperature and cation chemistry of the carbonate. Fractionation

factors for the types of carbonate present in ALH84001 are shown in equations (3) to (7), where $1000\ln\alpha_2$ denotes the fractionation between a carbonate and H_2O.

$$1000\ln\alpha_2 = \frac{3.14\times10^6}{T^2} - 2.00 \qquad \text{(dolomite)} \qquad (3)$$

$$1000\ln\alpha_2 = \frac{3.13\times10^6}{T^2} - 3.5 \qquad \text{(siderite)} \qquad (4)$$

$$1000\ln\alpha_2 = \frac{2.78\times10^6}{T^2} - 2.89 \qquad \text{(calcite)} \qquad (5)$$

$$1000\ln\alpha_2 = \frac{2.95\times10^6}{T^2} - 2.16 \qquad \text{(magnesite)} \qquad (6)$$

$$1000\ln\alpha_2 = \frac{2.78\times10^6}{T^2} + 0.11 \qquad \text{(ankerite)} \qquad (7)$$

Ankerite is used in modelling as the precipitated carbonate because the low $\delta^{18}O$ values with which most of the modelling is concerned are ankerite-calcite carbonates. Also the fractionation factor for ankerite-water is slightly greater than for calcite-water, thus any model which explains ankerite formation will also be applicable to calcite (figure 10.2).

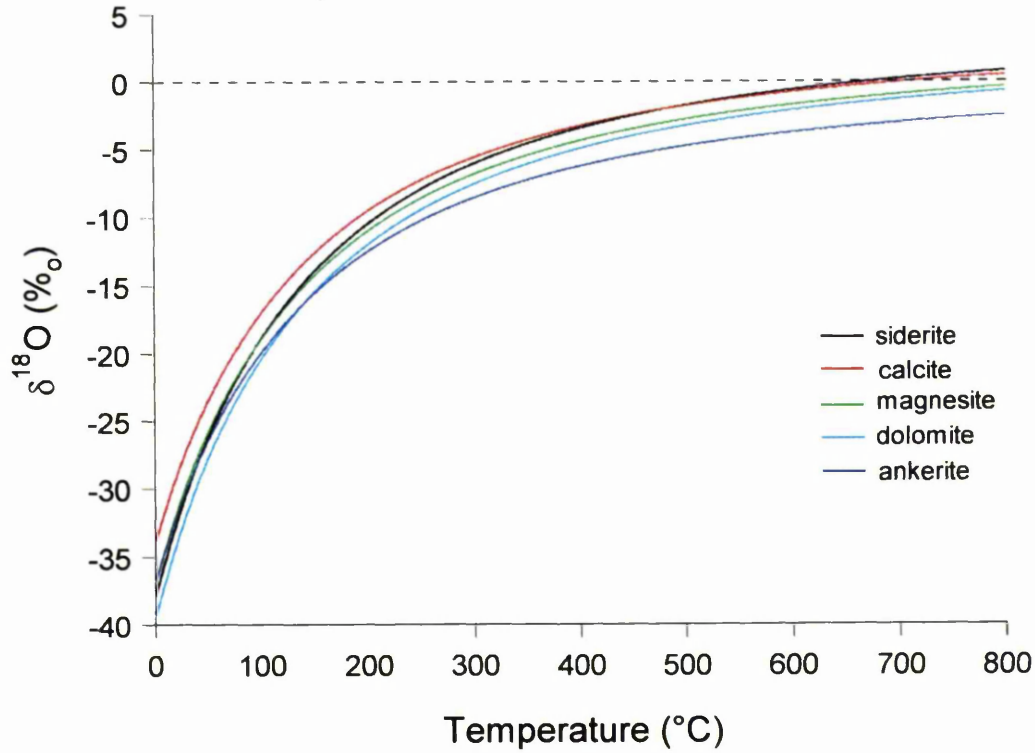

Figure 10.2: carbonate-water fractionation factors, expressed as $\delta^{18}O$ of H_2O in isotopic equilibrium with 0‰ carbonate (horizontal dashed line). Fractionation factors from Friedman and O'Neil (1977); Aarhon (1988); Chacko *et al.*, (1991)

10.3.2 Low temperature open systems, no silicate equilibrium

First I shall model a scenario in which an outgassed CO_2-H_2O hydrosphere is circulated through the crust in a low to medium temperature hydrothermal environment. If we assume 0°C CO_2-H_2O equilibrium after outgassing with X=0.8 (initial $\delta^{18}O_{CO2}$ +43.7‰, $\delta^{18}O_{H2O}$ –2.4‰ see table 10.1) followed by heating and precipitation in an open system, the ankerite precipitated from fluids of 0-500°C for all values of X is given by figure 10.3.

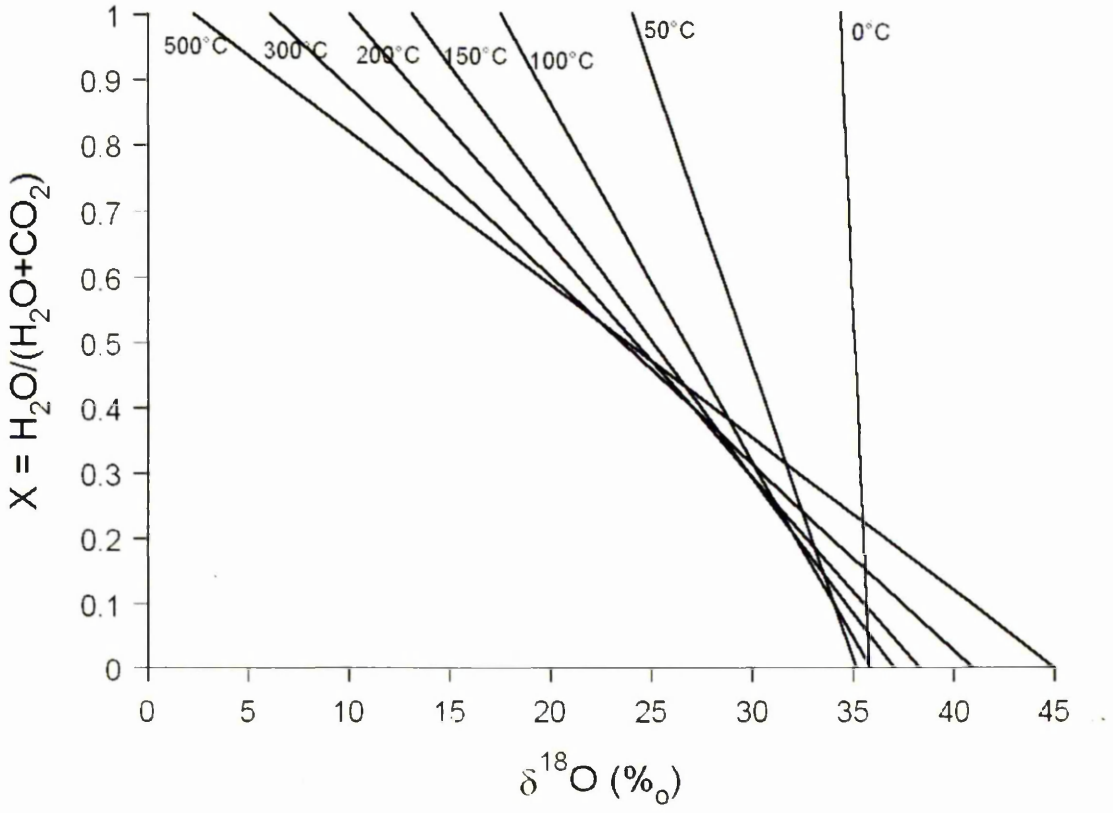

Figure 10.3: $\delta^{18}O$ of ankerite formed under a range of temperature and values of X.

This model is clearly capable of producing heavy carbonate as observed by Saxton *et al.* (2000) from CO_2 rich fluids over a large range of temperatures or, as is more likely for Nakhlites given the extent of hydrothermal alteration, a cool H_2O rich fluid. What is more difficult to produce is carbonate lighter than approximately +5‰ as observed in rosette cores. Therefore this model can explain all Martian carbonate except the very light Ca-rich carbonate.

10.3.3 Open systems after silicate equilibrium

If it is not possible to derive -10‰ carbonate from cool fluids isotopically isolated from the crust (an unfractionated global hydrosphere), could it be possible to generate this carbonate from fluids which have equilibrated isotopically with crustal silicate after formation of a global hydrosphere? This may be possible, although unlikely, in super-heated hydrothermal systems. Pyroxene, the dominant (95%) phase

in ALH84001, has a $\delta^{18}O$ of +4.6‰ (Shearer *et al.*, 1999). Fractionation between pyroxene and a CO_2-H_2O fluid at temperatures considered sufficient to allow isotopic equilibrium to be attained e.g. 1000°C (Clayton and Mayeda, 1988) would produce CO_2 of +8.5‰ and H_2O 6.4‰. Figure below, shows that $\delta^{18}O$ of carbonate produced from such a fluid as a function of temperature and relative proportion of H_2O and CO_2 is still limited to >0‰, therefore high temperature equilibrium cannot explain the $\delta^{18}O$ values of Ca-rich carbonate.

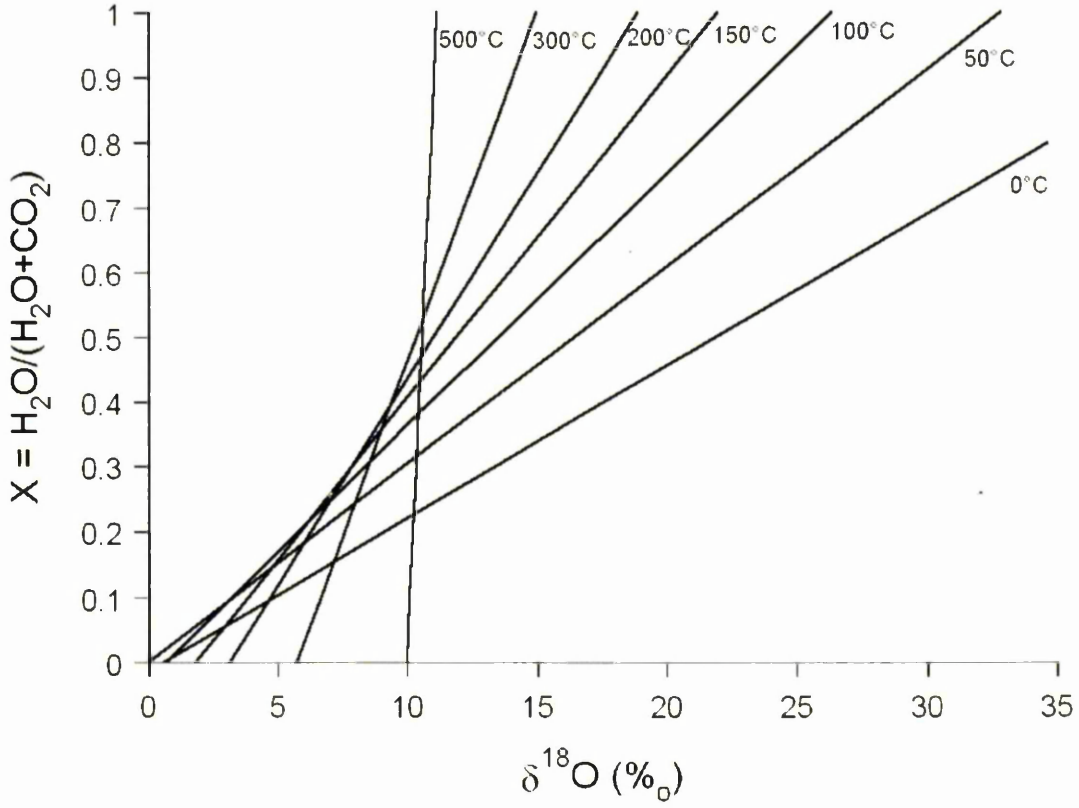

Figure 10.4: $\delta^{18}O$ of carbonate from an H_2O-CO_2 fluid after high temperature equilibrium with silicate

One may argue that this model can be ruled out on other grounds: namely a preservation of a positive $\Delta^{17}O$ in ALH84001 carbonate. $\Delta^{17}O$ measurements of water extracted from ALH84001 yielded values of +0.8‰ (Karlsson *et al.*, 1992) relative to

the terrestrial fractionation line (T.F.L.) and measurements of CO_2 from ALH84001 carbonates (Farquhar *et al.*, 1998) of +0.6 to +0.9‰ relative to T.F.L. (Farquhar and Thiemens, 2000). A high temperature environment leading to fluid-silicate isotopic equilibrium would have reset all $\Delta^{17}O$ values to +0.3‰. However, given the rarity of Ca-rich carbonate and the apparently unique textures and $\delta^{18}O$ values observed here, it is possible that the Ca-carbonate does not contribute to the $\Delta^{17}O$ anomalies and may conceivably have a $\Delta^{17}O$ of +0.3‰.

10.3.4 High temperature pyroxene-carbonate exchange

Another possible consequence of a high temperature environment is equilibration of carbonate and pyroxene, i.e. isotopic exchange after carbonate formation rather than isotopic alteration of the source fluids. Thus, it is necessary to consider the effects of isotopic equilibration with silicate on bulk carbonate isotopic composition. Orthropyroxene, constituting 95% of ALH84001, has $\delta^{18}O_{SMOW}$ +4.6‰ (Shearer et al., 1999).

Using the calcite-pyroxene fractionation factor from Chiba *et al.*, (1989):

$$1000\ln\alpha = \frac{2.37\times10^6}{T^2}$$

formation of carbonate at 500°C in equilibrium with pyroxene of +4.6‰ would yield carbonate of ~+8‰ C (or ~+6.5‰ at 700°C).

Closure temperatures for pyroxene crystals in geological environments are in the region 500-600°C (Cherniak, 2001). Diffusion rates for Ca in diopside (Dimanov *et al.*, 1996) and O in diopside (Ryerson and McKeegan, 1994) in figure 10.5 show that diffusion in pyroxene is feasible over hydrothermal timescales of 1000yrs (Gulick, 1991). Diffusion of cations and anions in carbonate is several orders of magnitude faster than pyroxene (Fisler and Cygan, 1998), hence pyroxene diffusion determines the

rate of exchange. Clearly prolonged high temperature deposition would remove isotopic heterogeneity observed between the inner Mg-rich region of +22‰ and the Ca-rich region of ~0‰ only 10μm apart. In addition the chemical heterogeneity between the inner-Mg rich region and the Ca-rich regions would also be erased so I conclude that carbonate assemblage (rosettes and Ca-rich carbonate) has not been heated during or subsequent to the formation of the Ca-rich carbonate.

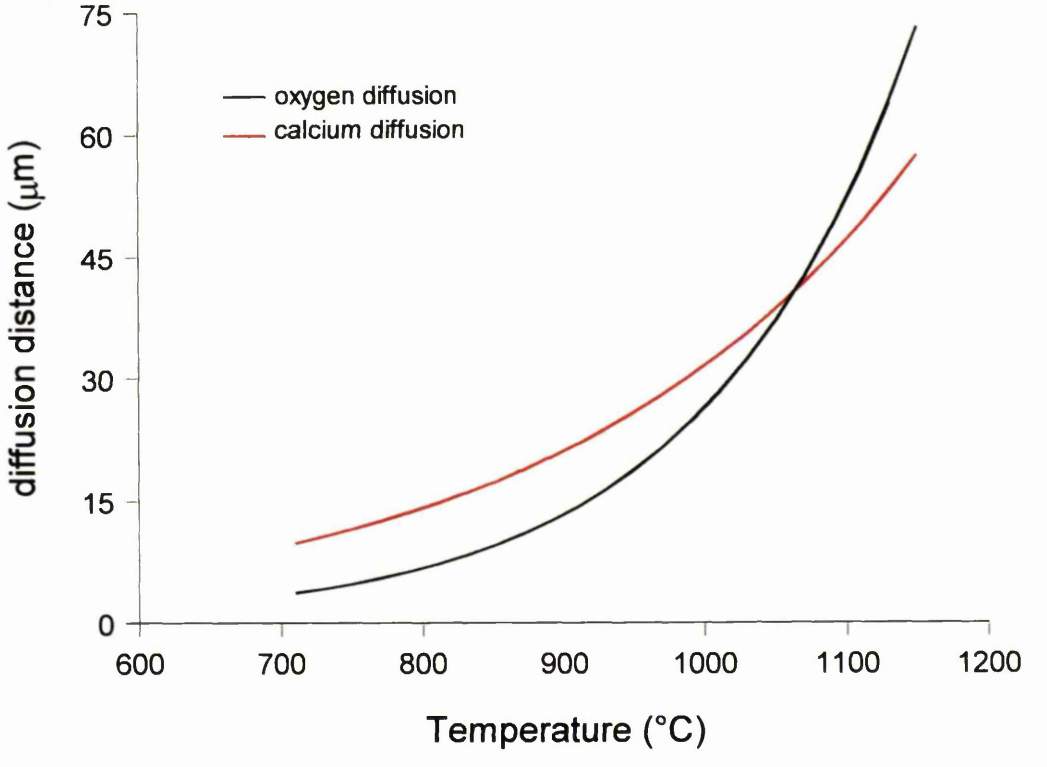

Figure 10.5: diffusion (per 1000yrs) of O and Ca in pyroxene

10.3.5 Shock mobilisation

Rapid deposition from a shock mobilized CO_2-rich impact melt has also been suggested as a possible origin for ALH84001 carbonate (Scott *et al.*, 1997; 1998a; 1998b). Although this model was invoked to explain texture observed in carbonate of rosette composition, this idea might be applicable to the (apparently later) Ca-rich carbonate presented here. Also, the impact model has been extended and amalgamated

with an evaporite model (Warren, 1998; McSween and Harvey, 1998) by hypothesizing a remobilized surface carbonate deposit (Scott *et al.*, 1999). Is it possible to remobilize and redeposit rosette carbonate to produce the Ca-rich generation carbonate? With an average $\delta^{18}O$ for ALH84001 carbonate between +15‰ (Jull *et al.*, 1997) and +19‰ (Romanek *et al.*, 1994) and no kinetic fractionation, the answer is no: the heaviest measured carbonate from the Ca-rich carbonate generation is +14‰ which is still lighter than the lightest average estimate of rosettes. However, if remobilization of rosette carbonate is accompanied by CO_2 devolatilisation then kinetic fractionation may occur (Martinez *et al.*, 1994). According to Grahams law, if either CO_2 or the CO_3^{2-} ion are mobilized, the maximum possible fractionation effect is given by the square root of the mass difference thus, for CO_2 and CO_3^{2-}, kinetic fractionation leads to enrichment of the light isotope in the product of, at most, 16‰ and 22‰ respectively. This means that remobilized, devolatilised rosette carbonate could possess an average $\delta^{18}O$ of approximately -2‰ (17‰ average rosette carbonate minus 19‰ for remobilization of CO_2-CO_3^{2-} mixture)(figure 10.7). On cooling, this CO_2 fluid fractionates as observed in the figure below:

$$1000\ln\alpha = \frac{1.0611\times10^4}{T} - \frac{1.8034\times10^6}{T^2} - 3.2798$$

If carbonate was redeposited as it cooled to, for example, from 1000°C, the first carbonate to form would have a $\delta^{18}O$ of approximately -5‰ to -9‰. Thus it appears that mobilization and volatilization of rosette carbonate can provide the very light carbonate observed here. If mobilization did occur, it is likely that the CO_2 fluid was a CO_2 liquid or CO_2 supercritical fluid. The fractionation factor used here is gaseous CO_2-calcite but this is still valid as supercritical CO_2 behaves very similarly to vapour CO_2 (Rosenbaum, 1997).

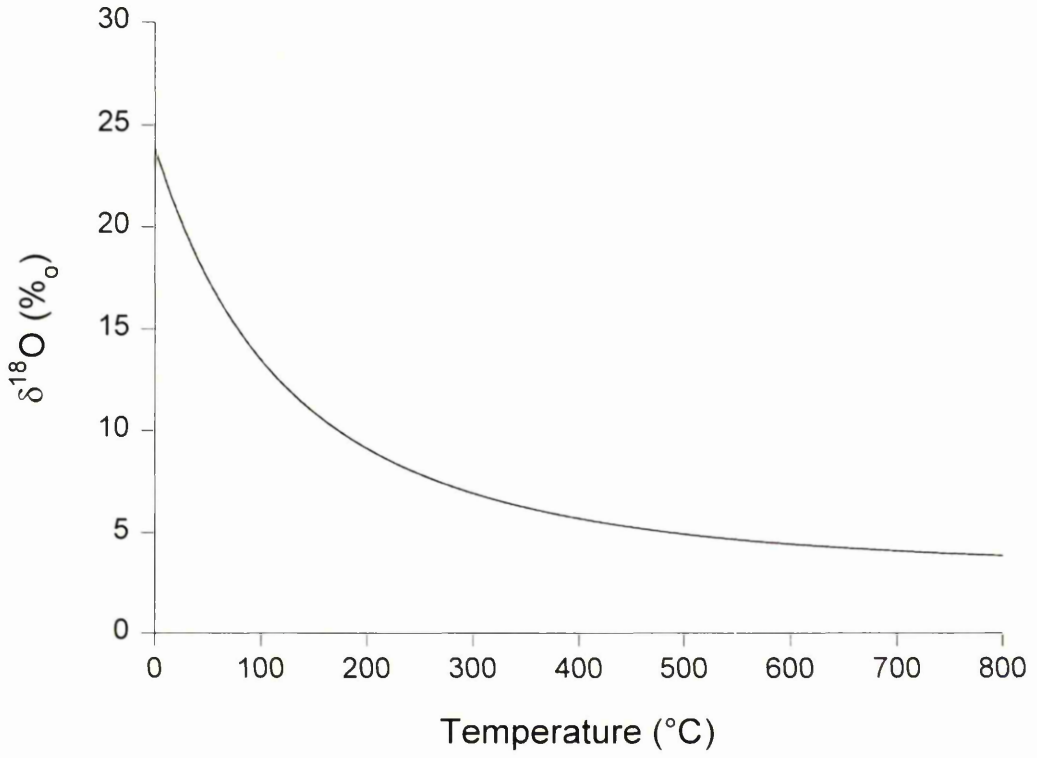

Figure 10.6: $\delta^{18}O$ of CO_2 fluid required to produce 0‰ calcite (Bottinga, 1968).

It is likely that shock mobilization acts as a closed system, in the sense that mobilized carbonate will reprecipitate without interaction with others fluids. This results in the average $\delta^{18}O$ of the remobilized carbonate equaling the average $\delta^{18}O$ of the carbonate prior to mobilisation. The figure below shows the isotopic evolution of the remobilized CO_2 in this closed system as defined by Rayleigh. In contrast to oxygen isotopic zoning of rosettes, there is similarity between theoretical isotopic zoning from Rayleigh fractionation and the observed zoning of the Ca-rich generation of carbonate.

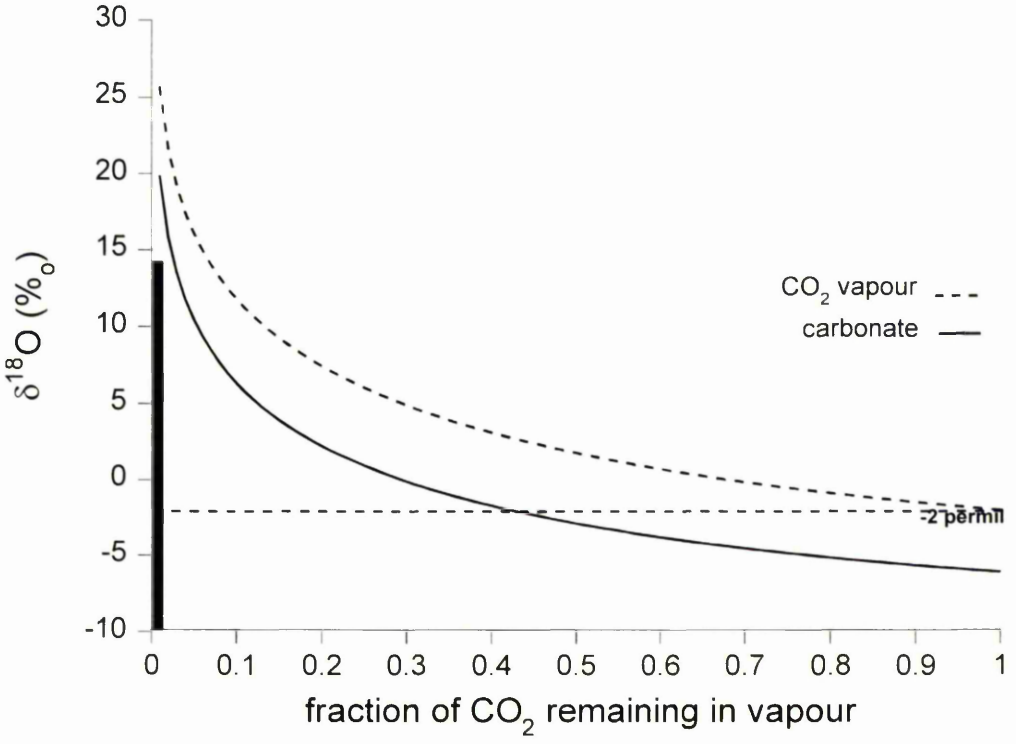

Figure 10.7: $\delta^{18}O$ of carbonate in a closed system from CO_2 vapour of initial composition $\delta^{18}O$ -2‰ (+17‰ rosette average – 19‰ maximum kinetic fractionation). Cooling from 1000°C to 700°C occurs during deposition. Black bar to left indicates $\delta^{18}O$ variation of Ca-rich carbonate generation.

Although shock mobilization may be plausible, textural features suggest this origin is unlikely. As noted in chapter 8, the embayed nature of the pyroxene-carbonate boundary and the apparent partial replacement and resorption of carbonate rosette fragments by Ca-rich carbonate is indicative of a slow, low temperature precipitation process from circulating fluids.

Also, the above model uses the maximum possible fractionation effect. A terrestrial example of shocked carbonate from Haughton crater exhibits $\delta^{18}O$ approximately 5‰ below similar but unshocked carbonate, and even this 5‰ reduction may have been due to high temperature equilibrium with quartz (Martinez *et al.* 1994).

In contrast, recent work (Skála and Žák, 2001) suggests the kinetic effect may reduce $\delta^{18}O$ of carbonates by as much as 20‰.

In addition these samples show none of the dendritic textures and highly vesiculated SiO_2 glass found in terrestrial carbonate-pyroxene impact melts (Martinez *et al.*, 1994) or the emulsion textures of silicate glass embedded in carbonate observed by Graup (1999) in Ries crater carbonates.

Finally, figure 10.7 shows that although <0‰ carbonate may be possible initially, a function of the closed system model is that the final average must equal that of the starting composition (-2‰), which is clearly not the case from ion probe data. Similarly, CO_2vapour-carbonate fractionation requires that 70% of the Ca-rich carbonate is precipitated with <0‰. The samples indicate carbonate <0‰ composes <10% of the Ca-rich carbonate generation.

10.3.6 Low temperature open systems revisited

In the first model, we assumed 0°C equilibrium temperature for a CO_2-H_2O fluid after outgassing with X=0.8, as this was used to explain +21‰ carbonate in EETA79001 and is therefore also applicable to +25‰ carbonate rosettes. However, this model is capable of producing carbonate of +35‰ (Clayton and Mayeda, 1988). If an initial outgassing value of X=0.5 is used, lighter carbonates can be generated (figure 10.8). With a revised value for X, it is now possible to precipitate -10‰ carbonate from a global hydrosphere at temperatures below high temperature equilibrium with silicate.

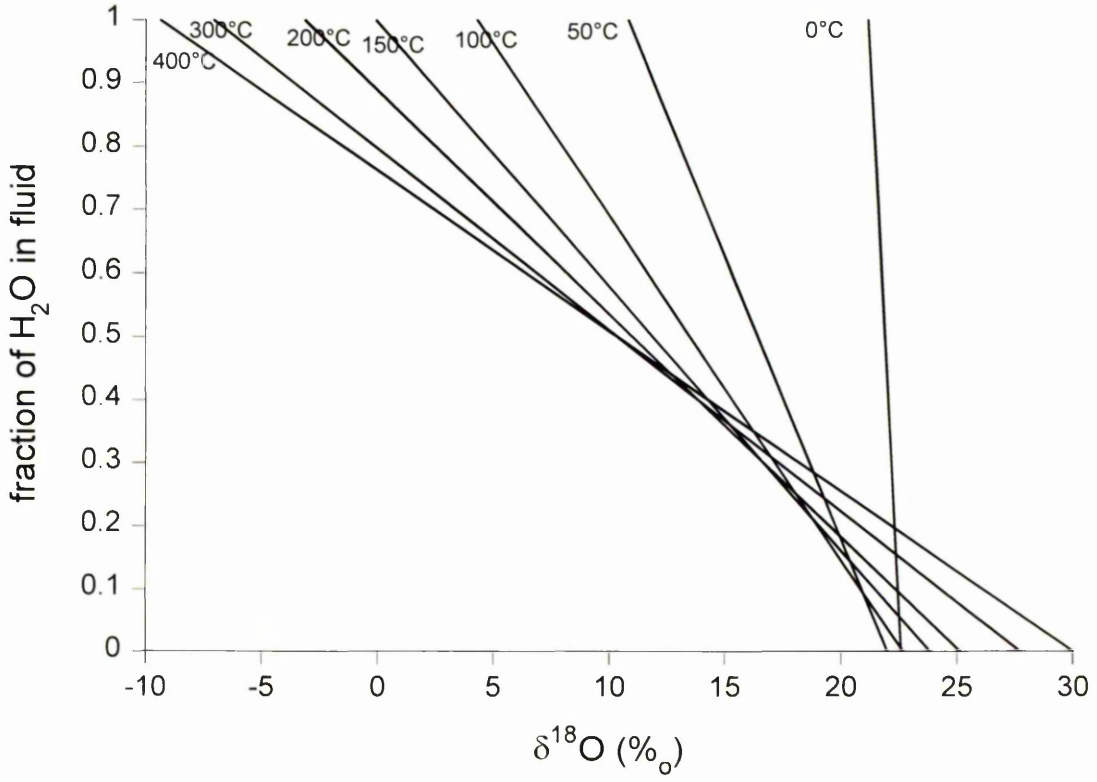

Figure 10.8: $\delta^{18}O$ of ankerite from H_2O-CO_2 fluid after outgassing with X=0.5

Thus far I have posed the question whether outgassed fluids, following isotopic re-equilibration over a broad range of temperatures, can provide plausible fluid reservoirs for formation of ALH84001 carbonate as light as $\delta^{18}O$ -10‰. We have demonstrated that these reservoirs cannot produce -10‰ carbonate without further fractionation unless X<0.5. Shock mobilization of pre-existing carbonate may provide a suitable source but textural evidence and the average isotopic composition of the Ca-rich carbonate suggests otherwise. Therefore I now discuss different models with a view to generating a suitable source fluid for these carbonates.

10.3.7 Atmospheric fractionation and loss processes

The $\delta^{18}O$ of CO_2 in the current Martian atmosphere is not well constrained, with estimates varying from $\delta^{18}O$ +20‰ ±50‰ (Nier and McElroy, 1977) obtained by Viking to $\delta^{18}O$ -80‰ ±35‰ (Bjoraker *et al.* 1989) and $\delta^{18}O$ -130‰ ±80‰ (Krasnopolsky, 1996) inferred from Earth based spectroscopy, the latter two requiring a substantially ^{18}O depleted Martian atmosphere. Given that initial outgassing for all values of X (table 10.2) suggest a significant ^{18}O enrichment in CO_2 and fractionation between $CO_2(s)$–$CO_2(g)$ (Eiler *et al*, 2000), $CO_2(g)$-carbonate (Bottinga, 1968) and loss processes to space all lead to ^{18}O enrichment in the gaseous form, it seems that buffering of the atmosphere by substantial regolith / polar cap reservoirs has occurred throughout Martian geological history.

One of the principal mechanisms for isotopically fractionating volatiles is gravitational separation followed by non-thermal loss due to, for example, photo-dissociative reactions. This can be represented as:

$$\alpha = \exp\left(\frac{(m_1 - m_2)gh}{kT}\right)$$

(Saxton *et al.*, 2000) where:

α is the isotopic ratio of the species being lost from the atmosphere (above the turbopause) divided by the isotopic ratio of the species in the lower atmosphere (below the turbopause).

h is height above the turbopause, m is mass in a.m.u.

Assuming that this fractionated atmosphere is well mixed with the non-atmospheric reservoir, fractionation of the whole system follows Rayleigh distillation, giving:

$$R/R_0 = f^{(\alpha-1)}$$

where R is $^{18}O/^{16}O$ (or $^{18}O/^{17}O$). Converting this to permil deviation from the terrestrial standard, Standard Mean Ocean Water (SMOW), the fractionation of the reservoir is given by:

$$\delta^{18}O = 1000 \times \left[f^{(\alpha-1)} - 1 \right]$$

The mass dependent relationship between $\delta^{17}O$ and $\delta^{18}O$ is therefore:

$$\delta^{17}O_f = 1000\left[\left(\delta^{18}O/_{1000}\right)+1\right]^{0.516} - 1000$$

and deviation from equilibrium fractionation is:

$$\Delta^{17}O = \delta^{17}O - \delta^{17}O_f$$

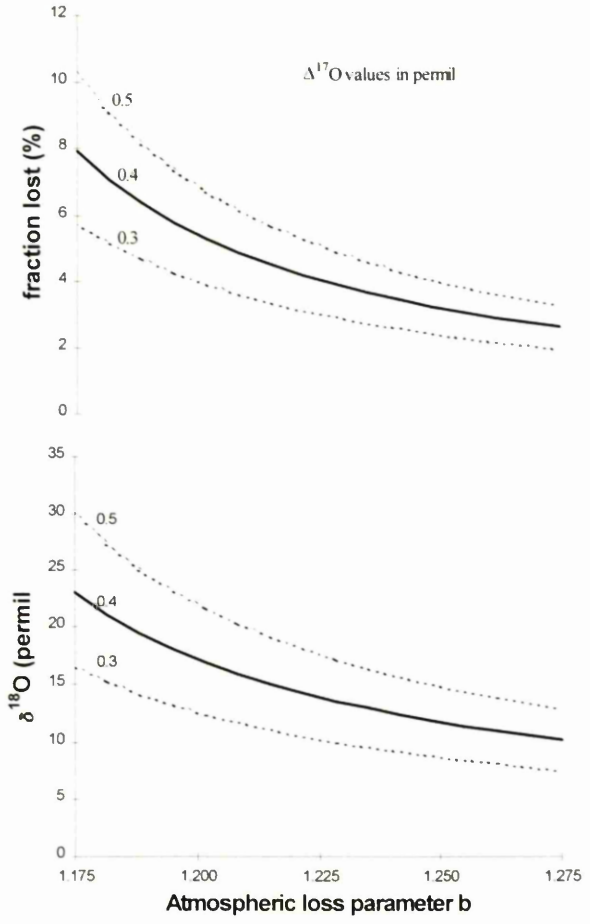

Figure 10.9: isotopic evolution of Martian atmosphere during Jeans escape of dissociated H_2O and CO_2

Table 10.3: the wide range of estimates of global water inventories on present-day Mars

Author	Basis of estimate	global water (m)
Donahue (1995)	D/H	0.5
Using ALH84001 data (earlier this chapter)	D/H	0.5-0.9
Clifford (1993)	regolith capacity	<1000
Ghosh and Mahajan (1998)	D/H	1-1000

Clearly the discrepancy between estimates of original volatile inventory is huge: 2-3 orders of magnitude, which makes estimating the fractional atmosphere loss (figure 10.9) difficult. Added to this is the two order of magnitude variation in the estimation of loss rates. Using the modelling of Ghosh and Mahajan (1998), percentage atmospheric loss could vary from approximately 1% to >95% and the corresponding $\delta^{18}O$ enrichment, anything from 2‰ to >1000‰.

Perhaps a better indicator of atmospheric loss is the $\Delta^{17}O$ value. In contrast to the $\delta^{18}O$ value, which can be altered by mineral formation and water-rock interaction, $\Delta^{17}O$ remains unaffected by these processes at low temperatures (with the exception of photochemical processes to be discussed later). If we assume that the atmosphere-hydrosphere at 4.5Ga had the same $\Delta^{17}O$ value as the bulk planet (+0.3‰) then enrichment in secondary minerals (and water) preserved in Martian meteorites may provide some constraints on atmospheric loss.

Table 10.4: the $\Delta^{17}O$ of a several secondary minerals. Data from Karlsson *et al.*, (1992); Farquhar and Thiemens (2000)

Meteorite and phase	Age of phase (Ga)	$\Delta^{17}O$ (‰)
ALH84001 carbonate	3.9	0.8
Nakhla carbonate	<1.3	1.05
Lafayette carbonate	<1.3	0.75

The first constraint is provided by $\Delta^{17}O$ in ALH84001. Assuming atmospheric loss as the cause of the anomaly, $\Delta^{17}O$ of +0.8‰ (+0.5‰ above bulk) requires loss of ~4-10% of the atmosphere, depending on b, where b is the factor that expresses the change in relative abundance of different isotopes with height above the turbopause and any additional fractionation, arising, for example, from velocity differences associated with the photo-dissociation processes (see figure 10.4). This would also increase the $\delta^{18}O$ by 15-25‰. If modern loss rates of $2.4\times10^{8}cm^{-2}s^{-1}$ are similar to those between 4.5 and 4 Ga ago, this amounts to a loss of 1.14m in the first 0.5Ga requiring an initial reservoir between 11m and 28.5m. If loss rates were significantly greater during this early period, as would be expected of a more massive atmosphere, the initial reservoirs also increase by the same factor: for a two order of magnitude increase in the loss rate, the initial water reservoir would be 1100m – 2850m. This interpretation is complicated by a second atmospheric process that can alter $\Delta^{17}O$: photochemical production of O by O_3 or CO_2 photolysis and subsequent exchange with CO_2 (Farquhar and Thiemens, 1998), who have shown this process is capable of producing 0.5‰ increase in $\Delta^{17}O$ of the Martian atmosphere with only a 1‰ increase in $\delta^{18}O$, which they claim is more in keeping with the $\Delta^{17}O$ +0.8‰ in ALH84001 carbonates and relatively unenriched $\delta^{18}O$ of +5‰ to +24‰. Whilst providing useful constraints on the sizes of volatile reservoirs neither of these processes are capable of reducing $\delta^{18}O$ in the atmosphere and therefore cannot be invoked to explain the origin of the source of light Ca-rich carbonate.

10.3.8 Martian reservoir exchange

It is likely that the $\Delta^{17}O$ and $\delta^{18}O$ in ALH84001 carbonate reflect enrichment by Jeans escape and photolysis. However this does not detract from the importance of a second feature of the $\Delta^{17}O$ data: the lack of obvious enrichment post 4.0Ga. Given that in 500Ma, a $\Delta^{17}O$ signature is observed in ALH84001 carbonate, further enrichment

would be expected in the much younger Nakhla and Lafayette carbonate. The same may be true of the D/H ratios, although most δD measurements probably sample water associated with the meteorite, which does not necessarily bear any temporal relationship to the crystallisation age of the meteorite. Lack of evolution of $\Delta^{17}O$ may be explained by mixing of volatile sources, one with an atmospheric signature and a mantle component. Figure 10.10 (Farquhar and Thiemens, 2000) plots D/H against $\Delta^{17}O$. If atmospheric loss were a dominant process, increase in $\Delta^{17}O$ and in δD would be expected. However, for secondary minerals in Martian meteorites, the opposite is observed. This situation may be explained by mixing between water (high O and H content) and rock (high O low H content) to the extent where the silicate alters the oxygen isotopic composition but not the hydrogen isotopic composition of the water.

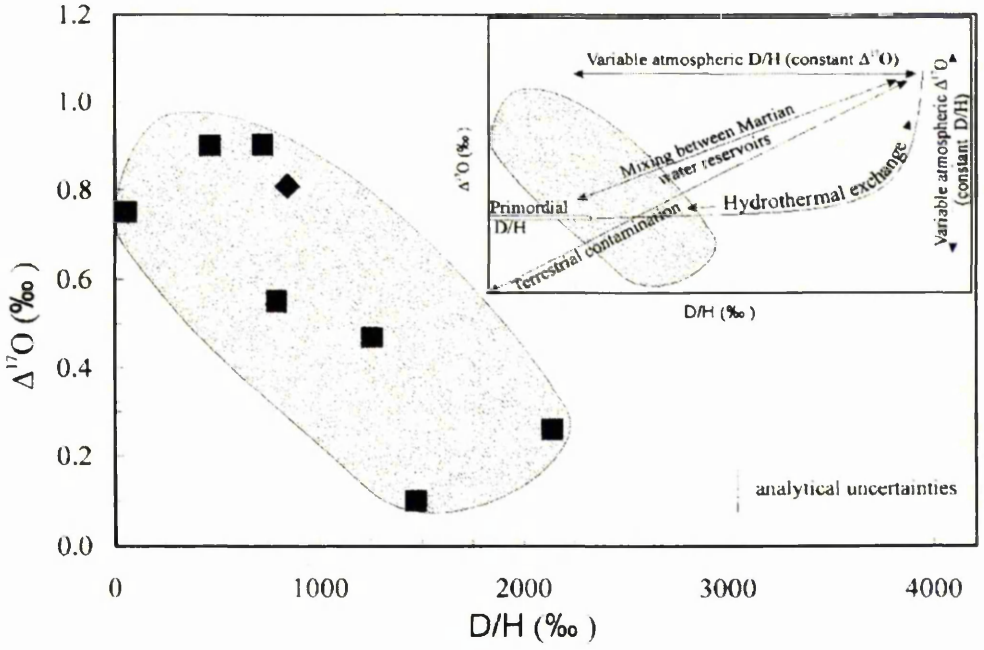

Figure 10.10: possible effects of water rock interaction on Mars (from Farquhar and Thiemens, 2000)

A second explanation for the minor evolution of $\Delta^{17}O$ over time is periodic resetting of the oxygen isotopic ratios. With igneous activity occurring relatively

recently (at least within the last few hundred million years) (Hartmann *et al.*, 1999) and related flooding events capable of supplying more volatiles than the entire Martian atmosphere (McKenzie and Nimmo, 1999), resetting of the atmospheric signature by magmatic outgassing and near surface melting appears feasible.

10.3.9 New models for formation of ^{18}O depleted reservoirs

10.3.9.1 CO_2 equilibration model

Section 10.3.4 described a model involving high temperature equilibrium of a H_2O-CO_2 fluid with the surrounding silicate, which then cooled prior to carbonate deposition. On cooling, oxygen isotope fractionation between H_2O and CO_2 permitted carbonate of between $\delta^{18}O$ ~0‰ and $\delta^{18}O$ ~40‰ to precipitate. If, however, we assume a CO_2 dominated environment (such as hydrothermally mobilised regolith CO_2) and permit high temperature silicate equilibrium followed by cooling, oxygen cannot partition between H_2O and CO_2. This prevents the increase in $\delta^{18}O_{CO2}$ which occurs during CO_2 – H_2O equilibrium. Using pyroxene-CO_2 fractionation factors of Bottinga and Javoy (1973; 1975) it is calculated that for temperatures between 600°C and 900°C, the CO_2 fluid will have $\delta^{18}O$ within 1‰ of the silicate, i.e. $\delta^{18}O_{CO2}$ will be between 3.5‰ and 5.5‰. Placing this CO_2 fluid in equilibrium with minimal amounts of water yields the range of $\delta^{18}O$ values in figure 10.11. Note that now, although negative $\delta^{18}O$ carbonates are possible, the range of $\delta^{18}O$ values is limited to approximately 10‰ (not ~25‰ observed in Ca-rich generation of carbonate) unless elevated temperatures are used, leading to the same problems of carbonate –pyroxene equilibration and removal of fine scale chemical zoning as noted earlier with high temperature deposition mechanisms for Ca-rich carbonate. However, the figure below shows that with fortuitous variations in temperature and X, the range of $\delta^{18}O$ observed in Ca-rich carbonates can be reproduced. $\Delta^{17}O$ measurements of the Ca-rich carbonate are a clear

goal for future ion microprobe analyses in order to determine if CO_2 - silicate isotopic equilibrium occurred in the source fluid of the Ca-rich carbonate.

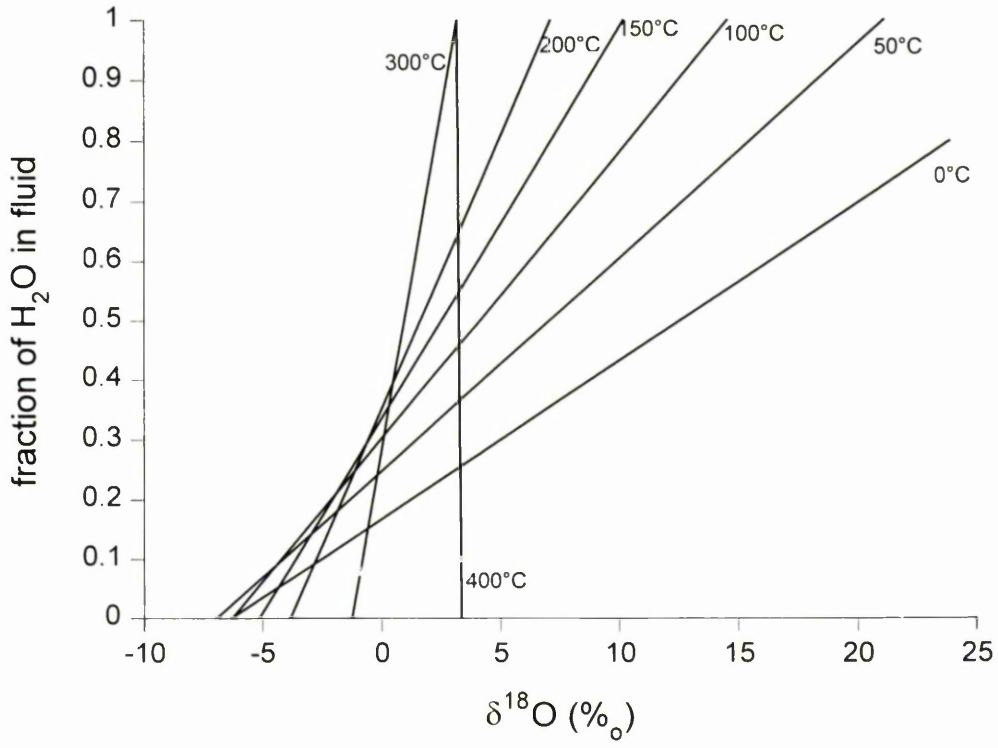

Figure 10.11: deposition of carbonate from CO_2 rich fluid after high temperature equilibrium with silicate but no H_2O-CO_2 equilibrium.

10.3.9.2 Meteoric fluids

If mixing of isotopically depleted and enriched reservoirs has occurred over a large percentage of Martian history, can it explain the observed $\delta^{18}O$ values? Although the composition, size and circulation of the early Mars atmosphere is not well constrained, many geological features strongly suggest a CO_2 dominated atmosphere of several bars which allowed liquid water at the surface. Early general circulation models (Haberle *et al.*, 1993) calculated that Mars has cross-equatorial zonal circulation from 30°S to 30°N with two roughly symmetrical Earth-like Hadley-Ferrel cells. Recent modeling (Wardle and Pierrehumbert, 2001) suggests that the width of the Hadley

circulation depends on the size and rotation rate but does not depend on the atmospheric gas constant (derived from density and composition of the atmosphere), which only affects Hadley cell intensity. Thus, for Mars, it is believed that an early, dense CO_2 atmosphere would have possessed less intense circulation but it would still have penetrated to high latitudes.

Thus it may be possible that with zonal circulation cells, evaporation/condensation cycles permitted significant isotopic fraction of oxygen with latitude, in a manner similar to that on Earth. Assuming typical Rayleigh distillation for a packet of water vapour of −2.4‰ (from planetary outgassing and cooling), the fractionation occurs as modeled below, meteoric water of −30‰ may be easily achievable (Antarctic ice can have $\delta^{18}O$ of −50‰).

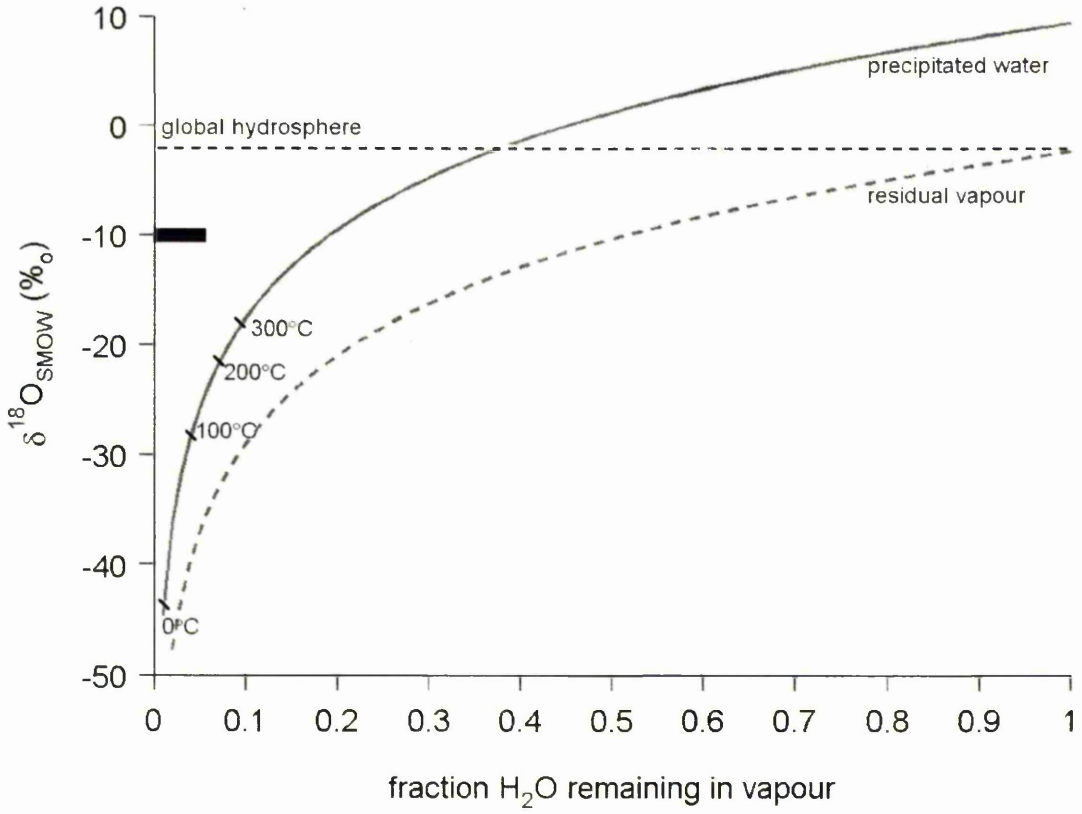

Figure 10.12: Rayleigh fractionation of water vapour with initial $\delta^{18}O$ –2.4‰ at 273 K. The black bar represents $\delta^{18}O$–10‰ Ca-rich carbonate. 0-300°C indicates the $\delta^{18}O$ of the precipitated water that will generate $\delta^{18}O$–10‰ carbonate at that temperature.

If this water (or ice) is trapped within the regolith, a later hydrothermal event can then remobilize (or melt) this isotopically isolated reservoir of $\delta^{18}O$ depleted water. Percolation of this water at or near the surface and mixing with atmospheric CO_2 supplies two $\delta^{18}O$ end member reservoirs of –30‰ and +44‰. For a range of temperatures and values of X, again assuming no silicate equilibrium, the carbonates indicated in figure below are possible.

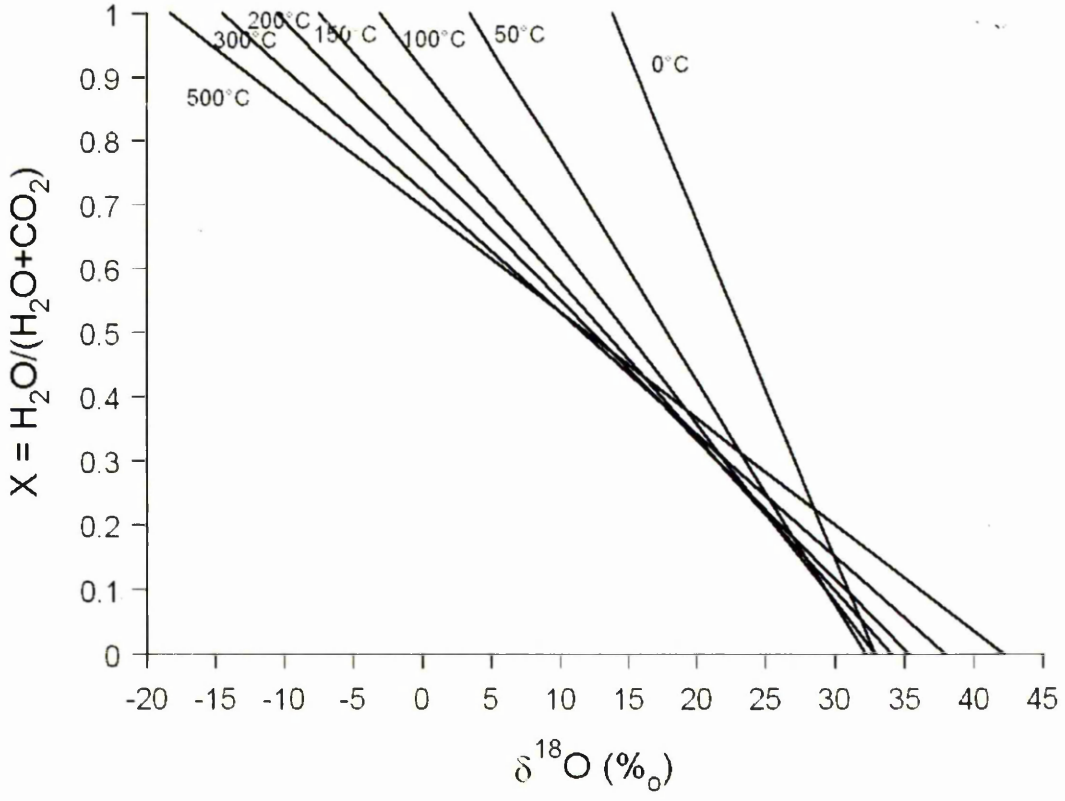

Figure 10.13: $\delta^{18}O$ of carbonate from H_2O-CO_2 fluid using H_2O of meteoric origin (–30‰) and CO_2 from initial volatile outgassing H_2O:CO_2 of 0.8 (CO_2 +43.7‰)

Clearly with such light H_2O, it is possible to precipitate very low $\delta^{18}O$ carbonates from H_2O rich fluid, particularly at hydrothermal temperatures when the H_2O-carbonate fractionation is less. The $H_2O_{(gas)}$-$H_2O_{(ice)}$ fractionation given by Mazoub (1971):

$$1000\ln\alpha = 0.012\frac{1000}{T} - 0.03$$

permits negligible gas-ice fractionation at any temperature, therefore the above model requires an environment similar to that envisaged when discussing a 'wet and warm' early Mars. As discussed in chapter 2, this appears to be difficult to maintain (Haberle, 1998) despite recent attempts to keep global temperatures on Mars above 0°C (Forget and Pierrehumbert, 1997). Thus a warm, wet Martian atmosphere capable of supporting latitudinal fractionation by evaporation and condensation may not be realistic. This is particularly true if the Ca-rich generation of carbonate is younger than the rosette generation of carbonate it appears to post-date. ALH84001 carbonate (Borg *et al.*, 1999) and maskelynite (Turner *et al.*, 1997) age determinations are associated with rosette carbonate so the age of Ca-rich carbonate is unknown and could, in theory, be as young as the most recent hydrothermal events capable of causing secondary mineralisation i.e. a few hundred million years (Hartmann *et al.*, 1999). In this type of environment, where the atmosphere is cold, CO_2 dominated and H_2O is rare (like the present day), Rayleigh distillation and CO_2 ice precipitation may be more realistic.

For this model, it is not clear what the atmospheric $\delta^{18}O$ of CO_2 could have been, particularly in view of evidence suggesting outgassing may have periodically altered the isotopic composition of the atmosphere (Farquhar and Thiemens, 2000). However, if we again assume a $\delta^{18}O$ of +43.7‰, then Rayleigh distillation proceeds via CO_2 ice-vapour fractionation

$$1000 \ln \alpha = \frac{2826}{T} - 14.5 \qquad \text{(Eiler } et\ al.\text{, 2000)}$$

Note from figure 10.14 that carbonate is between 0‰ and 10‰ lighter than the CO_2 from which it formed. Thus -10‰ carbonate requires a CO_2 source fluid of approximately 0‰. At plausible Martian atmospheric temperatures, figure 10.14 demonstrates that Rayleigh distillation between CO_2 vapour and CO_2 ice cannot produce these values: even at its most extreme this process can generate ice only 10‰ lower than the initial source fluid. Thus, in contrast to H_2O, production of 'meteoric' CO_2 by simple Rayleigh fractionation of initial outgassed CO_2 cannot be responsible for these light Ca-rich carbonates.

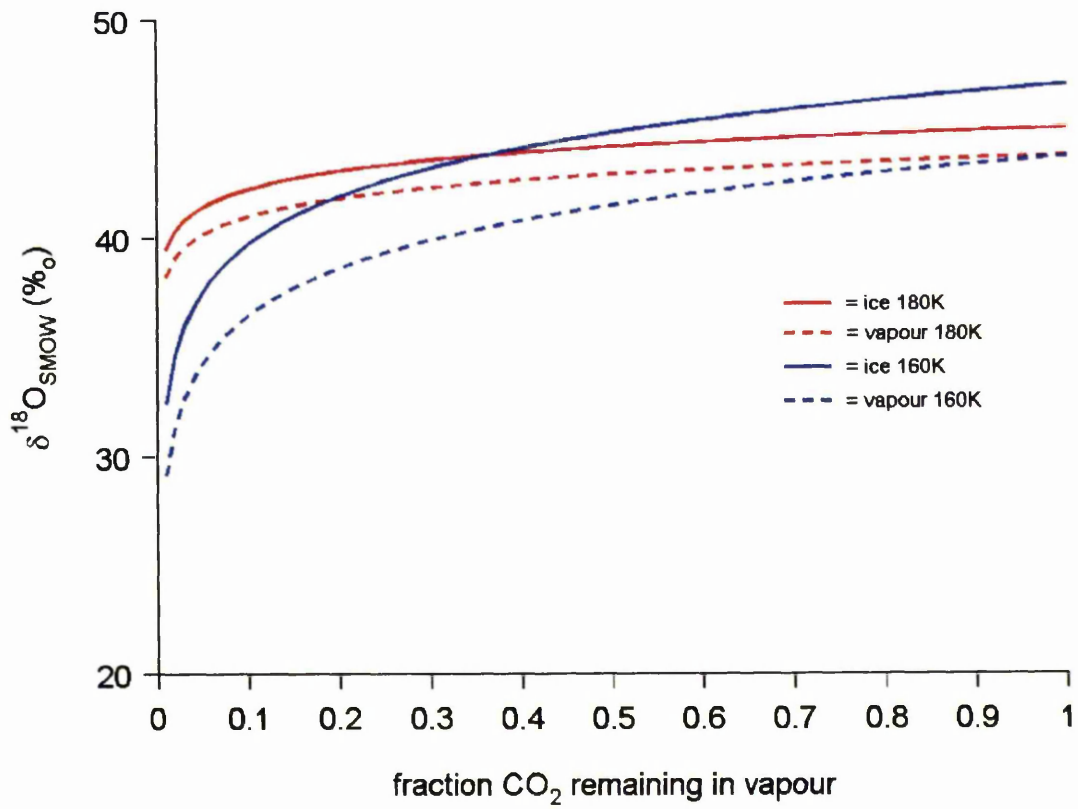

Figure 10.14: Rayleigh fractionation of a CO_2(g)-CO_2(s) system at plausible Martian atmospheric temperatures using outgassed CO_2 values (Clayton and Mayeda, 1988)

Perhaps, given the seasonal nature of CO_2 transport in the Martian regolith-atmosphere-polar cap system, this process could be repeated with one packet of CO_2 several times producing the necessary 0‰ CO_2 source fluid but keeping this fractionated CO_2 separated from the rest of the atmospheric during repeated evaporation-condensation cycles seems extremely difficult.

10.3.10 Can all carbonates originate from 1 fluid?

So far, we have attempted to find a model capable of precipitating −10‰ carbonate and have identified meteoric fluids as a possible source. These models may help understand the conditions at the time of formation of the Ca-rich carbonate, but do not provide any constraints on the evolution of the Martian hydrosphere and atmosphere over time.

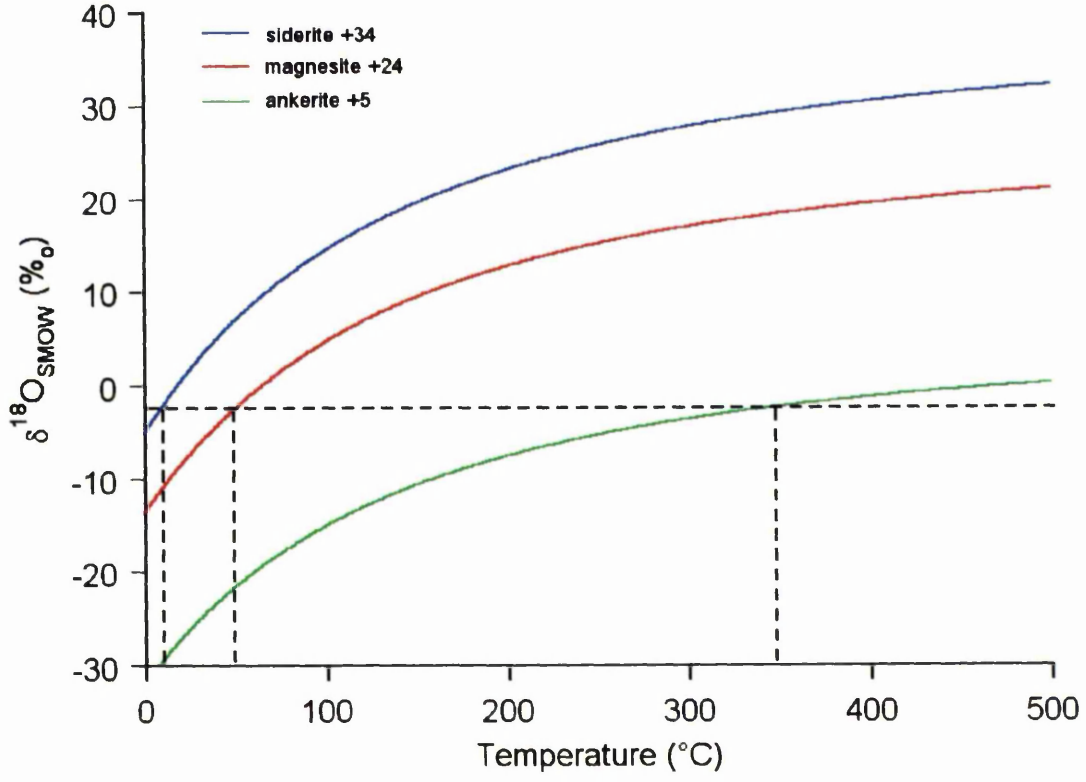

Figure 10.15: $\delta^{18}O$ of water in equilibrium with ALH84001 ankerite and magnesite (Saxton *et al,* 1998), and Nakhla siderite (Saxton *et al.*, 2000).

Figure 10.15 shows that outgassed water of $\delta^{18}O$ –2.4‰ can produce rosette cores at ~350°C. The rosette rims can then precipitate from this fluid at cooler temperatures ~50°C. Nakhla siderite can then form from this identical fluid at <10°C. However, if we require a water rich fluid to produce $\delta^{18}O$ -10‰ ankerite, this fluid cannot precipitate siderite of $\delta^{18}O$ +34‰ at any temperature (figure 10.16) thus requiring an evolution of the water reservoir to a $\delta^{18}O$ enriched composition (assuming both Ca-rich carbonate and Nakhla carbonate reflect a global water reservoir). This is perhaps not unexpected given that Nakhla secondary mineralisation is inferred to have formed in the final stages of an evaporite sequence (<10% original fluid) (Bridges and Grady, 2000) and would therefore have precipitated from just such $\delta^{18}O$ enriched fluid (see evaporite section later) although it is the first evidence that the H_2O reservoir must have evolved assuming formation temperatures >0°C.

This idea can be extended to considering the possibility of an evaporitic origin for the rosettes as well as Nakhla carbonate. Preliminary ToF-SIMS and EPMA analyses in chapter 12 hint at evidence for increasing brine concentration as deposition proceeded, implying an evaporitic environment. If this were the case, one could envisage a localised isotopically heavy source for both rosettes and Nakhla carbonate. This would permit, a lighter global value, for example water with $\delta^{18}O$ -20‰, which could precipitate carbonate of $\delta^{18}O$ -10‰ at moderate temperatures (~350°C) without the need for a meteoric source. Such an isotopically light global hydrosphere can be generated from an initial outgassing of equal amounts of CO_2 and H_2O, as already discussed in 10.3.6 and figure 10.8.

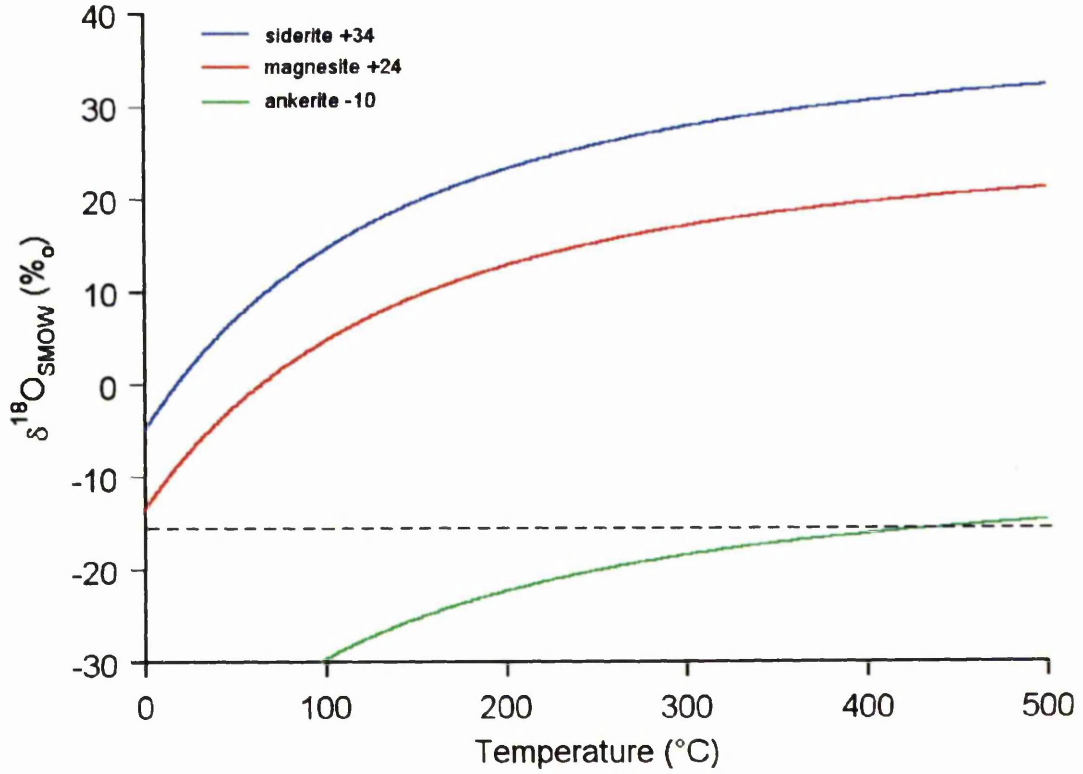

Figure 10.16: the difficulty of generating ALH84001 magnesite (Saxton *et al*, 1998), and Nakhla siderite (Saxton *et al.*, 2000) and new Ca-rich carbonate (this work) from water of one $\delta^{18}O$ value.

10.3.11 Deposition from ice

There is also a possibility that SNC carbonates formed at temperatures <0°C which would increase the range of possible source fluid isotopic compositions. Oxygen diffusivity in ice occurs at a rate of ~60μm per 10^6 years at 0°C decreasing to ~10μm per 10^6 years at −30°C (calculated from figure 10.17). This diffusion rate is fast enough to permit deposition of carbonates from ice (Fairchild *et al.*, 1993).

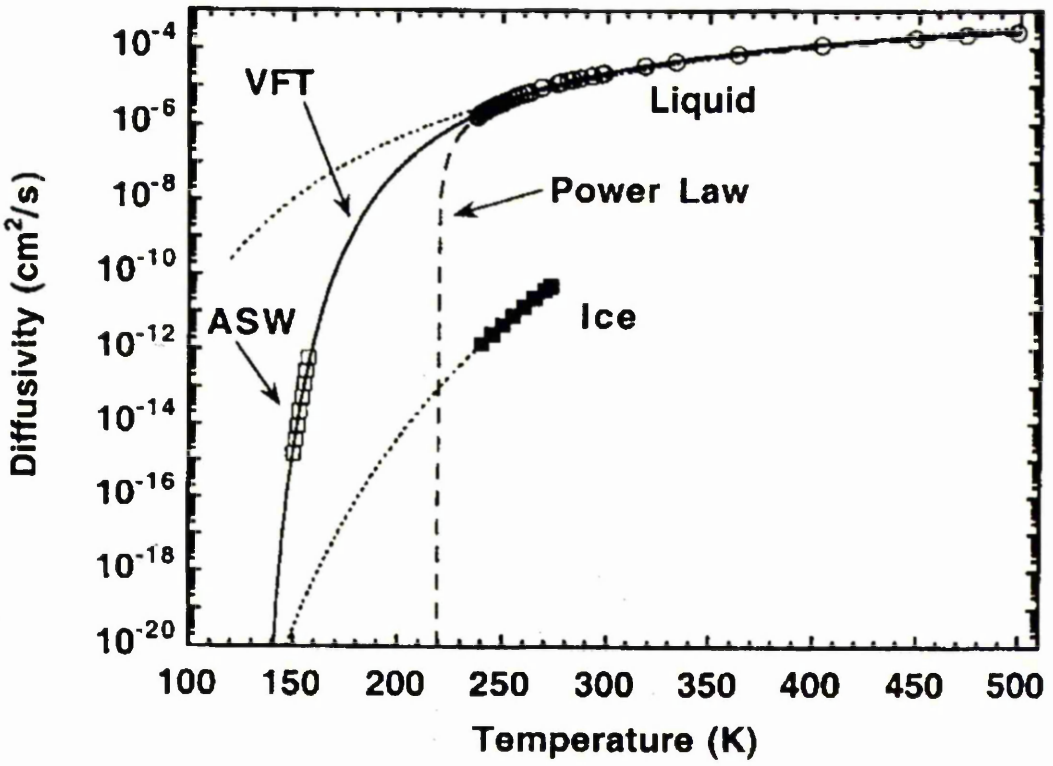

Figure 10.17: Self diffusivity of oxygen in ice showing relatively high diffusion rates in ice. (ASW is a supercooled liquid with enhanced diffusive properties) (data from Scott-Smith *et al.*, 2000)

Clearly, an increase in the range of source fluid composition relies on the assumption that carbonate-water fractionation continues to increase with decreasing temperature (<0°C). This is a valid assumption given that a liquid like layer exists on the surface of ice down to –30°C (figure 10.18)(Scott-Smith *et al.*, 2000). This liquid like layer is believed to behave kinetically as if it were "normal" water, therefore I assume the water carbonate fractionation formula still applies.

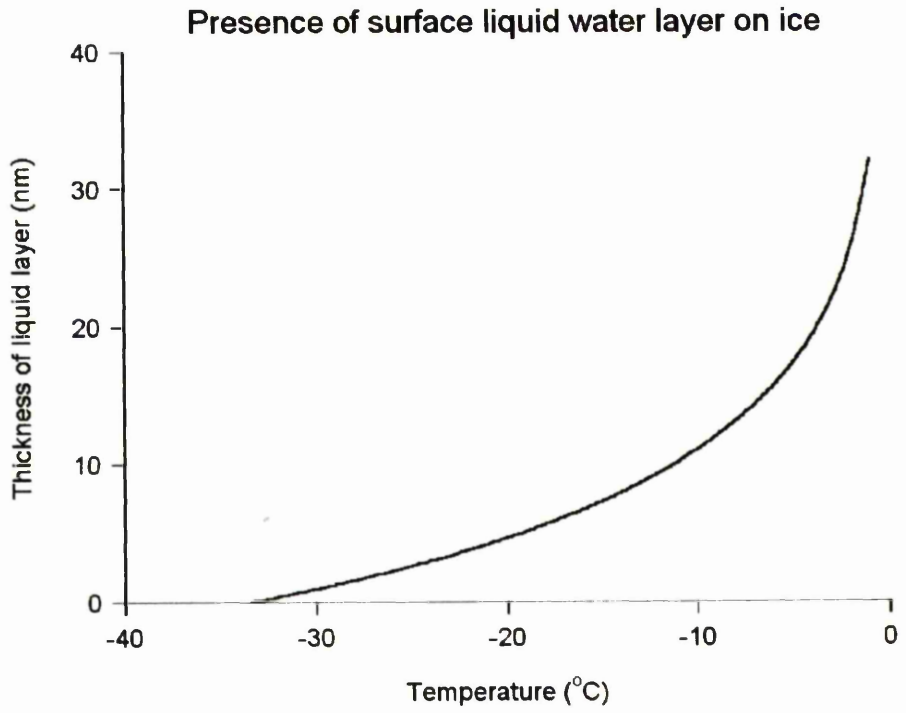

Figure 10.18: thickness of liquid water like layer on the surface of ice at temperatures <0°C.

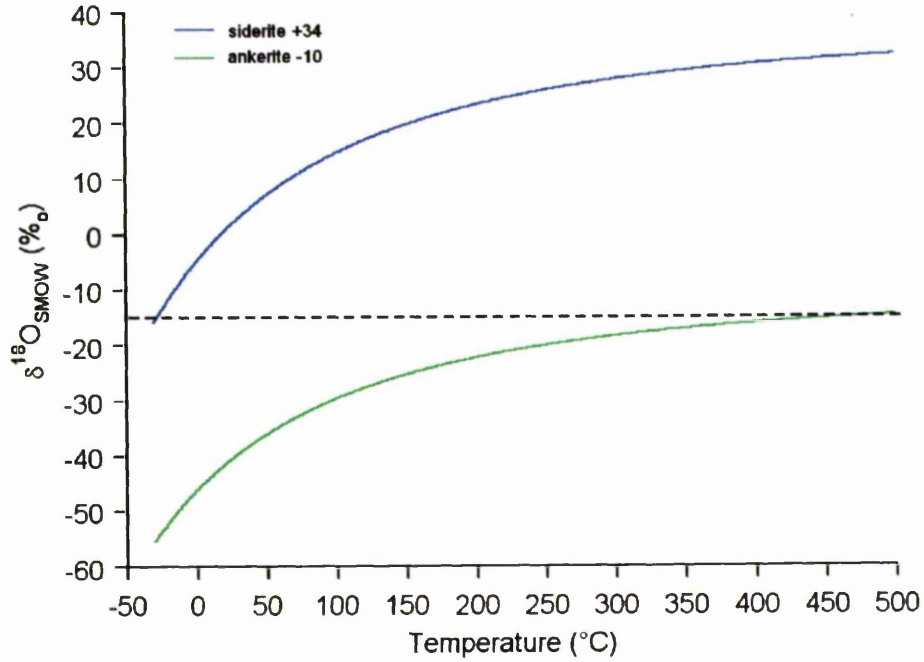

Figure 10.19: enhanced range of carbonate that is possible from a single source fluid that precipitates at temperatures <0°C.

For a given fluid composition e.g. –30‰ for a meteoric ice, the $\delta^{18}O$ of the carbonate would be higher. This does not help to explain the low $\delta^{18}O$ values of ALH84001 carbonate: it would require an even lower $\delta^{18}O$ source. However, it does permit a larger range of carbonate to be produced from a fluid of constant oxygen isotopic composition. This is important when comparing the full range of $\delta^{18}O$ in Martian carbonates. Earlier in this chapter we observed that the low $\delta^{18}O$ observed now make it impossible to precipitate isotopically light ALH84001 calcite and heavy Nakhla siderite from the same fluid. Clearly, if the Nakhla siderite formed at -30°C an isotopically light fluid could still precipitate +34‰ carbonate. Removing the requirement of fluid isotopic evolution from some time <4.0Ga to some time <1.3Ga. It is noted that precipitation from ice is a more likely scenario for Nakhla carbonate than ALH84001 carbonate given likely surface conditions over the last 1.3Ga.

Conversely, if carbonate precipitated from ice, it may be anticipated that gradually the main body of ice will become isotopically lighter over time in a kinetic fractionation process akin to closed system fractionation in the atmosphere (figure 10.12). Thus, sub-surface fractionation could provide the isotopically light source fluid for ALH84001 calcite, avoiding the need for an actively fractionating hydrosphere. Perhaps then it could be argued from a mass balance standpoint that some of the heavier carbonates reflect the isotopically heavy oxygen precipitated from ice. On Earth, carbonate diagenesis in ice is a known phenomenon where carbonate as light as $\delta^{18}O$ – 18.7‰ is formed in ice undergoing basal melting (Fairchild *et al.*, 1993). In addition, atmosphere and ocean circulation tend to homogenise H_2O reservoirs on Earth. It is unlikely, certainly in the last 1.3Ga, that this process was as efficient on Mars, allowing the possibility of permanent subsurface water reservoirs with varying $\delta^{18}O$ values.

10.3.12 Implications for ancient Mars

Two important implications follow from the above discussion of oxygen isotopic data: if the Ca-rich carbonate formed from a fluid representative of a global reservoir, the reservoir cannot be of the composition used by many authors (e.g. Clayton and Mayeda, 1988; Leshin *et al.*, 1998; Saxton *et al.*, 1998): it must be substantially ^{18}O depleted. In addition, isotopic evolution of such a reservoir would be required to produce Nakhla siderite of +34‰: previously a change in temperature of the source fluid was sufficient to produce $\delta^{18}O$ values observed in all SNC secondary minerals and a universal isotopic composition of the source fluid could be assumed.

If the source fluid for ALH84001 carbonates is not representative of a global water reservoir, some mechanism is required to generate a (possibly localised) reservoir of ^{18}O depleted water. Atmospheric fractionation by evaporation and condensation (precipitation) is a possible mechanism. Precipitation occurs when the vapour pressure of water approaches the saturation vapour pressure. Saturation vapour pressure of water is the maximum pressure exerted by water when in equilibrium with the liquid (or solid) phase. Between -35°C and +35°C, the saturation vapour pressure for water in millibars of H_2O is given by:

$$e_s = 6.112 \exp\left(\frac{17.67 \times T}{T + 243.5}\right)$$

where e_s is the saturation vapour pressure and T is the temperature in °C (Bolton, 1980).

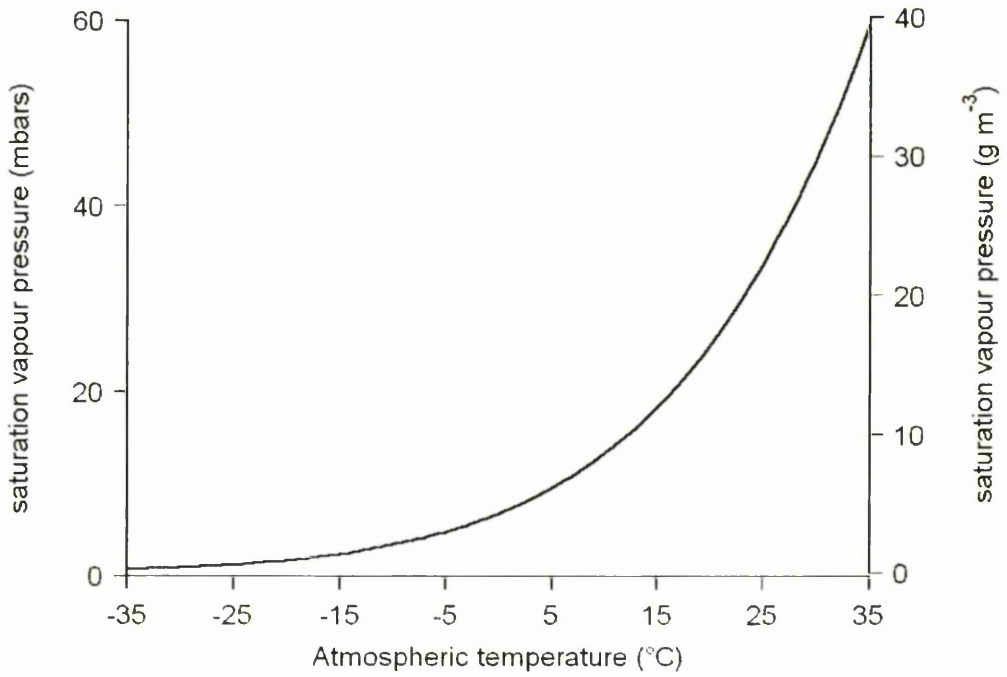

Figure 10.20: saturation vapour pressure of water given in millibars partial pressure H_2O and grams of H_2O per m^3 of dry air.

If the Ca-rich carbonate in ALH84001 was deposited soon after the rosettes from meteoric water, this is in agreement with the early wet and warm atmosphere, inferred from Noachian morphology (Chapter 2). If the source fluid was meteoric CO_2, a substantial Martian atmosphere is not necessarily required.

It is also possible that the Ca-rich carbonate represents an influx of CO_2-H_2O fluid significantly later than 4Ga. This is plausible given the evidence of water percolation of the nakhlites after their formation at 1.3Ga. If this were true, then the deposition event may have been induced by volcanic activity.

Two scenarios can then be envisaged:

i) A hydrothermal episode associated with volcanism could have remelted previously precipitated water ice with the light oxygen isotopic signature. This would not require an appreciable atmospheric change as the hydrothermal activity may be completely subsurface.

ii) Volcanically induced outgassing resulted in a substantial transient, atmosphere which then precipitated water for a relatively short period of time (McKenzie and Nimmo, 1999)

The chaotic obliquity of Mars (from 0° to 60°) and the subsequent release of CO_2 and H_2O in both ices and clathrates may also be capable of generating transient but substantial atmosphere (Jakosky *et al.*, 1995; Musselwhite and Lunine, 1995). This would homogenise any latitudinal heterogeneity in oxygen isotopes from earlier episodes of precipitation (see scenario (i) above)

The more interesting of these possibilities is an intermittent but substantial water rich atmosphere, similar to that envisaged in the early Noachian, present at some point in relatively recent Martian geological history. The inferred erosion rates for the Noachian are $10^2 - 10^4$mm per 10^6 years but post Noachian rates are significantly less: $10^{-1} - 10^{-2}$mm per 10^6 years (Golombek and Bridges, 2000). However, this is average erosion, integrated over geological time. If post-Noachian erosive periods are exceedingly short, as suggested by Baker (1991), then Noachian and post Noachian erosion rates are similar and therefore the size of the atmospheres inferred are comparable.

10.4 Summary

Through a series of isotopic models I have attempted to constrain the source fluid and formation conditions of carbonate in ALH84001. First, I began with a discussion of a common model which incorporates outgassing of H_2O and CO_2. Although this model is capable of producing $\delta^{18}O$ of ALH84001 rosettes and carbonates in other Martian meteorites, it cannot generate the isotopically light Ca-rich carbonates presented here. Another popular model, that of high temperature equilibrium between the source fluid and silicate, is also shown to be incapable of producing $\delta^{18}O$ –10‰ carbonate. The isotopic data presented in this thesis appear to require new models. The first new model I proposed is that of carbonate remobilisation by shock accompanied by isotopic fractionation. I have shown that although $\delta^{18}O$ –10‰ carbonates can be generated by this model, the remaining Ca-rich carbonate (up to +14‰) is inconsistent with closed system shock remobilisation.

On Earth, a well documented means of generating isotopically light H_2O (and therefore isotopically light carbonate), comparable to that required for data presented here, is by atmospheric precipitation (the generation meteoric water). I discussed the possibility of generating both meteoric H_2O and meteoric CO_2, but found that only H_2O can fractionate sufficiently be the source fluid. This implies a substantially denser and more water rich Martian atmosphere in the past than at present.

Modelling these data in concert with other Martian carbonate data also leads to the conclusion that all Martian carbonates can no longer be produced from one fluid unless precipitation occurs from ice. This supports the hypothesis of an evolving Martian atmosphere / hydrosphere that exchanges with near surface reservoirs.

Chapter 11

Carbon isotopes

11.1 Introduction

It has been demonstrated in the previous chapter that the presence of carbon with $\delta^{18}O$ -10‰ carbonate in ALH84001 precludes the high temperature and global hydrosphere formation hypotheses which are applicable to the range of $\delta^{18}O$ values of carbonate rosettes. However, if the carbon isotopic composition of rosettes are also measured by ion microprobe, the formation conditions of the rosettes can also be further constrained. This chapter will explore the range of temperatures and fluid compositions that satisfy both the oxygen and carbon isotope data. I will also attempt to constrain the $\delta^{13}C$ of the Martian atmospheric CO_2. In addition, comparisons of $\delta^{13}C$ in ALH84001 and in other Martian meteorites will be made to explore the possibility of evolution of atmospheric $\delta^{13}C$ over time.

11.2 Discussion

Before interpreting the carbon isotopic data in carbonate rosettes, it is constructive to comment on the validity of the carbon measurements. It has been noted that ALH84001 silicate also contains carbon with a $\delta^{13}C_{PDB}$ of ~+50‰. This carbon is significantly heavier than Martian magmatic carbon of –25‰ (Wright *et al.*, 1990) which one might expect to be distributed throughout the rock. Also, carbonate of $\delta^{13}C_{PDB}$ ~+50‰ cannot be Antarctic contamination as terrestrial organic carbon has $\delta^{13}C_{PDB}$ –20‰ to –30‰ and all other sources of terrestrial carbon (mantle bicarbonate and atmospheric CO_2) $\delta^{13}C_{PDB}$ <0‰ (Wright *et al.*, 1990). Thus, assuming there is no massive fractionation effect between carbon in silicate and carbon in carbonate, the +50‰ carbon in ALH84001 silicate must have a Martian origin. It may be possible to

shock implant carbon into a host mineral in a process similar to that observed for xenon (Gilmour *et al.*, 1998) or CO_2 (Bogard *et al.*, 2001), either by devolatilisation of carbonate or implantation from the Martian atmosphere. Rasternig of the primary beam over the surface of pyroxene grains yields variable (by a factor of ~100) but widespread carbon in the silicate. Therefore, perhaps the latter is more likely. If atmospheric implantation were responsible, the carbon in the carbonate may represent the atmosphere directly as well as a hydrosphere via equilibrium fractionation.

A useful starting point is to return to the global hydrosphere model (e.g. Clayton and Mayeda, 1989; Romanek *et al.*, 1994) which assumes $\delta^{18}O_{H2O}$ to be –2.4‰ and $\delta^{18}O_{CO2}$ to be 43.7‰. Unfortunately, we were unable to measure oxygen on the same spot which yielded $\delta^{13}C$ values but given that the $\delta^{18}O$ of ALH84001 carbonate rosettes is well known and has been verified by several authors (Valley *et al.*, 1997; Leshin *et al.*, 1998; Saxton *et al.*, 1998) I feel it is acceptable to assume a $\delta^{18}O$ value of +17‰ for the rosette mantle which provided $\delta^{13}C$ data.

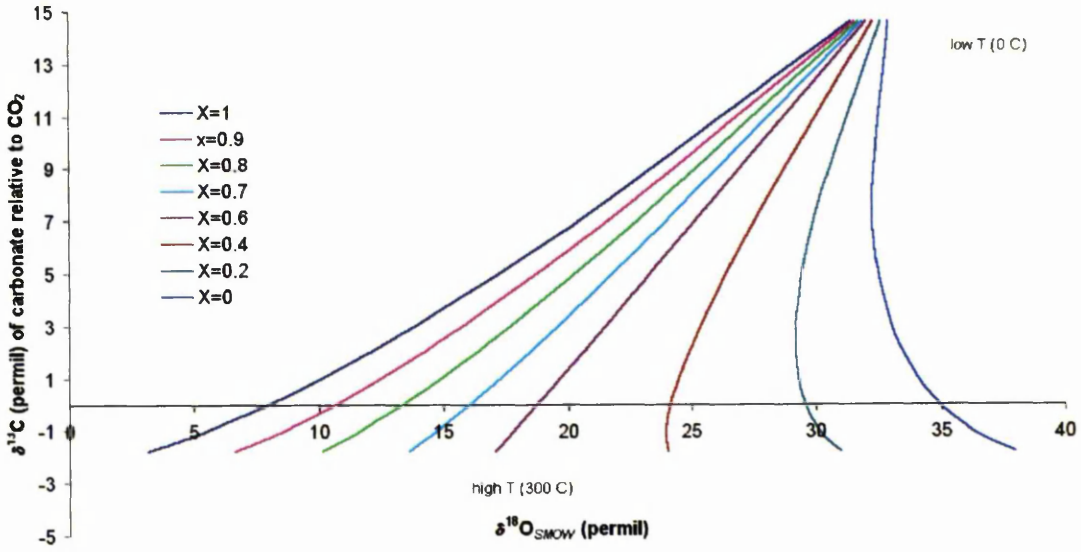

Figure 11.1: graph showing enrichments of carbonate $\delta^{13}C$ for a given value of X and temperature negative values indicate carbonate lighter than CO_2). X axis is the $\delta^{18}O$ carbonate to identify plausible values of X for generating $\delta^{18}O$ +17‰

If I fix the $\delta^{18}O$ of carbonate at +17‰, figure 11.1 demonstrates the range of X values capable of generating the carbonate is limited to 0.6-1.0 and the accompanying temperatures of formation vary from ~300°C to ~75°C respectively. It also shows carbonate – CO_2 fractionation (Bottinga, 1968) from 0°C to 300°C. Therefore, for a given value of X (and therefore a unique formation temperature if carbonate remains fixed at $\delta^{18}O$+17‰) we can determine the $\delta^{13}C$ of the CO_2 which is in equilibrium with rosettes at that temperature. Taking $\delta^{13}C$ of rosettes to be +50‰, the $\delta^{13}C$ of the source atmospheric CO_2 varies from $\delta^{13}C$+45‰ for a virtually pure water source (X~1) to $\delta^{13}C$+52‰ when X=0.6 (figure 11.2).

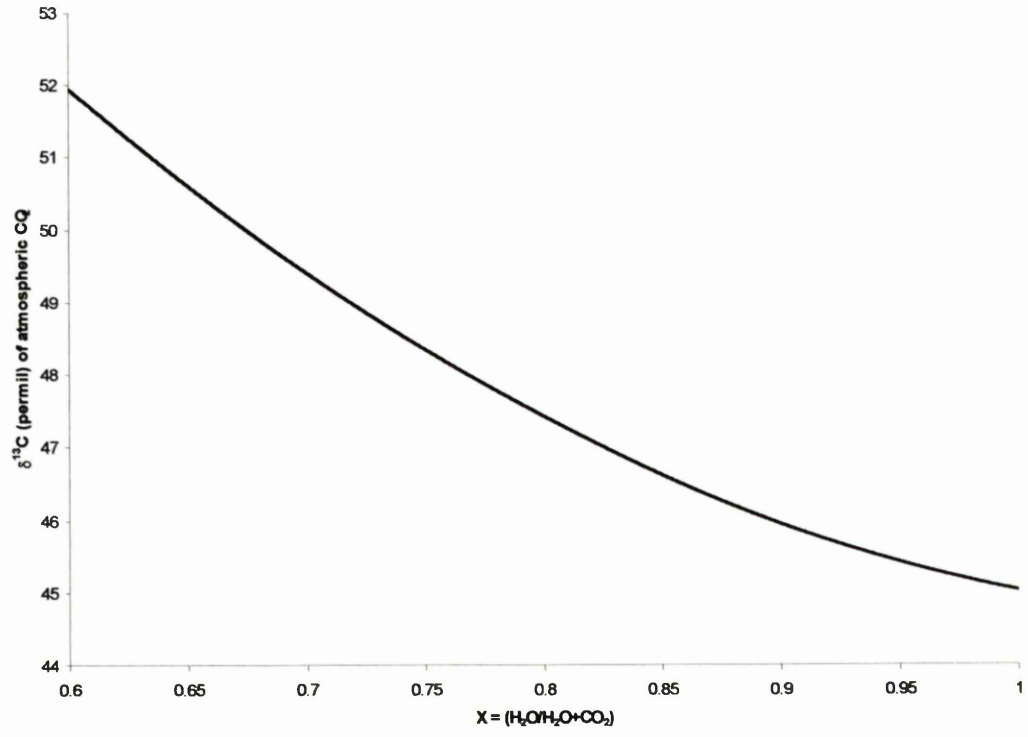

Figure 11.2: $\delta^{13}C$ of atmospheric CO_2 for plausible values of X

If carbonate $\delta^{13}C$ of +50‰ is correct, then the range of $\delta^{13}C$ in the atmospheric CO_2 from which the carbonate formed (+45‰>$\delta^{13}C$>+52‰) just overlaps (within error) the composition of trapped CO_2 in EETA79001, calculated by Carr *et al.* (1985) to be +36±11‰. The $\delta^{18}O$ enrichments possible from the complete range of $\delta^{18}O$ values in Martian carbonates are in the order of ~50‰. This would permit enrichment in $\delta^{13}C$ of only ~25‰ over the same period, which is sufficient to generate only 0‰ atmospheric CO_2 if the initial atmosphere was close to the magmatic value of -25‰, not the +36‰ required by trapped CO_2 in EETA79001 or the +50‰ required by this model.

Another comparison can be made between carbonates in ALH84001 and carbonates in Nakhla. We have assumed $\delta^{18}O$+17‰ as the ALH84001 rosette mantle. Nakhla carbonate has $\delta^{18}O$+34‰ (Saxton *et al.*, 2000). If we invoke the same source fluid for ALH84001 rosettes and Nakhla carbonate (regardless of the initial fluid composition) we are required to cool the fluid after ALH84001 deposition to account

for the $\delta^{18}O$ +17‰ increase in Nakhla siderite. I also assume a low T environment for the Nakhla carbonate (Bridges and Grady, 1999) of 0°C. Figure 11.3 shows the increase in $\delta^{13}C$ which must accompany the cooling of fluid required for the oxygen isotope enrichment.

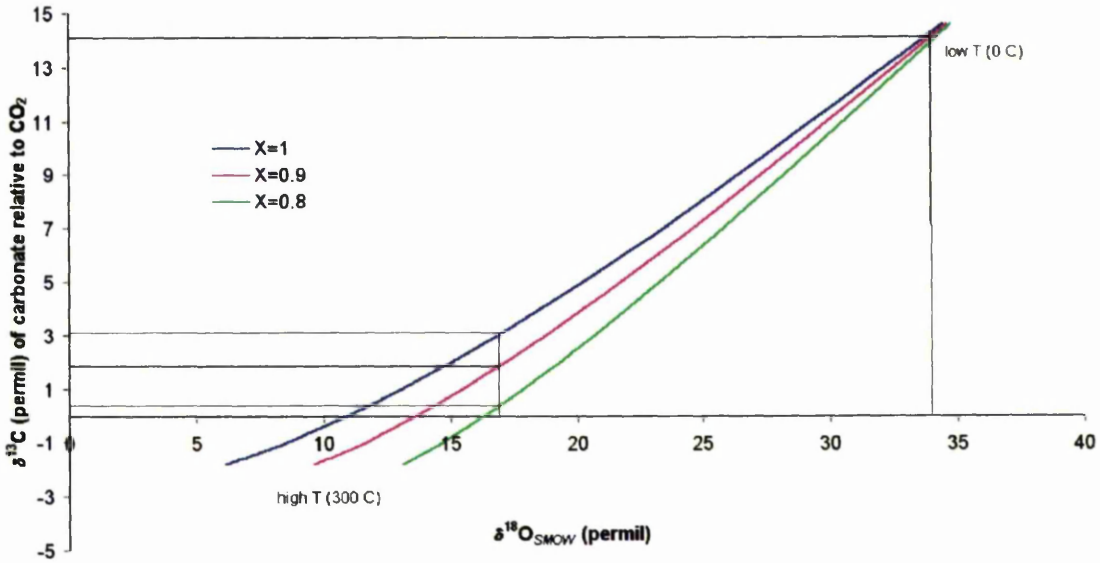

Figure 11.3: graph showing increase in carbonate-CO_2 fractionation necessary to accommodate oxygen isotope enrichment from ALH84001 rosette to Nakhla siderite

Therefore, depending on X, the carbonate in Nakhla is expected to be between 11‰ and 14‰ heavier than ALH84001 rosette formed from the same fluid at elevated temperatures. Nakhla carbonate has a $\delta^{13}C$ of up to +55‰ (Jull *et al.*, 1995), but if the same fluid deposited both carbonates, one might expect Nakhla carbonate to have $\delta^{13}C$ >+60‰ (50+11). Thus, although Nakhla carbonate is heavier the source CO_2 may actually have been *lighter*, again arguing against atmospheric fractionation of CO_2 post 4Ga. As atmospheric fractionation of CO_2 seems to have occurred before ALH84001 rosette deposition. It is possible that hydrodynamic escape early in Martian history had a role to play in fractionation of carbon isotopes as suggested by Wright *et al.* (1990).

At this stage, few detailed inferences can be drawn from the one carbon isotope measurement presented here. Given the $\delta^{13}C$ –25‰ inferred for the Martian mantle, an isotopically fractionated reservoir is clearly required to produce $\delta^{13}C$ +50‰ carbonate as equilibrium fractionation at any temperature cannot provide 75‰ enrichment in $\delta^{13}C$. It is also worth noting that the isotopic evolution of reservoirs from (earlier) ALH84001 carbonates to (later) nakhlite carbonates when discussing oxygen isotopes does not appear to be required for carbon isotopes.

Finally, one can note that with an outer mantle $\delta^{13}C$ +50‰ and an average carbonate $\delta^{13}C$ of +40‰ (Romanek *et al.*, 1994; Jull *et al.*, 1997) one might expect that the cores have a lighter $\delta^{13}C$. The only other reliable ion microprobe C data (Niles *et al.*, 2002) suggests this to be the case. Therefore one can rule out low temperature closed system CO_2 rich fluid as a deposition mechanism for carbonate rosettes because progressive precipitation should lead to lighter $\delta^{13}C$ (Chacko *et al.*, 1991) which is the opposite of inferred rosette zoning.

A future goal of carbon isotope work on the ion microprobe is therefore $\delta^{13}C$ analyses from a range Ca-rich carbonate compositions to determine temperature trends during carbonate deposition. It is also important to determine whether the Ca-rich generation of carbonate is $\delta^{13}C$ enriched which would favour a near surface source or is $\delta^{13}C$ depleted, which would imply a magmatic source and silicate equilibrium (see section 10.3.9.1).

Chapter 12

Halogens in ALH84001

12.1 Introduction

It has been suggested (Warren, 1998; Harvey and McSween, 1998) that the secondary minerals in ALH84001 may form part of an evaporite sequence that occurred near the Martian surface. In this scenario, the study of halogens may provide useful information on the evolution of the pore waters. In addition, iodine may act as a biomarker (Gilmour et al., 1999): biological processes within the terrestrial near surface environment have sequestered iodine into ocean sediment such that I/Cl ratios have reduced by a factor of 40 over the past 4Ga (Channer et al., 1997). Remobilisation of iodine from these unlithified sediments into pore fluids during diagenesis and from lithified rock during metamorphism produces I/Cl ratios as high as 10^4 above sea-water (Worden, 1996) which cannot be accounted for by evaporation. Therefore the distribution of iodine in ALH84001 may be of use in assessing whether biological I/Cl fractionation has played a role throughout the history of Mars. Time of flight secondary ionization mass spectrometry and electron probe micro analyses were obtained from three small (4-8mg) grains of ALH84001, 287 in an attempt to determine halogen concentrations and distributions between phases. Grain numbering is retained from chapter 8.

12.2 Grain 2 - concentrated iodine

Preliminary rastered analyses indicated the possibility of an iodine signal therefore analyses were concentrated on areas of 40μm^2 with several million shots per area. Iodine was observed in two chromite grains: lower left (region A) and near centre (region B) of figure 12.1. Analysis of an equivalent area of epoxy yields five times less iodine as

inferred from integrated peak counts therefore iodine contamination from epoxy is unlikely.

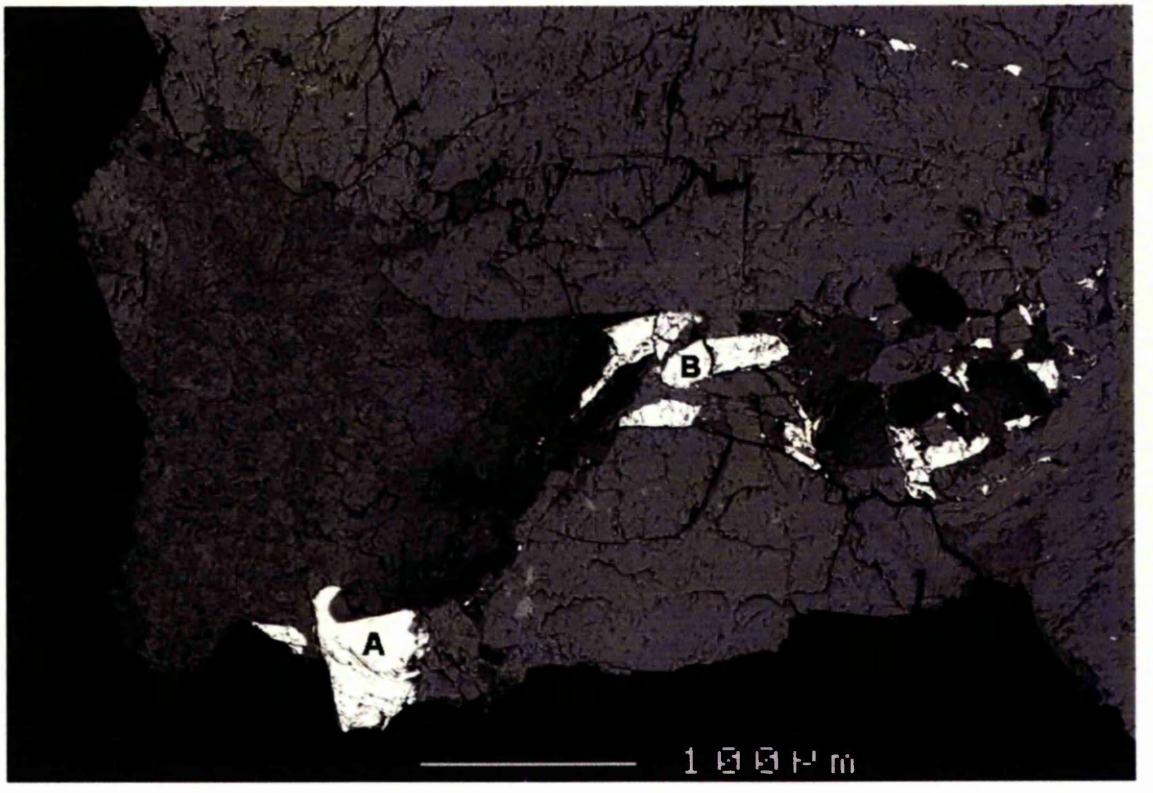

Figure 12.1: Back Scattered Electron (BSE) image of ALH84001 grain 2. White is chromite, black at bottom and left of image is epoxy, black bands are magnesite, light grey is pyroxene, mottled grey is interspersed carbonate and maskelynite

12.3 Grain 3 - chlorine zoning?

Figure 12.2 shows BioTofSIMS ion images of a region of ALH84001 grain 3. It can be seen that the carbonate rosette fragments contain a high, uniform concentration of chlorine whilst the fragment to the left is zoned in chlorine from core to rim. It is unclear why one fragment appears to contain chlorine zoning while the other does not. EPMA analyses indicate an increase in chlorine from core to rim in both fragments. Chromite also appears to be relatively abundant in chlorine compared to pyroxene. No iodine was observed in this sample using BioTofSIMS. Note the high abundance of chlorine present in the epoxy (top left of bottom left image) which suggests using BioTofSIMS to quantitatively measure chlorine in these ALH84001 samples may be suspect.

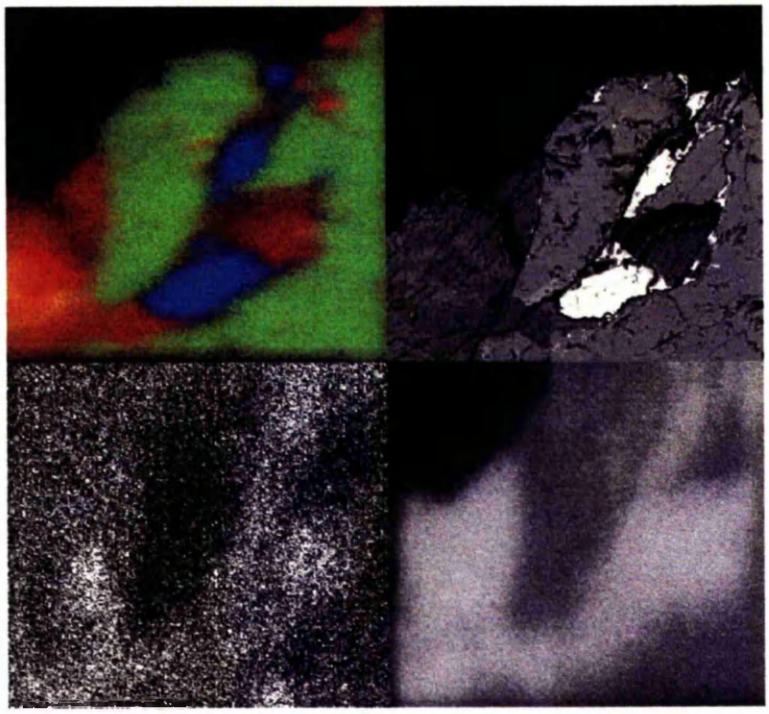

Figure 12.2: ion maps of ALH84001. Bottom left- Cl ion map negative ions; bottom right- OH ion map negative ions; top left- composite ion map of Cr (blue) Si (green) and Ca (red/yellow) positive ions; top right- BSE image of same region.

12.4 Grain 5 - chlorine zoning

Grain 5 is a different grain from those mapped by electron probe in chapter 8. It has not been analysed for halogens by EPMA and therefore may represent the best chance of observing Cl zoning in the carbonates, given the possibility of halogen loss under SEM and EPMA electron beam imaging. Figure 12.3 shows a BioTofSIMS $^{35}Cl^-$ image and accompanying backscattered SEM image of the same region. Note the increased abundance of chlorine in the carbonate compared to pyroxene and the increased abundance of Cl in the rosette rim compared to the fragment of the core and the region of carbonate near the top of the image. Spot analyses of this imaged region gives relative abundances (counts of $^{35}Cl^-$ per 106 shots) of 3000 for rosette cores, 5000 for rosette rims and 2000 for pyroxene.

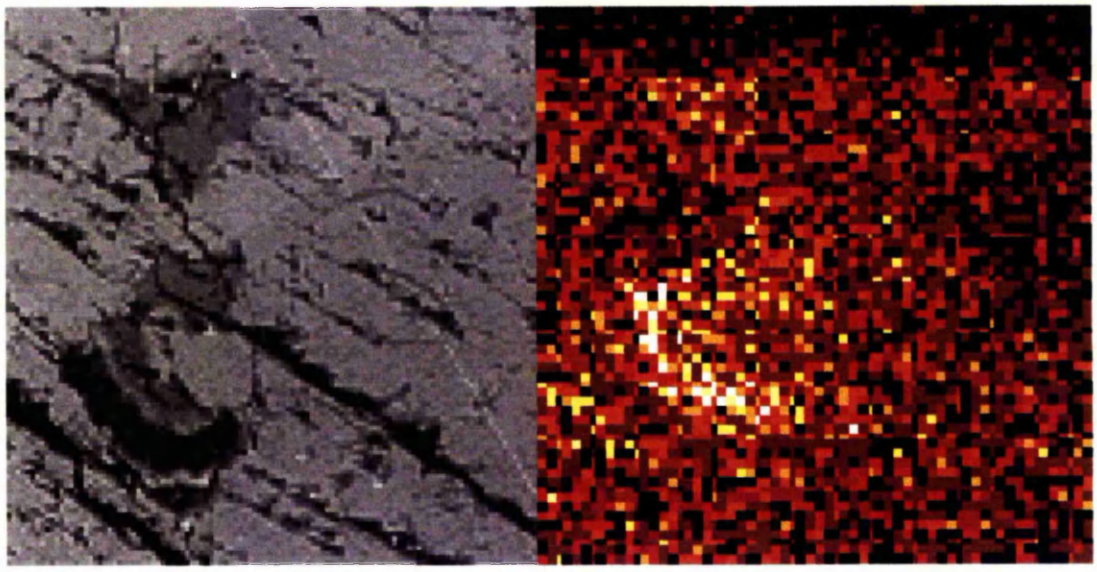

Figure 12.3: left is a backscattered SEM image of ALH84001 grain 5 carbonate rosette fragment. Right is a BioTofSIMS $^{35}Cl^-$ image of the same region. Image is ~70μm across, (~1μm^2 per pixel). The highest concentration of Cl is observed in Mg rich rosette rims, followed by Mg-Fe-Ca carbonate cores and pyroxene with the lowest chlorine content. The

crack (lower left) also appears to have significant amounts of chlorine, presumably from epoxy used to impregnate the sample.

Phase	Chlorine (p.p.m)
Grain 3 rosette rim	970 +/- 230
Grain 3 rosette core	464 +/- 177
Grain 3 chromite	687 +/- 323
Grain 3 pyroxene	42 +/- 30
Grain 2 rosette rim	368 +/- 102
Grain 2 rosette core	261 +/- 65
Grain 2 chromite	91 +/- 51
Grain 2 pyroxene	28 +/- 17
Epoxy	188 +/- 13

Table 12.1: EPMA chlorine analyses in different phases of ALH84001. No iodine was observed using EPMA.

12.5 Discussion

EPMA analyses of ALH84001 carbonate agree well with BioTofSIMS analyses: chlorine concentrations in the carbonate increase by ~100% from core to rim (grain 3) and by ~40% (grain 2). This is comparable to the ~65% increase in chlorine from core to rim observed in grain 5 by BioTofSIMS. Therefore, it is tentatively inferred that no significant BioTofSIMS matrix effect exists for chlorine (and presumably other halogens) over this range of carbonate compositions. EPMA analyses indicate chlorine concentrations ~2-3 times greater in grain 3 carbonate than in grain 2 carbonate. This may be an indicator of epoxy contamination if one assumes that all rosettes should have approximately the same chlorine concentrations. However, there is also more chlorine observed in the chromite and pyroxene of grain 3 than in grain 2, implying chlorine loss from all phases of grain 2. This is not unexpected because grain 2 has undergone extensive cathodoluminescence using high beam currents. EPMA analyses of chlorine

in chromite relative to carbonate agree reasonably well with estimates from integrated counts of carbonate and chromite regions in figure 12.3. Pyroxene does not show the same agreement between EPMA and ToF-SIMS: pyroxene chlorine concentrations are an order of magnitude lower than those of carbonate as measured by EPMA compared to only a factor of 2 reduction in chlorine using BioTofSIMS analysis. This suggests a matrix effect is present between different mineral phases in BioTofSIMS analysis. Assuming carbonate abundance of 1% (Mittlefehldt, 1994), average chlorine concentrations of approximately ~500p.p.m. are consistent with the bulk values of Turner *et al.* (1997).

Anticipated iodine concentrations in the different ALH84001 phases are very low: up to 2.5 p.p.m. in the carbonate with a bulk value of only 10-40 p.p.b. (Gilmour *et al.*, 1998). If similar halogen sensitivities in carbonate and chromite are assumed, chromite is estimated to contain 1.5 p.p.m. iodine. With a similar modal abundance to carbonate (1%), chromite could account for the bulk iodine content in ALH84001 if the true value is nearer the lower end of the 10-40 p.p.b. estimate.

12.6 Implications of halogen distribution

12.6.1 Chlorine

If one assumes that there is no major matrix effect for chlorine between ankerite and magnesite, evidence presented in this work is consistent with an evaporitic origin as envisaged by Warren (1998) and Harvey and McSween (1998).

12.6.2 Iodine

There is a possibility that iodine in chromite is merely contamination during sample preparation. However, the spatial association of chromite and carbonate may have some significance. If shock decarbonation of carbonate released iodine, it is conceivable that

it may have been implanted into chromite. Clearly more work is required on standardising halogen contents using BioTofSIMS but initial work has found some intriguing evidence for concentrated iodine and zoned chlorine. Iodine, in particular, will be studied further, extending the work of Gilmour *et al.* (1999) using a UV laser beam on the noble gas mass spectrometer RELAX to idenitify the siting of iodine below the detection limit of TOF-SIMS analyers.

Chapter 13

Conclusion

In conclusion, I shall briefly summarize the findings of this thesis in an attempt to answer the initial questions posed in the introduction.

I have presented stable isotope data from a previously undetected type of carbonate in ALH84001. This carbonate has a unique texture (intergrown carbonate and feldspar that encapuslates rosette-type carbonate), unique cation chemistry (significantly more Ca-rich than other ALH84001) and unique oxygen isotope ratios ($\delta^{18}O$ 10‰ lower than measured elsewhere). These new findings have considerable bearing on the questions posed at the beginning of this thesis:

- *What were the conditions under which ALH84001 carbonate formation took place and what has been the geological history of ALH84001 since then?*

  Although limited oxygen isotope data from ALH84001 rosettes was obtained during this research, the presence of a ~35‰ variation over a few microns between rosettes and Ca-rich carbonate suggests that in the last ~3.9Ga, ALH84001 has not been exposed to elevated temperatures. This, of course, includes the period of Ca-rich carbonate formation.

- *What were the environmental conditions approximately 4Ga ago on Mars? Although it seems clear that a more substantial Martian atmosphere existed in the past, was it warm and dense, possibly comparable with Earth?*

The age of the Ca-rich carbonate is not known, and therefore Ca-rich cannot, at present, contribute to a discussion of environmental conditions 4Ga ago. However, the possibility of meteoric processes involving rainout of liquid water suggests that a substantial Martian atmosphere may have existed. Whether this was transient volcanically induced atmosphere or a more long-term atmosphere is unknown.

- *If a warm, dense atmosphere once existed, what were the sources of the volatiles: solar wind? Outgassing? Comets?*

  To answer this question requires an age for the Ca-rich generation of carbonate. However, a post 3.9Ga (and therefore a post late bombardment and hydrodynamic loss) carbonate with δD of only +500‰ suggests that at the mantle and crust was not totally degassed of volatiles early in Martian history.

- *If a warm, dense atmosphere once existed, what was the fate of these volatiles: were they lost to space or fixed in surface minerals such as carbonates or a subsurface reservoir?*

  Again, an age for Ca-rich carbonate would be invaluable. If Ca-rich carbonate is found to be relatively young (perhaps <2Ga) one might infer that the $\delta^{18}O$ depleted (possibly meteoric) source has been remelted by relatively recent volcanism. This would be evidence that percolation and trapping of surface volatiles back into the regolith is a valid sink for volatiles.

- *How much exchange occurred between the different volatile reservoirs?*

Again, if meteoric water is a possible source of $\delta^{18}O$ depleted water, the presence of 'rain water' within a subsurface rock implies atmosphere-regolith exchange occurred on Mars. The absence of large enrichment in $\delta^{18}O$ also suggests a regolith buffer which reservoirs greater than that of the atmosphere. In addition, the likely absence of $\delta^{18}C$ enrichment between ALH84001 rosettes and Nakhla also suggests buffering of CO_2 by a subsurface reservoir.

Chapter 14

References

Aahron P., (1988) A stable-isotope study of magnesites from the Rum Jungle uranium field, Australia: implications for the origin of strata-bounded massive magnetites. *Chem. Geol.* **69**, 127-145.

Baker, V. R. (1991) Ancient oceans, ice sheets, and the hydrological cycle on Mars. *Nature* **352,** 589–594.

Bao-Long Xu and Yong-Fei Zheng (1999) Experimental studies of oxygen and hydrogen isotope fractionations between precipitated brucite and water at low temperatures, *Geochim. Cosmochim. Acta*, **63**, 2009-2018

Barlow G., Perez C.B. and Saldarriage P.C. (1999) Distribution of subsurface volatiles across the equatorial region of Mars. *Lunar Planet. Sci. XXX*, Abstract #1679, Lunar and Planetary Institute, Houston (CD-ROM).

Barrat J.A., Gillet P.H., Lécuyer C., Sheppard S.M.F., and Lesourd M. (1998) Formation of carbonates in the Tatahouine meteorite. *Science* **280**, 412-414.

Barrat J.A., Gillet P.H., Lesourd M., Blichert-Toft J., and Popeau G.R. (1999) The Tatahouine diogenite: Mineralogical and chemical effects of sixty-three years of terrestrial residence. *Meteoritics Planet. Sci.* **34**, 91-97.

Bhattacharya, S.K., Savarino, J. and Thiemens, M.H. (2000) A new class of oxygen isotopic fractionation in photodissociation of carbon dioxide: potential implications for atmospheres of Mars and Earth.

Becker R. H. and Pepin R. O. (1984) The case for a martian origin of the shergottites: Nitrogen and noble gases in EETA79001. *Earth Planet. Sci. Lett.* **69,** 225-242.

Bjoraker G.L., Mumma M.J. and Larson H.P. (1989) Isotopic abundance ratios for hydrogen and oxygen in the martian atmosphere. *Bull. Amer. Astron. Soc.*, **21**, 990.

Blake D.M., Treiman A.H., Amundsen H.E.F., Mojzsis S.J., and Bunch T. (1999) Carbonate globules, analogous to those in ALH 84001, from Spitzbergen, Norway: Formation in a hydrothermal environment. Lunar Planet. Sci. XXX, Abstract #1683, Lunar and Planetary Institute, Houston (CD-ROM).

Bockelee-Morvan, D., Gautier D., Lis, D.C., Young K., Keene J., Phillips T., Owen T., Crovisier J., Goldsmith P.F., Bergin A., Despois D. and Wootten A. (1998) Deuterated water in comet C/1996 B2 (Hyakutake) and its implications for the origins of comets. *Icarus*, **193**, 147-162.

Boctor N.Z., Wang J., Alexander C.M.O'D., Hauri E., Bertka C.M., Fei Y. and Humayun M. (1998) Petrology and hydrogen and sulphur isotope studies of mineral phases in

Martian Meteorite ALH84001. *Lunar Planet. Sci. XXIX*, Abstract #1787, Lunar and Planetary Institute, Houston (CD-ROM).

Boctor N.Z., Wang J., Alexander C.M.O'D., Hauri E.(1999a) Hydrogen isotope studies of carbonate and feldspathic glasses in martian meteorites ALH 84001 and EETA 79001. *62nd Meteoritical Society Conference* (#5210).

Boctor N.Z., Wang J., Alexander C.M.O'D., Hauri E., Bertka C.M. and Fei Y. (1999b) Hydrogen isotope studies of feldspathic and mafic glasses in martian meteorites ALH84001 and EETA 79001. *Lunar Planet. Sci. XXX*, Abstract #1397, Lunar and Planetary Institute, Houston (CD-ROM).

Bodnar R.J., (1999) Fluid inclusions in ALH 84001 and other martian meteorites: evidence for volatiles on Mars. *Lunar Planet. Sci. XXX*, Abstract #1222, Lunar and Planetary Institute, Houston (CD-ROM).

Bogard D.D. and Husain L. (1977) A new 1.3 aeon-young achondrite. *Geophys. Res. Lett.* **4**, 49-71.

Bogard D.D. and Johnson P. (1983) Martian gases in an Antarctic meteorite. *Science*, **221**, 651-654.

Bogard D.D. and Garrison D.H. (1999) Argon-39-Argon-40 "ages" and trapped argon in Martian shergottites, Chassigny, and Allan Hills 84001. *Meteorit. Planet. Sci.* **34**, 451-473.

Bogard D.D., Clayton R.N., Marti K., Owen T. and Turner G. (2001) Martian volatiles: isotopic composition, origin and evolution. In *Chronology and Evolution of Mars*, **96**, 425-458. Kluwer academic publishers.

Bolton D. (1980) The computation of Equivalent Potential Temperature. *Monthly Weather Review*, **108**, 1046-1053.

Borg L. E., Nyquist L. E., Taylor L. A., Wiesmann H. and Shih C.-Y. (1997b) Constraints on Martian differentiation processes from Rb-Sr and Sm-Nd isotopic analyses of the basaltic shergottite QUE94201. *Geochim. Cosmochim. Acta* **61**, 4915-4931.

Borg L.E., Connelly J.N., Nyquist L.E., Shih C.Y., Wiesmann H and Reese Y. (1999) The age of the carbonates in martian meteorite ALH84001. *Science* **286**, 90-94.

Bottinga Y. (1968) Calculation of fractionation factors for carbon and oxygen isotopic exchange in the system calcite-carbon dioxide-water. *Journ. Phys. Chem.* **72**, 801-805.

Bottinga Y. and Javoy M. (1973) Comments on oxygen isotope geothermometry. *Earth. Planet. Sci. Lett.*, **20**, 250-265.

Bottinga Y. and Javoy M. (1975) Oxygen isotope partitioning among the minerals in igneous and metamorphic rocks. *Rev. Geophys. Space. Phys.*, **13**, 401-418.

Bradley J.P., Harvey R.P. and McSween Jr. H.P. (1996) Magnetite whiskers and platelets in the ALH 84001 martian meteorite: Evidence of vapor phase growth. *Geochim. Cosmochim. Acta.* **60**. 5149-5155.

Brain D.A. and Jakosky B.M. (1998) Loss of martian atmosphere by impacts sine the formation of the martian geological record. *Lunar Planet. Sci. XXIX*, Abstract #1807, Lunar and Planetary Institute, Houston (CD-ROM).

Braun R.M., Blenkinsopp P., Mullock S.J., Corlett C., Willey K.F., Vickerman J.C., Winograd N. (1998) Performance characteristics of a chemical imaging time-of-flight mass spectrometer. *Rapid Comm. Mass Spec.*, **12**, 1246-1252.

Brearley A.J. (1998) Rare K-bearing mica in ALH 84001: additional constraints on carbonate formation. *Lunar & Planetary Institute contribution. Workshop on martian Meteorites* **956**, 6-8.

Brearley, A.J. (2000) Hydrous Phases in ALH84001: Further Evidence for Preterrestrial Alteration and a Shock-induced Thermal Overprint, *Proc. 31 st Lunar Planet. Sci. Conf.*, abstract #1203 (CD-ROM).

Bridges J.C. and Grady M.M. (1998) Traces of martian sediment in Nakhla and other SNC meteorites. (Abstract #5199) *61st Meteoritical Society Conference*,

Bridges J.C. and Grady M.M. (1999) A halite-siderite-anhydrite-chlorapatite assemblage in Nakhla: mineralogical evidence for evaporites on Mars. *Meteoritics Planet. Sci.* **34**, 407-415.

Bridges, J.C., and Grady, M.M. (2000) 'Evaporite Mineral Assemblages in the Nakhlite (Martian) Meteorites', *Earth Planet. Sci. Lett.* **176**, 267–279.

Bridges J.C., Catling D.C., Saxton J.M., Swindle T.D., Lyon I.C. and Grady M.M. (2001) Alteration assemblages in martian meteorites: implications for near-surface processes. In *Chronology and Evolution of Mars*, 96, 365–392. Kluwer Academic Publishers.

Carr M.H. (1986) Mars: A water rich planet? *Icarus*, **56**, 187-216.

Carr M.H. (1996) Water on Mars. Oxford University Press.

Carr M.H. (1997) Sample return and climate. In *Mars 2005 sample return workshop. (ed.* Gulick) *LPI Tech. Rpt.* **97-1,** 34-43. Lunar Planetary Institute, Houston.

Carr, R.H., Grady, M.M., Wright I.P., Pillinger C.T. (1985) Martian atmospheric carbon dioxide and weathering products in SNC meteorites. *Nature*, **314**, 248-250.

Chacko T., Mayeda T. K., Clayton R. N., and Goldsmith J. R. (1991) Oxygen and carbon isotope fractionations between CO2 and calcite. *Geochim. Cosmochim. Acta* **55,** 2867–2882.

Channer D.M.DeR., De Ronde C.E.J., Spooner E.T.C. (1997) The Cl-Br-I composition of ~ 3.23 Ga modified seawater: implications for the geological evolution of ocean halide chemistry, *Earth Planet. Sci. Lett.*, **150**, 325-335.

Chatzitheodoris E. and Turner G. (1990) Secondary minerals in the Nakhla meteorite (abstract) Meteoritics **25**, 354.

Chen A.H. and Wasserburg G.J. (1986) Formation ages and evolution of Shergotty and its parent planet from U-Th-Pb systematics. *Geochim. Cosmochim. Acta*, **50**, 955-968.

Cherniak D.J. (2001) Pb diffusion in Cr diopside, augite, and enstatite, and consideration of the dependence of cation diffusion of pyroxene on oxygen fugacity. *Chem. Geol.*, **177**, 381-397.

H. Chiba, T. Chacko, R.N. Clayton, J.R. Goldsmith (1989) Oxygen isotope fractionations involving diopside, forsterite, magnetite and calcite: Application to geothermometry. *Geochim. Cosmochim. Acta* **53**, 2985–2995.

Christensen P.R., Bandfield J.L., Hamilton V.E., Ruff S.W., Kieffer H.H., Titus T.N., Malin M.C., Lane M.D., Clark R.L., Jakosky B.M., Mellon M.T., Pearl J.C., Smith M.D., Clancy R.T., Kuzmin R.O., Roush T., Mehall, G.L., Gorelick N., Bender K., Murray K., Dason S., Greene E., Silverman S. (2001) Mars global surveyor thermal emission spectrometer experiment: Investigation description and surface science results. *Journal of Geophysical Research E: Planets*, **106**, 23823-23871.

Christensen P. (1998) Press release from American Geophysical Union meeting, May 27th, 1998.

Clayton R. N. (1993b) Oxygen isotope analysis of ALH 84001. In *Antarctic Meteorite Newsletter* **16 (3),** 4. JSC Curator's Office, Houston.

Clayton R. N. and Mayeda T. K. (1988) Isotopic composition of carbonate in EETA79001 and its relation to parent body volatiles. *Geochim. Cosmochim. Acta* **52,** 925-927.

Clayton R. N. and Mayeda T. K. (1996) Oxygen isotope studies of achondrites. *Geochim. Cosmochim. Acta*, **60**, 1999-2017.

Cliff, S.S. and Thiemens M.H. (1997) The $^{18}O/^{16}O$ and $^{17}O/^{16}O$ ratios in atmospheric nitrous oxide: a mass-independent anomaly. *Science*, **278**, 1774-1776.

Costard F. and Gautier E. (1998) Siberian rivers and martian outflows: an analogy. *Lunar Planet. Sci. XXIX*, Abstract #1268, Lunar and Planetary Institute, Houston (CD-ROM).

Craddock R.A., Maxwell T.A., Howard A.D., (1998) The evidence for rainfall on early Mars *Lunar Planet. Sci. XXIX*, Abstract #1429, Lunar and Planetary Institute, Houston (CD-ROM).

Craddock R.A., Maxwell T.A., Howard A.D., (1999) The evidence for climatic variations in early Mars *Lunar Planet. Sci. XXX*, Abstract #1977, Lunar and Planetary Institute, Houston (CD-ROM).

Dimanov A., Jaoul O. and Sautter V. (1996) Calcium self-diffusion in natural diopside single crystals. *Geochim. Cosmochim. Acta*, **60**, 4095-4106.

Donahue T.M. (1995) Evolution of water reservoirs on Mars from D / H ratios in the atmosphere and crust. *Nature* **374**, 432-434.

Dreibus G., Spettel B., Wlotzka F., Schultz L., Weber H. W., Jochum K. P. and H. Wänke (1996b) QUE94201: An unusual Martian basalt. (abs) *Meteoritics & Planet. Sci.* **31**, A39-40.

Dreibus G., Burghele A., Jochum K.L., Spettel B., Wlotzka F. and Wänke H. (1994) Chemical and mineral compositions of ALH 84001: A martian orthopyroxenite (abs) *Meteoritics* **29**, 461.

Dreibus, G. and Wanke H., (1987) Volatiles on Earth and Mars: a comparison. *Icarus*, **71**, 225-240.

Eiler J.M., Kitchen N. and Rahn T.A. (2000) Experimental constraints on the stable-isotope systematics of CO_2 ice/vapor systems and relevance to the study of Mars. *Geochim. Cosmochim. Acta*, **64**, 733-746.

Eiler J., Valley J. W., Graham C. M. and Fournelle J. (2002) Two populations of carbonate in ALH84001: Geochemical evidence for discrimination and genesis. *Geochim. Cosmochim. Acta,* **66**, 1285-1303.

Fairchild I.J., Bradby L. and Spiro B. (1993) Carbonate diagenesis in ice. *Geology*, **21**, 901-904.

Eugster O., Weigel A. and Polnau E. (1996) Two different ejection events for basaltic shergottites QUE94201, Zagami and Shergotty (2.6 Ma ago) and lherzolitic shergottites LEW88516 and ALHA77005 (3.5 Ma ago). (abs) *Lunar Planet. Sci.* **XXVII**, 345-346.

Fallick A.E. (1983) No unusual isotopic compositions of the stable isotopes nitrogen, carbon and hydrogen in the SNC meteorites. *Lunar. Planet. Sci.*, **XIV**, 183-184.

Fanale F.P., Postawko S.E., Pollack J.B., Carr M.H. and Pepin R.O. (1992) in *Mars* (eds Kieffer H.H., Jakosky B.M., Snyder C.W. and Matthews M.W.) Univ. Arizona Press, Tucson, Arizona. 1135-1179.

Farquhar J., Thiemens M.H. and Jackson T. (1999) $\Delta^{17}O$ anomalies in carbonate from Nakhla and Lafayette and $\Delta^{33}S$ anomalies in sulphur from Nakhla: implications for atmospheric chemical interactions with the martian regolith. *Lunar Planet. Sci. XXX*, Abstract #1675, Lunar and Planetary Institute, Houston (CD-ROM).

Farquhar, J. and Thiemens, M.H. (2000) Oxygen Cycle of the Martian Atmosphere-regolith System: $\Delta^{17}O$ of Secondary Phases in Nakhla and Lafayette, *J. Geophys. Res.* **105**, 11,991–11,997.

Faure, G. (1986) Principles of isotope Geology 2nd edition., John Wiley, New York.

Fisler D.K. and Cygan R.T. (1998) Cation diffusion in calcite: determining closure temperatures and the thermal history for the Allan Hills 84001 meteorite. *Meteor. Planet. Sci.* **33**, 785-789.

Forget, F. and Pierrehumbert, R.T. (1997) Warming early Mars with carbon dioxide clouds that scatter infrared radiation. *Science*, **278**, 1273-1276.

Franchi I.A., Wright I.P., Sexton A.S. and Pillinger C.T. (1999) The oxygen-isotopic composition of Earth and Mars. *Meteoritics Planet. Sci.* **34**, 657-661.

Friedman I. and O'Neil J.R. (1977) Data of geochemistry. Ch. KK. Compilation of stable isotope fractionation factors of geochemical interest. *Geol. Surv. Prof. Paper 440-KK* 6th edition.

Gale N.H., Arden J.W. and Hutchinson R. (1975) The chronology of the Nakhla achondritic meteorite. *Earth. Planet. Sci. Lett.* **26**, 195-206.

Geiss J. and Gloecker G. (1998) Abundances of deuterium and helium-3 in the protostar cloud. *Space Sci. Rev.* **84**, 239-250.

Ghosh S. and Mahajan K.K. (1998) Mars water abundance: an estimate from D / H ratio in SNC meteorites. *Journ. Geophys. Res.* **103**, 5919-5927.

Gilmour J.D., Lyon I.C., Saxton J.M., Turner G. and Whitby J.A. (1997a) Oxygen and noble gas isotope constraints on the origin of ALH84001 carbonate. *Lunar Planet. Sci. XXVII*, Abstract, Lunar and Planetary Institute, Houston.

Gilmour J.D., Wogelius R.A., Grime G.W., and Turner G. (1997b) Major- and trace-element distributions in Allan Hills 84001 carbonate: Indication of a high formation temperature. *In Conference on Early Mars* (eds. S.M.Clifford and A.H.Treiman), 37-38. LPI. Contribution No.916, Lunar Planetary Institute, Houston, Texas, U.S.A.

Gilmour J.D., Xenon isotopes in irradiated ALH84001: evidence for shock-induced trapping of ancient martian atmosphere (1998) *Geochim. Cosmochim. Acta.* **62**, 2555-2571.

Gilmour J.D., Whitby J.A. and Turner G. (1999) Comparative iodine geochemistry of Earth and Mars: a possible biomarker? *Lunar Planet. Sci. XXX*, Abstract #1661, Lunar and Planetary Institute, Houston.

Gleason J. D., Kring D. A., Hill D. H. and Boynton W. V. (1997) Petrography and bulk chemistry of Martian orthopyroxenite ALH 84001: Implications for the origin of secondary carbonates. *Geochem. Cosmochim. Acta,* **61**, 3503-3512.

Golombek, M. P. & Bridges, N. T. (2000) Erosion rates on Mars and implications for climate change: constraints from the Pathfinder landing site. *J. Geophys. Res.* **105,** 1841–1853.

Gooding J.L., (1986) Clay mineraloid weathering products in the Antarctic meteorites. *Geochim. Cosmochim. Acta.* 50, 2215-2223.

Gooding J. L., Wentworth S. J. and Zolensky M. E. (1988) Calcium carbonate and sulfate of possible extraterrestrial origin in the EETA79001 meteorite. *Geochim. Cosmochim. Acta,* **52,** 909-915.

Gooding J.L., Wentworth S.J. and Zolensky M.E. (1991) Aqueous alteration of Nakhla meteorite. *Meteoritics* **26**, 135-143.

Grady M.M., Wright I.P., Pillinger C.T. (1997) Carbon and nitrogen isotope study of Zagami. *Journ. Geophys. Res.* **102**, 9165-9173.

Greenwood J.P. and McSween H.Y. Jr. (2001) Petrogenesis of Allan Hills 84001: constraints from impact-melted feldspathic and silica glasses.

Griffith L.L and Shock E.L. (1995) A geochemical model for the formation of hydrothermal carbonates on Mars. *Nature*, **377**, 406-408.

Griffith L.L. and Shock E.L. (1997) Hydrothermal hydration of martian crust: Illustration via geochemical model calculations. *Journ. Geophys. Res.* **102**, 9135-9143.

Gulick V.C., Marley M.S. and Baker V.R., (1991) Numerical modelling of hydrothermal systems on martian volcanoes: Preliminary results (abstract) *Lunar. Planet. Sci.*, **22**, 509-510.

Haberle R.M., Tyler D., McKay C.P. and Davis W.L. (1994) A model for the evolution of CO_2 on Mars. *Icarus* **109**, 102-120.

Haberle R.M. (1998) Early Mars climate models. *Journ. Geophys. Res.*, **103**, 28467-28479.

Hartmann W.K., Malin M., McEwen A., Carr M., Soderbolm L., Thomas P., Danielson E., James P and Veverka J. (1999) Evidence for recent volcanism on Mars from crater counts. *Nature* **397**, 586-589.

Harvey R. P. and McSween H. Y., Jr. (1992b) Petrogenesis of the nakhlite meteorites: Evidence from cumulate mineral zoning. *Geochim. Cosmochim. Acta* **56,** 1655-1663.

Harvey R.P. and McSween H.Y. Jr. (1996) A possible high-temperature origin for the carbonates in the martian meteorite ALH 84001. *Nature,* **382,** 49-51.

Harvey R.P. (1998) Formation of carbonates in Allan Hills 84001 by impact metasomatism: cooking with gas. *Lunar & Planetary Institute contribution. Workshop on martian Meteorites* **956**, 20-22.

Head, J.W., H. Heisinger, M.A. Ivanov, M.A. Kreslavsky, S. Pratt, B.J. Thomson (1999) Possible ancient oceans on Mars: evidence from Mars Orbiter Laser Altimeter data.. *Science*, **286,** 2134-2137.

Hoefs J. (1997) Stable isotope geochemistry *Springer Berlin*, 201.

Hoffert, M.I., Calegeri A.J., Hsieh C.T. and Ziegler W. (1981) An energy balance climate model for CO_2/H_2O atmospheres. *Icarus*, **47**, 112-129.

Huff, A.K. and Thiemens, M.H. (1998) $^{17}O/^{16}O$ and $^{18}O/^{16}O$ isotope measurements of atmospheric carbon monoxide and its sources. *Geophys. Res. Lett.*, **20 (15),** 3509-3512.7

Hutchins K. S. and Jakosky B. M. (1997) Carbonates in martian meteorite ALH 84001: A planetary perspective on the formation temperature. *Geophys. Res. Let.* **24**, 819-822.

Jagoutz E. and Wänke H. (1986) Sr and Nd isotopic systematics of Shergotty meteorite. *Geochim. Cosmochim. Acta* **50,** 939-953.

Jakosky B.M. (1993) Mars volatile evolution: Implications of the recent measurement of ^{17}O in water from the SNC meteorites. *Geophys. Res. Lett.* **20,** 1591-1594.

Jakosky B.M., Henderson B.G. and Mellon M.T. (1995) Chaotic obliquity and the nature of the martian climate. *Journ. Geophys. Res.* **100**, 1579-1584.

Jull A.J.T., Eastoe C. J., Xue S. and Herzog G. F. (1995) Isotopic composition of carbonate in the SNC meteorites ALH 84001 and Nakhla. *Meteoritics* **30**, 311-318.

Jull A.J.T, Eastoe C.J. and Cloudt S. (1997) Isotopic composition of carbonates in the SNC meteorite Allan Hills 84001 and Zagami. *Journ. Geophys. Res.* **102**, 1663-1669.

Karlsson H. R., Clayton R. N., Gibson E. K., Jr. and Mayeda T. K. (1992) Water in SNC meteorites: Evidence for a martian hydrosphere. *Science,* **255,** 1409-1411.

Kass D. M. and Yung Y. L. (1996) Loss of atmosphere from Mars due to solar wind-induced sputtering. *Science* **268,** 697–699.

Kent A. J. R., Hutcheon I. D., Ryerson F. J. and Phinney D. L. (2001) The temperature of formation of carbonate in Martian meteorite ALH84001: constraints from cation diffusion. *Geochim. Cosmochim. Acta* **65**, 311-321.

Kerridge J. F. (1988) Deuterium in Shergotty and Lafayette (and on Mars?) (abs) *Lunar Planet. Sci.* **XIX**, 599-600.

Kieffer H.H., Jakosky B.M., Snyder C.W. and Matthews M.W. (1992) *Mars*. Univ. Arizona Press, Tucson, Arizona. p357

Krasnopolsky V.A. (1986) In *Photochemistry of the Atmospheres of Venus and Mars* (Berlin: Springer-Verlag) 69-74.

Krasnopolsky V.A., Mumma M.J., Bjoraker G.L. and Jennings D.E. (1996) Oxygen and carbon isotope ratios in martian carbon dioxide: measurements and implications for atmospheric evolution. *Icarus* **124**, 553-568.

Krasnopolsky, V.A., Mumma M.J. and Gladstone G.R. (1998) Detection of atomic deuterium in the upper atmosphere of Mars. *Science*, **280**, 1576-1580.

Kring D. A., Swindle T. D., Gleason J. D., and Grier J. A. (1998) Formation and relative ages of maskelynite and carbonate in the martian meteorite ALH 84001. *Geochim. Cosmochim. Acta* **62**, 2155-2166.

Leshin L.A., Epstein S. and Stolper E.M. (1996) Hydrogen geochemistry of SNC meteorites. *Geochim. Cosmochim. Acta* **60**, 2635-2650.

Leshin L. A., McKeegan K. D., Carpenter P. K., and Harvey R. P. (1998) Oxygen isotopic constraints on the genesis of carbonates from martian meteorite ALH 84001. *Geochim. Cosmochim. Acta* **62**, 3-13.

Leshin L.A. (2000) Insights into martian water reservoirs from analyses of martian meteorite QUE94201. *Geophys. Res. Lett.* **27**, 2017-2020.

Luz, B., Barkan E., Bender M.L., Thiemens M.H. and Boering K.A. (1999) Triple isotope composition of atmospheric oxygen as a tracer of biosphere activity. *Nature*, **400**, 547-550.

Lyon I.C., Saxton J.M. and Turner G. (1994) Isotopic Fractionation in Secondary Ionization Mass Spectrometry. *Rapid communications in mass spectrometry* **8**, 837-843.

Mahaffy, P.R. Donahue T.M., Atreya S.K., Owen T.B. and Niemann H.B. (1998) Galileo probe measurements of D/H and $^{3}He/^{4}He$ in Jupiter's atmosphere. *Space Sci. Rev.* **84**, 251-263.

Majzoub M. (1971) Fractionation of oxygen-18 and deuterium between water and its vapour. *Journ. Chem. Phys.* **63**, 563-568.

Martinez I., Agrinier P., Schärer U. and Javoy M. (1994) A SEM-ATEM and stable isotope study of carbonates from the Haughton impact crater, Canada, *Earth Planet. Sci. Lett.* **121**, 559-574.

Mazaud, A. Vimeux F., and Jouzel J. (2000) Short fluctuations in Antarctic isotope records: a link with cold events in the North Atlantic? *Earth Planet. Sci. Lett.* **177**, 219-225.

McKay, D.S., Gibson E.K., Jr., Thomas-Keptra K.L., Vali H., Romanek C.S., Clemett S.J., Chillier X.D.F., Maechling C.R. and Zare, R.N. (1996a) Search for past life on Mars: Possible relic biogenic activity in martian meteorite ALH 84001. *Science* **273**, 924-930

McKay G. A., Yang S.-R. and Wagstaff J. (1996) Complex zoned pyroxenes in shergottite QUE94201: Evidence for a two-stage crystallization history. (abs) *Lunar Planet. Sci.* **XXVII**, 851-852.

McKenzie D. and Nimmo F. (1999) The generation of martian floods by the melting of ground ice above dykes. *Nature*, **397**, 231-233.

McSween, H.Y .Jr., (1994) What we have learned about Mars from SNC meteorites. *Meteoritics* **29**, 757-779

McSween H. Y., Jr., Eisenhour D. D., Taylor L. A., Wadhwa M. and Crozaz G. (1996) QUE94201 shergottite: Crystallization of a Martian basaltic magma. *Geochim. Cosmochim. Acta* **60**, 4563-4569.

McSween H. Y. Jr. (1996) Evidence for ancient life in a Martian meteorite. *Meteoritics & Planet. Sci.* **31**, 691-692.

McSween H.Y. Jr. and Harvey R.P. (1998) An evaporation model for formation of carbonates in the ALH84001 Martian meteorite *Intl. Geol. Rev.*, **40**, 774-783.

Meier, R.T. Owen T., Jewitt D.C., Matthews H.M., Bockelee-Morvan, D., Biver N., Crovisier J. and Gautier D. (1998) A determination of the HDO/H_2O ratio in comet C/1995 O1 (Hale-Bopp). *Science*, **279**, 842-848.

Melosh H.J. and Vickery A.M. (1989) Impact erosion of the primordial atmosphere of Mars. *Nature*, **338**, 487-489.

Mikouchi T., Miyamoto M. and McKay G. A. (1998a) Mineralogy of Antarctic basaltic shergottite Queen Alexandra Range 94201: Similarities to Elephant Moraine A79001 (Lithology B) Martian meteorite. *Meteoritics Planet. Science* **33**, 181-189.

Mittlefehldt D. W., Lindstrom D. J., Lindstrom M. M. and Martinez R. R. (1997a) Lithology A in EETA79001-Product of impact melting on Mars. (abs) *Lunar Planet. Sci.* **XXVIII**, 961-962.

Mittlefehldt, D.W. (1994a) ALH 84001, a cumulate orthopyroxenite member of the martian meteorite clan. *Meteoritics* **29**, 214-221

Mojzsis S.J., Coath C.D., Bunch T., Blake D., and Treiman A.H. (1999) Carbonate "rosettes" in xenoliths from Spitzbergen: SIMS analysis of O and C isotope ratios in a potential terrestrial analogue to martian meteorite ALH 84001. *Lunar Planet. Sci. XXX*, Abstract #2032, Lunar and Planetary Institute, Houston (CD-ROM).

Musselwhite D. and Lunine J.L. (1995) Alteration of volatile inventories by polar clathrate formation on Mars. *Journ. Geophys. Res.* **100**, 23301-23306.

Nakamura N., Unruh D.M., Tatsumoto T. and Hutchinson R. (1982a) Origin and evolution of the Nakhla meteorite inferred from Sm-Nd and U-Pb systematics and REE, Ba, Sr, Rb abundances. *Geochim. Cosmochim. Acta* **46**, 1555-1573.

Neukum, G. & Wise, D.U. (1976) Mars, a standard crater curve and possible new time scale. *Science*, **194**, 1381-1387

Neukum, G., Ivanov B.A. and Hartmann, W.K. (2001) Cratering records in the inner solar system in relation to the lunar reference system. In *Chronology and Evolution of Mars*, **96**, 55-86. Kluwer academic publishers.

Nier A.O. and McElroy M.B. (1977) Composition and structure of Mars' upper atmosphere: results from the neutral mass spectrometers on Viking 1 and 2. *J. Geophys. Res.* **82**, 4341-4349.

Niles P.B., Leshin L.A., Guan Y. and Hervig R.L. (2002) Carbon isotopic composition of ALH84001 carbonates: an ion microprobe study. *Lunar Planet. Sci. XXXIII*, Abstract #1655, Lunar and Planetary Institute, Houston (CD-ROM).

Nyquist L.E., Horz F., Wiesmann H., Shih C.-Y. and Bansal B. (1987) Isotopic studies of shergottite chronology: effect of shock metamorphism on the Rb-Sr system (Abstract). *Lunar Planet. Sci.* **18**, 732-733.

Nyquist L. E., Bansal B., Wiesmann H. and C.-Y. Shih (1995) "martians" young and old: Zagami and ALH 84001. (abs) *Lunar Planet. Sci. XXVI*, 1065-1066.

Nyquist L.E., Reese Y., Wiesmann H. and Shih C.-Y., (2001) Age of EET9001B and implications for shergottite origins. *Lunar Planet. Sci. XXXII*, Abstract #1407, Lunar and Planetary Institute, Houston (CD-ROM).

Owen T., Biemann K., Rushneck D.R., Biller J.E., Howarth D.W. and Lafleur, A.L. (1977) The composition of the atmosphere at the surface of Mars. *J. Geophys. Res.*, **82**, 4635-4639.

Owen T., Maillard J.P., de Bergh C. and Lutz B.L. (1988) Deuterium on Mars: The abundance of HDO and the value of D/H. *Science*, **240**, 1767-1770.

Owen, T., (1992) Composition and early history of the atmosphere. In Mars (Kieffer H.H. *et al.*, eds) University of Arizona Press, Tucson, pp. 818-834.

Owen T. and Bar-Nun A. (2000) Volatile contributions from icy planetesimals *in Origin of the Earth and Moon*. R.N. Canup and K. Righter (eds) University of Arizona, Tucson.

Owen, T. (2001) Inner planet atmospheres: the case for cometary contributions (abs). *Meteoritics & Planet. Sci.* **36**, 9, A156.

Pepin R. O. (1991) On the origin and early evolution of terrestrial planet atmospheres and meteoritic volatiles. *Icarus*, **92**, 2-79.

Pepin R.O. (1994) Evolution of the martian atmosphere *Icarus* **111**, 289-304.

Pillinger C. T. (1984) Light element stable isotopes in meteorites - from grams to picograms. *Geochim. Cosmochim. Acta* **48**, 2739-2766.

Podosek F.A. (1973) Thermal history of the nakhlites by the $^{40}Ar/^{39}Ar$ method. *Earth Planet. Sci. Lett.* **19**, 135-144.

Pollack, J.B., (1979) Climate change on the terrestrial planets. *Icarus*, **37**, 203-224.

Pollack, J.B. and Black D.C. (1979) Implications of the gas compositional measurements of Pioneer Venus for the origin of planetary atmospheres. *Science*, **205**, 56-59.

Pollack, J.B., Kasting J.F., Richardson S.M. and Poliakoff K., (1987) The case for a warm, wet climate on early Mars. *Icarus*, **71**, 203-224.

Romanek C.S., Grady M.M., Wright I.P., Mittlefehldt D.W., Socki R.A., Pillinger C.T. and Gibson Jr. E.K. (1994) record of fluid-rock interactions on Mars from the meteorite ALH84001. *Nature* **372**, 655-656.

Rosenbaum J.M. (1997) Gaseous, liquid and supercritical H_2O and CO_2: oxygen isotopic fractionation behaviour. *Geochim. Cosmochim. Acta* **61**, 4993-5003.

Rieder R., Economou T., Wänke H., Turkevich A., Crisp J., Brückner J., Dreibus G. and McSween Jr.H.Y. (1997) The chemical composition of martian soil and rocks returned by the mobile alpha proton x-ray spectrometer: Preliminary results from the X-ray mode. *Science*, **278**, 1771-1774.

Ryerson F.J. and McKeegan K.D. (1994) Determination of oxygen self-diffusion in akermanite, anorthite, diopside and spinel: implications for oxygen isotopic anomalies and thermal histories in Ca-Al-rich inclusions. *Geochim. Cosmochim. Acta* **58**, 3713-3734.

Savarino, J. and Thiemens M.H. (1999) Analytical procedure to determine both $\delta^{17}O$ and $\delta^{18}O$ of H_2O_2 in natural water and first measurements. *Atmos. Environ.*, **33(22)**, 3683-3690.

Saxton, J.M., Lyon I.C., Turner G. (1996) The Manchester Isolab 54 ion microprobe. *Int. Journ. Mass Spec. and Ion Processes* **154**, 99-131

Saxton, J.M., Lyon I.C., Turner G. (1998) Correlated chemical and isotopic zoning in carbonates in martian meteorites ALH 84001. *Earth and Planet. Sci. Lett.* **160**, 811-822

Saxton, J.M., Lyon I.C., Chatzitheodoridis and Turner G. (2000) Oxygen isotopic composition of carbonate in the Nakhla meteorite: implications for the hydrosphere and atmosphere of Mars. *Geochim. Cosmochim. Acta* **64**, 1299-1309.

Schwandt C.S., McKay G.A. and Lofgren G.E. (1999) FESEM imaging reveals previously unseen detail and enhances interpretations of ALH84001 carbonate petrogenesis. *Lunar Planet. Sci.* **XXX**, Abstract #1346, Lunar and Planetary Institute, Houston (CD-ROM).

Score R. and Mittlefehldt D. W. (1993) Macroscopic and thin section description of ALH 84001. In *Antarctic Meteorite Newsletter* **16 (3)**, 3. JSC Curator's Office, Houston.

Scott E.R.D., Yamaguchi A. and Krot A.N. (1997) Petrological evidence of carbonates in the martian meteorite ALH84001. *Science*, **387**, 377-379.

Scott E. R. D., Krot A. N., and Yamaguchi A. (1998a) Carbonates in fractures of martian meteorite ALH 84001: Petrologic evidence for impact origin. *Meteorit. & Planet. Sci.* **33**, 709-719.

Scott E.R.D and Krot A.N. (1998b) Origin of carbonate in martian meteorite Allan Hills 84001. *Lunar & Planetary Institute contribution. Workshop on martian Meteorites* **956**, 44-45.

Scott E.R.D. (1999) Origin of carbonate-magnetite-sulfide assemblages in martian meteorite ALH84001. *Journ. Geophys. Res.* **104**, 3803-3813.

Scott-Smith R., Dohnalek Z., Kimmel G.A., Stevenson K.P. and McKay B.D. (2000) The self-diffusivity of amorphous solid water near 150K. *Chem. Phys.*, **258**, 291-305.

Sears D. W. G. and Kral T. A. (1998) Martian "microfossils" in lunar meteorites? *Meteorit. Planet. Sci.* **33**, 791-794.

Shearer C.K., Leshin L.A. and Adcock C.T. (1999) Olivine in martian meteorite Allan Hills 84001: evidence for a high-temperature origin and implications for signs of life. *Meteorit. Planet. Sci.* **34**, 331-339.

Shih C.-Y., Nyquist L.E., Bogard D.D., McKay G.A., Wooden J.L., Bansal B.M. and Wiesmann H. (1982) Chronology and petrogenesis of young achondrites Shergotty, Zagami, and ALHA77005: late magmatism on a geologically active planet. *Geochem. Cosmochem. Acta.* **46**, 2323-2344.

Shih C.-Y., Nyquist L. E. and Wiesmann H. (1996) Sm-Nd systematics of nakhlite Governador Valadares. (abs) *Lunar Planet. Sci.* **XXVII**, 1197-1198.

Skála R. and Žák K., (2001) Stable isotope study of carbonates from the Ries meteorite crater – evidence for impact induced carbonate decomposition. *Lunar Planet. Sci.* **XXXII**, Abstract #1572, Lunar and Planetary Institute, Houston (CD-ROM).

Smith D.E., Zuber M.T., Solomon S.C., Phillips R.J., Head J.W., Garvin J.B., Banerdt W.B., Muhleman D.O., Pettengill G.H., Neumann G.A., Lemoine F.G., Abshire J.B., Aharonson O., Brown D.C., Hauck S.A., Ivanov A.B., McGovern P.J., Zwally H.J. and Duxbury T.C. (1999) The global topography of Mars and implications for surface evolution. *Science*, **284**, 1495-1503.

Smith J. V. and Hervig R. L. (1979) Shergotty meteorite: Mineralogy, petrography, and minor elements. *Meteoritics* **14**, 121-142.

Stephan T. (2001) TOF-SIMS in cosmochemistry. *Planetary and Space Science*, **49**, 859-906.

Sugiura, N., and Hoshino, H. (2000) Hydrogen Isotopic Composition of Allan Hills 84001 and the Evolution of the Martian Atmosphere, *Met. Planet. Sci.* **35**, 373–380.

Swindle T.D., Treiman A.H., Lindstrom D.J., Burkland M.K., Cohen B.A., Grier J.A., Li B. and Olson E.K. (2000) Noble gases in iddingsite from the Lafayette meteorite:

Evidence for liquid water on Mars in the last few hundred million years, Meteoritics and Planetary Science, Volume 35, Issue 1, 2000, Pages 107-115

Tanaka, K.L. (1986) The stratigraphy of Mars. *J. Geophys. Res. Suppl.* **91**, E139-E158

Taylor, H.P. Jr. (1974) The application of oxygen and hydrogen isotope studies to problems of hydrothermal alteration and ore deposition. *Econ. Geol.*, **69**, 843-883.

Thiemens, M.H. (1999) Mass-independent isotope effects in planetary atmospheres and the early solar system. *Science*, **283**, 341-345.

Thomas-Keprta K.L., Bazylinski D.A., Golden D.C., Wentworth S.J., Gibson E.K.Jr., and McKay D.S. (1998) Magnetite from ALH84001 carbonate globules: Evidence of biogenic signatures? *Lunar Planet. Sci.* **XXIX**, Abstract #1494, Lunar and Planetary Institute, Houston (CD-ROM).

Thomas-Keprta K.L., Wentworth S.J., McKay D.S., Bazylinski D., Bell M.S., Romanek C.S., Golden D.C., and Gibson E. K. Jr. (1999) On the origins of magnetite in martian meteorite ALH84001. *Lunar Planet. Sci.* **XXX**, Abstract #1856, Lunar and Planetary Institute, Houston (CD-ROM).

Treiman, A.H., Barrett R.A. and Gooding J.L. (1993) Preterrestrial aqueous alteration of the Lafayette (SNC) meteorite. *Meteoritics* **28**, 86-97.

Treiman, A.H. (1995) A petrographic history of martian meteorite ALH 84001: Two shocks and an ancient age. *Meteoritics* **30**, 294-302

Treiman, A.H. (1998) The history of Allan Hills 84001 revised: Multiple shock events. *Meteorit. & Planet. Sci.* **33**, 753-764

Treiman, A.H. and Romanek C.S., (1998) Bulk and stable isotopic compositions of carbonate minerals in the martian meteorite Allan Hills 84001: No proof of high formation temperature. *Meteorit. & Planet. Sci.* **33**, 737-742

Treiman, A.H., Gleason J.D. and Bogard D.D. (2000) The SNC meteorites are from Mars. *Planet. Space. Sci.*, **48**, 1213-1230.

Turner G., Knott S. F., Ash R. D. and Gilmour J. D. (1997) Ar-Ar chronology of the martian meteorite ALH 84001: Evidence for the timing of the early bombardment of Mars. *Geochim. Cosmochim. Acta* **61**,3835-3850.

Valley J.W., Eiler J.M., Graham C.M., Gibson E.K.Jr., Romanek C.S., and Stolper E.M. (1997) Low-temperature carbonate concretions in the martian meteorites ALH 84001: Evidence from stable isotopes and mineralogy. *Science* **275**, 1633-1638.

Vicenzi, E.P. and Eiler J. (1998) Oxygen isotopic composition of martian carbonate and high-resolution secondary ion mass spectrometer imaging of the alteration assemblage in Lafayette meteorite. (abstract #5304) *61st Meteoritical Society Conference*

Wadhwa M., McSween H. Y., Jr. and Crozaz G. (1994) Petrogenesis of shergottite meteorites inferred from minor and trace element microdistributions. *Geochim. Cosmochim. Acta* **58**, 4213-4229.

Wadhwa, M. and Crozaz, G. (1995), Trace and minor elements in minerals of nakhlites and Chassigny. *Geochim. Cosmochim. Acta* **59**, 3629-3645

Wänke, H., Brückner, J., Dreibus G., Rieder R. and Ryabchikov I. (2001) Chemical composition of rocks and soils at the Pathfinder site. In *Chronology and Evolution of Mars*, **96**, 317-330. Kluwer academic publishers.

Wardle R. and R.T. Pierrehumbert (2001) On the Width of Planetary Hadley Circulations submitted to *Geophys. Res. Lett.*

Warren P. H., (1998) Petrologic evidence for low-temperature, possibly flood evaporitic origin of carbonates in the ALH 84001 meteorite. *Journ. Geophys. Res.* **103**, 16759-16773.

Watson L. A., Hutcheon I.D., Epstein S. and Stolper E.M. (1994) Water on Mars: clues from deuteurium / hydrogen and water contents of hydrous phases in SNC meteorites. *Science* **265**, 86-90.

Wentworth S.J. and Gooding J.L. (1994) Carbonates and sulphates in the Chassigny meteorite: further evidence for aqueous chemistry in the SNC parent planet. *Meteoritics* **29**, 860-863.

Wentworth, S.J., and Gooding, J.L. (2000), Weathering and Secondary Minerals in the Martian Meteorite Shergotty, *Proc. 31 st Lunar Planet. Sci. Conf.*, abstract #1888 (CD-ROM).

Wiens R. C. and Pepin R. O. (1988) Laboratory shock emplacement of noble gases, nitrogen, and carbon dioxide into basalt, and implications for trapped gases in shergottite EETA79001. *Geochim. Cosmochim. Acta* **52,** 295-307.

Withers, P. and Neumann G.A. (2001) Enigmatic ridges on the plains of Mars. *Nature* **410**, 652.

Wooden J.L., Nyquist L.E., Bogard D.D., Bansal B.M., Wiesmann H., Shih C.-Y. and McKay G.A. (1979) Radiometric ages for the achondrites Chervony Kut, Governador Valadares and Allan Hills 77005 (abstract) *Lunar. Planet. Sci.* **20**, 1380-1381.

Worden R.H. (1996) Controls on halogen concentrations in sedimentary formation waters. *Min. Mag.*, 60, 259-274.

Wright I.P., Grady M.M. and Pillinger C.T. (1988) Carbon, oxygen and nitrogen isotopic compositions of possible martian weathering products in EETA 79001. *Geochem. Cosmochem. Acta.* **52**, 917-924.

Wright I.P., Grady M.M. and Pillinger C.T. (1990) The evolution of atmospheric CO_2 on Mars: The perspective from carbon isotope measurements. *Journ. Geophys. Res.* **95**, 14789-14794.

Wright I.P., Grady M.M. and Pillinger C.T. (1992) Chassigny and the nakhlites: carbon-bearing components and their relationship to martian environmental conditions. *Geochim. Cosmochim. Acta.* **56**, 817-826.

Yang J. and Epstein S. (1985) A study of stable isotopes in Shergotty meteorite. *Lunar. Planet. Sci.*,**XVI**, 25-26.

Yung, Y.L., Wen J.-S., Pinto J.P., Allen M., Pierce K.K. and Paulson S. (1988) HDO in the martian atmosphere: implications for the abundance of crustal water. *Icarus*, **76**, 146-159.

Zahnle K.J., Kasting J.F. and Pollack J.B. (1990) Mass fractionation of noble gases in diffusion-limited hydrodynamic hydrogen escape. *Icarus*, **84**, 502-527.

Chapter 15

Appendix

Cameca SX100 WDS EPMA analyses of ALH84001 carbonate

Grain 1	Molar % Fe	Molar % Ca	Molar % Mg	Molar % Si	Molar % Mn	totals	Carb type
1	13.81	51.91	27.28	0.21	6.24	99.24	Ca-rich
2	2.07	34.36	59.49	0.28	3.49	99.41	Ca-rich
3	19.30	6.48	71.58	0.59	1.05	98.41	rosette
4	11.57	9.18	74.98	1.77	1.15	96.89	rosette
5	21.72	6.41	68.90	0.72	0.93	97.96	rosette
6	22.86	4.63	69.84	0.26	1.05	98.37	rosette
7	21.30	5.69	70.65	0.18	1.01	98.64	rosette
8	26.03	15.34	41.69	11.53	2.95	86.01	Ca-rich
9	7.11	65.36	14.49	4.59	7.57	94.52	Ca-rich
10	12.77	53.27	27.14	0.24	6.28	99.46	Ca-rich
11	21.89	30.31	43.21	0.15	3.86	99.28	Ca-rich
12	29.51	18.69	46.80	1.09	2.41	97.40	Ca-rich
13	28.69	14.04	53.99	0.43	2.10	98.82	Ca-rich
14	31.30	16.07	48.36	0.19	3.25	98.98	Ca-rich
15	28.97	25.35	39.07	0.20	5.40	98.78	Ca-rich
16	6.51	70.27	15.34	0.10	7.71	99.83	Ca-rich
17	13.29	52.50	25.61	0.27	7.95	99.35	Ca-rich
18	5.32	73.80	12.73	0.40	7.18	99.04	Ca-rich
19	8.55	42.97	39.80	5.15	2.15	93.47	Ca-rich
20	8.57	11.89	71.02	6.79	0.48	91.96	rosette
21	12.27	30.03	48.05	7.56	0.60	90.96	rosette
22	4.61	73.07	14.47	0.32	7.10	99.26	Ca-rich
23	28.12	23.33	43.59	0.84	3.14	98.17	Ca-rich
24	32.38	17.57	46.20	0.48	2.45	98.59	Ca-rich
25	31.92	20.77	40.54	0.70	4.67	97.90	Ca-rich
26	28.42	25.14	40.97	0.31	4.20	98.73	Ca-rich
27	27.76	23.84	44.27	0.14	2.99	98.86	Ca-rich
28	30.48	18.05	48.30	0.16	2.31	99.14	Ca-rich
29	31.21	15.97	49.82	0.11	2.16	99.17	Ca-rich
30	32.18	14.30	49.94	0.36	2.33	98.75	Ca-rich
31	32.38	13.50	50.56	0.29	2.38	98.81	Ca-rich
32	30.37	15.80	45.71	3.24	3.86	95.73	Ca-rich
33	32.53	6.37	41.82	13.23	3.29	84.00	Ca-rich
34	18.08	40.59	34.37	1.62	4.69	97.73	Ca-rich
35	4.77	73.49	12.95	0.33	8.38	99.59	Ca-rich
36	6.71	53.51	28.58	3.87	6.57	95.37	Ca-rich
37	13.18	15.63	50.57	15.94	2.15	81.53	rosette
38	27.59	3.55	66.10	0.42	0.76	97.99	rosette
39	26.95	3.90	66.39	0.47	0.81	98.05	rosette
40	26.81	4.08	66.21	0.60	0.76	97.86	rosette
41	25.64	4.42	67.27	0.54	0.77	98.11	rosette
42	26.26	4.80	65.73	0.81	0.88	97.66	rosette
43	24.41	11.77	51.75	7.86	2.20	90.12	rosette

Grain 2	Molar % Fe	Molar % Ca	Molar % Mg	Molar % Si	Molar % Mn	totals	Carb type
1	22.91	12.11	61.81	1.01	0.78	97.60	rosette
2	0.60	4.31	94.41	0.42	0.06	99.38	rosette
3	9.92	6.41	82.83	0.23	0.29	99.44	rosette
4	14.29	5.15	79.87	0.13	0.18	99.49	rosette
5	26.94	8.03	64.00	0.17	0.25	99.22	rosette
6	31.20	9.89	56.68	0.58	0.17	97.95	rosette
7	8.01	5.09	18.29	26.66	0.10	31.50	rosette
8	9.94	0.99	27.04	34.14	0.23	38.19	rosette
9	2.75	6.12	87.87	1.15	0.27	97.02	rosette
10	5.27	4.68	89.49	0.24	0.04	99.49	rosette
11	15.27	4.80	78.64	0.07	0.69	99.41	rosette
12	2.30	3.66	93.58	0.30	0.04	99.58	rosette
13	29.17	8.60	60.95	0.43	0.20	98.92	rosette
14	29.85	10.28	58.12	0.67	0.41	98.65	rosette
15	3.18	5.19	7.52	31.68	0.07	15.96	rosette
16	31.79	17.56	48.41	0.20	2.07	99.83	rosette
17	21.97	30.16	43.65	0.41	3.52	99.30	Ca-rich
18	25.83	24.64	46.93	0.09	2.71	100.10	Ca-rich
19	35.88	15.42	46.51	0.12	2.31	100.12	Ca-rich
20	32.04	12.99	54.29	0.13	0.74	100.06	Ca-rich
21	34.11	16.79	46.88	0.22	2.00	99.78	Ca-rich
22	9.21	66.75	17.83	0.36	5.89	99.69	Ca-rich
23	13.80	50.55	28.55	0.49	6.31	99.21	Ca-rich
24	4.42	5.68	5.80	31.82	0.14	16.05	Ca-rich
25	18.22	11.25	22.63	18.76	1.30	53.41	Ca-rich
26	30.09	16.32	50.76	0.42	1.81	98.99	Ca-rich
27	0.36	4.00	0.10	36.35	0.02	4.49	Ca-rich
28	0.69	4.51	1.12	36.04	0.05	6.37	Ca-rich
29	5.35	75.89	12.05	0.36	6.34	99.63	Ca-rich
30	8.19	72.18	12.76	0.78	5.43	98.56	Ca-rich
31	15.28	46.01	33.13	0.34	5.34	99.76	Ca-rich
32	15.61	26.41	29.10	10.62	2.81	73.93	Ca-rich
33	24.37	21.42	30.43	7.44	3.21	79.43	Ca-rich
34	1.76	4.66	3.04	34.93	0.15	9.61	Ca-rich
35	29.40	17.38	39.11	4.71	3.62	89.51	Ca-rich
36	15.68	12.87	21.57	19.38	1.33	51.45	Ca-rich
37	15.23	47.68	31.28	0.51	5.13	99.31	Ca-rich
38	21.14	22.56	40.92	5.90	2.76	87.38	Ca-rich
39	28.99	13.54	54.76	0.56	1.71	99.00	Ca-rich
40	7.29	4.01	88.16	0.25	0.20	99.66	Ca-rich
41	24.81	7.76	50.77	9.21	0.16	83.50	Ca-rich
42	20.12	3.01	75.40	0.52	0.37	98.91	Ca-rich
43	15.92	42.27	30.61	3.64	4.06	92.85	Ca-rich

Grain 3	Molar % Fe	Molar % Ca	Molar % Mg	Molar % Si	Molar % Mn	totals	Carb type
1	24.14	8.75	64.93	0.23	0.82	98.63	rosette
2	5.12	72.03	15.13	0.07	7.42	99.69	Ca-rich
3	13.19	49.88	28.55	0.11	7.66	99.28	Ca-rich
4	14.16	44.59	35.04	0.13	5.39	99.17	Ca-rich
5	18.49	37.92	37.34	0.55	4.51	98.27	Ca-rich
6	33.67	18.90	40.07	1.17	3.98	96.62	Ca-rich
7	30.80	14.86	51.19	0.07	2.08	98.93	Ca-rich
8	33.47	14.32	48.39	0.21	2.45	98.63	Ca-rich
9	33.35	12.76	51.06	0.56	0.92	98.10	Ca-rich
10	27.48	9.70	61.05	0.28	0.62	98.84	Ca-rich
11	16.56	8.82	72.04	0.38	0.60	98.03	rosette
12	23.19	7.09	67.31	0.28	0.30	97.88	rosette
13	28.14	8.38	60.66	0.51	0.22	97.40	rosette
14	26.85	8.77	61.71	0.38	0.37	97.71	rosette
15	27.76	9.35	60.27	0.24	0.50	97.88	rosette
16	19.20	6.15	71.72	0.37	1.21	98.29	rosette
17	21.29	4.87	70.83	0.66	0.99	97.98	rosette
18	10.81	35.49	49.44	0.28	3.40	99.14	Ca-rich
19	5.86	74.33	11.97	0.02	7.66	99.81	Ca-rich
20	10.89	57.58	23.05	0.21	7.76	99.27	Ca-rich

Grain 4	Molar % Fe	Molar % Ca	Molar % Mg	Molar % Si	Molar % Mn	totals	Carb type
1	26.55	4.65	66.48	0.16	0.58	98.27	rosette
2	8.93	18.96	69.95	0.18	1.75	99.59	rosette
3	8.77	66.62	17.25	0.27	6.74	99.38	Ca-rich
4	19.42	34.10	41.07	0.33	4.37	98.96	Ca-rich
5	5.41	5.14	7.77	53.35	0.13	18.44	Ca-rich
6	4.54	4.54	11.09	55.87	0.13	20.30	Ca-rich
7	0.68	4.60	0.32	60.73	0.04	5.64	Ca-rich
8	19.10	35.95	39.59	0.29	4.53	99.18	Ca-rich
9	16.87	41.84	35.11	0.38	5.27	99.10	Ca-rich
10	14.75	45.43	33.21	0.12	6.06	99.45	Ca-rich
11	13.63	21.64	44.76	15.35	1.75	81.77	rosette
12	25.35	23.29	47.42	0.12	3.00	99.05	Ca-rich
13	30.15	15.37	51.51	0.03	2.19	99.23	Ca-rich
14	28.52	18.67	49.37	0.08	2.58	99.14	Ca-rich
15	25.71	24.10	46.47	0.03	3.18	99.47	Ca-rich
16	15.20	44.18	34.70	0.00	5.57	99.65	Ca-rich
17	29.96	17.53	49.21	0.12	2.44	99.13	Ca-rich
18	32.42	18.11	44.13	0.12	4.43	99.09	Ca-rich
19	25.66	7.77	42.20	19.81	1.37	76.99	Ca-rich
20	32.49	14.44	49.96	0.09	2.27	99.16	Ca-rich
21	33.92	13.55	48.66	0.50	2.65	98.77	Ca-rich
22	8.83	66.15	17.30	0.56	6.67	98.95	Ca-rich
23	5.85	75.47	9.58	0.06	8.79	99.71	Ca-rich

Note the high silica content of several analyses which is due to analysis volume (sub-surface) overlapping regions of carbonate and feldspathic glass. This is not unexpected given the 3 dimensional nature of the intermingled carbonate and feldspar.

Jeol SEM EDS analyses of ALH84001 maskelynite showing the homogeneity of composition. A representative selection of SEM data is presented.

Al	Si	Fe	Mg	K	Na	Ca	totals
10.26	25.02	1.30	0.77	1.05	2.48	3.30	44.19
12.40	27.18	0.61	0.00	0.59	3.89	4.20	48.87
12.25	26.75	0.48	0.00	0.61	4.00	4.16	48.25
11.44	24.90	0.61	0.00	0.61	2.80	4.24	44.60
11.64	25.02	0.92	0.38	0.50	3.49	4.57	46.53
11.11	25.13	0.65	0.08	0.76	3.03	4.21	44.97
11.70	26.96	0.50	0.00	1.11	3.75	3.66	47.69
11.99	26.51	0.47	0.00	0.64	3.35	4.19	47.16
11.79	27.09	0.50	0.00	0.93	3.76	3.61	47.66
12.47	28.33	0.55	0.00	0.96	4.05	3.90	50.26
12.37	27.56	0.49	0.00	1.08	3.23	3.99	48.72
12.57	27.73	0.52	0.00	0.65	1.40	4.18	47.04
12.33	27.27	0.54	0.00	0.00	3.81	4.10	48.04
12.31	27.42	0.48	0.00	0.83	3.76	3.86	48.66
11.86	27.09	0.52	0.00	0.84	3.27	4.05	47.63
12.15	27.34	0.71	0.34	0.54	0.73	4.65	46.47

Cations only

Al	Si	Fe	Mg	K	Na	Ca	
23.23	56.62	2.95	1.74	2.37	5.62	7.47	
25.38	55.61	1.25	0.00	1.20	7.97	8.58	
25.39	55.43	0.99	0.00	1.27	8.29	8.62	
25.65	55.83	1.37	0.00	1.37	6.28	9.50	
25.03	53.78	1.99	0.82	1.08	7.49	9.82	
24.70	55.89	1.45	0.18	1.68	6.73	9.37	
24.54	56.53	1.05	0.00	2.32	7.87	7.68	
25.43	56.21	1.00	0.00	1.36	7.10	8.89	
24.73	56.83	1.05	0.00	1.94	7.88	7.57	
24.80	56.36	1.10	0.00	1.91	8.06	7.77	
25.39	56.56	1.00	0.00	2.22	6.63	8.20	
26.71	58.95	1.11	0.00	1.38	2.97	8.88	
25.66	56.76	1.12	0.00	0.00	7.93	8.54	
25.30	56.34	0.98	0.00	1.71	7.73	7.93	
24.91	56.89	1.09	0.00	1.76	6.86	8.50	
26.15	58.84	1.53	0.72	1.17	1.58	10.00	

Forcing totals to 100%